Using 1D and 2D Nanomaterials in Halide Perovskite Solar Cells to Enhance Light Harvesting and Charge Collection

by

Ujwal Kumar Thakur

A thesis submitted in partial fulfillment of the requirements for the degree of

Doctor of Philosophy

In
Solid State Electronics

Department of Electrical and Computer Engineering
University of Alberta

Abstract:

The increasing global energy demand and scarcity of available energy resources have spurred research efforts to find cheap and abundant alternative energy sources. Solar energy is the inexhaustible renewable energy resource that has the potential to supply more than 15 TW/annum of carbon-neutral energy. Among solar energy harvesting devices, solar cells are the most efficient, directly converting solar energy into electricity.

Inorganic solar cells based on materials such as crystalline silicon, cadmium telluride and copper indium germanium selenide constitute mature technologies that exhibit a relatively high-power conversion efficiency of around 12−20% in deployed modules and thus dominate commercially available photovoltaic technologies. However, the relatively long energy payback times of inorganic solar cells have partially impeded their pace to widespread deployment, and thus alternative approaches are being explored. Organic photovoltaics (OPV), dye-sensitized solar cells (DSSCs), halide perovskite solar cells (HPSCs) and quantum-dot solar cells are examples of next-generation solution-processable solar cell technologies that have emerged as low cost, short energy payback time alternatives to replace conventional solar cells. Among these low-cost solar cells, HPSCs have revolutionized the field of photovoltaics by exhibiting the potential for ultralow cost fabrication and short energy payback times while simultaneously achieving solar-to-electricity power conversion efficiencies comparable to inorganic solar cells. Two major issues preventing deployment and commercialization of perovskite solar cell technology are stability and efficiency. Simple and economical encapsulation technologies have been developed to provide excellent encapsulation of OLED displays in commercial smartphones and OPV modules. It is therefore reasonable to expect that such techniques will be adapted to encapsulate HPSCs and thus

potentially solve the stability issue. On the other hand, boosting the efficiency of HPSCs to their theoretical limit is more challenging. The efficiency of such solar cells mainly depends on (i) their ability to capture and trap the photons of the light (ii) the ability to manipulate the directionality, entropy and quantum efficiency of re-radiated photons (i.e. fluorescence) and (iii) the efficient separation and collection of photogenerated charge carriers.

HPSCs contain a thin film of the halide perovskite active layer sandwiched between an electron transport layer and a hole transport layer. Halide perovskites have different electron and hole diffusion lengths because of which a nanostructured charge transporting layer is generally used to improve the charge collection efficiency. In the state-of-the-art *n-i-p* type solar cells, mesoporous TiO_2 is used as the electron transport layer which suffers from poor charge transport (due to a random-walk type dispersive hopping of charge carriers) and poor light management inside the solar cells. Vertically aligned and near horizontally aligned TiO_2 nanorod arrays were fabricated and used as the electron transporting material in the perovskite solar cells to realize high-efficiency *n-i-p* type perovskite solar cells. 17.6 % champion efficiency was realized with a solar cell architecture comprising monocrystalline vertically standing TiO_2 nanorods (TNRs) infiltrated with perovskite and synthesized using facile solution processing without non-routine surface conditioning. TNR ensembles are desirable as electron transporting layers (ETLs) HPSCs because of potential advantages such as vectorial electron percolation pathways to balance the longer hole diffusion lengths in certain halide perovskite semiconductors, ease of incorporating nanophotonic enhancements, and optimization between a high contact surface area for charge transfer (good) vs. high interfacial recombination (bad). These advantages arise from the tunable morphology of hydrothermally grown rutile TNRs, which is a strong function of the conditions of growth. Horizontal nanowires have received much less attention despite their higher photonic

strength due to overlapping electric and magnetic dipolar Mie resonance modes. Horizontal TiO_2 nanorods were fabricated on FTO substrates *via* a facile hydrothermal route. The HATNRs are employed as the ETL to achieve 15.03% power conversion efficiency (PCE) in HPSCs which is higher than the PCE of compact TiO_2 based devices (10.12 %) by a factor of nearly 1.5. Also, the hole transporting property of a NiO nanostructure with Ni^{3+} defect deposited by the solvothermal method has been studied in *p-i-n* type perovskite solar cells. With an optimized nanostructure, a high-efficiency solar cell with a power conversion efficiency ~34% higher than that of the conventional compact NiO based perovskite solar cells have been fabricated. Also, the effects of g-C_3N_4 and C_3N_5 doping on the charge transport properties of the perovskite active layer and hence on photovoltaic properties of perovskite solar cells have been studied.

Preface:

Chapter 1 has been adapted from a published article, Thakur UK, Kisslinger R, Shankar K. One-dimensional electron transport layers for perovskite solar cells. Nanomaterials. 2017 May;7(5):95.

Results of the research presented in **Chapter 2** have been published as Thakur UK, Askar AM, Kisslinger R, Wiltshire BD, Kar P, Shankar K. Halide perovskite solar cells using monocrystalline TiO_2 nanorod arrays as electron transport layers: impact of nanorod morphology. Nanotechnology. 2017 Jun 14;28(27):274001. I designed and performed the experiments and collected *J-V*, IPCE, SSIS and PL data. Ryan Kisslinger collected SEM images, Benjamin Wiltshire collected UV-vis data, Piyush Kar performed collection and analysis of FLIM data.

Results of research presented in **Chapter 3** have been published as Thakur UK, Zeng S, Kumar P, Patel S, Kisslinger R, Zhang Y, Kar P, Goswami A, Thundat T, Meldrum A, Shankar K. Nanophotonic enhancement and improved electron extraction in perovskite solar cells using near-horizontally aligned TiO_2 nanorods. Journal of Power Sources. 2019 Mar 31;417:176-87. In this work, I designed the experiment, fabricated devices, collected *J-V*, IPCE, PL, TRPL, SEM data. Sheng Zeng performed FDTD simulation. Sahil Patel fabricated TiO_2 nanorods under my supervision. Pawan Kumar performed XPS analysis. Ryan Kisslinger collected TEM images. Yun Zhang collected UV-vis and XRD data. Piyush Kar assisted with IMPS and IMVS analysis, and Ankur Goswami contributed by collecting KPFM data.

Results presented in **Chapter 4** have published as Thakur U, Kumar P, Gusarov S, Kobryn AE, Riddell S, Goswami A, Alam K, Savela S, Kar P, Thundat T, Meldrum A. Consistently high

V_{oc} values in pin type perovskite solar cells using Ni^{3+}-doped NiO nanomesh as the hole transporting layer. ACS Applied Materials & Interfaces. 2020 Jan 6. I planned and performed the experiments, made solar cells, collected *J-V*, C-V, IPCE, PL, TRPL, IMPS and IMVS data. Pawan Kumar assisted in explaining TEM, XPS and UPS data. Sergey Gusarov and Alexander E. Kobryn performed DFT modeling. Saralyn Riddell collected UV-vis data for dye desorption measurements. Kazi M. Alam collected UV-vis and Raman data. Piyush Kar helped in data analysis and interpretation. Spencer Savela assisted in the preparation of NiO samples. Ankur Goswami collected KPFM data.

Results presented in **Chapter 5** are a portion of the article Kumar P, Vahidzadeh E, Thakur UK, Kar P, Alam KM, Goswami A, Mahdi N, Cui K, Bernard GM, Michaelis VK, Shankar K. C_3N_5: A Low Bandgap Semiconductor Containing an Azo-Linked Carbon Nitride Framework for Photocatalytic, Photovoltaic, and Adsorbent Applications. Journal of the American Chemical Society. 2019 Feb 14;141(13):5415-36. In this work, Pawan Kumar made g-C_3N_4 and C_3N_5. I fabricated perovskite solar cells and hole only devices, and collected *J-V*, CV, EIS, EPR, PL, TRPL data and SEM images. Piyush Kar assisted in EIS analysis while Kai Cui helped with TEM image collection.

Acknowledgments:

Foremost, I am thankful to Professor Karthik Shankar for being the coolest supervisor ever. I wouldn't be where I am today without his constant encouragement and guidance, patience and constructive suggestions. I thank him for trusting me and giving me the freedom to explore on my own and always being there to listen and advise. For all this, I will always be thankful to him. I would also like to express my special thanks of gratitude to Professor Alkiviathes Meldrum for training me and letting me use his laboratory instruments, and for his invaluable support and constructive advice throughout my Ph. D. studies. I would also like to express my special thanks of gratitude to Professor Thomas Thundat for his invaluable support and constructive advice. I would like to thank my defense committee members as well for their insightful comments, critical questions and helpful suggestions related to my dissertation work.

I would also like to extend my sincerest appreciation to Dr. Pawan Kumar for guiding me and inspiring me throughout my Ph. D. journey. This thesis would not have been possible without Dr. Pawan Kumar's help and guidance. I would also like to thank my lab alumni Professor Ankur Goswami, Professor Partha Roy and Dr. Piyush Kar for their help and support. I would also like to thank my lab mates Sheng, Yun, Weidi, Najia, Ryan, Ben, Dr. Kazi and Ajay for always being there whenever I needed them.

Last but not the least, I would like to thank undergraduate student interns Phillip, Sahil, Spencer, Taryn and Darren for working on several projects with me during my Ph.D. studies.

Table of Contents:

List of Tables:

List of Figures:

Chapter-1 Introduction

1.1 Motivation:

The increase in world energy demand depends upon the population and economic growth of the people. The world's population was reported to be 7.6 billion in 2017 and it is to reach about 8.4-8.7 billion, 9.4-10.2 billion and 9.6-13.2 billion in 2030, 2050 and 2100 respectively [1]. Energy demand is clearly expected to increase in order to accommodate such a huge population expansion. US Energy Information Administration projects a 28% increase in world energy consumption by 2040 (739 quadrillions Btu) [2]. Fossil fuels are playing a crucial role in today's world energy market as on average about 86% of the energy consumed per year is being generated by burning fossil fuels [3, 4]. The burning of fossil fuels releases greenhouse gas which is responsible for global warming (increase in mean global temperature) and climate change causing an imbalanced ecosystem and jeopardization of the safety of human activities. On the other hand, reserves of fossil fuels are not unlimited which means sooner or later they are going to be used up. There is worldwide research going on to find other reliable energy resources to replace fossil fuels as they diminish; this is mainly being driven due to the uncertainty surrounding the future supply of fossil fuels. Nuclear Energy has the potential to meet world energy demand, however, because of hazards involved with nuclear power generation, it is not considered as a sustainable energy source. This leaves renewable energy as the only option to solve the energy hunger problem that humanity is facing. The increasing global demand for energy and limited availability of energy sources have spurred research efforts to find new and improved sources of cheap, environmentally neutral, renewable energy. There is only one renewable energy source with technical potential safely exceeding 15 TW: solar. Though wind has significant extractable potential, its technical potential

is much less, in large part because much of its power resides geographically over the relatively inaccessible deep oceans. The same is true for solar, but, because its extractable potential is so huge, its land-based technical potential remains large. There are several ways to tap solar energy such as by using solar water heaters, concentrated solar power, and photovoltaics. Among these technologies, photovoltaics is the most popular and has the highest potential [5].

Inorganic solar cells based on materials such as crystalline silicon, cadmium telluride, or copper indium germanium selenide (CIGS) constitute mature technologies that exhibit a relatively high power conversion efficiency (PCE) of around 12−20% in deployed modules [6] and thus dominate commercially available photovoltaic technologies. However, the relatively long energy payback times of inorganic solar cells [7, 8] have partially impeded their pace to widespread deployment, and thus alternative approaches are being explored. Organic photovoltaics [9], dye-sensitized solar cells [10], halide perovskite solar cells [11] and quantum-dot solar cells [12] are examples of next-generation solution-processable solar cell technologies that have emerged as lower cost, lower energy payback time alternatives to replace conventional solar cells [13, 14]. Organometal trihalide perovskite materials with the composition ABX_3 [A=Cs^+, $CH3NH_3^+$ (MA), or $NH{=}CHNH_3^+$ (FA); B = Pb or Sn; X= Br or I] are the focus of intense worldwide research interest for use as light-absorbing materials in photovoltaic cells because of their outstanding optoelectronic properties such as a direct optical bandgap, broadband light absorption, ambipolar transport, and long carrier diffusion lengths devices [15]. In the last decade, a remarkable enhancement in the photoconversion efficiency (PCE) of perovskite solar cells has been demonstrated. Miyasaka *et al.* reported the first halide perovskite solar cells in 2006 [16] with a PCE of 2.2 %, which they improved to 3.8 % in 2009 [17]. A major breakthrough occurred in 2012 when Snaith *et al.* [18] reported an HPSC device with a PCE of 11% using a mixed halide perovskite layer

($CH_3NH_3PbI_{3-x}Cl_x$) as the active layer on nanoporous aluminum oxide. Intensive research into the development of HPSCs is now in progress which has led to a current highest certified PCE of 25.2 % in an astonishingly short period of time [19-21]. Halide perovskite has a high absorption coefficient ($>10^5$ cm^{-1}) throughout the visible spectrum. Because of its direct bandgap (2.3 eV, 1.55 eV, 1.5 eV and 1.3 eV for $CH_3NH_3PbBr_3$, $CH_3NH_3PbI_3$, $NH_2CH{=}NH_2PbI_3$, and $CH_3NH_3SnI_3$ respectively) and high absorption coefficient, a film thickness of few hundreds of nanometers is enough to absorb a considerable amount of light [22].

1.2 Deposition techniques for halide perovskites:

The performance of perovskite solar cells is highly dependent on the crystal structure and morphology of the perovskite absorber, as well as bonding between perovskite and charge-transporting layers. These variables vary according to the perovskite deposition procedure. Furthermore, the thickness of the perovskite layer should be optimized. The perovskite should be thinner than electron and hole diffusion lengths and should be sufficiently thick to prevent direct contact between the electron transporting layer and hole transporting layer.

Typically, single-step spin coating, two-step spin coating, and sequential deposition techniques are used to deposit the active layer in perovskite solar cells. The one-step spin casting method involves the mixing of AX and BX_2 in polar solvents such as γ-butyrolactone (GBL), dimethylformamide (DMF) and dimethyl sulfoxide (DMSO) to make the perovskite precursor solution. The precursor solution is spin-cast at sufficient revolutions per minute (RPM) to achieve the desired film thickness. This technique generally involves two spinning steps - one at low RPM and another at high RPM. In a typical synthesis, antisolvents such as toluene, chlorobenzene or ether are added to the spinning substrate prior to the completion of the second spinning step to

remove polar solvents from the film. After the spin coating step, the substrates are annealed in order to force the crystallization of the deposited perovskite layer. This procedure for perovskite active layer deposition was initially introduced by Miyasaka and coworkers in 2009 [23].

In the sequential deposition technique, BX_2 is dissolved in polar solvents such as DMF and DMSO while another solution of AX is made in alcohols such as 2-propanol and methanol. First, BX_2 is spin-coated over the substrate followed by calcination. After cooling down the substrate to room temperature, it is dipped into AX solution followed by annealing to crystallize the perovskite. The sequential deposition procedure was initially developed by Mitzi and colleagues in 1998 [24] while Gratzel and co-workers re-introduced this technique to fabricate perovskite solar cells in 2013 [25]. A major problem with this methodology is the length of time needed to convert BX_2 into ABX_3, during which some of the formed ABX_3 can be leached away from the substrate.

Two-step spin coating is a modified version of sequential deposition in which BX_2 is first spin-coated over the substrate followed by calcination. After cooling down the substrate to room temperature AX dissolved in alcohol is spin-coated over the dry BX_2 layer. Another important deposition technique that has the ability to produce high-performance perovskite solar cells is the dual-source vapor deposition technique which was reported in 2013 by Snaith *et al.* [26]. AX and BX_2 are evaporated simultaneously from two different sources with distinct evaporation ratios to form ABX_3 film on a substrate which is then annealed. Other deposition techniques include sequential vacuum deposition [27], chemical vapor deposition [28], inkjet printing [29, 30], spray coating [31, 32] and slot die coating [33], but these methods have not been successful thus far in producing high-efficiency photovoltaic devices.

1.3 Architecture and operating principle of perovskite solar cells:

As shown in Figure 1.1, perovskite solar cells can be fabricated in two major architectures, *p-i-n,* and *n-i-p*-type. In the *p-i-n*-type architecture, light enters the perovskite layer through the *p*-type hole transporting layer. In such devices, a *p*-type hole transporting layer (HTL) such as CuO, NiO or PEDOT: PSS is deposited on a transparent conductive oxide (TCO)-coated glass substrate. This is followed by the deposition of the perovskite active layer which is then coated over by an *n*-type film of PCBM, ZnO, or C60 which acts as an electron transporting layer (ETL) and subsequently a low work-function metal such as aluminum is evaporated to complete the device [34-39]. In the *n-i-p* type architecture, light enters the perovskite layer through the *n*-type electron transporting layer. In such devices, *n*-type ETL such as TiO_2, ZnO, SnO_2 or WO_3 is deposited on a TCO-coated glass substrate which is then followed by perovskite deposition. Over the perovskite, a *p*-type hole transporting layer (typically spiro-OMeTAD) is deposited and finally, a high work function metal such as gold is deposited to complete the device [36, 40-47]. This *n-i-p* configuration is necessarily used for the formation of solar cells involving 1D-ETLs to allow for proper infiltration of the perovskite into the ETL. Also of note is that ETL-free and HTL-free perovskite solar cells do exist, but their photovoltaic performance is low [36, 42].

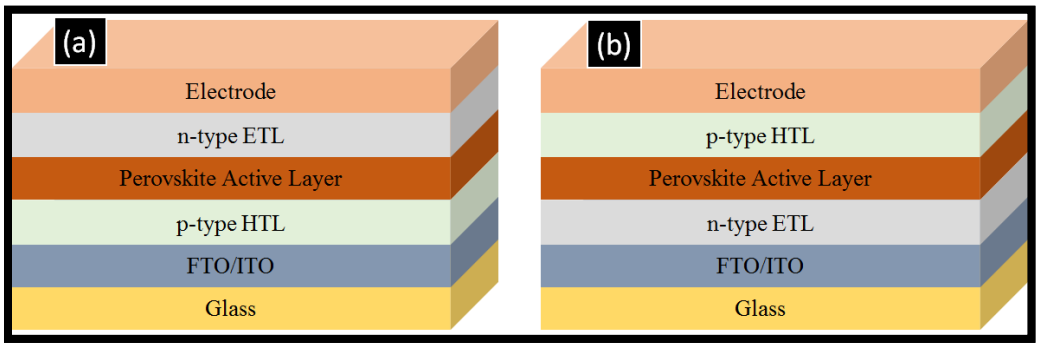

Figure 1.1. Layer configuration for (a) *p-i-n* type and (b) *n-i-p* type perovskite cell architectures.

Ideally, halide perovskites are intrinsic in nature and have low binding energy (2-55 meV) resulting in the generation of free electron-hole pair in the perovskite layer after photon absorption at room temperature [48-50]. As the charges are generated and dissociated in perovskite itself giving rise to the photovoltage. If perovskite is sandwiched between two metal (or metal and TCO), electrons and holes will diffuse towards their respective interface simply by diffusion. The work function difference of two metals (or metal-TCO) is beneficial as it introduces a built-in potential. However, because of the low selectivity of charges at the interface, huge recombination occurs. To prevent such recombination and improve charge selectivity to produce high-efficiency perovskite solar cells, perovskite layer is sandwiched between two different charge transport layers (CTLs) namely electron transport layer (ETL) and hole transport layer (HTL) [51]. ETL should only allow electrons to pass and block holes and HTL should let holes to pass and block electrons. ETL should have a large energy barrier for hole transfer at valence band and HTL should have high energy barrier for an electron at its conduction band. The charge transporting layer reduces the interfacial recombination (recombination at the surface of the perovskite layer) and the work function difference of charge transporting layer allows to drift charges and improves charge collection efficiency.

One challenge associated with perovskite solar cells is the choice of CTLs in solar cell architecture. It is important for them to possess certain properties including an appropriate work function, high bandgap, high conductivity, fast charge transport, and a low recombination rate at the interface. As shown in Figure 1.2, the free charge carriers formed inside the perovskite layer after photon absorption can quickly be injected into the charge transporting layers and finally the electrons and holes are extracted to their respective contacts resulting in an open circuit voltage between the contacts when no load is connected.

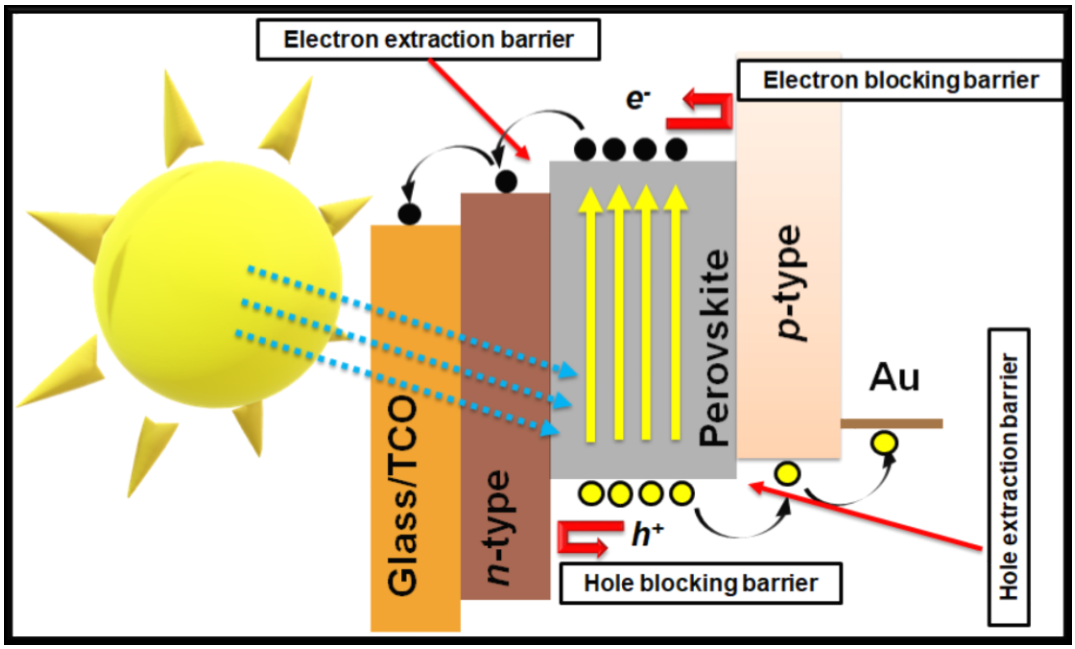

Figure 1.2. Schematic illustration of the working principle of *n-i-p* type halide perovskite solar cells.

Table-1.1 shows the electronic properties of commonly used ETL, HTL and $CH_3NH_3PbI_3$. ETL and HTL form *n-i* and *p-i* junctions with the perovskite layer at their respective interfaces. Electrons get injected into the ETL. The *n-i* selective to the passage of the electrons and blocks the holes while the *p-i* junction is selective to the passage of the holes and blocks the electrons. These junctions are responsible for the creation of a built-in electric field at the interface which allows efficient charge separation electrons move to the ETL and holes to the HTL. The stronger built-in electric field provides more efficient charge separation and reduced bulk recombination of the carriers. Since both ETL and HTL have different Fermi levels, charges flow until equilibrium is reached and a space charge region is created at the respective interface as a result of which band bending is observed. The doping concentration of *n*-type ETL and *p*-type HTLs which are commonly used in perovskite solar cells are generally in the range 10^{18}-10^{19} cm^{-3} while average

value of carrier density in perovskite is approximately 10^{15} cm^{-3} because of which the entire thickness (300-500 nm) of the absorber layer is generally fully depleted [52-57].

Table 1.1: Electron affinity, bandgap, ionization potential, work function, carrier density and carrier mobility of TiO_2, $CH_3NH_3PbI_3$ and Spiro-MeOTAD.

Parameter (unit)	Electron Affinity (eV)	Band Gap (eV)	Ionization Potential (eV)	Work Function (eV)	Carrier Concentration (cm^{-3})	Electron mobility (cm^2/Vs)	Hole mobility (cm^2/Vs)	Ref.
Anatase TiO_2	4	3.2	7.2	4.65	1.70×10^{19}	0.1-4	4	58-63
$CH_3NH_3PbI_3$	3.6	1.6	5.2	Variable dependent (VD)	10^{10}-10^{15} (VD)	3 (VD)	17 (VD)	64-68
Spiro-MeOTAD	1.5	3.5	5	4.4	10^{18}	1.6×10^{-4}	1.6×10^{-4}	69-72

1.4 Objectives of this thesis:

Figure 1.3 represents the photovoltaic performance of the maximum reported efficiency of various solar cells in terms of the ratio of J_{sc} versus $FF \times V_{oc}$ relative to the SQ-limiting values of the solar cell materials. $J_{sc}/J_{SQ}<1$ suggests the incomplete absorption of light in the solar cells which generally calls for the application of nanophotonic structures in the solar cells to boost its efficiency. On the other hand $V_{oc}FF/V_{SQ}FF_{SQ}<1$ indicates the presence of carrier recombination, parasitic resistance and other electrical nonidealities and efficiency of such solar cells can be improved by using proper strategies to improve the carrier management [19]. Theoretically, an efficiency of 30.14% (J_{sc}=25.47 mA/cm^2, V_{oc}= 1.309V and FF=90.5%) can be obtained from the single-junction solar cell made with the semiconductor with the bandgap of 1.6 eV. As can be seen in Figure 1.3, there is room to improve the efficiency of perovskite solar cells by improving light management in the cells. It can be done by introducing well designed nanophotonic structures in the cell architecture to enhance light coupling and trapping. The photonic losses include losses due

to inadequate harvesting of incident photons in sunlight with energies close to perovskite band-edge and thermodynamic losses due to non-radiative recombination and changes in the entropy of radiated photons. In this thesis, I worked on nanophotonic structures such as vertically oriented nanorod arrays and horizontally aligned nanorods to enhance forward scattering and suppress back-scattering, which in turn enhanced the harvesting of photons near the band-edge and enabled the achievement of higher solar cell efficiencies. $V_{oc}FF/V_{SQ}FF_{SQ}$ for perovskite solar cells is ~75% which indicates that there is still much room to improve the efficiency of HPSCs by improving carrier collection in the cell. I also have worked on optimizing charge transport layers (both the electron transport layer and the hole transport layer) to maximize the extraction of photogenerated charge carriers in HPSCs.

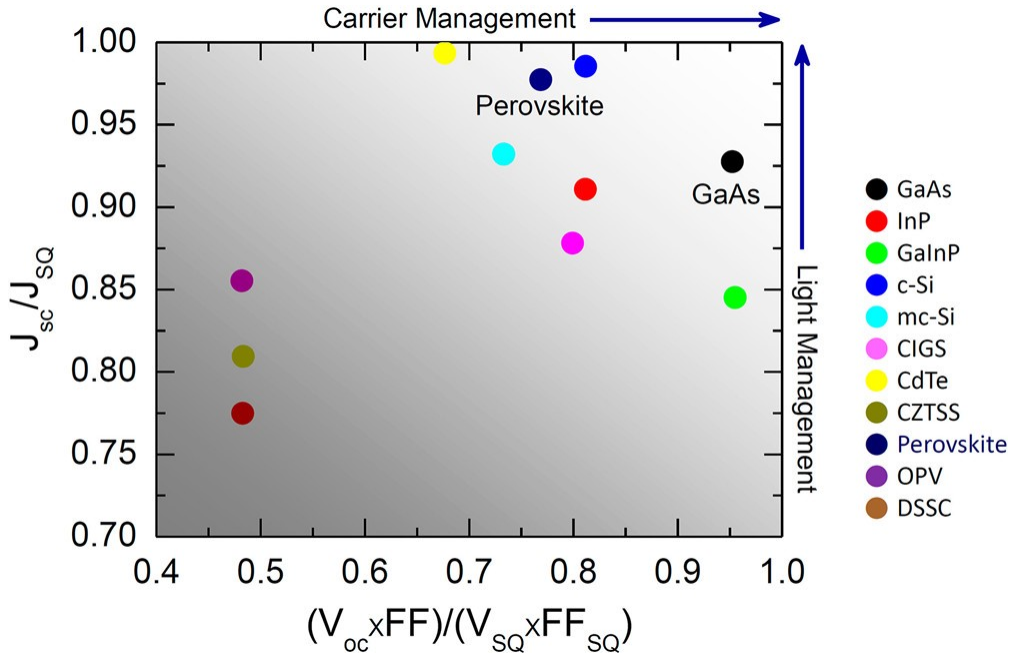

Figure 1.3: J_{sc}/J_{SQ} versus the $V_{oc}FF/V_{SQ}FF_{SQ}$ for the record efficiency solar cells [73]. Copyright 2018, American Chemical Society.

The mobility and hence diffusion length of photogenerated electron and holes in the perovskite layer are not the same, which calls for the application of nanostructured CTLs [74-76]. Both inorganic and organic semiconductors have been used as ETL, with TiO_2 being most common and achieving greater success. The morphology of the ETL layer is also of importance with planar film layers, mesoscopic particulate layers, and nanostructured layers being used. Planar film layers, while being the easiest to fabricate, do not provide the mesoscopic effect as they can't collect electrons from the bulk of perovskite. To improve the charge collection efficiency, a thin mesoporous layer is generally deposited on top of the planer ETL. Mesoporous TiO_2 is the most common ETL used for perovskite solar cells as it provides a good mesoscopic effect. The mesoporous architecture is comprised of a large number of ca. 20-30 nm-sized nanoparticles with many grain boundaries; this restricts the flow of electrons, resulting in poor charge transfer. Mesoporous architecture does not provide a unified path to photogenerated electron flow which leads to a random walk of electrons through the ETL as illustrated in Figure 1.4a [77, 78]. Such a random walk-type transport increases the path length electrons must travel to the collecting electrode and increases recombination probability. To overcome problems associated with the mesoscopic structure, I have used the 1D TiO_2 nanorods as an ETL to fabricate high-efficiency perovskite solar cells. The directional charge transport properties (Figure 1.4b) of 1D nanostructures enables improvement in the charge collection efficiency as the overall length of the path a charge takes on its way to being collected is reduced and thus charge recombination is limited ultimately improving the solar cell efficiencies [79-82]. In **Chapter 2** and **Chapter 3**, I have tried to explain the advantages of using 1D TiO_2 nanorod arrays in perovskite solar cells. The effect of morphology and orientation of nanorods on the photovoltaic properties of solar cells has also been explained in detail.

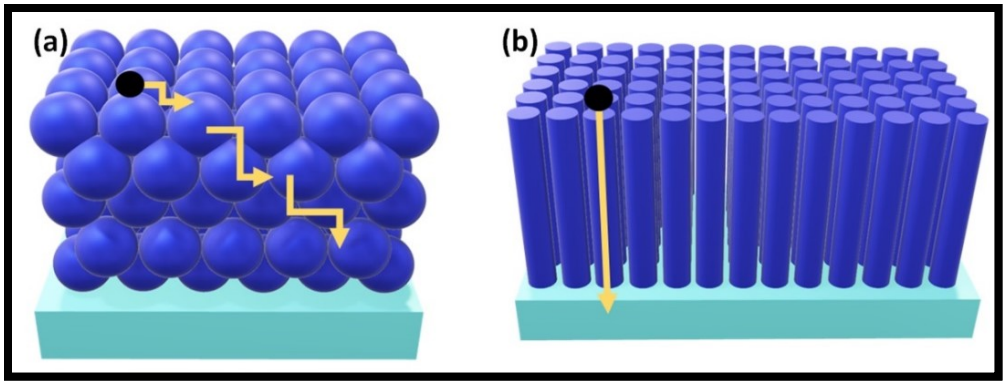

Figure 1.4. Schematic illustration of (a) random walk in the mesoporous charge-transporting layers and (b) vectorial charge transport property of nanorod type charge transporting layer.

It is noteworthy that *p-i-n* type PSCs using a PEDOT: PSS HTL struggle to achieve V_{oc} values > 1 V. Energy level mismatch of PEDOT: PSS with perovskite, its high acidic nature, high hydrophilic property, low conductivity, and formation of pinholes in perovskite layer deposited over PEDOT: PSS are some reasons because of which most PEDOT:PSS based *p-i-n* type PSCs have a low open-circuit voltage.[83-86] Several inorganic metal oxides and hybrid oxides and such as VO_x, MoO_x, Cu_2O, CuO_x, NiO_x, CoO_x and CrO_x are being investigated as the HTL for high-efficiency PSCs; however, only nickel oxide-based PSCs have been able to achieve PCEs above 20% till date.[39, 87-93] In **Chapter 4**, I present a scalable, hydrothermal method to fabricate high mobility NiO HTL. Hydrothermal growth offers exceptional control over the morphology, chemical composition, and defect density of nanostructured NiO. I have shown that this approach provides nanostructured NiO which can be used as an HTL to achieve an open-circuit voltage as high as 1.14 V.

Traps in perovskite active layers are another major issue that must be addressed in order to achieve high-efficiency perovskite solar cells. Traps in perovskite active layer are generally

formed because of its low stability and also because of polycrystallinity (i.e. at grain boundaries). Traps acts as recombination centers in the perovskite active layer and are thus responsible for non-radiative recombination, low carrier lifetime and short carrier diffusion lengths which degrade the photovoltaic properties. Use of interfacial layer, modified deposition techniques for perovskite layer, chemical doping and addition of additives to promote crystallization are some of the strategies that are being used to reduce trap states in perovskite active layers. **Chapter 5** of this thesis talks about the unique way to passivate traps in the perovskite layer by doping the perovskite layer using 2D carbon nitride sheets. The hole mobility of the doped perovskite layer was improved almost two times because of which recombination in the perovskite was lowered and hence high-power conversion efficiency was realized.

In **Chapter 6**, the main limitations, achievements and the findings of the thesis are summarized. Other loss mechanisms in perovskite solar cells have been identified and prospective methods to overcome them has been discussed. Also, a low temperature, solution-processable electrochemical deposition of ZnO nanorods for flexible perovskite solar cells has been discussed.

Chapter-2 Vertically Aligned TiO_2 Nanorod Array ETL

2.1 Introduction:

Organometal trihalide perovskite materials with the composition ABX_3 [A=Cs^+, $CH_3NH_3^+$ (MA), or $NH{=}CHNH_3^+$ (FA); B = Pb or Sn; X= Br or I] are the focus of intense worldwide research interest for use as light-absorbing materials in photovoltaic cells because of their outstanding optoelectronic properties such as a direct optical bandgap, broadband light absorption, ambipolar transport, and long carrier diffusion lengths. In the last decade, a remarkable enhancement in the photoconversion efficiency (PCE) of perovskite solar cells has been demonstrated. Miyasaka *et al* reported the first perovskite solar cell in 2006 [16] with a PCE of 2.2 %, which they improved to 3.8 % in 2009 [17]. Intensive research into the development of HPSCs is now in progress which has led to a current highest certified PCE of 22.1 % [94]. In general, certain members of the organometal trihalide perovskite semiconductor family including $MAPbI_3$ and $FAPbI_3$ have a lower effective electron diffusion length compared to the effective hole diffusion length in solution cast thin films [95, 96], an issue which one-dimensional electron transport layers (1D-ETLs) can assist with, because of which nanostructured ETLs offer the potential to enhance the performance of HPSCs [74, 95, 97]. The nanostructured ETL not only improves electron transport but also provides mechanical support and scaffold for the perovskite absorber layer in solar cells. Nanostructured ETLs could also be used to reduce thermodynamic losses related to photons [98, 99] through incorporation of a number of nanophotonic effects such as photonic bandgap crystals [100-103], resonant and non-resonant Mie scatterers [104, 105], whispering gallery modes [106] and waveguide modes [107]. Transparent semiconducting metal oxides such as TiO_2, SnO_2, ZnO, $SrTiO_3$ and WO_3 are the most commonly used ETL materials that ensure efficient contact with the perovskite active layer and selectively

transfer photogenerated electrons to the underlying electrode while also blocking holes [40, 45, 108-110]. Mesoporous TiO_2 is the most common ETL used for perovskite solar cells. The mesoporous architecture is comprised of a large number of *ca.* 20 nm-sized nanoparticles with many grain boundaries; this restricts the flow of electrons, resulting in poor charge transfer. Furthermore, the mesoporous architecture does not provide a unified path to photogenerated electron flow which leads to a random walk of electrons through the ETL [77, 78]. Such random walk-type transport increases the length of the path electrons must travel to the collecting electrode and increases the probability of recombination. To overcome problems associated with the mesoscopic structure, a tremendous effort is being devoted towards the application of 1D-ETLs in HPSCs. 1D-ETLs provide a direct path for photogenerated electron transport and have a large internal surface area, leading to fast charge transport, efficient charge separation, and a superior charge collection efficiency. 1D-ETLs also provide better pore filling of the perovskite absorber than the nanoparticulate structure in mesoscopic TiO_2 thin films because of their open pore structure [111-113]. TiO_2, ZnO, WO_3, and CdS nanorods and nanotubes have been tested as ETLs for perovskite solar cells, but only TiO_2 nanorods (TNRs) have consistently produced HPSCs with PCEs above 15 % [47, 114-116]. Several works on the application of TNRs as ETLs have been documented. Qui *et al* reported TNRs sensitized using an extra thin layer of $CH_3NH_3PbBr_3$ having a PCE of 4.87 % [117]. Park *et al* compared the photovoltaic performance of long (> 1 μm) and short (< 1 μm) TNRs and found that the shorter nanorods provided better infiltration of perovskite. By using 560 nm long nanorods, they achieved a PCE of about 9.4 % [113]. Jiang *et al* tried to further optimize the length of nanowires for high-performance HPSCs; they found that increasing the length of nanowires to 900 nm helped improve the PCE by enhancing the short-circuit current density while increasing the nanowire length to 1.2 μm drastically reduced the short circuit current and open-

circuit voltage [118]. Recently, Li *et al* [115] reported perovskite solar cells with a PCE of 18.2 %. They tuned the morphology of titania nanorods by using different organic acids in the growth solution of nanorods and used a UV-ozone treatment to improve the TNR/perovskite interface [115]. Unlike the use of organic acids or plasma treatment or ALD coatings on the surface, the only surface treatment employed by us was the well-established $TiCl_4$ treatment, which is considered routine for nanostructured TiO_2 [119-121]. Herein, we present an in-depth discussion of the electrical behavior of HPSCs based on TNR ETLs, which is extremely necessary in order to understand the sources of both underperformance and outperformance in various device parameters so as to enable the achievement of even higher efficiencies close to the S-Q limit [122]. We performed a detailed study of the effect of the nanorods on the optical properties of the resulting HPSCs. We demonstrated the effect of morphology on charge separation and recombination at the perovskite/TNR interface. We optimized the morphology of hydrothermally grown rutile nanorods to produce perovskite solar cells with a champion PCE of 17.6 %.

2.2 Experimental:

2.2.1 Synthesis of TiO_2 nanorod arrays:

Titanium (IV) *n*-butoxide, titanium (IV) isopropoxide, acetonitrile**,** lead iodide, and lead bromide were purchased from Acros Organics. Acetic acid, HCl, formamidinium iodide, 4-tert-butylpyridine, lithium bis(trifluoromethanesulfonyl)-imide and spiro-OMeTAD were purchased from Sigma-Aldrich. Methylammonium bromide was obtained from Dyesol. Chlorobenzene, titanium (IV) chloride, dimethylformamide (DMF) and dimethylsulfoxide (DMSO) were purchased from Fisher Scientific. Chemicals were used as received without any further purification. Fluorine-doped tin oxide (FTO) coated glass slides (Hartford Tec Glass Company)

were used as substrates and were first cleaned by sonicating in acetone, methanol and deionized water for 10 minutes each. A thin compact layer of TiO_2 was deposited on the cleaned FTO:glass substrate (Figure 2.1a). The precursor solution for the deposition of compact TiO_2 was prepared by a method described elsewhere; in brief, 369 µl of titanium (IV) isopropoxide and 70 µl of 1 M HCl were separately diluted in 2.53 ml of isopropanol. Diluted HCl was added drop by drop into the diluted titanium (IV) isopropoxide solution under stirring. After overnight stirring of the mixed solution, it was filtered using a 0.2 µm filter and deposited over cleaned FTO:glass substrates by spin-casting at 3000 RPM for 30 seconds, followed by calcination at 450 ºC for 30 min [123-125]. The TiO_2 nanorod array was grown on the FTO/TiO_2 substrate by a simple hydrothermal method. 2.5 ml of HCl (37%) and 2.5 ml of glacial acetic acid were mixed with 5 ml of DI water in ambient conditions. The mixture was processed in a Teflon-lined stainless steel autoclave after adding the proper amount of titanium (IV) *n*-butoxide (TBO) into it. The substrate was placed in the autoclave at an angle such that the FTO/TiO_2 side faced downwards. The autoclave was then sealed, and hydrothermal growth was conducted at 200º C for 30 min in a laboratory oven (Figure 2.1b). Subsequent to nanorod growth, the autoclave was cooled to room temperature in ambient air; the resulting transparent nanorod array (Figure 2.1c) was rinsed with DI water for 2 min and dried in a stream of flowing nitrogen. The TNR array was then treated with 40 mM of $TiCl_4$ at 70 ºC for 30 minutes and annealed at 500 ºC for 30 mins. Mesoporous TiO_2 ETLs were deposited on FTO/TiO_2 by spin-casting followed by calcination at 500 ºC for 30 min.

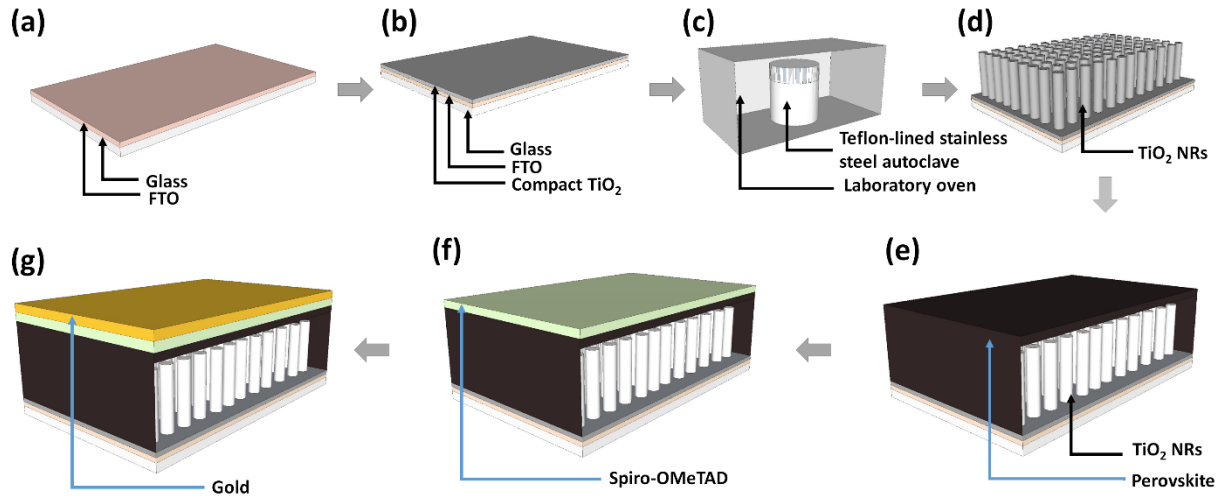

Figure 2.1. Schematic illustration of perovskite solar cell fabrication based on TiO_2 nanorods (a) Compact TiO_2 layer deposited over clean FTO:glass substrate (b) Hydrothermal growth of TNRs on FTO:glass substrates in laboratory gravity convection oven at 200°C for 1 hr (c) Grown rutile TNR array and (d, e, and f) Perovskite active layer, spiro-OMeTAD and gold electrode deposited over $TiCl_4$-treated rutile nanorods respectively.

2.2.2 Characterization:

The morphologies of the TNRs and the TNR-perovskite solar cells were imaged using a Hitachi S4800 cold field emission scanning electron microscope (FESEM) using an accelerating voltage of 5 kV and a beam current of 20 μA. UV-Vis-NIR spectroscopy was performed using a Perkin Elmer Lambda-1050 spectrophotometer equipped with a 100 mm integrating sphere accessory. Steady-state photoluminescence (PL) spectra were collected using a Varian Cary Eclipse spectrofluorometer. The fluorescence lifetime imaging microscopy (FLIM) was performed by exciting the samples using the 750 nm output of a femtosecond Ti:sapphire laser, and then imaging the resulting PL using a Zeiss LSM 510 NLO multi-photon microscope equipped with a FLIM

module that consisted of a Hamamatsu RS-39 multichannel plate detector, a filter wheel, and a Becker Hickl Q5 SPC730 photon counting board. The fluorescence decay curve was constructed by synchronizing information from a photodiode and from the laser pulses. Solid-state impedance spectroscopy (SSIS) was performed in a two-electrode configuration using a CHI-600E potentiostat.

2.2.3 Device fabrication and testing:

Devices were fabricated on FTO coated glass substrates (henceforth referred to as FTO:glass) having a sheet resistance of 8 Ω/□. To prevent shunting upon contact with measurement pins, the FTO:glass substrates were patterned using 35 % HCl and Zn powder. The perovskite precursor solution consisted of 1 M formamidinium iodide (FAI), 1.1 M PbI_2, 0.2 M methylammonium bromide (MABr) and 0.22 M $PbBr_2$ in a 4:1 mixture of DMF and DMSO. The precursor solution was stirred for 2 hours at 70 ºC before being deposited on the TNRs. The perovskite solution was deposited on nanorods in a two-step procedure: first at 1000 rpm for 10 sec and then at 4000 rpm for 20 sec. 100 µl of chlorobenzene was dropped on the spinning substrate at the 15th second of the second step for rapid crystallization. Substrates were then annealed at 100 ºC for 30 min (Figure 2.1d). A hole transporting layer was deposited by spin-casting a solution containing 35 mg of Spiro-OMeTAD mixed with 1 ml of chlorobenzene and additives, namely 4.4 mg of lithium bis(trifluoromethanesulfonyl)-imide, 14 µl of 4-tert-butyl pyridine and 17.5 µl of acetonitrile; this resulted in a hole transporting layer roughly 200 nm thick (Figure 2.1e). A 70-nm thick layer of gold was then thermally evaporated to complete the devices (Figure 2.1f). The current-voltage characteristics of the samples were measured using a Keithley 4200 semiconductor parameter analyzer. For solar cell testing, one sun AM1.5 illumination from a collimated Class A

solar simulator (Newport Instruments) was used. All the photovoltaic devices were masked with a thin black mask which was used to define the active area to be 2 mm * 2mm. Incident photon-to-electron conversion efficiency (IPCE, also known as external quantum yield or EQE) was measured using a lab-assembled set-up consisting of a Xe arc lamp, chopper, filter-wheel, computer-controlled monochromator, calibrated silicon photodetector and optical power meter.

2.3 Results and discussions:

The concentration of the Ti precursor used in the hydrothermal growth process plays a crucial role in determining the morphology of grown nanorods. Figure 2.2 shows cross-sectional and top-view FESEM images of rutile TNR arrays grown with different concentrations of TBO in the acid digestion vessel. For a constant growth temperature and duration - the length, width and packing density of square cross-sectioned nanorods increase with increasing concentration of TBO in the precursor solution. The dimensions of the nanorods were determined to be ~ 100 nm long and ~ 20 nm wide for 400 µl of TBO (A-type), ~ 300 nm long and ~ 40 nm wide for 600 µl of TBO (B-type), ~ 650 nm long and ~ 80 nm wide for 800 µl of TBO (C-type) as shown in Figures 2.2 a−f, and ~ 800 nm long and ~ 150 nm wide for 1000 µl of TBO (D-type). The length and packing density of the nanorods are important parameters which decide the photovoltaic performance of the final HPSCs. Short nanorods with large inter-wire spacing between nanorods do not provide a sufficient number and areal density of heterojunctions for charge separation because of a low roughness factor and a low surface area. High loading of the perovskite absorber and an interwire spacing well below half the electron diffusion length are essential to ensure maximum transfer of photogenerated electrons from the perovskite active layer to the rutile nanorods. On the other hand, a very long and densely packed TNR array suffers from poor infiltration of perovskite compared

to relatively shorter nanorods with larger interspacing [113, 115, 126, 127] and also increases the probability of recombination of electrons transiting through the TNRs toward the FTO electrode with holes transiting in the perovskite toward the Au electrode. Therefore, the morphology of nanorods must be optimized so that it can provide a large surface area with sufficient infiltration of the active layer while also controlling interfacial recombination.

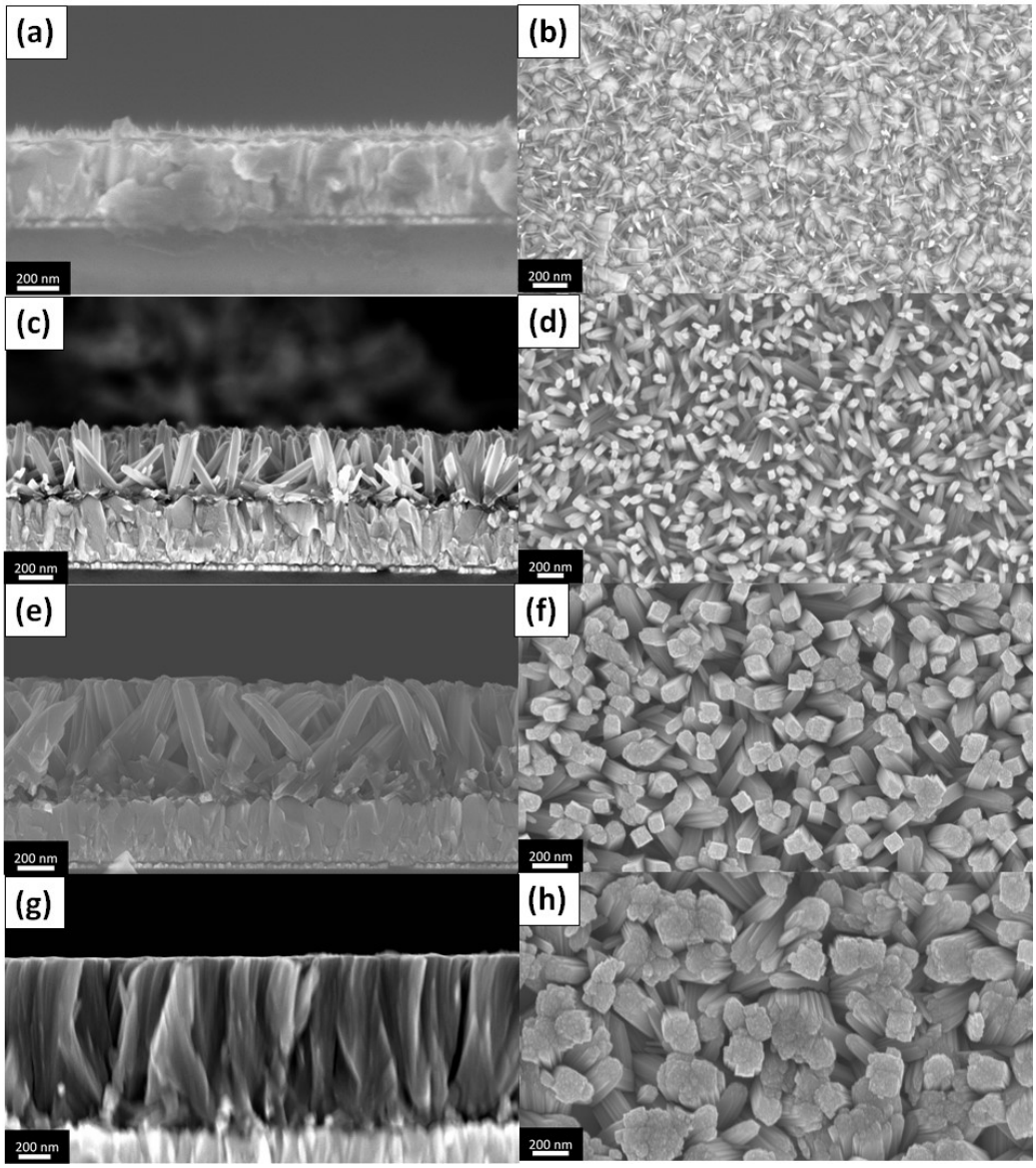

Figure 2.2. Cross-sectional and top-view SEM images of A-type, B-type, C-type and D-type TiO_2 nanorod arrays grown on FTO substrate at 200°C for 1 h using (a, b) 400 µl (c, d) 600 µl (e, f) 800 µl and (g, h) 1000 µl of titanium (IV) *n*-butoxide in the hydrothermal precursor solution respectively.

The dimensions of the nanorods also play a considerable role in their light scattering behavior which in turn, has a significant effect on the light-harvesting efficiency of a solar cell. In dye-sensitized solar cells (DSCs), the correct design and incorporation of Mie scatterers have been used to improve the light-harvesting efficiency of near band-edge photons (~ 700-750 nm) by increasing the optical path lengths of red photons inside the nanostructures [128-130]. However, DSCs consist of a 10-12 µm thick dye-coated nanostructured TiO_2 film coupled to a 3-5 µm thick scattering layer which allows backscattered light from the rear of the solar cell to be efficiently absorbed in the rest of the dye-coated film. On the other hand, the thickness of the active layer in HPSCs is typically much smaller than 1 µm, due to which the conditions of scattering are different. Furthermore, in the *n-i-p* type solar cell geometry used in this study (see Figure 2.1), the TNRs are the scatterers and are placed at the front of the solar cell rather than at the rear, due to which backscattering can actually decrease light harvesting by coupling light out of the solar cell, and forward scattering needs to be matched to the absorption of succeeding layers to improve light harvesting. The light-scattering properties of TNR arrays grown with different concentrations of TBO were studied and are depicted in Figure 2.3. For A-type nanorods, Mie scattering is not significant and the reflectance spectrum is dominated by interference fringes (black curve in Figure 2.3a). The peak in the total reflectance spectrum plateaus and red-shifts as the characteristic dimension increases [105, 131-133], a behavior also observed in Figure 2.3 for TNRs of larger widths formed using increasing concentrations of TBO. Several different TiO_2 nanostructures with

dimensions in the range 50−300 nm are reported to exhibit maximum backscattering at ~ 400 nm [105, 131-133] similar to that observed in Figure 2.3a. The reflectance spectra of the perovskite-filled TNRs are shown in the inset of Figure 2.3b whose most obvious feature is the nearly identical values of total reflectance exhibited by each of the four nanorod morphologies investigated in this study. Since Mie scattering is a strong function of the dimensions of the nanostructures, the lack of morphology dependence is indicative of the dominance of specular reflection rather than diffuse reflection for the nanorod morphologies studied. Interfaces with sharp changes in the refractive index give rise to strong specular reflection. There are three such interfaces for the samples studied here: (i) The air-glass interface (ii) the glass-FTO interface and (iii) the FTO-blend film interface. Over the UV-Vis-NIR spectral range, the refractive index of glass is ~ 1.5 and that of FTO is ~ 2.0. As far as the TNR-perovskite blend is concerned, both the rutile phase of TiO_2 and the perovskite have refractive indices of ~ 2.6 over the wavelength range of interest. Therefore, strong reflections are expected from each of the aforementioned interfaces. Two prominent peaks are seen in the reflection spectra in the inset of Figure 2.3b, one at ~ 350 nm and the other at ~ 500 nm. Rutile-phase TiO_2 exhibits a maximum refractive index of 3.95 at ~ 330 nm and Tec-8 FTO:glass substrates such as those used in this study, are known to have a maximum in their reflection spectra at ~ 350 nm [134], and the peak in the ultraviolet corresponding to these maxima is clearly seen in the inset of Figure 2.3b. The reflectance peak at ~ 500 nm is due to the perovskite exhibiting a maximum refractive index of 2.79 at ~ 500 nm [135]. Figure 2.3b shows that B-type TNRs blended with perovskite (red curve in Figure 2.3b) have the lowest total transmittance indicating it to be the morphology resulting in the most efficient harvesting of light.

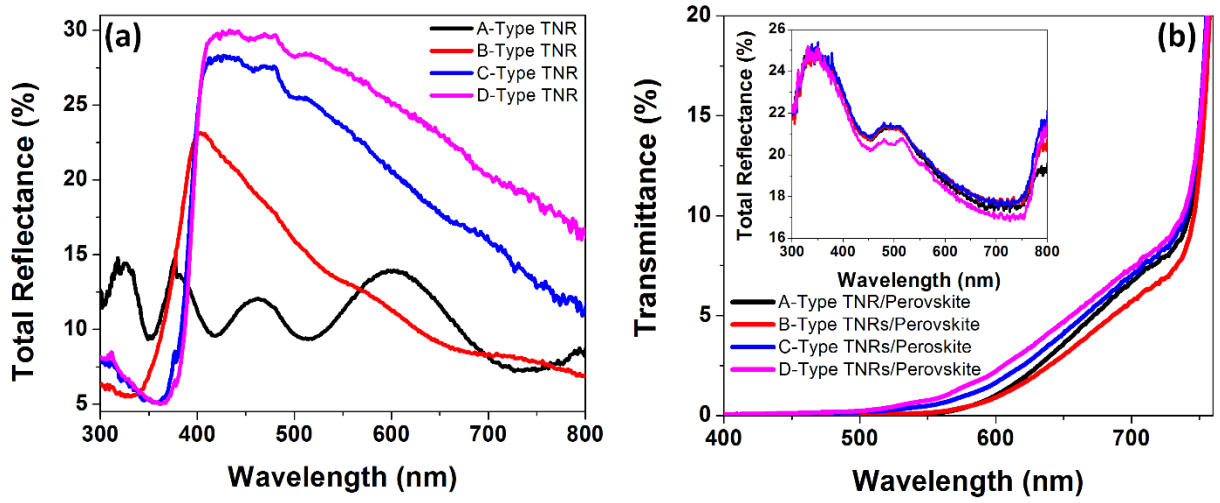

Figure 2.3. (a) Total reflectance (including both specular and diffuse reflectance) spectra of TiO_2 nanorods made with different concentrations of TBO; light is incident directly on the TNRs (b) Total transmittance (including both direct transmission and forward scattering) spectra of TiO_2 nanorod-perovskite blends with the inset showing the total reflectance of the same blends; light is incident through the FTO:glass substrate. Black, red, blue and purple colors represent A-type, B-type, C-type and D-type TiO_2 nanorods with lengths of 100 nm, 300 nm, 650 nm and 1000 nm respectively formed by adding 400 µl, 600 µl, 800 µl and 1000 µl of titanium (IV) *n*-butoxide into hydrothermal precursor solution respectively.

The photovoltaic performance of perovskite solar cells with fabricated on different types of TNR arrays are summarized in Table 2.1 and Figure A1. The photovoltaic performance of champion cells based on A-type, B-type and C-type nanorod morphologies is shown in Figure 2.4 (a) while the same for D-type TNRs are shown in Figure A2. One sun illumination of solar cells based on A-type nanorod arrays yielded an average PCE of 14.08 ± 0.70%, resulting from the open-circuit voltage (V_{oc}) of 1.01 ± 0.02 V, photocurrent density (J_{sc}) of 21.86 ± 1.07 mA cm^{-2} and fill factor (FF) of 0.64 ± 0.02. The solar cell based on the B-type TNR arrays showed improvement

in J_{sc} and FF with the corresponding improvement in PCE to 16.57 ± 1.04 %. Upon further increasing the length of the nanorods to ~ 650 nm and the width to ~ 80 nm (C-type NRs), a significant decrease in V_{oc}, J_{sc}, and FF was observed resulting in the corresponding decrease in PCE to 11.74 ± 0.47 %. The maximum J_{sc} being obtained for B-type TNR arrays correlates well with this morphology, harvesting light most efficiently as shown in Figure 2.3 and Figure 2.4d and explained previously. J_{sc} is proportional to IPCE which is a product of light-harvesting efficiency (η_{lh}), charge separation efficiency (η_{cs}) and the charge collection efficiency (η_{cc}). Figure 2.4c shows that for all three nanorod morphologies whose IPCE action spectra are plotted, the lowest external quantum yields occur for at ~ 400 nm (other than in the near band edge spectral region). A partial explanation of this phenomenon is the high specular reflection observed for blue and ultraviolet photons as seen in Figure 2.3b. A second reason is that the absorption of blue and ultraviolet photons is competitive between the perovskite, the spiro-OMeTAD and the rutile TNR ETL, all three of which have high absorption coefficients in this spectral range. Previous reports have shown that photons absorbed by the spiro-OMeTAD layer are not efficiently harvested and mostly lost to recombination [136]. Furthermore, while electron-hole pairs generated in the perovskite are well-separated through electron transfer to the TiO_2 and hole transfer to spiro-OMeTAD following hole diffusion in the perovskite layer, it is unclear if photogenerated holes in TiO_2 are able to efficiently transfer into the perovskite layer. The high optical path lengths due to scattering within the ETL and active layer of HPSCs based on C-type TNRs, for photons with 500-600 nm wavelengths (Figure 2.3a), enables improved quantum yields in this spectral range as seen in Figure 2.4c. It is clear in the IPCE spectra in Figure 2.4c that HPSCs fabricated using B-type long TNRs exhibit superior external quantum yields over the entire spectral range compared to HPSCs fabricated using other TNR morphologies.

Table 2.1. Photovoltaic performance of HPSCs under AM 1.5 simulated light as a function of the morphology of TiO_2 nanorods used as the ETL.

Morphology		V_{oc} **(V)**	J_{sc} **(mA/cm^2)**	**FF**	**PCE (%)**
A-type	Average	1.01±0.02	21.86±1.07	0.64±0.02	14.08±0.70
	Champion	1.01	21.19	0.67	14.3
B-type	Average	0.99±0.03	23.17±0.32	0.72±0.03	16.57±1.04
	Champion	1.00	23.08	0.76	17.6
C-type	Average	0.91±0.04	20.85±1.15	0.62±0.02	11.74±0.47
	Champion	0.96	20.72	0.62	12.26

Figure 2.4b compares the dark *J-V* characteristics of devices with different types of nanorods. Solar cells based on B-type TNRs (red curve in Figure 2.4b) exhibit the smallest dark current in the reverse bias region followed by solar cells based on A-type and C-type TNRs (black curve and blue curve respectively in Figure 2.4b). This indicates a higher shunt resistance and consequently a better fill factor for solar cells based on B-type nanorods. It is apparent that decreasing the length of the nanorods increased the onset of the dark current; this implies better suppression of charge recombination in devices with smaller nanorods. It is therefore not a coincidence that the solar cells exhibiting the smallest dark current (red curve in Figure 2.4b) also result in the highest efficiency (see Figure 2.4a). In the forward bias region, solar cells based on B-type and C-type nanorods exhibit the clear signature of space charge limited currents with the green oval in Figure 2.4b highlighting the several orders of magnitude increase in the dark current for C-type nanorods when the majority carriers (electrons) injected from the contact electrodes exceed the concentration of deep traps in the nanorods (the trap-free limit), a phenomenon well-explained by us in prior reports [137, 138]. The lowering of the equilibrium carrier concentration in the nanowires due to a high density of deep level surface traps paradoxically enables the achievement of high efficiencies by suppressing the process of back electron transfer i.e. the

recombination of electrons in the ETL with photogenerated holes in the perovskite at the TiO_2-perovskite interface. Such a deep trap-mediated suppression of interfacial recombination is maximized for a certain morphology, namely B-type nanorods ~ 300 nm long and ~ 40 nm wide, as deduced from the electrical characteristics in Figure 2.4. For ~ 20 nm wide A-type nanorods, the concentration of the local electric field at the needle-like NRs seen in Figure 2b produces a higher dark current due to field emission. For C-type nanorods that are ~ 80 nm wide, interfacial recombination is insufficiently suppressed due to the low surface-to-volume ratio of these NRs as seen in Figure 2.2f and the concomitant smaller number of deep level surface traps.

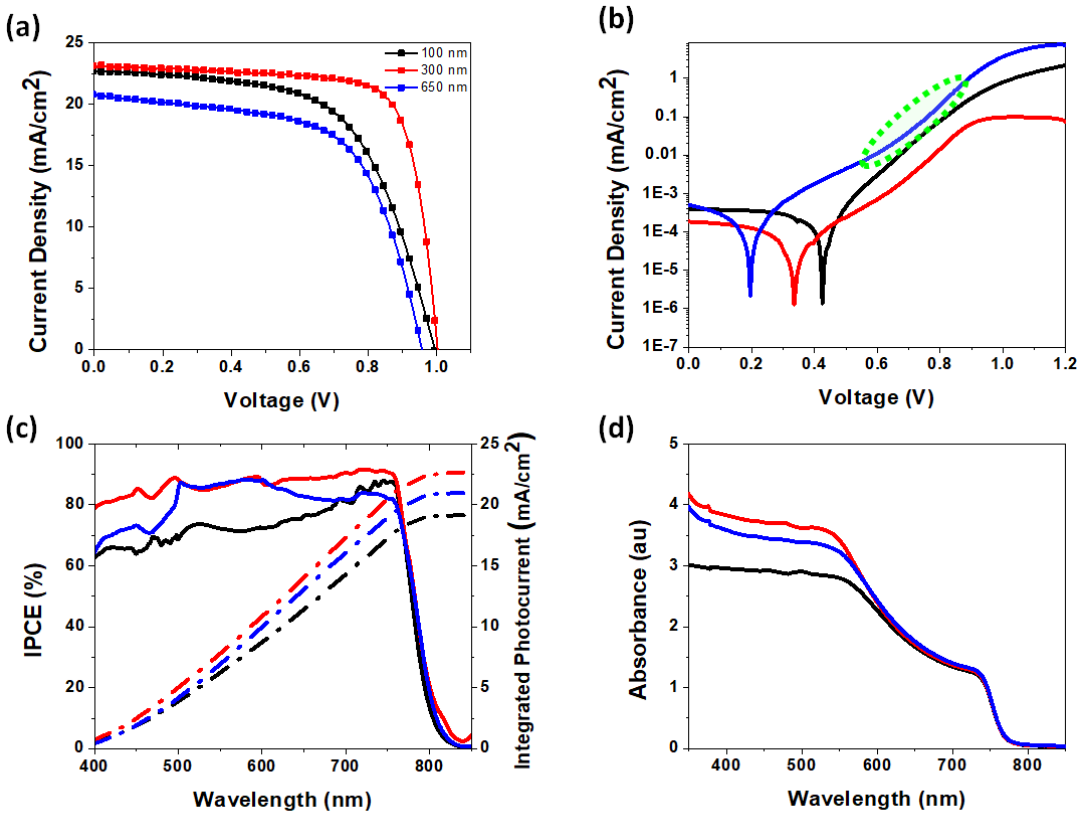

Figure 2.4. (a) Current-voltage characteristics under AM 1.5 one sun illumination (b) Dark current-voltage characteristics plotted on a semi-log scale (c) Action spectra showing the external quantum yields of perovskite solar cells with different TNRs (d) UV-vis of perovskite layer over

different TNRs. Black, red, and blue colors represent A-type, B-type and C-type morphologies titania nanorods respectively.

As can be seen in Table 2.1 and Figure A1, the open-circuit voltage and fill factor of solar cells fabricated using C-type and D-type TNRs were significantly lower than those fabricated using A-type and B-type TNRs. Apart from the work functions of the electron- and hole- transporting layers, the interfacial recombination rate plays a crucial role in determining the V_{oc} value [139-141]. Thus, to have a better understanding of the effect of nanorod morphology on recombination at the TNR/perovskite interface, we performed solid-state impedance spectroscopy in the dark at a forward bias of 1 V [141-145]. Nyquist plots are shown in Figure 2.5 were dominated by the large semicircle for the low-frequency region while no arc for high-frequency region related to perovskite/Spiro-OMeTAD was observed. An arc related to the perovskite/HTL interface is typically only observed if the TiO_2 ETL thickness is 2-3 μm thick or higher [145]. Detailed analysis to calculate the recombination resistance was performed by extracting the equivalent circuit shown in the inset of Figure 2.5. R_s represents the series resistance attributed to the connecting wires and FTO substrate. R_1 and C_1 represent the resistance and capacitance at the interface between TiO_2 nanorod and perovskite active layer respectively. Recombination at the TiO_2/perovskite interface is inversely proportional to the recombination resistance (R_1). A higher value of R_1 implies a lower recombination rate at the interface, which in turn correlates to a higher value of V_{oc} and a higher FF. In Figure 2.5, the diameter of the arc corresponding to solar cells based on A-type TNRs is longest followed by that of solar cells based on B-type and C-type TNRs respectively. The recombination resistance decreased with increment in the length of the nanorods which corresponds to the expected higher recombination rate for longer nanorods, due to the longer

interaction times of electrons transiting through the nanorods with holes in the perovskite, resulting in a lower open-circuit voltage and fill factor for the solar cells based on longer nanorods.

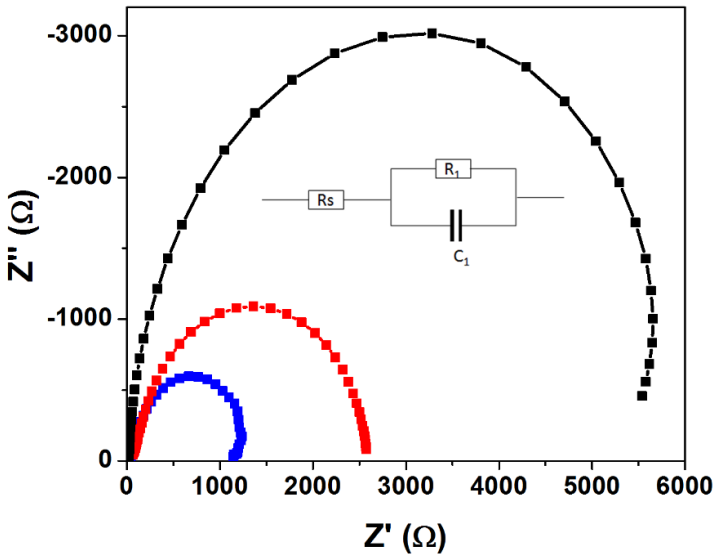

Figure 2.5. Nyquist impedance plot of solar cells with different types of nanorods, in the frequency range 1 MHz - 1 Hz at a forward bias of 1 V. Black, red, and blue color represent A-type, B-type and C-type TiO_2 nanorods respectively.

To compare the photovoltaic performance of TiO_2 nanorod with mesoporous TiO_2 and compact TiO_2 we prepared perovskite solar cells using compact TiO_2 and mesoporous TiO_2 as ETL while other fabrication conditions keeping unchanged. Figures A3, A4, and A5 show cross-sectional images of TiO_2 nanorod, mesoporous-based, and planar type devices respectively. Devices using a compact TiO_2 layer as ETL showed an inferior PCE of 7.46% with J_{sc}, V_{oc} and FF of 15.40 $mAcm^{-2}$, 0.91 V and 0.53 respectively. Devices using mesoporous TiO_2 were found to have a PCE of about 11.23 % with V_{oc}, J_{sc}, and FF of 0.99 V, 19.47 $mAcm^{-2}$ and 0.58 respectively. The current-voltage characteristic of devices with different TiO_2 under layers under AM 1.5 G

solar irradiance is depicted in Figures 2.6a. The trend of short circuit density obtained using different types of TiO_2 layer is in good agreement in the IPCEs in Figure 2.6b. The IPCE values of devices with TNRs are superior to devices with mesoporous TiO_2 and compact TiO_2 because of enhanced charge separation and charge carrier collection efficiencies.

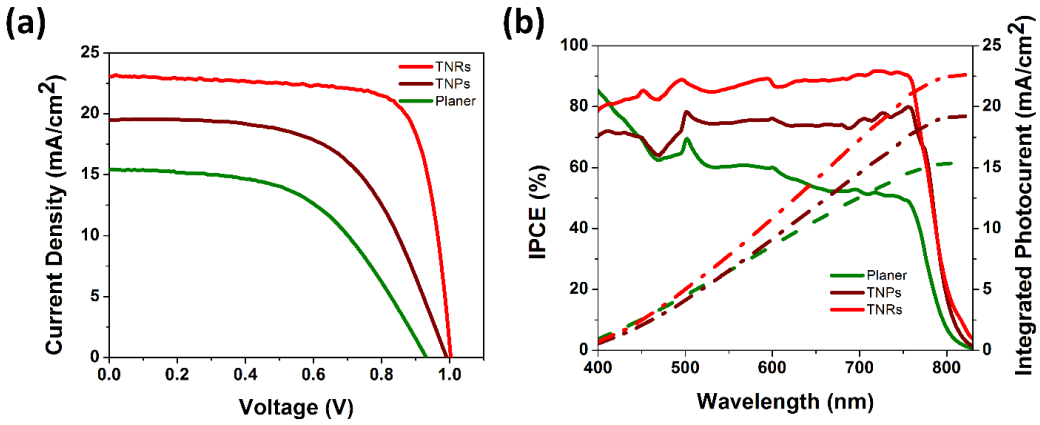

Figure 2.6. (a) Current-voltage characteristics (b) IPCE spectra of perovskite solar cell with different TiO_2 underlayer. Red, wine and olive-colored lines represent corresponding curves for TiO_2 nanorods, mesoporous TiO_2, and planar TiO_2 respectively.

To further study the charge transfer properties of different TiO_2 ETLs in HPSCs, steady-state photoluminescence measurements were performed. As shown in the inset of Figure 2.7, TiO_2 nanorods perform a stronger quenching of the perovskite photoluminescence (PL) compared to mesoporous TiO_2 and compact TiO_2. The same trend is observed in the time-resolved PL data obtained through two-photon fluorescence lifetime imaging microscopy (FLIM), as shown in Figure 2.7. The use of two-photon excitations enables uniform optical excitation of the entire thickness of the perovskite layer, which is particularly important considering the high single-photon absorption coefficient of halide perovskites for supra-bandgap illumination. The PL lifetime of perovskite/TNRs was found to be the smallest compared to compact TiO_2 and

mesoporous TiO_2. The decay curves of each sample were convoluted using a bi-exponential function. The fitted parameters are summarized in Table A1. According to bi-exponential fitting, perovskite/TNR sample have higher weight ratio and faster quenching time compared to the compact and mesoporous TiO_2, suggesting that TNRs have faster charge injection ability compared to the other two types of electron transporting layers which are indicative of photogenerated electron-hole pairs being well-separated in solar cells based on TNRs (through electron injection into TiO_2) before geminate recombination. Taken together, the steady-state and time-resolved PL spectra point to superior charge separation at the TiO_2 nanorod-perovskite interface compared to the interfaces of perovskite with mesoporous TiO_2 and compact TiO_2 films, which likely also explains the superior photovoltaic performance of solar cells based on TiO_2 nanorod arrays, particularly with regards to the J_{sc} values obtained (Figure 2.6).

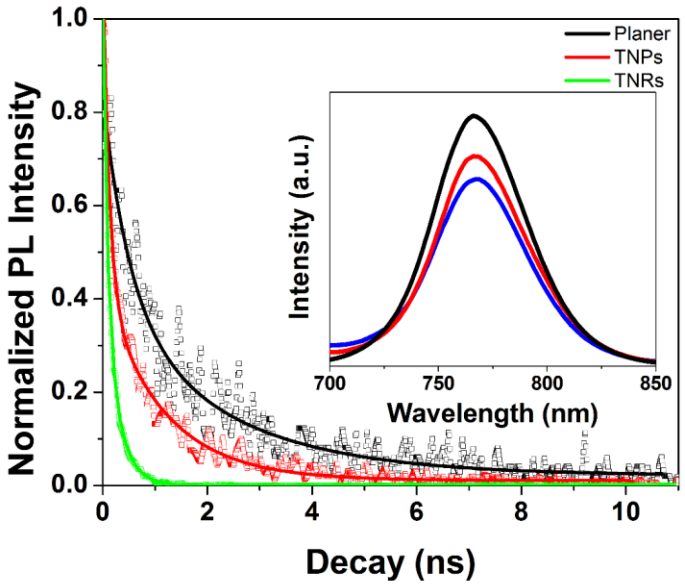

Figure 2.7. FLIM spectra of perovskite on different TiO_2 electron transporting underlayers with the inset showing the steady-state photoluminescence spectrum. Red, wine and olive-colored lines represent corresponding curves for TNR, mesoporous TiO_2 and planar TiO_2 respectively.

2.4. Conclusion:

In summary, changing the size of the nanorods by varying the concentration of the titanium source in the hydrothermal precursor solution was found to have dramatic effects on the photovoltaic performance of halide perovskite solar cells that used monocrystalline rutile nanorod arrays as the electron transport layer. B-type titania nanorod arrays with a width of ~ 40 nm and a length of ~ 300 nm outperformed other nanorod morphologies as well as mesoporous TiO_2 and planar TiO_2 ETLs in perovskite solar cells with a power conversion efficiency of 17.6 %. The superior performance of B-type TiO_2 nanorod was due to optimal light-harvesting, excellent charge separation, and low interfacial recombination.

Chapter-3 Near-horizontally aligned TiO_2 nanorod ETL

3.1 Introduction:

Sunlight is by far the most abundant renewable energy resource, and it will be necessary to harvest increasing amounts of sunlight to meet steadily growing global energy demand, estimated to reach 50 TW by 2050. The field of non-silicon non-chalcogenide photovoltaics has seen astonishing improvements in performance through the use of halide perovskite semiconductors in the active layer. While photoconversion efficiencies (PCEs) of over 23% have been demonstrated, there remains further room for improvement in the open-circuit voltages (V_{oc}) and short circuit current densities (J_{sc}) achievable [19-21]. To improve the efficiency of perovskite solar cells several possibilities are being investigated such as developing and doping electron/hole transporting materials, incorporating quantum dots in perovskite absorbing layers [146-153]. However, not much effort was devoted to light management in solar cells for efficiency improvements. Atwater et al. reported that inefficiencies in the management of photons that are the largest source of losses in J_{sc} and V_{oc} due to poor harvesting of photons near the semiconductor band-edge, non-radiative carrier recombination losses limiting the match of the solar cell to a black body radiator at the same temperature, poorly optimized angular distribution of emission due to radiative recombination of carriers, and changes in the entropy of photons [98]. The use of active layer light management through the use of nanophotonic architectures offers the largest potential to overcome these losses.

Strong forward scattering in the layer immediately preceding the halide perovskite absorber concomitant with suppressed backscattering is extremely useful in boosting solar cell efficiencies by allowing the use of thinner absorber layers. Multiple scattering slows down light propagation

and increases the probability of photons being absorbed in the active layer. Thinner absorber layers that harvest the same amount of sunlight result in improved performance parameters (V_{oc}, J_{sc}, FF) due to shorter carrier extraction paths and reduced recombination. Thinner absorber layers are associated with lower non-radiative recombination losses, which in turn increases V_{oc} [99].

Keeping this in mind, we examined near-horizontal nano-raft geometries to improve the utilization of photons. There are a number of theoretical works (and some experimental ones as well) showing that horizontal disc-shaped structures made of high refractive index materials can preferentially suppress backscattering by approaching the first Kerker condition [154-156]. While Kerker found that magnetic spheres suppressed backscattering, overlapping or interfering electric dipole and magnetic dipole modes in ellipsoidal or disc-shaped high index materials such as GaAs and Si have been used to generate either a similar broadband suppression of the backscattering or a relative enhancement of the forward scattering [157-160]. Rutile phase TiO_2 has a lower refractive index (2.7) than GaAs (3.5) and Si (3.7) but is nevertheless high enough to show appreciable nanophotonic effects in the proper geometry.

One dimensional nanostructure such as nanotubes and nanorods possess unique light trapping and charge transport properties [161-165]. Nanorods exhibit high electron mobility, long diffusion length, and better pore-filling properties in comparison to compact and mesoporous TiO_2 films [111]. Most reports on the use of nanorods have applied vertically oriented TiO_2 nanorod arrays as the electron transport layer in perovskite solar cells [115, 166-168]. In comparison, there are almost no reports on horizontal or near-horizontal nanorods as the ETL in perovskite solar cells in spite of their superior photonic strength. Hydrothermal growth is the primary route for the synthesis of various TiO_2 nanostructures, wherein a TiO_2 precursor is hydrolyzed in the presence of water, heat, and stabilizers. The hydrothermal method provides us the flexibility to engineer the architecture

of the grown nanorods by changing the physical parameters such as growth time, temperature, precursor concentration, solvent, and the substrate positioning inside of the autoclave [166, 169].

3.2. Experimental:

3.2.1 Materials:

Titanium (IV) *n*-butoxide (99%), titanium (IV) isopropoxide (98+%), acetonitrile (99.8%), lead iodide (99%) and lead bromide (98+%) were purchased from Acros Organics. Acetic acid (99.8 %), HCl (37%), Formamidinium iodide (≥98%), 4-tert-butylpyridine (96%), lithium bis(trifluoromethanesulfonyl)-imide (99.95%) and spiro-OMeTAD (99%) were procured from Sigma-Aldrich. Methylammonium bromide (98%) was obtained from Dyesol. Chlorobenzene (99+%), titanium (IV) chloride (99.9%), dimethylformamide (DMF) (≥99.8%) and dimethylsulfoxide (DMSO) (≥99.9%) were purchased from Fisher Scientific. The obtained chemicals were used as received without any further purification. All other chemicals were of HPLC grade. Fluorine-doped tin oxide (FTO) coated glass slides purchased from Hartford Tec Glass Company were cleaned by ultrasonication in acetone, methanol and deionized water respectively for 10 minutes each. Cleaned substrates were dried using a nitrogen gun. About 60 nm of compact TiO_2 seed layer was then deposited onto the cleaned FTO: glass substrates. The precursor solution for the deposition of compact TiO_2 was prepared by a method described in our previous report [166].

3.2.2 Synthesis of horizontally aligned TiO_2 nanorod (HATNR) arrays:

Horizontally aligned TiO_2 nanorod (TNR) arrays were grown on FTO substrates seeded with TiO_2 compact layer by a simple hydrothermal approach. In brief, 85 µL of titanium (IV) *n*-

butoxide was added to a 10 mL solution of HCl/HAc/DI water in a volume ratio of 1:1:2. The obtained mixture was transferred into a Teflon-lined stainless-steel autoclave. The FTO substrate having the TiO_2 seed layer was oriented vertically inside the autoclave by maintaining an angle of 90º to the bottom of the autoclave. The autoclave was then sealed and put in the oven at 190ºC for 60 min to achieve hydrothermal growth of nanorods. After completion of the reaction, the autoclave was cooled to room temperature under ambient air and resultant transparent nanorod array on FTO substrate was rinsed with DI water for 2 min and dried in a stream of flowing nitrogen. To completely cover any exposed with TiO_2, a thin layer of TiO_2 was deposited by treating HATNR arrays with 40 mM of $TiCl_4$ at 70ºC for 60 min and annealed at 500ºC for 30 min.

3.2.3 Device fabrication:

The perovskite precursor solution was made by dissolving 1 M of formamidinium iodide (FAI), 1.1 M PbI_2, 0.2 M methylammonium bromide (MABr) and 0.22 M $PbBr_2$ in a 4:1 mixture of DMF:DMSO respectively. The obtained precursor solution was then stirred at 70ºC for 2 h followed by deposition on top of the TNRs. The perovskite solution was deposited on TNRs in a two-step procedure: firstly at 1000 rpm for 10 seconds, and secondly at 4000 rpm for 20 seconds respectively. Further, 100 µL of chlorobenzene was dropped on the spinning substrate after 15 seconds after the second step for rapid crystallization. The substrates were then annealed at 100ºC for 30 min. After that, approx. 300 nm thick hole transporting layer was deposited by spin-casting the solution containing 72 mg Spiro-MeOTAD, 17.5 µL of stock solution of 520 mg mL^{-1} bis(trifluoromethanesulfonyl)-imide in acetonitrile and 28.8 µL of 4-*tert*-butylpyridine in 1 mL of

chlorobenzene. Finally, about 70 nm of gold was evaporated using an e-beam evaporator to complete the device.

3.2.4 Characterization:

The morphological characteristics of the TiO_2 layers on FTO and fabricated perovskite solar cells were elaborated by using field emission scanning electron microscopy (FE-SEM) on Zeiss Sigma FESEM with an accelerating voltage 3 kV equipped with GEMINI in-lens detector. Figure A7 shows cross-sectional images of the compact TiO_2 ETL and HATNR ETL. The UV-Vis-NIR absorption spectroscopy was performed using a Perkin Elmer Lambda-1050 spectrophotometer equipped with a 100 mm integrating sphere accessory in configuration(s) illustrated in Figure A11. When a transmission measurement was performed without the use of the integrating sphere, photons scattered out of the sample in the forward direction are not captured by the photodetector due to which the sample extinction is overestimated. When the sample is placed at the entrance of the integrating sphere, corresponding to the position (a) in Figure A11, photons scattered out of the sample in the forward direction are reflected off the walls of the integrating sphere and registered by the photodetector, thus providing a more accurate estimate of the overall extinction. When the sample is placed at the exit of the integrating sphere, corresponding to the position (c) in Figure A11 without a spectral chuck behind the sample, a direct measurement of the diffuse reflectance i.e. backscattered intensity, is obtained. When the sample is placed in the middle of the integrating sphere, corresponding to the position (b) in Figure A11 with port (c) closed, both the transmitted and reflected photons remain in the sphere and are captured by the photodetector. However, one problem with this configuration is that photons bouncing off the walls of the sphere might perform multiple passes through the sample, thus

causing the absorptance of the samples to be overestimated. When the sample is placed at the exit of the integrating sphere, corresponding to position (c) in Figure A11 but with a spectralon chuck behind the sample, no light is transmitted; previously transmitted photons are reflected off the spectralon chuck and make a second pass through the sample such that the only photons leaving the sample to be recorded by the photodetector are photons not absorbed by the sample. Thus, a direct measurement of the sample absorptance is rendered possible. This configuration also provides the closest approximation to the real situation in a photovoltaic device since the vacuum deposited metallic top electrode contact reflects photons back into the active layer similar to the spectralon chuck.

Steady-state photoluminescence (PL) spectra were collected using a Varian Cary Eclipse Spectrofluorometer. Time-resolved photoluminescence (TRPL) curves were recorded using a lab-assembled single-photon counting setup. Samples were photoexcited by a 405-nm picosecond diode laser (Alphalas GmbH) operated at a frequency of 1 MHz to excite the samples, and a Becker-Hickl HPM-100-50 PMT interfaced to an SPC-130 pulse counter system. This setup has a response time of ~100 ps. Intensity-modulated photovoltage spectroscopy (IMVS) and intensity-modulated photocurrent spectroscopy (IMPS) measurements were carried out on a Zahner Zennium electrochemical workstation (Zahner, Zennium) with a frequency response analyzer under a modulated 629 nm light-emitting diode driven by a Zahner, PP211 source supply. The modulated light intensity was less than 10% base light intensity. The frequency range was set from 100 kHz to 0.1 Hz. The current-voltage characteristics of the samples were measured using a Keithley 4200 semiconductor parameter analyzer. For solar cell testing, one sun AM 1.5 G illumination from a collimated Class A solar simulator (Newport Instruments) was used. The incident photon-to-electron conversion efficiency (IPCE), also known as the external quantum

efficiency (EQE) was calculated using a lab-assembled set-up consisting of a Xe arc lamp, a chopper, a filter-wheel, a computer-controlled monochromator, a calibrated silicon photodetector, and an optical power meter.

The fine morphological features of material were determined using High-resolution transmission microscopy (HR-TEM) EDX spectra and elemental mapping. The low-resolution TEM images and EDX spectral mapping was performed on a JEOL JEM-ARM200CF S/TEM equipped with STEM EDX detector, operating at an acceleration voltage of 200 keV. While high-resolution TEM images were recorded on a JEOL 2200 FS TEM/STEM equipped with STEM EDX detector, operating at an acceleration voltage of 200 keV. The sample for low magnification images was prepared by scratching the samples using a razor and sonicating in methanol to separate nanorods from the substrate followed by deposition on a lacy carbon-coated copper TEM grid. For high magnification images, the scratched sample was deposited directly on the lacy carbon-coated TEM grid. The acquired electronic images in .dm3 format were processed using Gatan micrograph to determine the size of nanorods and interplanar d spacing. Elemental mapping files were processed with INCA Energy software.

To determine the surface chemical composition and oxidation state of materials, the binding energy of compact TiO_2 and HANTR arrays were determine using XPS measurement acquired on a XPS (Axis-Ultra, Kratos Analytical) instrument equipped with monochromatic Al-Kα source (15 kV, 50 W) and photon energy of 1486.7 eV under ultrahigh vacuum ($\sim 10^{-8}$ Torr). Exact binding energies were determined from the position of the adventitious C 1s peak at ≈ 284.8 eV and peaks of other elements were assigned with respect to C1s peak. The deconvolution of raw data was done by using CasaXPS and extracted .csv files were later plotted in Origin 8.5. Work function spectra and valence band spectra of materials were acquired by ultraviolet photoemission

spectroscopy (UPS) performed with a 21.21 eV He lamp source. Peak force KPFM was performed on ETL and STNL samples using a Dimension Fast Scan Atomic Force microscope (Bruker Nanoscience Division, Santa Barbara, CA, USA) in the presence and absence of diode laser (Thorlabs) of 450 nm wavelength. The laser was shone perpendicularly from the sample through a custom-made optical setup. A Pt coated SiN cantilever of 2.5 N/m stiffness was employed to conduct the KPFM experiments. The surface potential of the samples was measured at 100 nm lift height at 1 kHz lockin bandwidth. The scan speed was maintained at 0.5 Hz. Both the samples were grounded with the AFM chuck with conducting copper tape. The surface potential was mapped by sample routing at zero tip bias. Dark and illuminated conditions were maintained for 5 min before performing the experiments in order to obtain the equilibrium condition of carrier transport. The work function of Pt-Ir tip was calibrated by measuring the contact potential difference (CPD) of HOPG and the Pt tip using the following equation and found to be 5.04 eV.

$$E_{F(tip)} = 4.6 \text{ eV (Work function of HOPG)} + V_{CPD}\text{(HOPG and Pt tip)}$$

3.2.5 Simulations:

Simulations were performed using Lumerical FDTD Solutions. All the morphological parameters are based on FESEM images. In each case, the compact TiO_2 and HATNR ETLs were immersed in a $MAPbI_3$ perovskite layer of the relevant thickness. The compact anatase layer was set to be 100 nm thick. The nanorafts constituting the HATNR ETL were 600 nm in width, 200 nm in length and 60 nm in thickness, which is a cuboid whose long edge is inclined at an angle of 30 degrees to the underlying FTO glass substrate. A TFSF (time-field scattered-field) light source with wavelengths starting from 300 nm to 1000 nm produced a plane wave that propagated upward with a wave-vector normal to the FTO surface. A far-field *close box* was set to monitor the

scattered light power. An *Abs* monitor was applied to analyze the spatial and total absorption profiles. Several frequency-domain fields and power monitors were employed to obtain information regarding the reflection, transmission, electric field, and Poynting vector.

3.3 Results and discussions:

Compact TiO_2 film on FTO glass substrate was obtained by spin coating precursor solution and annealing at 500ºC while the HATNRs were grown on TiO_2 seed layers deposited on FTO glass *via* a facile hydrothermal reaction using titanium (IV) *n*-butoxide as TiO_2 precursor in the presence of hydrochloric acid (HCl), acetic acid (HAc) and water. Both films showed negligible parasitic absorption loss over the entire visible range (Figure A6). Figures 3.1a and b are schematic illustrations of *n-i-p* type perovskite solar cells made with compact TiO_2 and HATNR respectively. Figures 3.1c and d are the top-view field emission scanning electron microscope (FESEM) images of the compact TiO_2 and HATNR respectively. In our previous report, we demonstrated the effect of the precursor concentration on the morphology of the resulting vertically oriented TiO_2 nanorods and its impact on the performance of perovskite solar cells based on them [165, 166]. In this non-organic recipe, we used titanium *n*-butoxide (TBO) as a precursor and DI water as the primary solvent in which the nanorod growth reactions took place. HCl and HAc both affect the morphology of the structure during growth. More specifically, the acids provide H^+ ions which suppress the fast hydrolysis of the TBO precursor, thereby leaving more precursors available for the growth of the nanorods. The growth of the crystal is mainly determined by the relative growth of the various crystal faces which bound a unit cell of the TiO_2 lattice. In rutile TiO_2, each Ti atom is bound to 6 oxygen atoms in an octahedral unit cell, and the growth of each face depends on the available coordination polyhedron. The crystal grows in the direction which minimizes surface

energy, and thus is the most thermodynamically stable. The FTO substrate has a tetragonal rutile crystal structure, the lattice mismatch between the tetragonal FTO (a = b = 0.4687 nm) and rutile TiO_2 (a= b= 0.4594) is only about 1.98% which promotes the nucleation and growth of the rutile phase TiO_2 nanostructures on the substrate [170-175]. Furthermore, the acids contribute Cl^- and CH_3COO^- ions which helps in tuning the morphology of the crystalline nanostructures by retarding the growth rate of the (110) plane. The size of the solvated ion affects the spacing between the individual nanorods grown. The morphology of the nanostructures is dependent on the recipe used during fabrication as well as on the substrate orientation. It is known that the effect of the angle at which the substrate is placed (with respect to the base of the Teflon reaction vessel) greatly affects the direction in which the nanorod arrays grow. This is true since the substrate orientation affects the precursor deposition which in turn affects the nucleation sites for further growth. We used these principles to tune the morphology of the TiO_2 nanostructures *via* the hydrothermal growth process such that near-horizontal bunches of nanorods ("nano-rafts") formed instead of the typically observed vertical nanowire arrays.

The FESEM images (Figures 3.1c and e) of compact TiO_2 deposited on FTO depicts an irregular film thickness with numerous discontinuous features or pinholes (see also Figures A7a and d). The deposition of perovskite over this irregular and discontinuous TiO_2 layer results in a high probability of direct contact between bare FTO substrate and perovskite layer. The formation of this poor hole blocking layer promotes faster electron-hole recombination between the FTO and the perovskite layer which in turn reduces the charge transport efficacy of the ETL. The non-uniform compact TiO_2 layer, along with the presence of pinholes significantly reduces the performance of the device. These pinholes can be reduced by increasing the thickness of the compact TiO_2 film which would improve the hole blocking property of the film. However, the

resulting thick and smooth compact TiO_2 surface increases the series resistance and reduces the interfacial area between the perovskite and ETL. This results in deterioration in the fill factor and the current density of the device. The FESEM images of Titania nanorods grown on TiO_2 compact layer deposited FTO glass exhibit randomly distributed near-horizontally aligned nanorods bunched together as nanorafts (Figure 3.1d). It can be seen in Figures 3.1f, A7b and A7c that hydrothermally grown TiO_2 nanorod film deposited over the FTO substrates provides better film uniformity and well defined near-horizontally oriented nanorods. It is evident that the hydrothermal treatment promotes filling of the pinholes present in the compact TiO_2 layer and hence provides a superior hole blocking property. On the other hand, it also provides a highly irregular surface which significantly improves the mesoscopic effect, thus helping to improve the current density, and hence the PCE of the device.

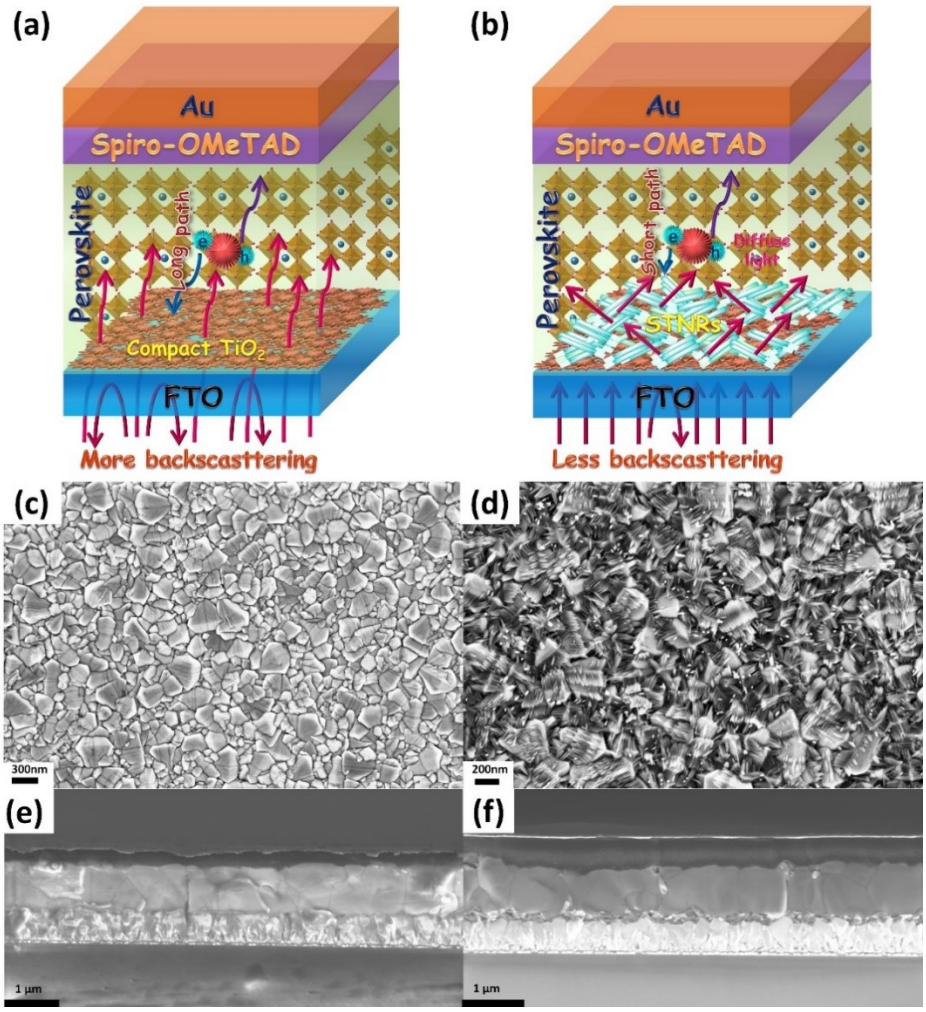

Figure 3.1. Graphical representation of perovskite solar cells made with (a) compact TiO_2 and (b) nanostructured HATNRs obtained by hydrothermal method. (c) topographic FE-SEM image of compact and (d) HATNRs. The cross-sectional views of a perovskite solar cell made with compact TiO_2 layer (e) and (f) HATNR arrays.

Ultrafine morphological attributes of HATNRs were determined using high-resolution transmission electron microscopy (HR-TEM). TEM images of HATNRS at low magnification shows cylindrical nanorods clumped together as bundle and average diameter of single nanorod was found to be approx. 17-19 nm (Figures 3.2a and b). The high-resolution TEM images at higher

magnification clearly show lattice fringes with 0.33 nm interplaner corresponding to the (110) plane of rutile phase TiO_2. Further, EDX pattern of clearly demonstrates sharp peaks of Ti and O confirms the presence of TiO_2 (Figure 3.2e). The peaks corresponding to C and Cu arose from carbon-coated TEM grids. EDX elemental mapping in STEM mode shows even distribution of Ti and O in nanorods and averaged images showing homogeneous composition further confirms well fabricated TiO_2 nanorods (Figure 3.2f).

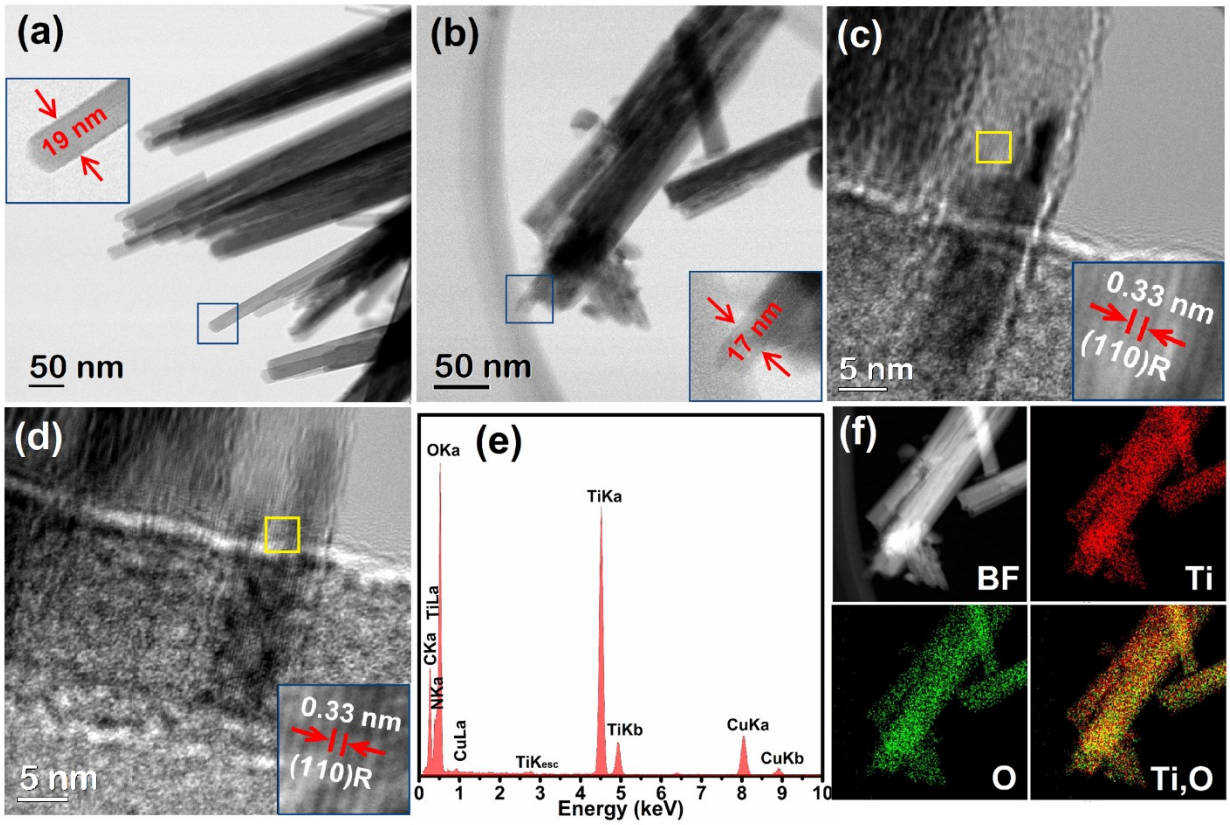

Figure 3.2. HR-TEM images HATNRs (a)(b) images at 50 nm scale bar showing bundles of nanorods and inset showing individual nanorods and their respective diameter (c)(d) high magnification images at 5 nm scale bar showing lattice fringes (e) EDX pattern showing presence of Ti and O and (f) bright-field image and EDX elemental mapping for Ti, O and their sum-up image.

The surface and sub-surface (up to ~10 nm) chemical composition of compact TiO_2 and HATNR was investigated by using X-ray photoelectron microscopy (XPS) (Figures 3.3a and 3.3b). XPS survey scan for elemental analysis of compact TiO_2 and HATNRs exhibited all the peaks relevant to Ti2p, O1s along with other low and high core level peaks (Ti3s, Ti3P, TiLLM, OKLL, and O3s, etc.) (Figure A8). Core-level high-resolution XPS (HR-XPS) spectra of both compact TiO_2 and HATNRs show two symmetric peaks at binding energy 458.57 and 464.22 eV assigned to $Ti2p_{3/2}$ and $Ti2p_{1/2}$ peak components of Ti^{4+} state in TiO_2 crystal lattice (Figure 3.3a) [176, 177]. The position of $Ti2p_{3/2}$ and $Ti2p_{1/2}$ peaks with a peak splitting of 5.76 eV verify O^{2-} coordinated Ti^{4+} in compact TiO_2 and HATNR [178, 179]. However, being of different phase, there was no visible change in Ti2p peaks was observed for anatase phase compact TiO_2 and rutile phase HATNRS. HR-XPS spectra of compact TiO_2 in O1s region can be deconvoluted into two peak components located at BE ≈ 529.78 and 531.34 eV. The peak component at BE value 529.78 eV was attributed to crystal lattice oxygen bonded to Ti (Ti-O-Ti), while peak component centered at binding energy 531.34 eV originated from surface adsorbed -OH groups and non-lattice adventitious oxygens (Figure 3.3b) [180]. The two O1s peak components for HATNRs located at BE ≈ 529.74 and 531.11 eV corresponded to lattice bonded oxygens and surface adsorbed non-lattice adventitious oxygens. Very small shifts (0.04 eV) in O1s components of HATNRs at 529.74 eV might be due to different chemical environments of oxygens in rutile TiO_2 (tetragonal geometry with slightly orthorhombic distortion of TiO_6 octahedron) than anatase state (tetragonal) in compact TiO_2 [181, 182]. To investigate the electronic band structure of materials, work function and valence band spectra were measured by using ultraviolet photoelectron spectroscopy (UPS) (Figures 3.3c and 3.3d). The value of the work function was estimated from the work function spectra by using expression WF (ϕ) = $21.21 - E_{\text{cut-off}}$, where 21.21 eV is the energy of the incident

He laser light and $E_{cut\text{-}off}$ is the cut-off energy of secondary electrons. The point of intersection by extrapolation of linear region of graph in horizontal and vertical region gives the value of cut-off energy of secondary electrons $E_{cut\text{-}off}$). The $E_{cut\text{-}off}$ for compact TiO_2 and HATNR arrays was found to be 17.17 and 16.96 eV and corresponding work function value (ϕ) was calculated to be 4.04 and 4.25 eV, respectively (Figure 3.3c and inset). Further, the intersecting point of the linear region in UPS valence band spectra gave the position of valence band maxima (VB_{max}). The VB_{max} value for the compact TiO_2 and HATNRs was calculated to be 2.95 and 3.08 eV below Fermi level (Figure 3.3d).

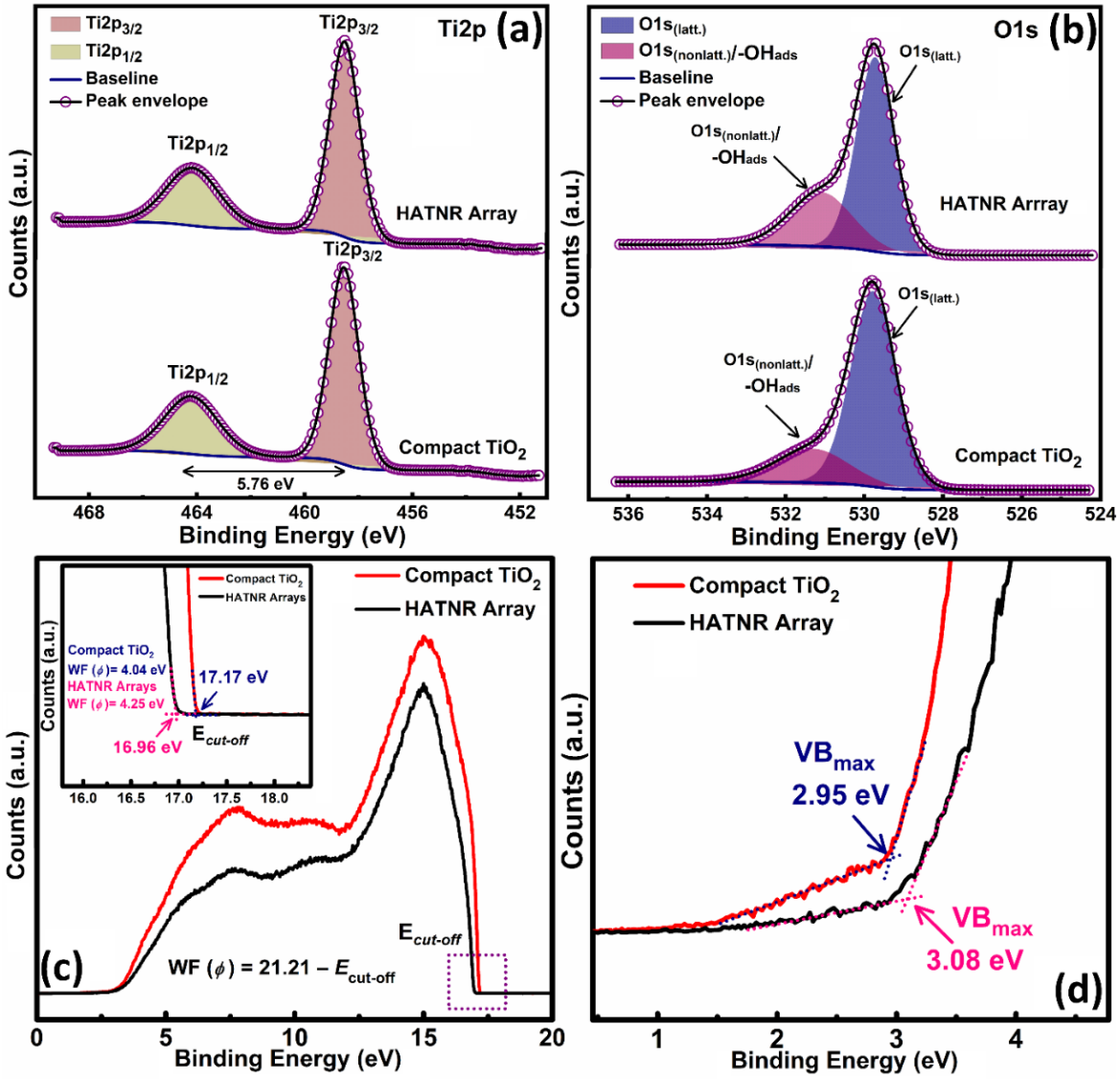

Figure 3.3. HR XPS spectra of compact TiO2 and HATNR array in (a) Ti2p region, (b) O1s region. (c) UPS work function spectra of compact TiO2 and HATNR array. Inset shows cut-off energy ($E_{cut\text{-}off}$) of the secondary electron and value of Work function (WF) was determined by using equation, WF (ϕ) = 21.21 – $E_{cut\text{-}off}$, where 21.21 eV is energy of the incident He laser used for UPS, and (d) UPS Valence band spectra showing position of valence band maxima (VB_{max}) below Fermi level.

X-ray diffraction patterns of compact TiO_2 thin film and HATNR arrays were collected to investigate any change in crystallinity and phase structure (Figure 3.4a). The XRD pattern of compact TiO_2 layer over FTO does not reveal any peak corresponding to the very thin compact TiO_2 layer and suppression of TiO_2 peaks by strong FTO diffraction peaks. However, the XRD pattern of blocking the TiO_2 layer over bare glass substrate clearly reveals anatase peaks that match with JCPDS file no. 21-1272 and confirms the compact layer was composed of anatase TiO_2 (Inset of Figure 3.4a). For HATNR, two distinct rutile peaks at 62.82 ° and 36.09 ° were observed which was in excellent agreement with JCPDS file no. 21-1276 for tetragonal rutile phase TiO_2. HATNRs array on compact TiO_2 can be considered as mixed-phase TiO_2 because of the presence of underlying anatase compact TiO_2 and rutile nanorods. It is well documented in literature that the conduction band of anatase phase TiO_2 is 0.2 eV higher than rutile phase TiO_2 in the absence of any heterojunction [183, 184]. This also evident from UPS data where the difference between Fermi levels of anatase form in compact TiO_2 and rutile phase HATNRs was calculated to be 0.21 eV. Based on the UPS results we constructed the energy band diagram of solar cells made with compact TiO_2 and HATNR arrays which is shown in Figures 3.4b and c. While heterojunction formation anatase and rutile phase leads to type II (staggered) configuration, Fermi level alignment in mixed-phase anatase-rutile heterojunction proceeds *via* charge redistribution and band bending which creates n-n heterojunctions possessing higher conduction band positions in rutile TiO_2 than anatase state. Scalon *et al.* demonstrated that in heterojunctions, the conduction band of rutile phase TiO_2 was 0.4 eV higher than in anatase form TiO_2 which facilitates facile transfer of electrons from the rutile to anatase TiO_2 [185]. Further, anatase TiO_2 possesses low energy shallow traps 0.8 eV below the conduction band of rutile so electrons can flow from rutile to anatase [185-187] which further helps in electron transfer resulting in significant improvement in the photovoltaic performance of

HATNRs based solar cells. It is well known that the carrier transport efficiency of mixed-phase TiO_2 is better compared to the pure anatase TiO_2 [188-192]. Furthermore, because of presence of pinholes in the compact TiO_2, perovskite can contact directly with the FTO electrode forming a Schottky contact. The free-electron that has already been transferred to FTO can get reinjected into the valence band of perovskite because of a low interfacial energy barrier resulting in front surface recombination. In HATNRs, the samples' exposed FTO surface is passivated by rutile nanorods which result in the elimination of direct contact between FTO and the perovskite layer.

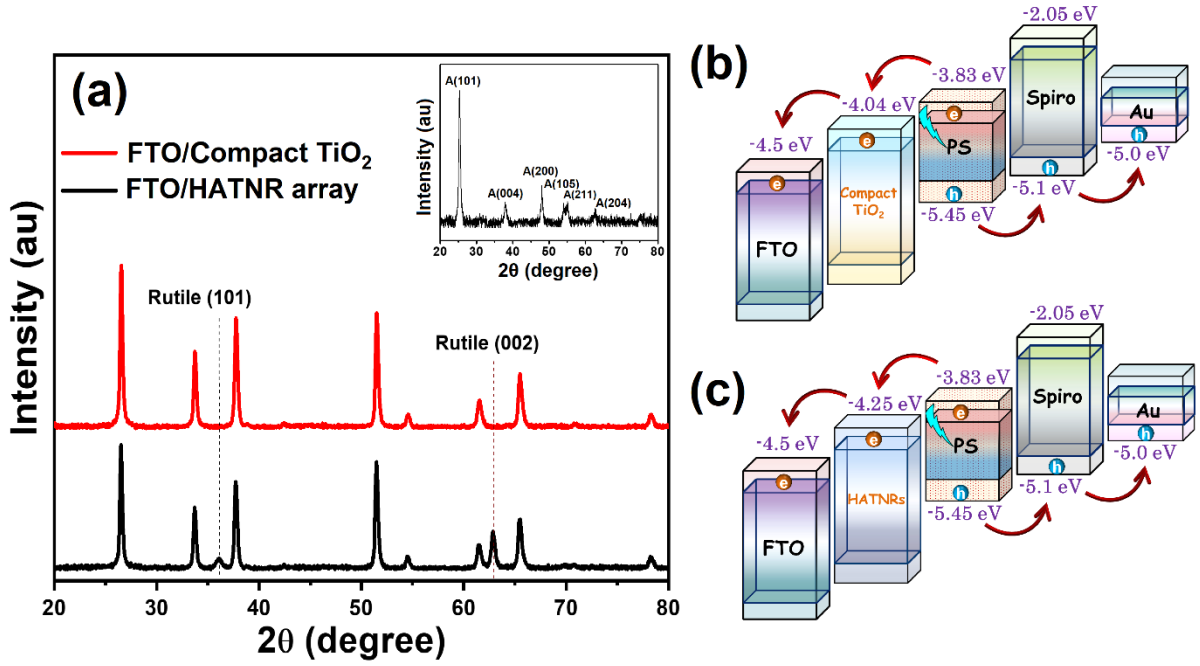

Figure 3.4. (a)X-ray diffractograms of compact TiO_2 (red) and HATNR array (black) on the FTO substrate. Inset shows XRD pattern of compact TiO_2 on bare glass substrate. Energy band diagram of perovskite solar cells made with (c) compact TiO_2 and (c) HATNR arrays.

To probe the carrier dynamics of these two different TiO_2 electron transporting layers, we compared the steady-state photoluminescence (PL) spectra of perovskite on FTO glass with perovskite/compact TiO_2/FTO glass and perovskite/HATNR arrays/FTO as shown in Figure 3.5

(a). The PL spectra of all samples exhibit a PL peak at 775 nm. The integrated PL intensity of perovskite on FTO glass was found to be highest, followed by perovskite/compact TiO_2/FTO glass, and perovskite/HATNR arrays/FTO samples respectively. Therefore, the HATNR array produced the greatest quenching of the perovskite luminescence. This observed PL quenching behavior was attributed to charge carrier extraction from the perovskite layer to the TiO_2 layers (ETLs). The higher PL quenching for nanostructured HATNR samples in comparison to the compact TiO_2 sample clearly indicates that the rate of electron transfer from the perovskite to the HATNR array assembly was faster than for compact TiO_2. Time-resolved photoluminescence (TRPL) decay data were collected from the samples with compact TiO_2 and HTNR layers coated with perovskite, as well as from a perovskite sample without TiO_2 layers (Figure 3.5b). The PL decay curves were fitted with the bi-exponential model using the equation (3.1):

$$I(t) = A_1 e^{-t/\tau 1} + A_2\, e^{-t/\tau 2} \qquad (3.1)$$

where A_1 and A_2 are scaling parameters and τ_1 and τ_2 are the lifetimes of the shorter and longer decay components respectively. Both components are present almost equally in the perovskite layer, even in the absence of the ETLs, and the corresponding lifetimes τ_1 and τ_2 were 19.7 ns and 282.3 ns respectively, while the system response time was ~0.1 ns. For the ETL-free samples, the decay is attributed mainly to trap-assisted recombination. The fast component is attributed to the bimolecular recombination of charge carriers trapped at the perovskite grain boundaries while the longer-lived component is most likely the radiative recombination of free electron-hole pairs. For the samples with ETL, the faster component is mainly related to the electron extraction from the perovskite layer to the electron transporting layer and longer component is attributed to the excited-state decay time or recombination dynamics of perovskite absorber [74, 193-200]. For the sample with the compact TiO_2 layer, the pre-factor was slightly larger for the fast decay process

while the corresponding lifetimes τ_1 and τ_2 were both significantly shorter (2.4 ns and 36.3 ns, respectively). For the HATNR based sample, the fast decay was dominant (the prefactor was almost 4 times larger) and the values of τ_1 and τ_2 were 2.9 ns and 23.4 ns, respectively. From these biexponential components, an average lifetime (τ_{ave}) can be obtained from a weighted mean by using equation (3.2) [201, 202].

$$\tau_{ave} = (A_1\tau_1^2 + A_2\tau_2^2)/ (A_1\tau_1 + A_2\tau_2). \qquad (3.2)$$

The average lifetimes of ETL-free, compact TiO_2, and HATNR samples were found to be 265.7 ns, 34.3 ns and 17.3 ns respectively. Thus, the HATNRs appear to create an especially fast non-radiative decay pathway, indicating that they effectively capture excited charge carriers in the perovskite layer. The shorter average lifetime of HATNRs relative to compact TiO_2 is consistent with a more effective electron transfer from the perovskite layer to the HATNRs, in agreement with the observed quenching of the steady-state PL.

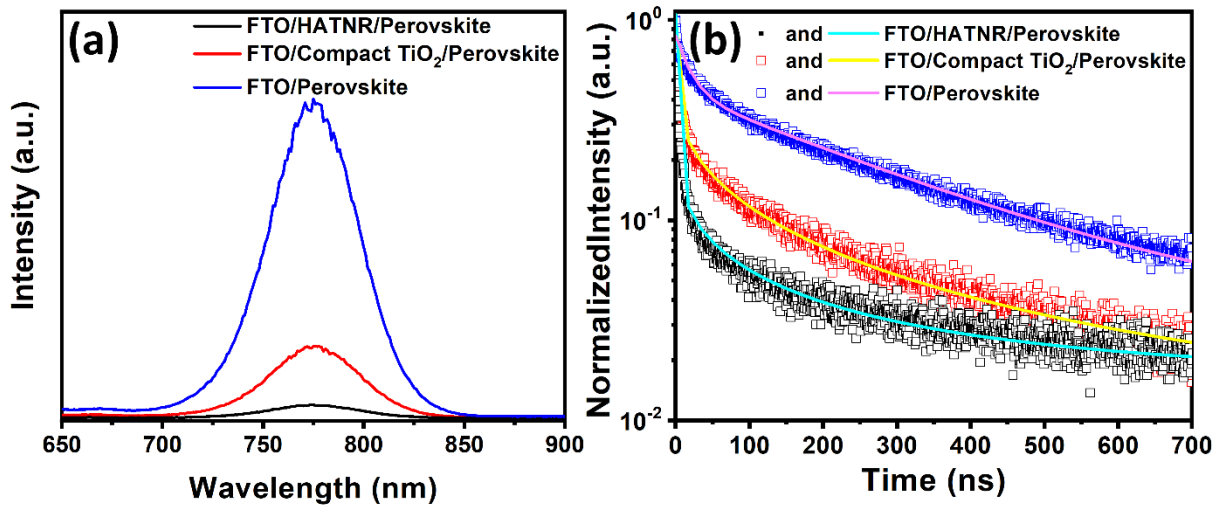

Figure 3.5. (a) Steady-state photoluminescence (PL) spectra of glass/perovskite (blue), perovskite deposited over compact TiO_2 (red) and perovskite/HATNR array (black); (b) The PL lifetime

decay curve of perovskite with no ETL (blue; double exponential fit, magenta line), compact TiO_2 (red; double exponential fit, yellow line) and perovskite/HATNR array (black, double exponential fit, cyan).

Figure 3.6 shows the topographical image of the perovskite layer deposited on top of the compact (Figure 3.6a), and HATNR layers (Figure 3.6b). Generally, the grain size of the polycrystalline perovskite layer depends on the deposition technique and the precursor used. However, we found that, despite having an identical deposition technique and precursors, the average grain size of the perovskite deposited over the HATNR samples was larger than the average perovskite grain size deposited over the compact TiO_2 layer. The large grain size of perovskite over HATNRs can be explained by better entrapment of perovskite precursor solution in voids of HATNR. As recombination (trap) centers in polycrystalline perovskite layer are generated by the grain boundaries, having a larger grain size helps to reduce undesirable non-radiative recombination and improve device performance [200, 203-206].

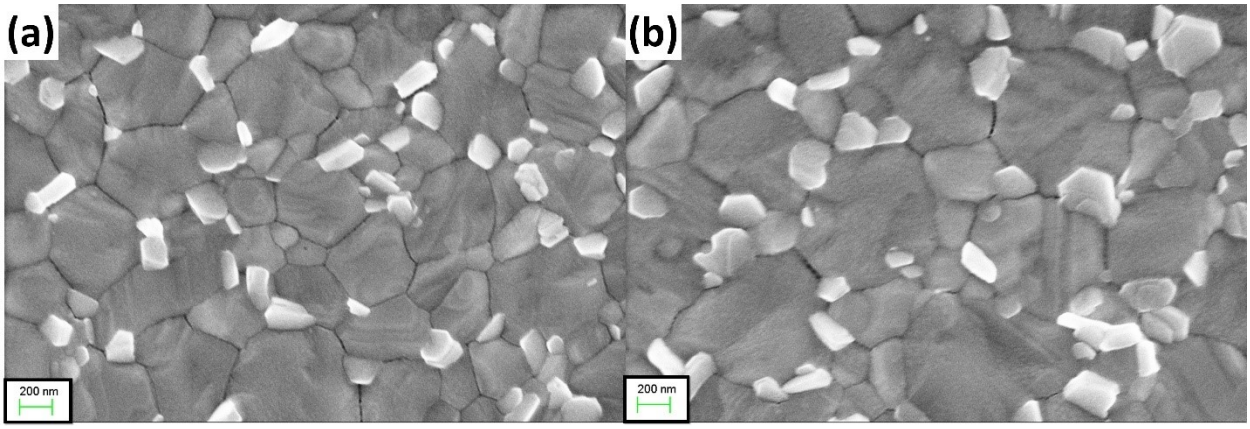

Figure 3.6. FE-SEM topographic image of perovskite layer deposited over (a) compact TiO_2 layer and (b) HATNR arrays.

Kelvin Probe Force Microscopy (KPFM) is used to elucidate the nature of charge transport and recombination dynamics of charge-transporting layers; we utilized it here to probe the transport properties of compact TiO_2 and HATNR [60, 95, 207-215]. Figures 3.7a and b reveal the topography of the halide perovskite layer deposited over compact TiO_2 film and HATNR arrays respectively. Figures 3.7c and d represent the surface potential distribution on perovskite layer deposited over the compact TiO_2 and HATNR arrays, respectively, when measured in the dark. A key observation is that the surface potential is distributed evenly over the surface for perovskite coated on both the compact TiO_2 sample and the HATNR sample and is not influenced by the topographical variations seen in the AFM images. The KPFM measurement in dark (Figures 3.7c and d) shows a contact potential difference (CPD) of -668 mV and -368 mV for compact TiO_2 and HATNR samples respectively. Thus, in the dark, the CPD (with respect to the FTO substrate) was strongly negative in both kinds of samples, which is attributed to downward bending of the electronic bands of perovskite at the perovskite-TiO_2 interface, a result that agreed well with previous reports [212, 213]. The surface potential of FTO/compact TiO_2/perovskite sample was more negative compared to FTO/HATNR/perovskite sample, indicating greater band-bending and redistribution of charge at the interface of the perovskite and compact TiO_2. The higher surface potential (less negative) in the dark in FTO/HATNR arrays/perovskite sample is indicative of a lower equilibrium electron density (N_D) in the HATNR arrays, in harmony with previously published reports on the low carrier concentrations obtained in hydrothermally synthesized TiO_2 nanorods [138, 216]. In a subsequent scan at the same position, the CPD recorded with continuous illumination using a 450 nm laser was found to be shifted *ca.* +50 mV and +170 mV for compact TiO_2 and HATNRs (Figures 3.7e and f) respectively due to effective charge separation, i.e. electrons moving to FTO through TiO_2 after extraction from perovskite with hole remaining in the

perovskite (Figures 3.7d and e). The much higher surface potential of HATNR/perovskite samples provides direct evidence of superior charge separation and lower carrier recombination, which in turn is indicative of lower surface defects and hence fewer electron traps compared to compact TiO_2/perovskite sample. The observed shift was found to be reversible after switching off the laser, which confirms that holes are accumulated on the surface of the perovskite while electrons transit through the ETL to the ground electrode (FTO substrate). Taken together, the surface potential data implies better charge separation and transportability of HATNR ETL compared to compact TiO_2 ETL.

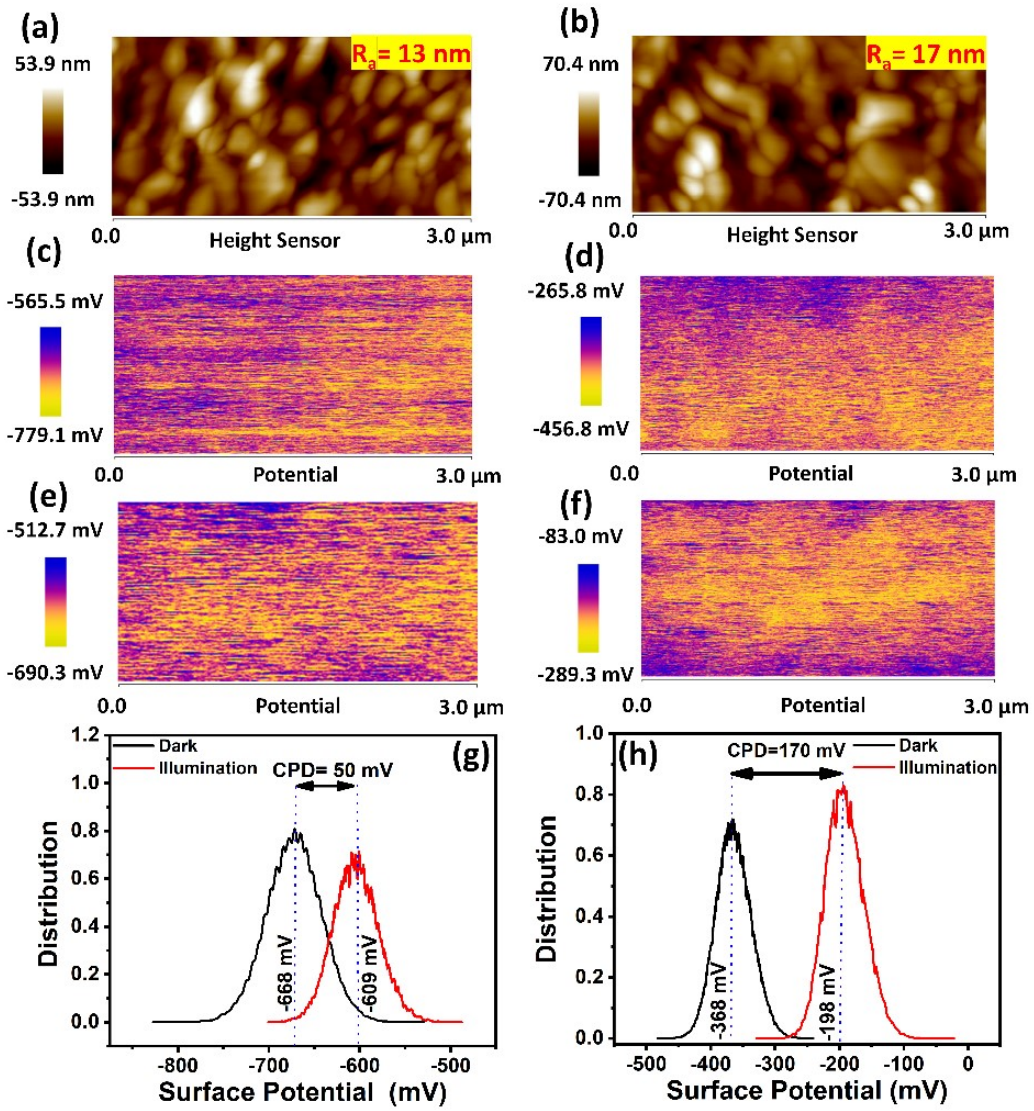

Figure 3.7. The topography of perovskite layer deposited over compact TiO_2 (a) and HATNR (b). Surface potential map of perovskite deposited over compact TiO_2 (c) and HATNR (d) in dark. Surface potential map of perovskite deposited over compact TiO_2 (e) and HATNR (f) under illumination with 450 nm laser. Surface potential distribution on perovskite layer deposited over (g) compact TiO_2 and (h) HATNR in dark and under illumination with 450 nm laser.

To probe the advantages of the near-horizontally aligned TiO_2 nanorods over the compact TiO_2, we fabricated perovskite solar cells with the procedure described in the methodology section.

Figure 3.8a depicts the *J-V* curves of perovskite solar cells fabricated with the compact TiO_2 and HATNR ETLs. The device employing the HATNRs exhibits a power conversion efficiency (PCE) of 15.03%, with a short circuit current density, open-circuit voltage, and fill factor of 22.85 mA cm^{-2}, 0.99 V and 0.67 respectively. The device employing the compact TiO_2 layer exhibits a power conversion efficiency of 10.12% with a short circuit current density, open-circuit voltage, and fill factor of 16.58 mA cm^{-2}, 0.99 V and 0.62 respectively. The ETL composed of an assembly of HATNRs dramatically outperformed the compact TiO_2 and vertically oriented TiO_2 nanorod ETL and displayed 48.5% higher device efficiency compared to compact TiO_2 ETL. Performance of halide perovskite solar cells made with compact TiO_2 and HATNRs measured at AM 1.5G is summarized in Figure A9 and Table A2. The improvement in the PCE was due to improvements in the short circuit current density and the fill factor which are related to the electron transfer and transport properties of ETL. To obtain additional insights into the electron transport and recombination dynamics in the photovoltaic devices with compact TiO_2 and HATNRs ETLs, small-signal perturbation techniques, namely intensity-modulated photovoltage spectroscopy (IMVS) and intensity-modulated photocurrent spectroscopy (IMPS), were performed. Recently, these small perturbation techniques have been frequently used to study the charge carrier dynamics in perovskite solar cells [217-226]. Figure 3.8b shows the IMVS response of a perovskite solar cell in the range of 0.1 Hz to 100 kHz. From the measurements, two semicircles, one in the high-frequency region and another in the low-frequency region, were obtained with time constants τ_{hf} and τ_{lf} respectively. The obtained plot clearly shows two well-resolved semicircles similar to the planar perovskite solar cells reported by Pockett *et al.* [227]. The recombination lifetimes of perovskite solar cells fabricated with HATNR and compact TiO_2 film were calculated by

considering the frequency of the minimum point (f_{min}) of the high-frequency semicircle by using equation (3.3).

$$\tau_r = 1/2\pi f_{min|IMVS} \quad (3.3)$$

$$\tau_{et} = 1/2\pi f_{min|IMPS} \quad (3.4)$$

The recombination time τ_r was calculated to be 3.14 µs for HATNR and 3.20 µs for compact TiO_2 solar cells. Similarly, the recombination lifetime of HATNR and compact TiO_2 based solar cells in dark was calculated using solid-state impedance spectroscopy (Figure A10). As time constants corresponding to carrier recombination for both types of electron transport layers are almost identical, no significant difference in the open-circuit voltage is expected. To understand the charge transport properties of HATNR and compact TiO_2 films as ETLs, IMPS was used, and the resulting Nyquist plots are shown in Figure 3.8c. The IMPS Nyquist plot of the perovskite solar cell has two distinct semicircles. One semicircle is in the first quadrant and the other is in the lower quadrant as reported in the literature for perovskite solar cells [227, 228]. Electron transport times (τ_{et}) within each ETL at short-circuit conditions were calculated by using the equation (3.4), at the frequency corresponding to the minima of the imaginary photocurrent. τ_{et} was calculated to be 36.70 µs for HATNR and 73.80 µs for compact TiO_2 based solar cells. Lower transport time of HATNR indicated better charge transport efficiency of HATNRs which may lead to improvement in the charge collection efficiency of the HATNR and hence the short-circuit current density.

$$D = d^2/2.35.\ \tau_{et} \quad (3.5)$$

$$L_D = (D.\tau_r)^{1/2} \quad (3.6)$$

Charge transport rates within the ETL were calculated by estimating the electron diffusion coefficient, D, using equation (3.5), where the thicknesses (d) of the ETLs in the solar cells were considered. Values of D were found to be 46.70×10^{-6} cm^2 s^{-1} for HATNR arrays and 28.25×10^{-6} cm^2 s^{-1} for compact TiO_2 based solar cells, implying faster electron transport in HATNRs than in compact TiO_2. The corresponding carrier mobilities were estimated using the Einstein relation to be 1.80×10^{-3} cm^2 V^{-1}s^{-1} for the HATNR and 1.09×10^{-3} cm^2 V^{-1}s^{-1} for the compact TiO_2 ETL. Due to their high surface area, the nanorods are expected to have a large population of carrier traps that limit their mobility [216]. However, the diffusion coefficient (and electron mobility) of the HATNRs are more in line with surface passivated rutile TiO_2 nanorods [111, 138, 229], suggesting that the perovskite coating might be at least partially passivating the surface of the HATNRs. Considering the values of D and τ_r, the effective electron diffusion length L_D was determined using equation (3.6) and was calculated to be 12.16 μm for the HATNR based solar cell and 10.61 μm for the compact TiO_2 based solar cell. The 15% higher electron diffusion length is expected to result in higher photocurrent densities and fill factors in HATNR array-based perovskite solar cells. The incident photon-to-electron conversion efficiency (IPCE) shown in Figure 3.8d agreed well with the J_{sc} values obtained in the J-V curve. The IPCE values for the HATNR based perovskite solar cells were significantly larger than those for the compact TiO_2 based perovskite solar cells for the spectral range from 430 nm to 770 nm. The IPCE is given by the product of the light-harvesting efficiency (LHE), the charge separation efficiency (CSE), and the charge collection efficiency (CCE) in equation (3.7),

$$\text{IPCE (\%)} = \eta_{LHE} \times \eta_{CSE} \times \eta_{CCE} \qquad (3.7)$$

The improved carrier extraction by the HATNR ETL demonstrated through stronger PL quenching and CPD shift in KPFM implies a higher charge separation efficiency while the higher electron

diffusion lengths in the HATNR ETL inferred from IMPS data implies a higher charge collection efficiency resulting in higher IPCE and hence short-circuit current density of perovskite solar cells made with HATNR compared to the compact TiO_2.

To understand the light-harvesting properties (η_{LHE} in equation 3.7) of the compact and HATNRs nanostructures, we performed UV-Vis measurements. The UV-Vis spectra of perovskite layer deposited TiO_2 structures are depicted in Figure A11. The significantly lower diffuse reflectance of the perovskite coated HATNR ETL (black curve in Figure A12) compared to the perovskite coated compact TiO_2 ETL (red curve in Figure A12a) for the same perovskite thickness demonstrates the suppression of backscattering in the HATNR ETL-based solar cells. Likewise, the integrated absorptance of perovskite films on the HATNR ETL was found to be dramatically higher in comparison to the compact TiO_2 film in Figure A12b over the entire visible range. The methodology of measurement of the integrated absorptance is explained in Section 3.2 and Figure A11. The strong forward light scattering by the HATNR slows down the propagation of light and also randomizes the direction of propagation, and both these effects enhance the absorption of photons within the perovskite active layer. When the morphology consists of one-dimensional nanostructures aligned horizontally on the substrate, they act as light scattering centers and facilitate the diffusion of photons, and hence increase the light absorption. Similar results have been reported by Gao *et al.* when they used a TiO_2 nanotube network as the electron transport layer for perovskite solar cells [230].

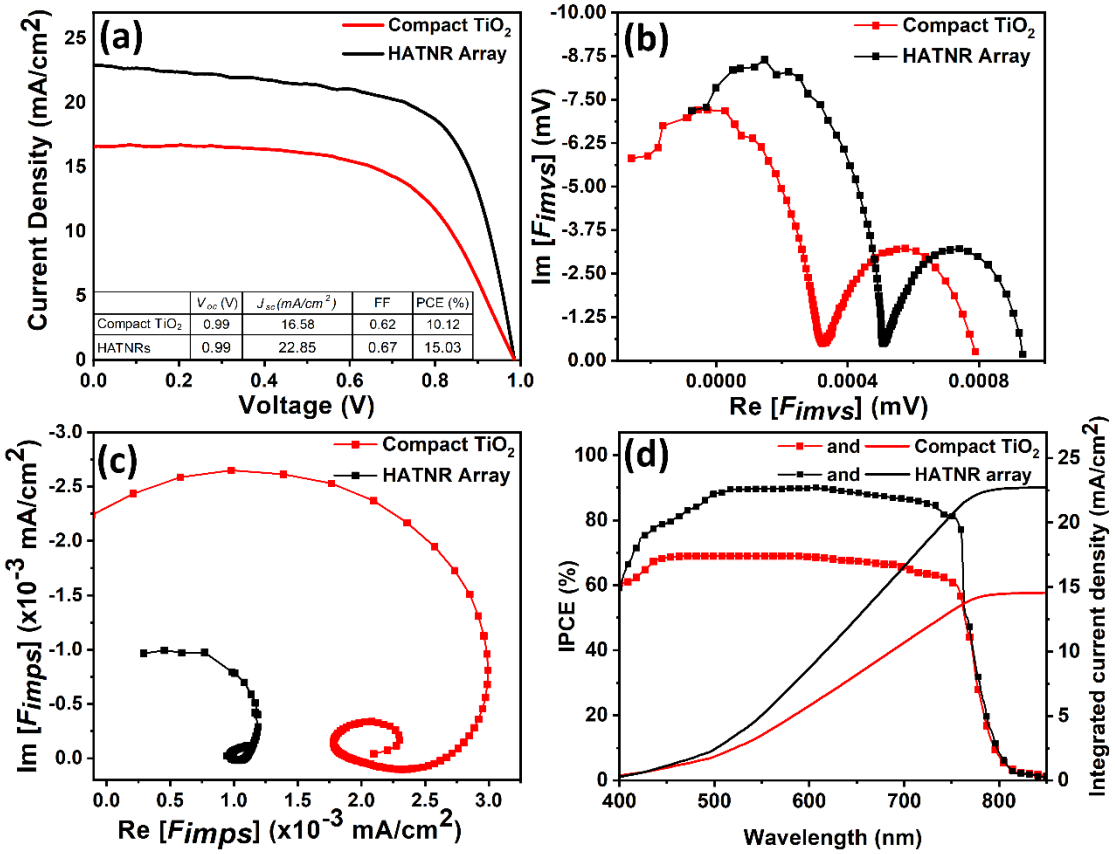

Figure 3.8. Current density–voltage (*J-V*) curves measured under AM 1.5G condition (a), IMVS Nyquist plots measured with 633nm LED (b), IMPS Nyquist plots measured with 633nm LED (c) and External quantum yield of best-performing perovskite solar cells based on compact TiO_2 (red) and HATNR (black) electron transporting layers.

Electromagnetic simulations were performed to validate our hypothesis regarding the nanophotonic enhancement effect using Lumerical FDTD Solutions. The compact layer was set up as 60 nm thick anatase TiO_2, while the individual nanorods were 20 nm in width and 100 nm in length. The HATNR ETL was composed of nanorafts composed of square-shaped rutile TiO_2 nanorods tilted at 30 degrees lying on FTO glass. All the simulation parameters were based on FESEM images. Our hypothesis is that the HATNR nanostructure serves as a scatterer, which

facilitates light diffusion and enhanced light absorption. To better understand light scattering effects and their relationship with the film morphology, far-field scattering simulations were performed for both compact TiO_2 and HATNR ETLs with and without perovskite. Two different perovskite layer thicknesses were used, 200 nm and 800 nm. The polar plots directly reveal the direction and intensity of scattering light. In the simulation, the light source is placed below the sample and the sample is illuminated upwards along the *z*-direction. The substrate lies in the *x*-*y* plane. Forward-scattering is presented as the top semicircle from 0º to 180º while backscattering is from 180º to 360º in both polar plots. Figure 3.9a demonstrates that the compact TiO_2 ETL samples exhibit extremely strong backscattering, which is a major source of photon losses. For the compact TiO_2 ETL, although the forward-scattering decreases after increasing the thickness of the perovskite layer, the backscattering is little changed as seen in Figure 3.9a. Meanwhile, it is obvious from Figure 3.9b that backscattering is well suppressed for the HATNR ETL, and the dramatic decrease of forward scattering intensity is attributed to enhanced absorption of diffused light by the perovskite layer on the top of the HATNR ETL. Figure 3.9c is a simulated Poynting vector distribution in the *x*-*y* plane showing hotspots near the extremities of the major axis of the nanorods where maximum light absorption takes place. Figure 3.9d consists of the simulated absorption spectra of two ETLs after coating with perovskite, and the enhanced light harvesting by the HATNR ETL based samples seen in the experimental data (Figure 3.8d) is confirmed. These results fully validated our theory that high photonic strength of the near-horizontally aligned nanorods coupled with near-perfect refractive index matching with the perovskite layer ensures maximum utilization of incident light within the perovskite layer. These results are applicable to other types of solar cells as well (such as those based on Si and GaAs). Nanorafts consisting of non-absorbing or weakly absorbing horizontal nanorods aligned in the substrate plane will

suppress backscattering and enhance forward scattering, provided that the refractive index of the nanorods is well-matched with the real part of the complex refractive index of the medium in which the nanorafts are embedded (typically the active layer absorber). More information about the simulations is provided in section 3.2 such as architecture parameters, light source, and monitors.

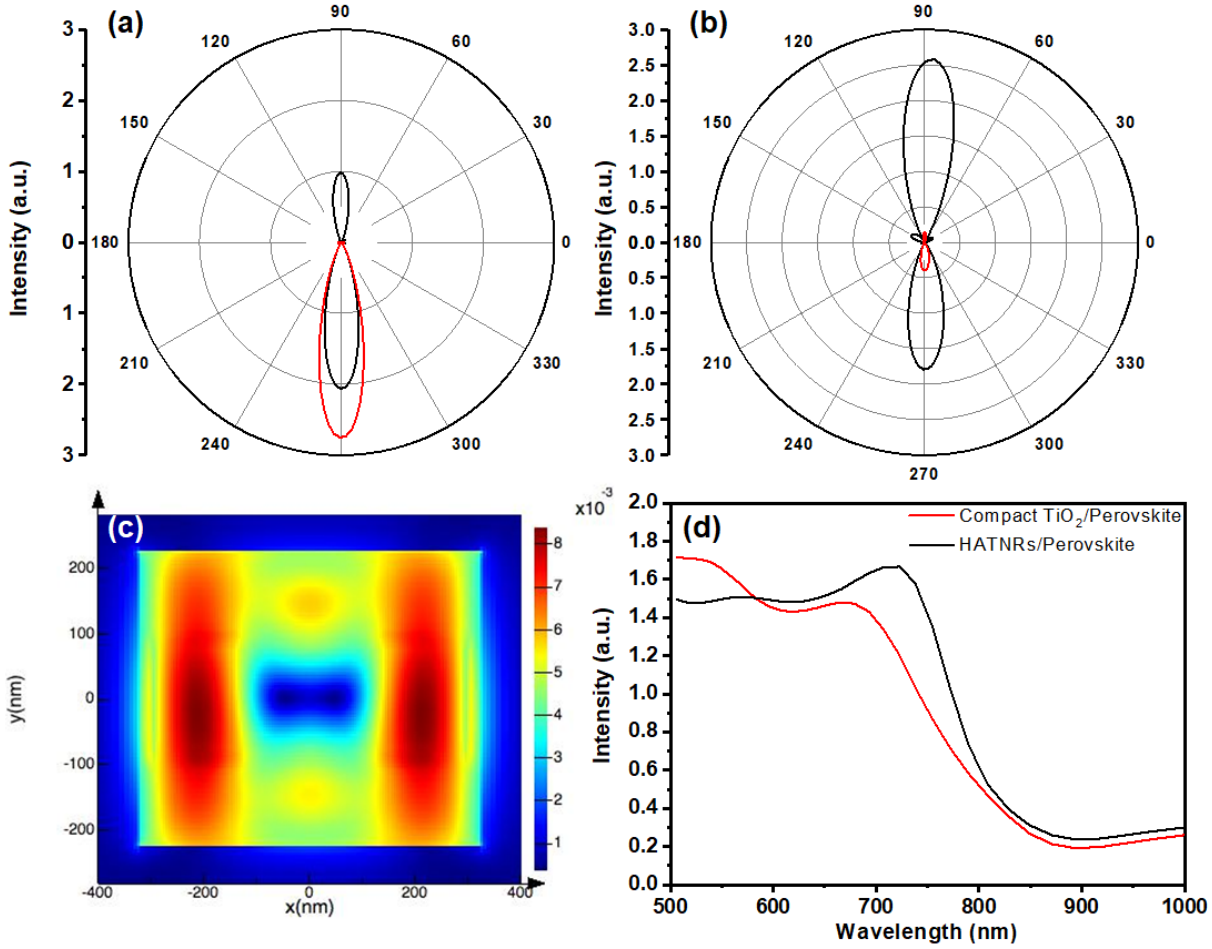

Figure 3.9. Simulation data showing (a) scattering polar plot of compact TiO_2 ETL coated with perovskite thin films of 200 nm thickness (black curve) and 800 nm thickness (red curve) (b) scattering polar plot HATNR ETL coated with perovskite thin films of 200 nm thickness (black curve) and 800 nm thickness (red curve) (c) Poynting vector in substrate plane for HATNR ETL

immersed in perovskite matrix and (d) Absorption of compact TiO_2 (red) and TiO_2 nanorods (black) with 800 nm thick perovskite layer deposited on top.

3.4 Conclusion:

In summary, we demonstrated a facile approach to prepare near-horizontally aligned TiO_2 nanorod (HATNR) arrays *via* a hydrothermal route. Scanning electron microscopy showed the formation of larger grained perovskite films on the HATNR electron transport layer (ETL). Time-resolved photoluminescence measurements indicated that the HATNR extracted electrons more efficiently from the perovskite layer compared to the commonly used compact TiO_2 electron transport layer while intensity-modulated photocurrent spectroscopy suggested faster transport in the HATNR ETL. The HATNR ETL also resulted in a nanophotonic enhancement of the absorption in the perovskite active layer. Both experimentally measured and simulated optical spectra demonstrated a strong suppression of the backscattering in perovskite-coated nanorod layers relative to perovskite-coated compact TiO_2 layers, and a forward scattering-mediated enhancement of the light-harvesting. As a consequence of the nanophotonic enhancement in the utilization of photons in the active layer as well as improved electron extraction and electron transport in perovskite solar cells employing HATNR ETLs, a dramatic enhancement of the overall solar cell performance was observed. Perovskite solar cells constructed using the HATNR ETL exhibited an average photoconversion efficiency (PCE) of 13.9 ± 0.8% and a champion device PCE of 15.0%, which is nearly 50% higher than perovskite solar cells constructed using the compact TiO_2 ETL, which exhibited an average photoconversion efficiency (PCE) of 9.4 ± 0.8% and a champion device PCE of 10.1%.

Chapter-4 Nanostructured NiO HTL

4.1 Introduction:

Halide perovskites have great potential for photovoltaic applications due to their extraordinary properties such as direct optical bandgap, broadband light absorption, bipolar transport, and long carrier diffusion length. Halide perovskite solar cells (HPSCs) generally contain a hole transporting layer (HTL), an electron transporting layer (ETL), and a perovskite absorber layer. The ETL transports the photogenerated electron from the perovskite layer to the electrode and blocks the holes. Similarly, the HTL transfers the photogenerated holes to the counter electrode and impedes the electrons. The use of the HTL to extract holes from perovskites and transport them to the electrode remains indispensable in the preparation of highly efficient HPSCs regardless of the device architecture.

Small organic molecules, polymers, carbon derivatives, and inorganic semiconductors are the four major types of hole transporting layers being investigated to produce high-efficiency HPSCs [213, 231-238]. Several *p*-type small molecules have been tested for the HTL in perovskite solar cells; however, the most efficient small molecules to date are the spiro-based triphenylamine derivatives [235, 236, 239-243]. However, these HTLs generally suffer from low charge mobility and low long-term durability. Chemical doping is required for these triphenylamine derivatives to achieve adequate hole-transporting capability while maintaining low interfacial charge recombination at the HTL-perovskite interface [239, 241, 244-246]. Polymers have the advantage that only a few nanometers of polymeric HTL are needed to obtain a uniform coating of the perovskite surface while offering higher hole mobility compared to undoped small molecules, a low tendency to

crystallize, and the ability to be used either as top or bottom contacts for HPSCs [246-252]. In addition, batch-to-batch variation in polymer synthesis is a challenge for large scale applications. Alternatively, carbon nanotubes, although promising, need an expensive purification procedure to isolate them from the associated carbon impurities.

Nickel oxide is a cubic, wide-bandgap *p*-type semiconductor extensively used as the hole transporting layer in polymer, dye-sensitized, perovskite solar cells and as a *p*-type electrode [253-260]. Commonly utilized techniques to deposit NiO on a conductive glass substrate include spin-coating of dispersed NiO nanoparticles, electrochemical anodization of Ni, and hydrothermal growth [261]. Ongoing efforts aim toward the structural and compositional optimization of the nanoparticles in the HTL [12, 236, 262-266]. Hydrothermal growth is a method that could potentially offer exceptional control over the morphology, chemical composition, and defect density of NiO nanostructures. Herein, we report a facile hydrothermal synthesis of experimentally controllable nanostructures directly on FTO-glass substrate. We show that this approach provides nanostructured NiO yielding a high open-circuit voltage of 1.14 V and better power conversion efficiency with a $FA_{0.83}MA_{0.17}Pb(I_{0.83}Br_{0.17})_3$ perovskite active layer compared to thin-film NiO based devices.

4.2. Experimental details:

4.2.1 Materials:

Analytical grade urea (≥99%), chloroacetic acid (≥99.0%), $NiCl_2.6H_2O$ (≥97.0%), formamidinium iodide (FAI) (≥99%), PbI_2 (99%), methylammonium bromide (MABr) (98%) and $PbBr_2$ (≥98%), PCBM (>99.5%) was procured from Sigma Aldrich and used as received without

any further purification. HPLC grade DMF, DMSO, chlorobenzene, isopropanol, and methanol were used in all the experiments without any further purification. Deionized water was used throughout experiments. Fluorine doped tin oxide (F: SnO_2, FTO) glass (transmittance 80-82%) was purchased from Hartford Tec Glass Company.

4.2.2 Characterization:

The morphological features of thin films were investigated using Field emission scanning electron microscopy (FE-SEM) on a Zeiss Sigma FESEM operating at a 5 kV accelerating voltage. The fine morphological features of NiO thin films were determined by using high-resolution transmission electron microscopy (HR-TEM), on a JEOL JEM-ARM200CF S/TEM equipped with EDX operating at an acceleration voltage of 200 kV. To see the film features, the sample was sliced by using a focused ion beam (FIB) with a Ga^+ ion source. Before FIB operation the sample was coated with carbon and then a few nanometers of gold to protect film morphology and to reduce the charging effect. The obtained samples were analyzed under HRTEM and acquired .dm3 images were processed by using Gatan micrograph to calculate d spacing and diffraction planes. The phase structure and crystalline properties of materials were determined by X-ray diffraction (XRD) pattern collected on a Bruker D8 Discover instrument using Cu-Kα radiation (40 kV, λ = 0.15418 nm) equipped with a LynxEYE 1-dimensional detector. The spectra were collected in the range of 2θ values 4–60° and step size was 0.02°.

Raman spectra to investigate specific vibrational features of materials were recorded on a Thermo Scientific DXR2Raman Microscope using the 532 nm excitation line with an incident power of 20 $mWcm^{-2}$. The spectra were accumulated for 300 seconds using 50 μm confocal pinhole apertures and a 2 cm^{-1}/CCD pixel element spectral dispersion grating. The sample was

deposited on a glass slide for the Raman measurement samples and the laser spot was focused on the sample surface and the scattered light was collected.

X-ray photoelectron spectroscopy (XPS) for evaluating the surface chemical composition and oxidation state of NiO materials on FTO was acquired on an XPS (Axis-Ultra, Kratos Analytical) instrument equipped with monochromatic Al-Kα source (15 kV, 50 W) and photon energy of 1486.7 eV under ultrahigh vacuum ($\sim 10^{-8}$ Torr). The core level C1s XPS of adventitious carbon at BE ≈ 284.8 eV was used as a standard for carbon correction to assign binding energy (BE) of other elements. CasaXPS software was used for processing of raw spectra and obtained deconvoluted spectra were plotted in Origin. Ultraviolet photoemission spectroscopy (UPS) was performed to determine work function and valence band spectra of samples were performed using a 21.21 eV He lamp as the excitation source.

To measure the optical band gap of NiO materials UV-Vis absorption spectra in diffuse reflectance mode was executed using a Perkin Elmer Lambda-1050 UV–Vis-NIR spectrophotometer equipped with an integrating sphere accessory. Photoluminescent behavior of the thin film was determined with steady-state photoluminescence (PL) spectra acquired on Varian Cary Eclipse fluorimeter xenon lamp excitation source and a slit width of 5 nm. The time-resolved photoluminescence (TRPL) lifetime decay curve to calculate the average lifetime of materials was recorded using a lab-assembled single-photon counter. A 405 nm picosecond diode laser (Alphalas GmbH) operated at a frequency of 13 MHz was used to excite the samples, and a Becker-Hickl HPM-100-50 PMT interfaced to an SPC-130 pulse counter system was used to measure the response. The response time of setup was ~100 ps.

4.2.3 Synthesis and fabrication of solar cells:

The fabrication process for inverted perovskite solar cells with NiO nanoparticle HTLs is a multistep procedure (Figure 4.1). First, fluorine-doped tin oxide (F: SnO_2, FTO) substrates were cleaned by sonicating in acetone, isopropyl alcohol, and DI for 10 minutes each. The substrates were then dried by using a nitrogen gun followed by 5 minutes in O_2 plasma. A 0.2 M solution of $NiCl_2.6H_2O$ was then prepared in methanol. The solution was stirred for 2 h at room temperature before spin coating for 30 s onto the clean FTO substrate using a 3000 rpm spin rate. The substrates were pre-dried at 100 °C for 10 min and then calcinated at 500 °C for 30 minutes to produce NiO thin films on the FTO substrate. The NiO nanoparticles were then grown on the NiO thin films by a hydrothermal process. A solvent was prepared to consist of 1 g of urea and 60 mg of chloroacetic acid dissolved into 80 mL of DI water and 1 mL of HCl (37 wt%). Precursor solutions were made, consisting of different concentrations of $NiCl_2.6H_2O$ (1 mM, 3 mM, and 5mM) dissolved into the previously prepared solvent. The resulting precursor was then transferred into a Teflon-lined stainless-steel autoclave. The FTO substrate with the NiO thin film was placed inside the autoclave vertically. The autoclave was then sealed and placed in an oven kept at 200 ºC for 30 min to achieve hydrothermal growth of nanoparticles. After completion of the reaction, the autoclave was cooled to room temperature under ambient air and the resultant nanostructure grown on FTO glass was rinsed with DI water for 2 min and dried in a stream of flowing nitrogen, followed by annealing at 500 ºC for 30 min.

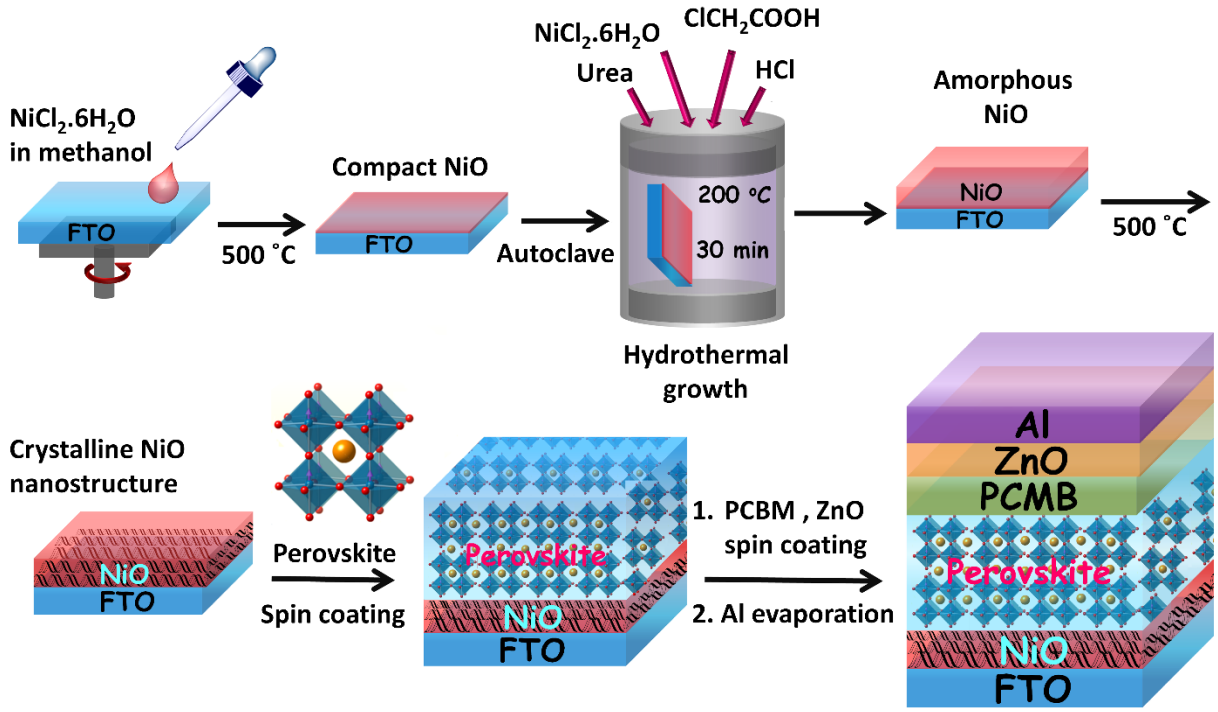

Figure 4.1. Schematic diagram illustrating the NiO nanostructure synthesis procedure (top row) and perovskite solar cell (bottom row) fabrication methods.

The perovskite precursor solution was prepared by dissolving 1 M of formamidinium iodide (FAI), 1 M PbI_2, 0.2 M methylammonium bromide (MABr) and 0.2 M $PbBr_2$ in a 4:1 mixture of DMF: DMSO respectively. This precursor solution was then stirred at 70 ºC for 2 h followed by deposition on top of the as-fabricated NiO nanostructure in a two-step spin coating procedure. The first step was at 2000 rpm for 10 s; the second one at 4000 rpm for 20 s. After 15 s in the second step, 100 µL of chlorobenzene was deposited onto the spinning substrate to achieve rapid crystallization. The substrates were then annealed at 100 ºC for 30 min. Next, a 20 mg/mL solution of PCBM in chlorobenzene was spin-coated at 1000 rpm for 10 s on top of the perovskite layer, followed by annealing 110 °C for 10 min. An approximately 200 nm thick layer of ZnO nanoparticles was deposited on top of the PCBM layer by spin coating a colloidal solution of ZnO

(2.5 wt% in isopropanol) at 4000 rpm for 30 s followed by annealing at 70 °C for 30 min. Finally, an e-beam evaporator was used to deposit about 70 nm of Al on top of the stack, completing the device. The thicknesses of the various layers were estimated by scanning electron microscopy using a Sigma ZESIS field emission scanning electron microscope (FESEM).

4.3 DFT Modeling:

To illustrate the electronic band alignment of NiO with perovskites and investigate the charge transport mechanism in NiO-based inverted perovskite solar cells, we performed electronic structure calculations of $CH_3NH_3PbBr_3$ ($MAPbBr_3$) and $CH_3NH_3PbI_3$ ($MAPbI_3$) nanoparticles interacting with an NiO (100) crystal surface. The nanoparticles are represented by clusters containing eight elementary cells. As the first step, we optimized noninteracting perovskite geometries by means of Density Functional Theory (DFT) realized in OpenMx (Open source package for Material eXplorer) package [267]. This software allows combining the DFT+U approach with non-collinear spin-orbit coupling needed to better describe the electronic structure of perovskite-type materials [268]. For all calculations, we used relativistic pseudopotentials (VPS) and pseudo-atomic orbitals (PAO) optimized for the LDA type function. The NiO surface is represented by a (100) slab of the bulk structure NiO exhibiting antiferromagnetic ordering of type 2 with planes of opposite spins repeated in alternating order along the (111) direction [269]. The magnetization features of NiO with different morphologies have been investigated [270] and, as we will show, they present an important feature of the HTLs developed here. The LDA+U method with the appropriate Hubbard parameter for Ni (4.0) represents the correct electronic structure for metal oxides with localized d-states [271].

Specifically, we calculated three geometries with the different mutual orientations of the perovskite and NiO surfaces. In Geometry 1 (G1) the surfaces were separated by ~1 nm (Figure 4.2). The spatial orientation of the cluster is inconsequential at this distance (~ 1 nm) as it does not assume strong interaction with the surface of NiO. Geometries G2 and G3 reflect cases wherein the perovskite and NiO are in very close proximity (<0.3 nm) but have different crystallographic orientations. In G2 the perovskite contacts the NiO (100) surface via the closest halogen atoms and MA ions, while in G3 they approach via the halogen and lead atoms. The perovskite clusters were oriented to maximize the contact surface, which means that in each case we have about four nearest-contact interaction sites.

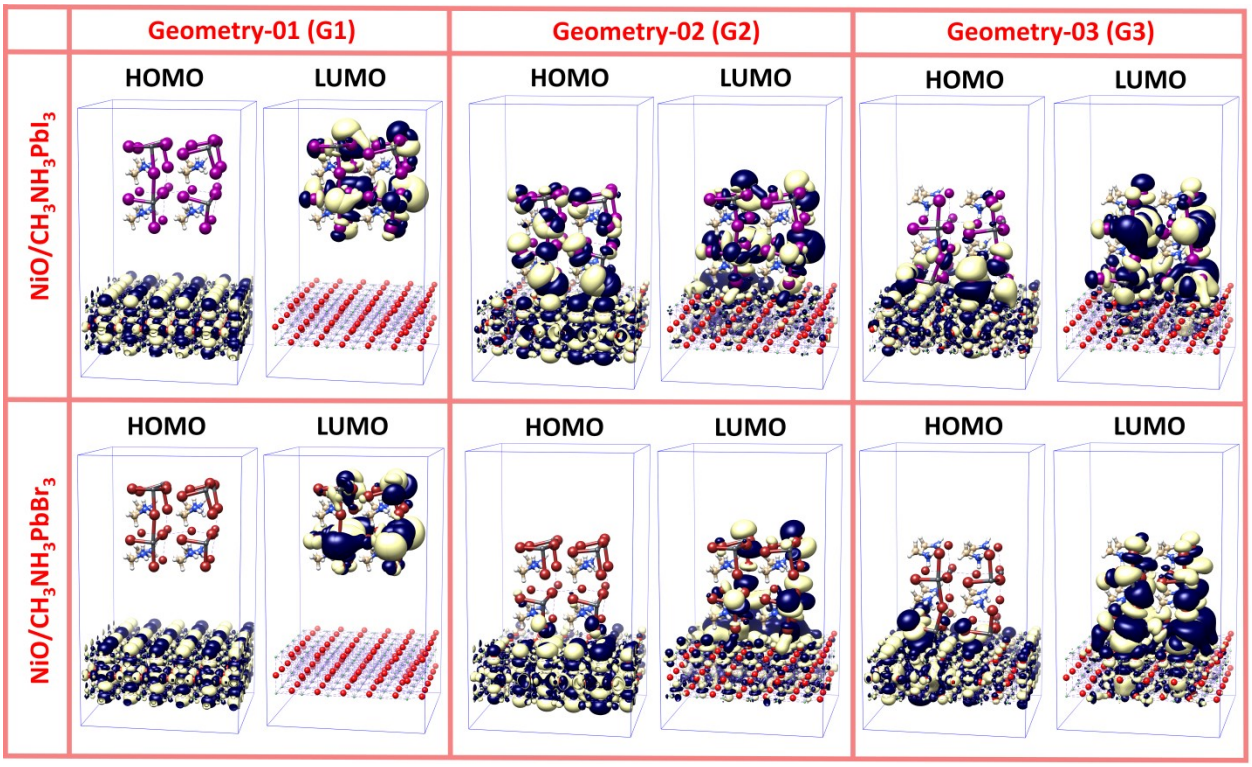

Figure 4.2. Optimized structures showing the HOMO (left) and LUMO (right) orbitals for three mutual orientations of an NiO (lower) – perovskite (upper) interfacial region. These geometries are referred to as G1, G2, and G3. The upper row shows the $MAPbI_3$ and the lower row represents

the $MAPbBr_3$ perovskite nanoparticles. In the NiO structure, nickel atoms are represented by green spheres and oxygen atoms are represented by red ones. In the perovskite structure, the brown and pink spheres represent Br and I, respectively, dark gray ones represent Pb atoms, and the other colors indicate the atomic components of MA groups.

The HOMO-LUMO orbitals for all geometries are visualized in Figure 4.1. The calculated adsorption energies for G2 and G3 and HOMO-LUMO energy for G1 are reported in Table-A3. There is a somewhat stronger interaction for the $CH_3NH_3PbBr_3$ case compared to the case of $CH_3NH_3PbI_3$. For both perovskites, G1 shows clear localization of HOMO orbitals on NiO surface and LUMO orbitals on perovskite clusters. This separation fully corresponds to the Type I charge transfer mechanism discussed in [272].

In G2 and G3 we see the tendency for mixing of the orbitals. The mutual penetration for G3 is stronger than for G2, which suggests a higher probability for charge transfer in this case. The projected DOS distributions for surface and clusters presented in Figure A13 illustrate this concept in detail. One can see that the HOMO and LUMO orbitals for G1 and G2 change insignificantly, while for G3 the substantial redistribution of charge results in narrowing of the gap. Although a HOMO-LUMO analysis is only approximate, it demonstrates the charge transfer mechanism and relates it to the mutual orientation of perovskite clusters and the NiO surface.

4.4 Results and discussion:

The energy level diagram for the as-built device explains the expected charge separation process in the NiO/perovskite/PCBM/ZnO multilayer architecture (Figure 4.3). The electron-hole pairs are initially generated in the perovskite layer. The electrons are transferred into the PCBM conduction band and subsequently to the ZnO layer, while the photogenerated holes are injected

to the NiO valence band. Electrons and holes are then collected by the back Al and front FTO contacts, respectively, in order to generate photocurrent. The ideal theoretical V_{oc} (V_{oc} for the Shockley−Queisser Limit) for cells are 1.122, 1.215, and 1.309 V for the active layers with the E_g = 1.4, 1.5, and 1.6 eV, respectively [232, 273] whereas, the largest V_{oc} voltage observed in undoped NiO based perovskite layer in practice is about 1.12 V with $MA_{1-y}FA_yPbI_{3-x}Cl_x$ perovskite layer [73, 274-276]. Various recombination processes (radiative or non-radiative) *i.e.* exciton annihilation, back electron transfer at the perovskite/ETL interface, back hole transfer at HTL/perovskite interface, and recombination at those interfaces limit the efficiency of perovskite solar cell to a maximum theoretical value of 30.14% (for the case of E_g = 1.6 eV, corresponding to a wavelength of 775 nm). Critically, as we show here, the NiO nanostructured layer with Ni^{3+} defects demonstrate extraordinary hole-transporting properties which can increase the open-circuit voltage up to 1.14 V with the active layer with bandgap of about 1.5 eV.

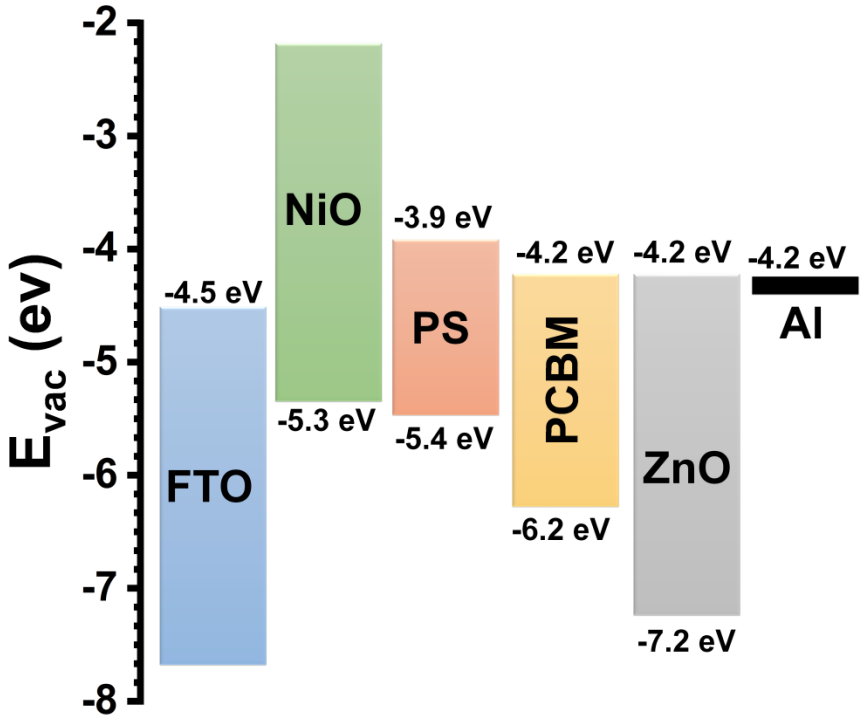

Figure 4.3. Energy band diagram for an inverted perovskite solar cell with the structure of FTO/NiO nanostructure/perovskite absorber layer/PCBM/ZnO/Al.

The concentration of $NiCl_2.6H_2O$ in the growth solution was found to play an important role in determining the thickness and morphology of the NiO nanostructured film. A low concentration of $NiCl_2.6H_2O$ produces a non-uniform NiO nanostructure (Figure A14; NiO nanostructure grown with a $NiCl_2.6H_2O$ concentration of 0.5 mM), which results in low shunt resistance and hence yields a poor power conversion efficiency. Increasing the $NiCl_2.6H_2O$ concentration leads to an increase in the thickness of the nanostructured film, which increases light absorption by the HTL and results in less light incident on the perovskite layer. Thus, it is of crucial importance to optimize the thickness of NiO to achieve maximum efficiency. This can be achieved by changing the concentration of $NiCl_2.6H_2O$ in the growth solution (1 mM, 3 mM, and 5 mM).

Optimization of the nanostructured NiO layer was performed by using different concentrations of the starting materials, examining the resulting morphology by FESEM, HRTEM, and XRD, and then by measuring the photovoltaic performance. The FESEM results show that the optimized NiO nanostructured HTL has a distinct morphology compared to a conventional thin film NiO layer. The reference compact NiO thin film showed continuous thin film of NiO (Figure 4.4a and 4.4b while the nanostructured NiO layer consists of a fibrous mesh-like assembly of NiO crystallites (Figure 4.4d, 4.4e and A15). Increasing the concentration of $NiCl_2.6H_2O$ to 3 mM and 5 mM resulted in an increase in the thickness and density of nanostructured films (Figure A16). To investigate the thickness of the NiO layers we have again recollected cross-sectional and top view FESEM images of the solar cell device (Figure 4.4c and 4.4f). The FESEM micrographs clearly demonstrate that the thickness of NiO layer for compact and nanostructured NiO containing device is approximately 25-30 nm and 150-160 nm respectively that was well-matched with the

value obtained from HR-TEM. Further to probe the layer observed in cross-sectional SEM is truly NiO, we have performed EDX elemental mapping of the top (Figure 4.4g-j) of the nanostructured NiO sample and cross-section of the HPSC fabricated with nanostructured NiO (Figure 4.4k-r). The EDX map of the device clearly demonstrates a dense distribution of Ni element just above the Sn layer (originated from FTO substrate) that verifies the presence of NiO layer on the top of FTO. All other composing elements present in the perovskite layer and ZnO ETL were also visible on the top of NiO layer. Composite image (Figure 4.4r) further verify well built nanostructured solar cell assembly.

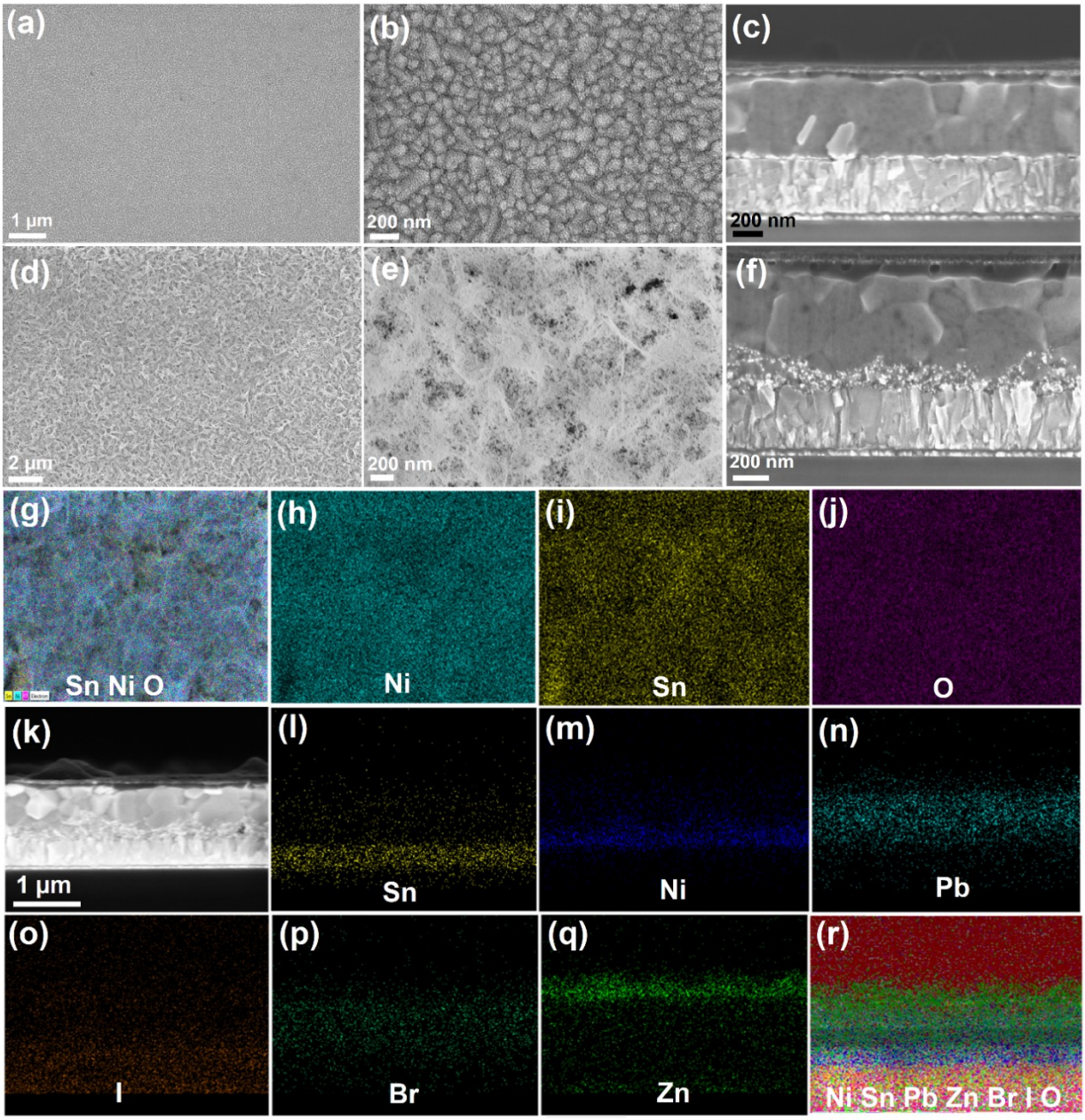

Figure 4.4. Top-view FE-SEM images of NiO (a, b) compact film and a device cross-section (c), a NiO nanostructured layer fabricated with 1 mM, of $NiCl_2.6H_2O$ in the growth solution (d, e) and the device cross-section (f). Top-view FE-SEM image of nanostructured NiO deposited over FTO substrate used for EDX mapping (g), and mapping for Ni (h), Sn (i) and O (k). Cross-sectional FESEM image of nanostructured NiO based solar cell used for the EDX mapping (k), and mapping for Sn (l), Ni (m), Pb (n), I (o), Br (p), Zn (q) and overlaid image (r).

The fine structural features of NiO thin films were investigated by HRTEM. The cross-sectional view of the NiO nanostructured sample (1 mM $NiCl_2.6H_2O$) showed the presence of a rough, polycrystalline NiO film on the FTO substrate (Figure 4.4(a) and Figure A17). The NiO film was composed of randomly oriented nanoparticles. The average thickness of the film was found to be approx. 150-160 nm. In contrast, the compact NiO sample showed a thickness of only 25-30 nm (Figure 4.5(b) and Figure A18). The high magnification HRTEM images of nanostructure NiO shows a grain size of ~10-15 nm while the compact NiO showed a grain size of ~8-17 nm (Figure 4.5(c) and 4.5(d)). Both samples displayed lattice fringes with 0.24 nm interplanar *d*-spacing correlating to the (111) plane of NiO (Figure 4.5c and d insets).

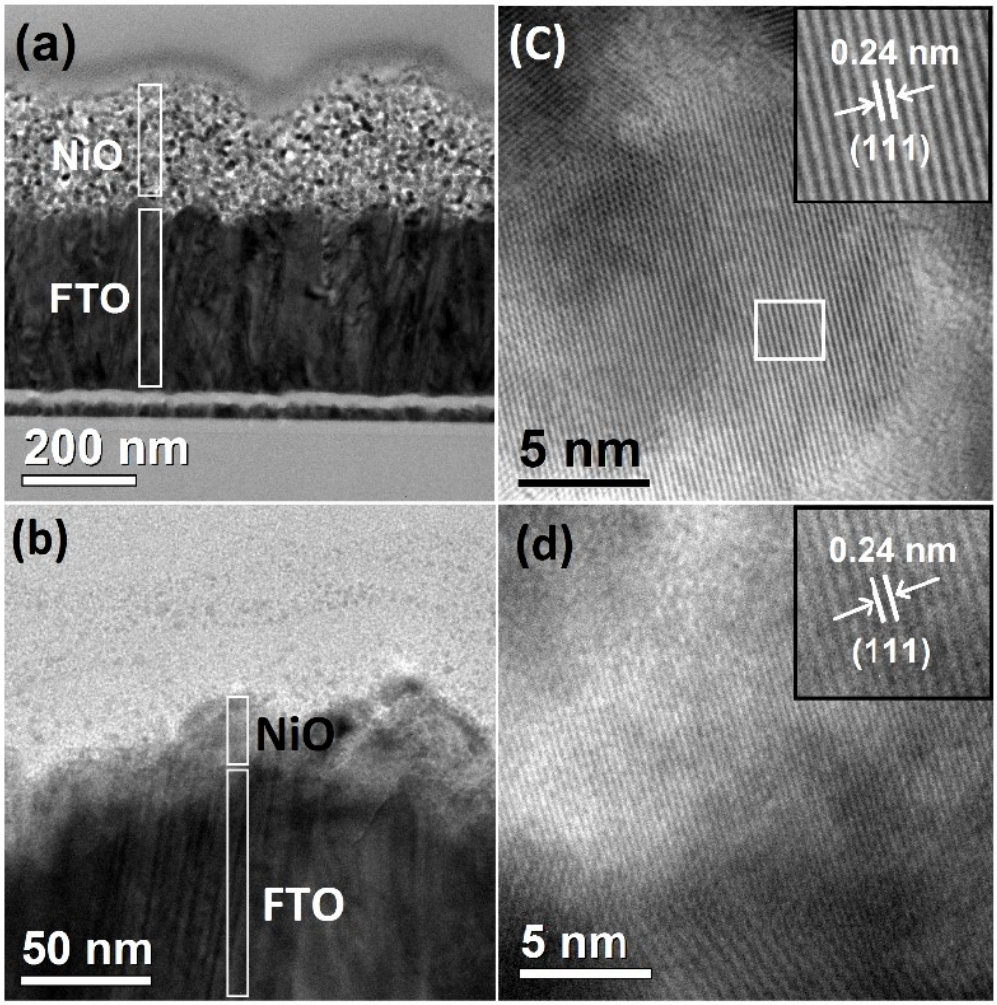

Figure 4.5. HRTEM image showing cross-sectional view of (a) nanostructured NiO (1 mM $NiCl_2.6H_2O$) and (b) compact NiO thin films showing the thickness and morphology of NiO deposited on the FTO (note: the less dense layer above NiO is carbon film coated on the sample to prevent samples charging during FIB treatment; (c) and (d) high-resolution TEM images of nanostructured and compact NiO films showing lattice fringe contrast. The inset shows a 0.24 nm interplaner spacing consistent with the (111) planes of NiO.

XRD plots of compact and nanostructured NiO on FTO substrates grown by using a different concentration of $NiCl_2.6H_2O$ are shown in Figure A19. The XRD diffraction peaks at 2θ = 37.5º, 43.4º, 63.0º, and 75.2 º was assigned to the (111), (200), (220) and (311) planes of cubic NiO, respectively (JCPDS card No. 47-1049). The remainder of the XRD peaks arises from the FTO substrate. Raman spectra of compact and nanostructured NiO on FTO substrates show one-phonon (1P) longitudinal and transverse modes at 558 cm^{-1}, two-photon (2P) transverse mode at 792 cm^{-1}, 2P longitudinal and transverse modes at 950 $cm^{-1,}$ and two 2P longitudinal modes at 1095 cm^{-1}, in close agreement with previously reported literature (Figure A19b) [277, 278].

The dye desorption technique was used to estimate the surface area of the compact and nanostructured samples. Freshly prepared compact and nanostructured NiO samples on FTO (1.5 × 2.5 cm) were treated with O_2 plasma for 5 min followed by overnight immersion in 1 mM SQ2 solution in methanol to form a monolayer of SQ2 dye over the available NiO surface. The obtained samples were rinsed with methanol and dried under nitrogen flow. For reference, 7.8 x 10^{-6} M methanolic solution of SQ2 containing 0.1 M KOH was also prepared. The absorbtion spectrum of reference sample is shown in Figure 4.6a. The absorption spectra of nanostructured and compact NiO are presented in Figure 4.6b and 4.6c, respectively. The sharp absorption peak at around 656 nm in monolayer deposited nanostructured NiO and compact NiO validates the presence of SQ2

monolayer on the samples (Figure 4.6d and 4.6e). After that, the monolayer of SQ2 was etched-away from the nanostructured and compact NiO samples using 3 mL of 0.1 M KOH dissolved in methanol. The absorption spectra of desorbed dye from nanostructured NiO and compact NiO samples is shown in Figure 4.6f and 4.6g. Considering linear dependancy of the absorption of SQ2 on NiO surface, the concentration of dye desorbed from nanostructured and compact NiO samples was calculated to be 4.17 $\times 10^{-6}$ and 1.44$\times 10^{-6}$ moles respectively. The surface area of vertically standing SQ2 has been reported to be 2.5 nm^2 [279, 280] which gave a total surface area value of nanostructured NiO and compact NiO to be 1.42and 0.072 m^2, respectively. The high interfacial surface area of nanostructured NiO helps in better loading of the active layer and also improves charge collection from the bulk of the perovskite layer.

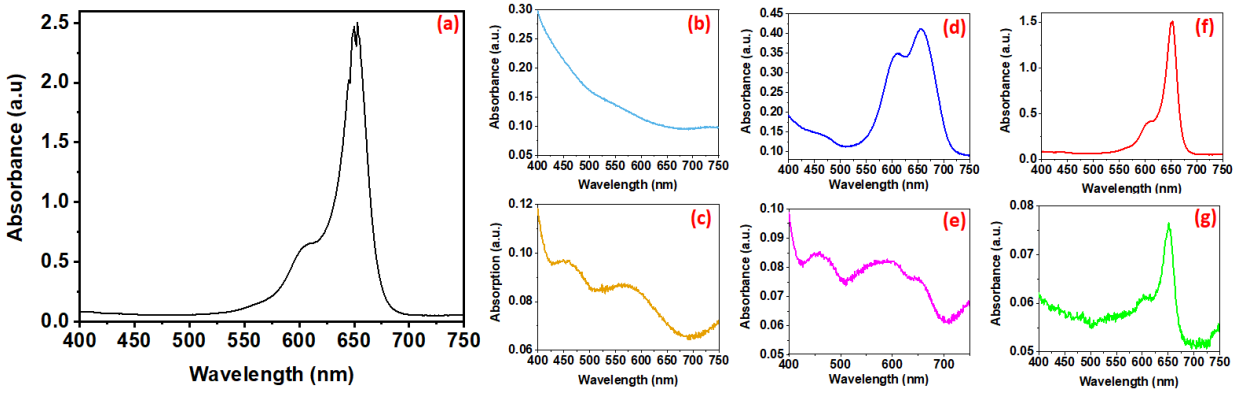

Figure 4.6: UV-vis absorption spectra of (a) SQ2 dissolved in 0.1 M KOH, (b), FTO deposited nanostructured NiO and (c) compact NiO, monolayer SQ2 deposited over (d) nanostructured NiO and (e) compact NiO, KOH assisted desorbed SQ2 from (f) nanostructured and (g) compact NiO.

The bandgap can be extracted from the optical absorption spectra (Figure A20) following the Tauc method, where the absorption coefficient is related to the bandgap via

$$(\alpha h\nu)^n = (h\nu - E\mathrm{g}) \qquad (4.1)$$

Here, α is the absorption coefficient, h is Plank's constant (6.626×10^{-34} J.s), v is frequency, and n indicates either a direct (n = 2) or indirect (n = 1/2) bandgap (E_g), Values of E_g were obtained as usual by extrapolating the linear regions of the Tauc plots to $(\alpha hv)^n = 0$, assuming from the literature reports that the NiO transition is direct [281-283]. The resulting bandgap values were 3.39 eV for the optimized nanostructured NiO films, in agreement with the literature [282, 284, 285].

X-ray photoelectron spectroscopy (XPS) was used to evaluate the surface chemical composition and oxidation states of the optimized NiO nanostructure made with 1 mM $NiCl_2.6H_2O$ (Figure 4.7). The XPS survey scan shows various peaks corresponding to Ni2p, Ni2s, Ni3s, Ni3p, NiLLM, O1s, and OKLL core-level electrons, consistent with NiO (Figure A21). The core-level high resolution-XPS spectra of nanostructured NiO in Ni2p region can be deconvolved into five peak components. Two intense peaks at BE ≈ 854.5 and 872.5 eV were ascribed to $Ni2p_{3/2}$ and $Ni2p_{1/2}$ peak components and their satellite peaks located at binding energy value 861.1 and 879.2 eV originated due to spin-orbital coupling of N2p orbital validating the presence of NiO (Figure 4.7a) [286-288]. The Ni $2p_{3/2}$ peak consisted of a main peak at 853.8 and a shoulder centered at 855.7 eV, which we attribute to the $Ni2p_{3/2}$ peak components of Ni^{2+} and Ni^{3+}, respectively. The existence of the Ni^{3+} component might be due to the contribution of signal from a small fraction of Ni_2O_3/NiOOH formed by surface oxidation of NiO thin film [289, 290]. The deconvolved spectra in the O1s region depict three peak components centered at 529.4, 531.0 and 532.7 eV corresponding to oxygen atoms in NiO lattice, surface adsorbed –OH, and C=O from adventitious carbon (Figure 4.7b).

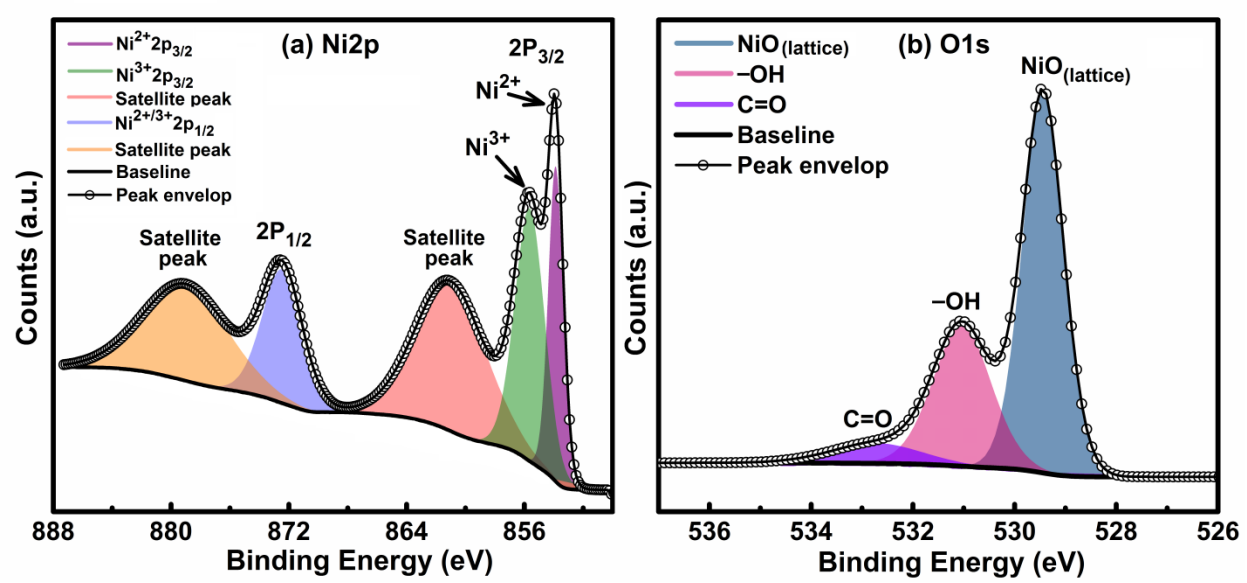

Figure 4.7. Core level HR-XPS spectra of NiO nanostructure fabricated with 1 mM, of $NiCl_2.6H_2O$ in (a,) Ni2p region (b) O1s region.

To compare the hole transporting properties of the nanostructured and the compact NiO layers, perovskite solar cells were prepared with an architecture consisting of FTO/NiO/ $FA_{0.83}MA_{0.17}Pb(I_{0.83}Br_{0.17})_3$/PCBM/ZnO/Al (shown in Figure 4.3). Solar cells made with a compact NiO hole transporting layer yielded a short circuit current density (J_{sc}) of about 20 mA/cm^2, an open-circuit voltage (V_{oc}) of 1.01 V, and fill factor (FF) of about 58% resulting in the overall power conversion efficiency (PCE) of about 12%. While NiO nanostructured solar cells, made with 1 mM of $NiCl_2.6H_2O$, showed a short circuit current density of about 23 mA/cm^2, these devices yielded a V_{oc} of 1.11V and fill factor of about 70% resulting in the power conversion efficiency of about 17.75% (Figure 4.8a). For comparison we fabricated solar cells with PEDOT:PSS as the HTL. The $V_{oc,}$ $J_{sc,}$ and FF of PEDOT:PSS based device was 0.93V, 19.31 mA/cm^2 and 55% respectively which gave a PCE of about 9.9% (Figure A22). As shown in Table 4.1 and Figure A23, the optimized nanostructured NiO-based solar cells have improved current density, fill factor and open-circuit voltage, which could be related to improved hole transfer and

transport properties, lower interfacial and bulk recombination, and better energy level alignments in nanostructures compared to compact NiO based device. IPCE spectra of solar cell with nanostructured NiO hole transporting layers showed a better overall performance for the nanostructured film over a wide range of wavelengths (Figure 4.8b), yielding an integral short-circuit current value comparable to those obtained from *J-V* curves (i.e., higher for the nanostructured NiO HTL device).

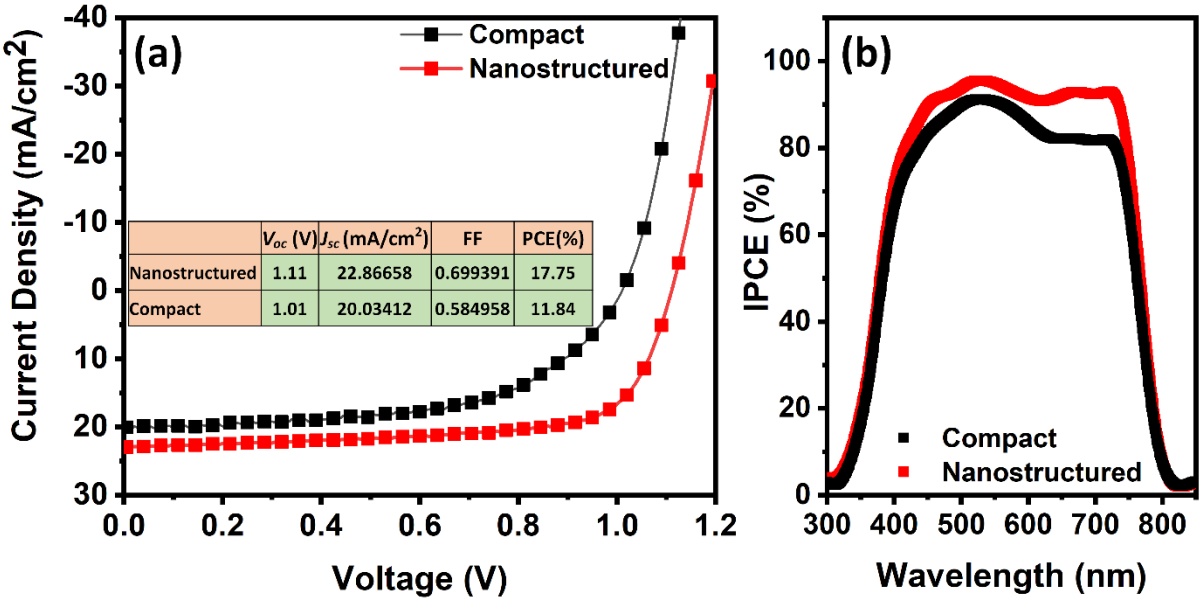

	V_{oc} (V)	J_{sc} (mA/cm^2)	FF	PCE(%)
Nanostructured	1.11	22.86658	0.699391	17.75
Compact	1.01	20.03412	0.584958	11.84

Figure 4.8: (a) Current-voltage curves of perovskite solar cells made with compact and nanostructured NiO hole transporting layers. The measurement was carried out under AM1.5 G illumination at 100 mW/cm^2 with an active area of 5 mm^2. (b) Normalized IPCE spectra of perovskite solar cells made with different NiO hole transporting layers.

Table 4.1: Photovoltaic performance summary of perovskite solar cells made with compact and nanostructured NiO, the latter with different concentrations of $NiCl_2.6H_2O$ in the growth solution.

		V_{oc}(V)	J_{sc}(mA/cm^2)	FF	PCE(%)
1 mM	Best	1.11	22.87	0.7	17.75
	Average	1.11±0.02	20.60±1.84	0.63±0.08	14.27±2.22
3 mM	Best	1.14	21.57	0.65	15.93
	Average	1.14±0.02	19.70±1.82	0.59±0.07	13.31±2.24
5 mM	Best	1.13	19.3	0.59	13.02
	Average	1.06±0.05	19.75±1.05	0.58±0.04	12.03±0.70
Compact	Best	1.01	20.03	0.58	11.84
	Average	1.03±0.02	18.78±2.94	0.55±0.04	10.66±1.90

The band alignment photoactive layer, hole, and electron transporting materials play a crucial role in determining the charge separation and open-circuit voltage in a perovskite solar cell. The open-circuit voltage in such solar cells depends on the lowest unoccupied molecular orbital level (LUMO) of perovskite and the highest occupied molecular orbital (HOMO) level of the hole transporting layer, or the potential gradient between the quasi-Fermi level of the electron at the electron transporting layer and that of the hole at the hole transporting layer - a deeper HOMO level generally indicates a larger open-circuit voltage [291]. To probe the difference in the quasi-Fermi level of compact and nanostructured NiO and to investigate the change in the electronic band structure and work function of compact NiO and nanostructured NiO, ultraviolet photoelectron spectroscopy (UPS) was performed. The value of work function (WF) was determined by using the following expression: WF $(\phi) = 21.21 - E_{\text{cut- off}}$, where 21.21 eV is the energy of the incident He laser light (UV light) and $E_{\text{cut-off}}$ is the cut-off energy of the secondary electrons. The value of the work function for compact NiO thin film and nanostructured NiO was found to be 0.83 eV for both materials (Figures 4.9a, b, and insets). Furthermore, from the UPS

spectra, the position of the valence band maxima (VBM) for the NiO thin film and NiO nanostructured layers was calculated to be 0.81 and 0.83 eV, respectively, below the Fermi level (Figure 4.9c and d). The depression in the VBM position of the NiO nanostructured layer can be attributed to its inherently porous structure exposing a Ni atom at the edge that can bind to additional oxygen atoms due to free valency, resulting in downshifting of VBM position.

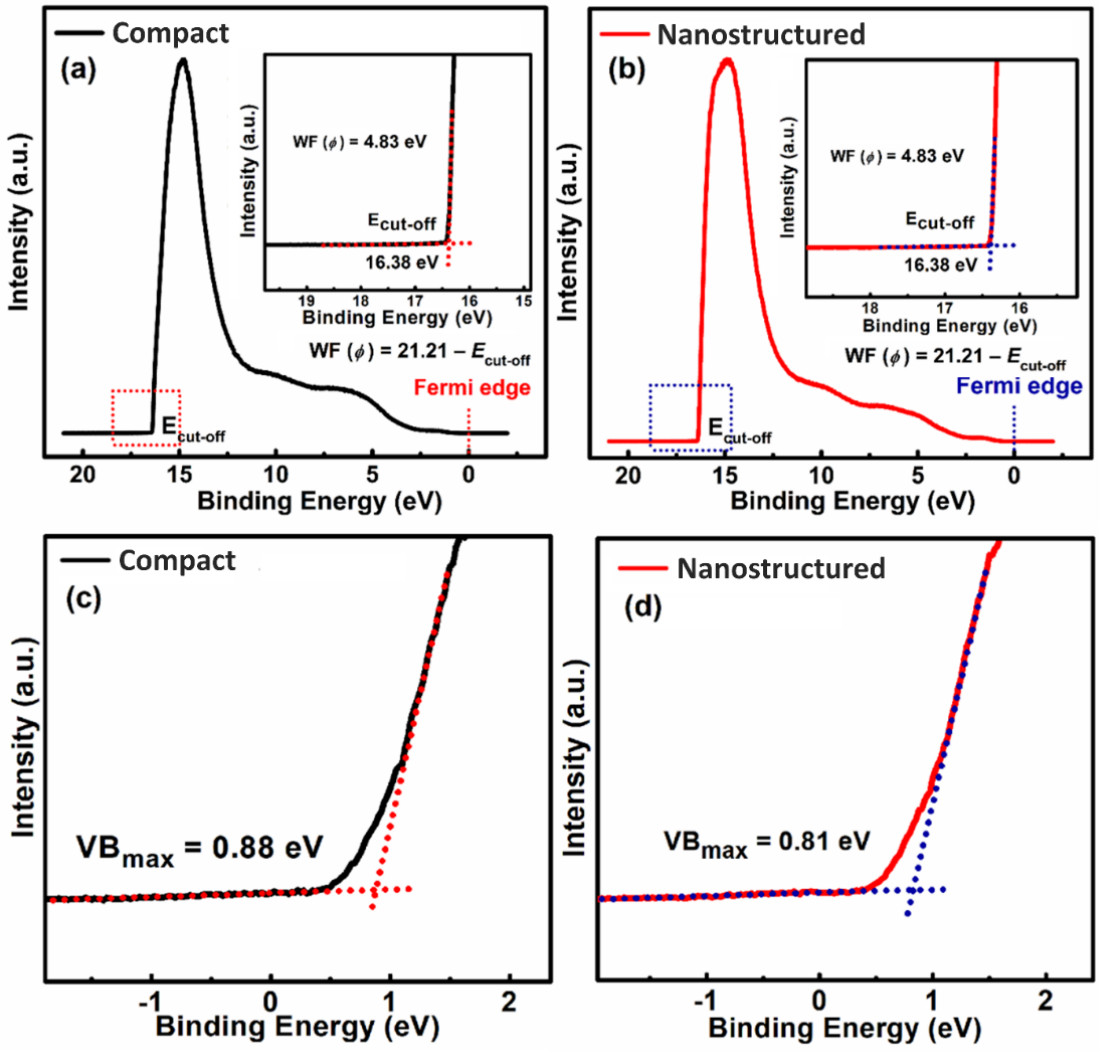

Figure 4.9 UPS work function spectra of the (a) thin-film compact NiO, (b) nanostructured NiO. Insets show the calculation of cut-off energy ($E_{cut\text{-}off}$) of the secondary electron and the UPS

valence band spectra showing valence band maxima positions below Fermi level for (c) thin-film compact NiO, (d) nanostructured NiO.

Interfacial and bulk recombination processes in perovskite solar cells are also key factors affecting the open-circuit voltage of a perovskite solar cell. In order to investigate the role of interfacial recombination in the photovoltaic performance of compact and nanostructured NiO based solar cells, the light intensity (633 nm) dependence of V_{oc} was measured and depicted in Figure 4.10a. As all the photogenerated excitons recombine within the cell under open-circuit voltage conditions, the study of light intensity dependence of V_{oc} helps to precisely understand the recombination mechanism occurring in solar cells [88, 274, 292-294]. Compact NiO based devices showed a strong dependence of open-circuit voltage on the light intensity compared to the nanostructured NiO based devices. The slopes of the curves were approximated using a linear fit. Compact NiO based devices have a slope of $1.7k_bT/q$ and the slope for nanostructured NiO based devices was found to be $1.17k_bT/q$, where k_b, T and q are the Boltzmann's constant, the temperature in Kelvin, and elementary charge, respectively. The lower slope of the nanostructured NiO based device compared to the compact NiO based device indicates that bimolecular recombination dominates in nanostructured NiO based devices while trap-assisted recombination dominates in compact NiO based devices. Furthermore, intensity-modulated photovoltage spectroscopy (IMVS) was used to determine the charge recombination lifetime (τ_r) of the solar cells made with compact and nanostructured NiO hole transporting layers. Figure 4.10b and c show the Nyquist plot of IMVS and the imaginary part of IMVS as a function of frequency, respectively. The values of τ_r were obtained from the IMVS analysis using equation (4.2);

$$\tau_r = \frac{1}{2\pi f_{\min\,(IMVS)}} \qquad (4.2)$$

where f_{min} is the minimum current of the imaginary part in the IMVS spectra. There is a clear difference in the IMVS curve for the devices in the range of 50 kHz to 100 kHz. The recombination lifetime of solar cells based on compact and nanostructured NiO hole transporting layers were found to be about 1.56 μs and 3.13 μs, respectively. The result suggests that improved V_{oc} in nanostructured NiO based solar cells is mainly affected by interfacial recombination at perovskite/HTL interfaces. We also performed capacitance-voltage measurements on the devices at the 90 kHz frequency under dark conditions to probe the carrier accumulation and transport properties at the interface [167, 274, 291-299]. Mott-Schottky plots for the devices made with compact and nanostructured NiO are shown in Figure 4.10d.

$$\frac{1}{C_{sc}^2} = \frac{2}{e\varepsilon_0\varepsilon_r N_D}\left\{(V - V_{FB}) - \frac{kT}{e}\right\} \qquad (4.3)$$

$$N_D = \frac{2}{e\varepsilon_0\varepsilon_r n} \qquad (4.4)$$

Flat-band potential (V_{fb}) and doping density (N_D) were calculated using equation (4.3) and equation (4.4), respectively, where C_{sc} is the space-charge capacitance (*i.e.* film capacitance) per unit area, ε_r is the dielectric constant of the material, ε_0 is the vacuum permittivity, k is Boltzmann constant, T is the temperature in Kelvin, e is the electron charge, and V is the applied potential. The measured V_{fb} of compact and nanostructured NiO was determined to be 0.91 V and 1.15 V, respectively, while the carrier concentration of compact and nanostructured NiO was found to be 2.73×10^{16} cm^{-3} and 4.09×10^{16} $cm^{-3,}$ respectively. Higher built-in potential indicates reduced charge accumulation and improved hole extraction which eventually led to higher power conversion efficiency as a result of higher V_{oc} in the nanostructured NiO based solar cells [292, 294, 300].

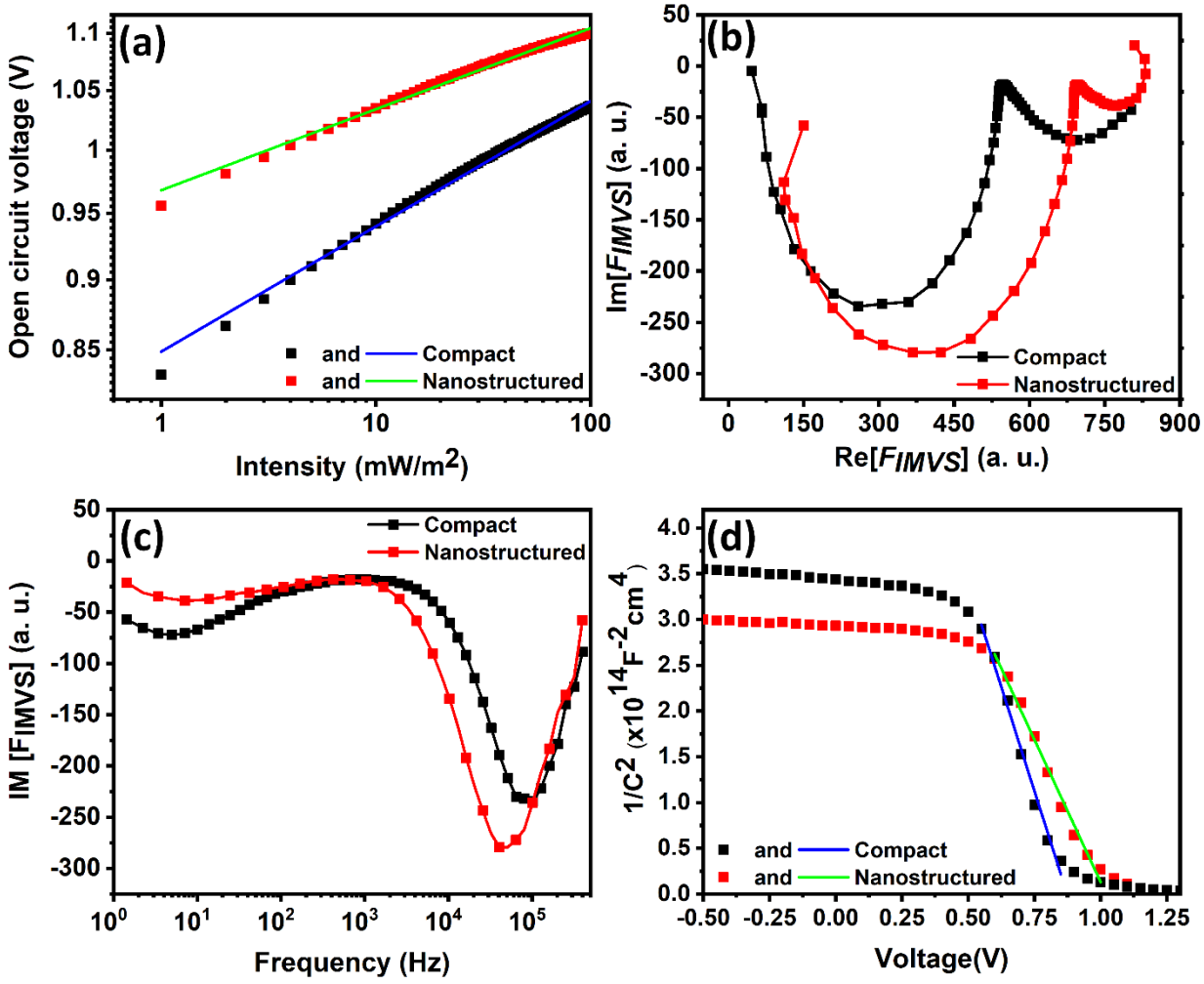

Figure 4.10 (a) Photovoltage as a function of the intensity of 633 nm LED (b), Nyquist plot of intensity-modulated photovoltage spectroscopy (IMVS), (c) Imaginary part of IMVS as a function of frequency (d) and Mott-Schottky plot of the perovskite solar cells based on compact and nanostructured NiO hole transporting layer.

To further discern the hole extraction and transfer mechanism that influences photovoltaic performance of perovskite solar cells, steady-state photoluminescence (PL) and time-resolved photoluminescence (TRPL) spectroscopy were performed on samples of the perovskite layer fabricated over the bare FTO, the compact NiO on FTO, and the nanostructured NiO grown on

FTO substrates (Figure 14.11a and 14.11b). The addition of the NiO layer on top of the FTO substrate led to more efficient PL quenching compared to the bare FTO while the nanostructured NiO displayed the highest PL quenching. In order to understand the charge extraction ability of planar and nanostructured NiO, time-resolved photoluminescence (TRPL) studies of FTO/compact NiO/perovskite and FTO/NiO nanostructure/perovskite samples were carried out with the FTO/perovskite sample serving as the reference. The PL decay curve of each sample was fitted to the multi-exponential model defined as:

$$I(t) = \sum_{i=1}^{n} A_i e^{\frac{-t}{\tau_i}} \tag{4.5}$$

$$\tau_{avg} = \frac{\sum_{i=1}^{n} (A_i \tau_i)^2}{\sum_{i=1}^{n} A_i \tau_i} \tag{4.6}$$

The PL decay curve of the HTL free sample has two decay constants. As photogenerated charge carriers are generally captured quickly by defects, the fast decay component in the TRPL curve is attributed to the early event of recombination of charge carriers trapped at the perovskite grain boundaries and the FTO/perovskite interface while the long-lived component is most likely due to the radiative recombination of free carriers. The samples with the HTL appear to have at least three decay components. The fastest decay component is attributed to the trap assisted recombination, the second fastest component in samples with HTL is likely due to the charge extraction from the perovskite layer to the HTL and the longest lifetime is associated with the band to band recombination of the photogenerated careers.[37, 293] The decay curves are plotted in Figure 4.11(b) and the fitting parameters are shown in Table A14. NiO is a potent electron blocker. Holes trapped or accumulated at the FTO/NiO interface are unlikely to participate in the aforementioned recombination pathways. For these holes, the only electrons available for recombination are at the

NiO/perovskite interface. Recombination of non-geminate carriers in low mobility materials proceeds through the bimolecular i.e. Langevin mechanism,[301] which requires electrons and holes to be within a Langevin radius of each other. The Langevin radius (*a.k.a.* Coulomb radius) [302] is given by $r_C = {e^2}/{4\pi\epsilon_0\varepsilon_r kT}$ where *e* is the elementary charge, ε_0 is the permittivity of free space, ε_r is the relative permittivity of NiO (11.9) and *T* is the absolute temperature (300 K in our case). In our system, $r_c \sim 4.6$ nm. However, the thickness values of the NiO nanomesh (> 90 nm) and the compact NiO film (~25 nm), as observed in Figures 4.5a and 4.5b respectively, are much larger than the Langevin electrode due to which holes accumulated or trapped at the FTO/NiO interface are too far away from the electrons at the NiO/perovskite interface for recombination to occur. By using equation (4.5), the weighted average PL lifetime of perovskite deposited over bare FTO substrate was estimated to be 54.73 ns while the average lifetime of perovskite deposited over FTO/compact NiO and FTO/nanostructured NiO was found to be about 20.17 ns and 1.51 ns, respectively. These results validate the hypothesis that the nanostructured NiO facilitates faster and more efficient photogenerated hole extraction compared to the compact NiO, which ultimately contributes to the higher short circuit current and fill factor of the solar cells.

To probe the charge transfer efficiency of compact and nanostructured NiO, intensity-modulated photovoltage spectroscopy was performed. Nyquist plots for IMVS spectra are shown in Figure 4.11c while Figure 4.11d depicts the imaginary part of IMPS as a function of frequency. The charge transfer time of compact and nanostructured NiO was calculated by using equation (4.7)

$$\tau_{ct} = \frac{1}{2\pi f_{\min\,(IMPS)}} \qquad (4.7)$$

where f_{min} is the frequency at which the current of the imaginary part is minimum. The calculated τ_{ct} values for the compact and nanostructured NiO based perovskite solar cells were 1.9 µs and 1.5 µs, respectively, which suggest that the nanostructured NiO promotes better charge transport compared to the compact NiO. It is worth noting that the τ_{ct} for compact NiO is higher compared to the τ_r which indicates there must be high charge accumulation and recombination at the compact NiO/perovskite interface.

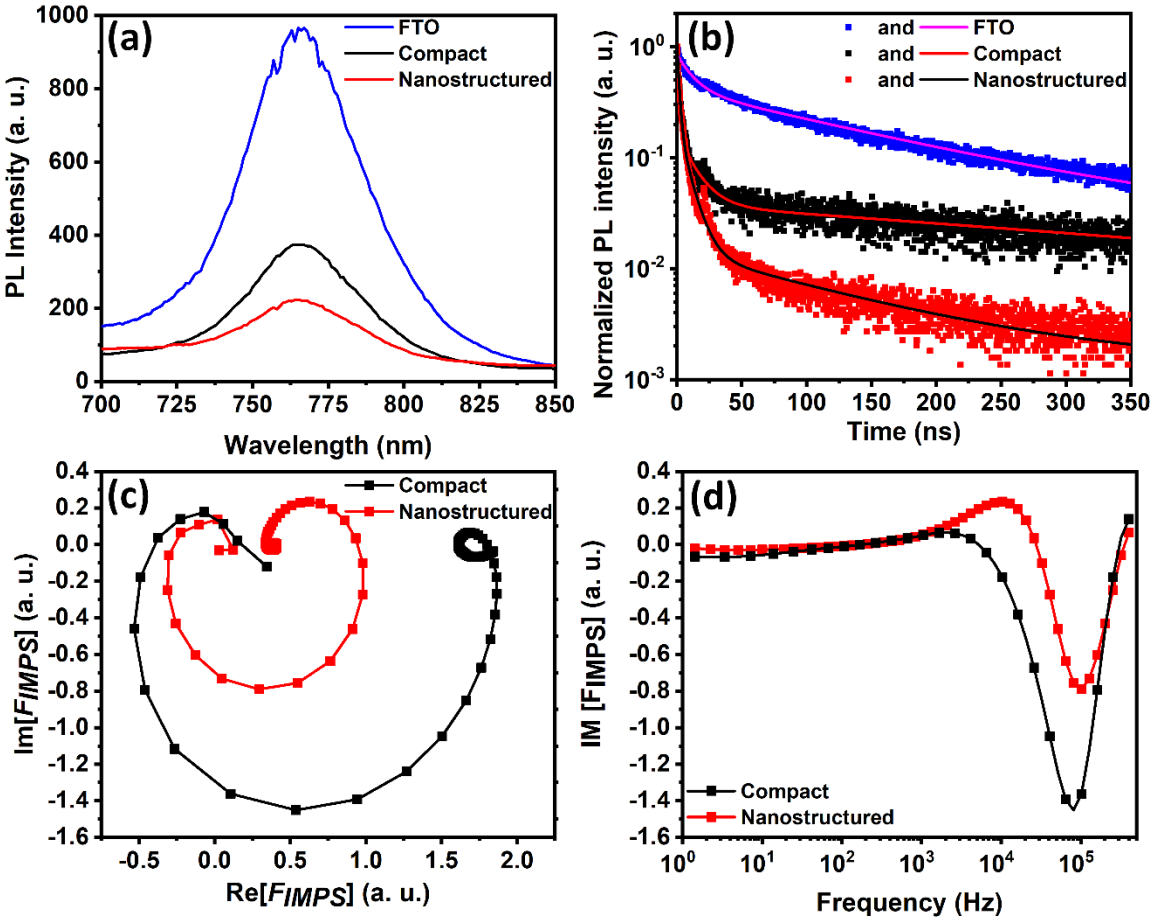

Figure 4.11: (a) Steady-state PL spectra, (b) Time-resolved photoluminescence spectra, (c) Nyquist plot of IMPS spectra, and (d) Imaginary part of IMPS as a function of the frequency of the perovskite solar cells based on compact and nanostructured NiO hole transporting layers.

To investigate the interfacial charge accumulation and to discern the interfacial charge recombination and transport properties of compact and nanostructured NiO based solar cells, we performed Kelvin probe force microscopy (KPFM) measurements. Figure 4.12b illustrates the contact potential distribution (CPD) on the perovskite layer deposited over compact NiO under dark and illumination conditions. Figures 4.12e and f show the surface potential map under dark and illumination respectively. Similarly, Figure 4.12c shows the CPD on the perovskite layer deposited over nanostructured NiO under dark and illumination. Figures 4.12h and i show the surface potential map under dark and illumination respectively. Figures 4.12d and g show the topographical AFM image of the perovskite layer deposited over compact and nanostructured NiO, respectively. Figure 4.12a depicts the schematic illustration of the KPFM experimental set up where a 450 nm of diode laser was used to generate electron-hole pairs in the perovskite active layer deposited over FTO/NiO. Generated holes transferred to the ground through NiO and FTO while electrons moved to the surface of the perovskite. As shown in Figure 4.12c, after illumination, CPD of nanostructured based samples negatively shifted by approximately 190 mV, while in the case of compact NiO based samples CPD was shifted to a more positive value (Figure 4.12b), which suggests better charge extraction property in nanostructured NiO samples. Poor charge extraction and transport properties of compact NiO samples and charge accumulation at the interface causing high interfacial recombination are thought to be responsible for the low V_{oc} in compact NiO based device compared to that in nanostructured based devices.

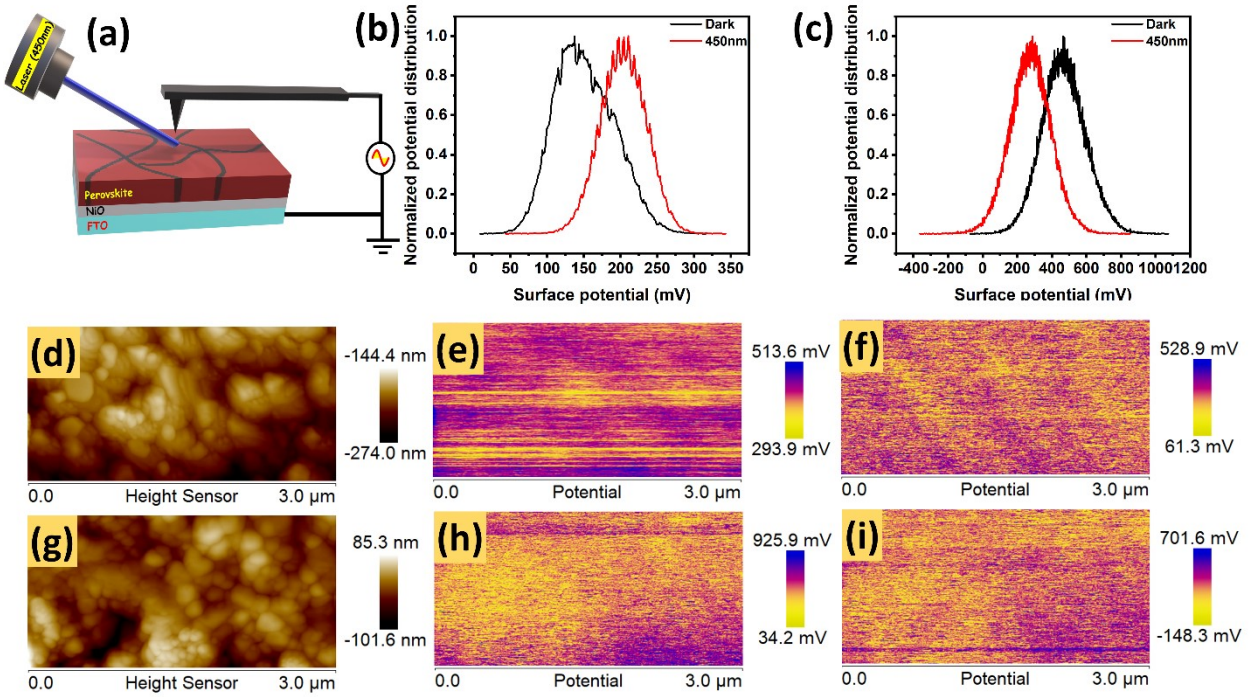

Figure 4.12: (a) Schematic illustration of the KPFM measurement setup, (b) CPD distribution in dark and under illumination for compact NiO based sample (c) CPD distribution in dark and under illumination for nanostructured NiO based sample. The topography AFM image of the perovskite layer deposited over (d) compact NiO and (g) NiO nanostructure. Surface potential map measured in the dark of perovskite layer deposited over (e) compact NiO and (h) NiO nanostructure. Surface potential map measured under the illumination of perovskite layer deposited over (f) compact NiO and (i) NiO nanostructure.

4.5 Conclusion:

In this present study, we have focused on both computational and experimental analysis of charge transfer processes occurring in systems composed of compact or nanostructured NiO substrates and perovskite. To better understand the charge transport mechanism at the interface of NiO/perovskite, we have performed computational modeling by DFT methods for which we used

relativistic pseudopotentials and pseudo-atomic orbitals optimized for LDA+U type functional with the Hubbard correction. In the process, we have calculated the HOMO/LUMO orbitals, the energy of adsorption of perovskite clusters on the NiO surface, and the density of state distribution on the NiO surface for three different geometries of perovskite particles representing three different scenarios of particle distance to the surface and their orientation in space. The modeling results have demonstrated that a somewhat higher probability of charge transfer is predicted when the perovskites are in close proximity to the NiO surface and contacted by halogen and lead atoms. Better charge transportation in such a configuration was found because of stronger mutual penetration and reduced bandgap due to the substantial redistribution of charge. We have shown that a nanostructured NiO hole transporting layer can be fabricated by a facile hydrothermal process. Using a NiO nanostructure, the V_{oc} of the device improved up to 1.14 V; the usage of nanostructured NiO in perovskite solar cell devices resulted in a much higher V_{oc} than that achieved in devices utilizing the commonly used compact NiO (1.01 V). This enhancement in open-circuit voltage was found to be attributed to the reduced interfacial and bulk charge recombination in the nanostructured NiO based solar cell. IMVS, IMPS, KPFM, PL, and TRPL measurements indicated that the defective nanostructured based NiO sample has better charge transfer and transport properties compared to the planar NiO sample. XPS results revealed that hydrothermally grown NiO contains Ni^{3+} defects. It is well known that the nickel vacancy Ni^{3+} is self-dopant in NiO which results in more p-type behavior [12, 303-306]. Thus, NiO nanostructures are more electrically conductive than the defect-free compact NiO leading to better charge transport properties of the nanostructured NiO based perovskite solar cells. As a result, perovskite solar cells based on a nanostructured NiO hole transporting layer demonstrate improved photovoltaic performance.

Further work in the structural and compositional optimization of the NiO nanostructure is expected to lead to enhanced photovoltaic performance.

Chapter-5 g-C_3N_4 and C_3N_5 Passivation and Transport Layers

5.1 Introduction:

The interfacial layer has a huge role in the charge collection efficiency of perovskite solar cells. A well-designed interfacial layer helps to reduce the interfacial charge recombination which ultimately improves the photovoltaic property of the solar cells. Intensive research has been done to improve the photovoltaic property of solar cells by using several interfacial layers including SnO_2, ZnO, mesoporous TiO_2, C_{60}, PCBM, etc. While many of these interfacial layers work very well, the synthesis and deposition of these materials generally require energy-intensive methods and some of them have stability issues. To reduce the energy payback time of the solar cells, a high-efficiency HPSC with low fabrication cost is highly desirable. Traps in perovskite active layers are another major issue that must have to be addressed in order to achieve high-efficiency perovskite solar cells. Traps in perovskite active layer are generally formed because of its low stability and also because of polycrystallinity (i.e. at grain boundaries). Traps acts as recombination centers in the perovskite active layer and are thus responsible for non-radiative recombination, low carrier lifetime and short carrier diffusion lengths which degrade the photovoltaic properties. Use of interfacial layer, modified deposition techniques for perovskite layer, chemical doping and addition of additives to promote crystallization are some of the strategies that are being used to reduce trap states in perovskite active layers.

Among graphitic semiconductors, graphitic carbon nitride (g-C_3N_4), composed of tris-*s*-triazine (*s*-heptazine, C_6N_7) units bridged together with nitrogen atoms to give a 2D graphitic

structure has gained significant interest due to a combination of highly desirable electronic, optical, and physicochemical properties [307]. Continuous repetition of the heptazine motif leads to a bandgap of 2.7 eV with band edge positions (E_{CB}, –1.1 eV and E_{VB}, +1.6 eV) that render it compatible with sunlight-driven water splitting, CO_2 photoreduction and the photooxidation of a number of organic compounds [298, 308, 309]. Further, the plentiful presence of electron-rich sites and basic nitrogens in the g-C_3N_4 scaffold enables the promotion of various catalytic reactions i.e. alkylation, esterification, oxidation, pollutant removal (dye adsorption), etc [310-313]. The somewhat wide bandgap of g-C_3N_4 means that it can absorb only the ultraviolet and blue fraction of solar spectrum (λ < 450 nm) which limits its performance in photocatalytic and photovoltaic applications. Doping with various heteroatoms such as P, F, B, and S has been utilized to improve the visible light absorption profile and photo efficiency [314-319]. Like all semiconductors, g-C_3N_4 suffers the innate drawback of carrier recombination detrimental to catalytic and photocatalytic processes. Many surface modification approaches such as increasing the surface area *via* soft and hard templating, using two or more precursors, transformation of bulk material into sheets, doping with metals (Ag, Cu, Rh, Pt, Na, *etc.*) and metal oxides (CoO_x) for electron and hole capture, coupling with other semiconductors/metal complexes to form heterojunctions, and blending with graphene have been employed to improve the photocatalytic and catalytic performance of g-C_3N_4 [320-322]. However, less attention has been paid to chemical structure modification which can lead to the generation of a more robust, band edge tuned g-C_3N_4 framework with entirely new physicochemical properties for efficient catalytic/photocatalytic applications. It has been found that addition of extra nitrogen-rich moieties in the g-C_3N_4 scaffold to increase the N:C ratio from 4:3 ratio in CN can reduce the bandgap significantly, due to a more extended conjugated network and the participation of the lone pair on the N atom with the π conjugated system of heptazine

motif. Vinu et al. demonstrated the synthesis of N-rich carbon nitride (MCN-8) using 3-amino-1,2,4-triazole to afford C_3N_5 stoichiometry resulting in a significant decrease in band gap (2.2 eV) due to extended conjugation [323]. However, this increase in N:C ratio to 5:3 (from the 4:3 ratio in g-C_3N_4) was due to the presence of the N-rich 1,2,4-triazole moiety linked to the heptazine motif and not because of the direct incorporation of the extra N atom in the heptazine nucleus. Herein, we demonstrated the synthesis of novel modified carbon nitride framework with a C_3N_5 stoichiometry by thermal deammoniation of 2,5,8-trihydrazino-s-heptazine, also known as melem hydrazine (MH), as a safe and environmentally benign precursor (Figure 5.1). The obtained carbon nitride modified framework was denoted as C_3N_5 due to its 3:5 C:N stoichiometric ratio. Characterization studies revealed that the C_3N_5 framework contains heptazine moieties bridged together by azo linkage (–N=N–). The presence of azo linkage extends the π conjugated network due to overlap between the *p* orbitals on N atoms constituting the azo bond and π system of heptazine motif which resulted in the reduction of the electronic bandgap to 1.76 eV. Solar cell devices fabricated using low bandgap C_3N_5, as the electron transporting layer (ETL) in $MAPbBr_3$ based perovskite solar cells demonstrates improved power conversion efficiency (PCE), open-circuit voltage (V_{oc}), *etc*. than g-C_3N_4 based ETL due to tuned band alignment. While blending of small amount of C_3N_5 (4.0 wt%) with PbX_2 based $MA_xFA_{1-x}Pb(I_{0.85}Br_{0.15})_3$ perovskite active layer leads to increase in PCE up to 16.68% with V_{oc} of 1.065V, J_{sc} of 22.87 mA/cm^2 higher than conventional and g-C_3N_4 blended solar cell architecture. Multi-facet applications of C_3N_5 materials were probed by excellent performance of C_3N_5 in surface catalyzed plasmon-exciton co-induced reactions at much low intensity.

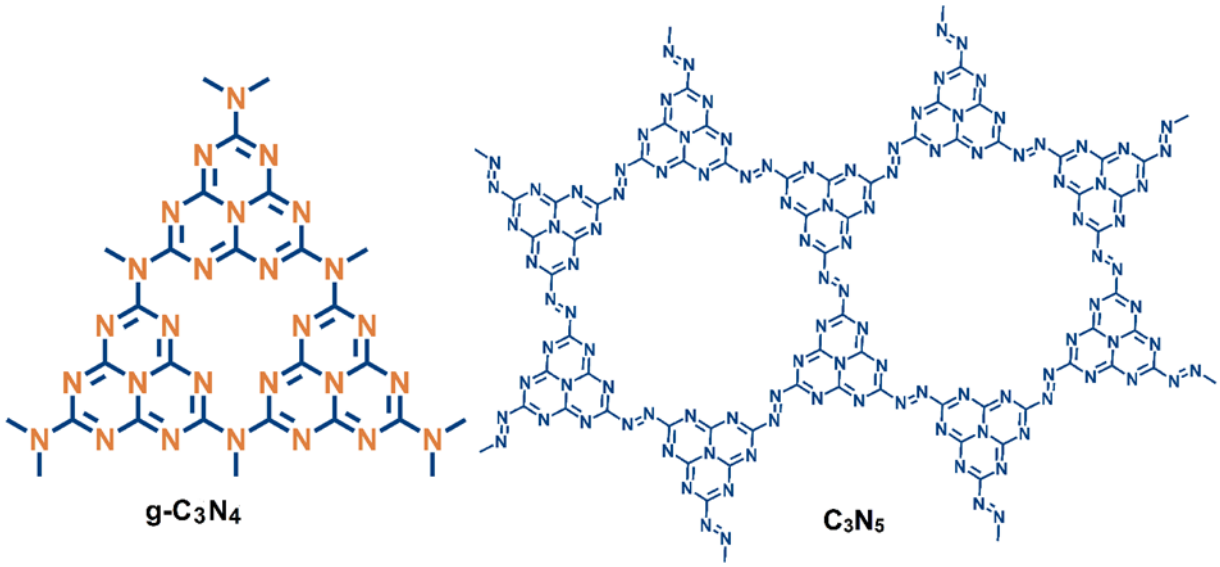

Figure 5.1. Chemical structure of g-C_3N_4 and carbon nitride modified C_3N_5 framework.

5.2 Experimental:

5.2.1 Materials:

Analytical grade pure melamine (99%), hydrazine hydrate (55%), methylene blue ($C_{16}H_{18}ClN_3S \cdot xH_2O$), NaOH (97%), HCl (37%), anhydrous Na_2SO_4 (99%), titanium (IV) isopropoxide (97%), titanium (IV) butoxide (97%), 4-nitrobenzene thiol (80%), $Na_2S \cdot 9H_2O$ (≥99.99%), Acetic acid (≥99.85%), HCl (37%), formamidinium iodide (≥99%, anhydrous), 4-tert-butylpyridine (96%), lithium bis(trifluoromethanesulfonyl)-imide and spiro-OMeTAD (99%) were procured from Sigma Aldrich. Acetonitrile (99.8%), lead iodide (99%) and lead bromide (+98%) were purchased from Acros Organics. Methylammonium bromide was obtained from Dyesol. Chlorobenzene (99.8%), titanium (IV) chloride (99.9%), dimethylformamide (DMF) (99.8%) and dimethylsulfoxide (DMSO)(≥99.9 %) were purchased from Fisher Scientific. Transparent titania paste (18NR-T)(Average Nanoparticle Size (active) - 20nm) was purchased from Greatcell Solar. Chemicals were used as received without any further purification. Fluorine doped tin oxide (FTO)

glass (80-82% transmittance) was purchased from Hartford Tec Glass Company and surface was cleaned by ultrasonication for 10 min in each acetone, methanol and de-ionized water. HPLC grade water and solvents were used throughout experiments.

5.2.2 Characterization:

The UV-Vis absorption spectra of materials in diffuse reflectance mode were collected using a Perkin Elmer Lambda-1050 UV–Vis-NIR spectrophotometer equipped with an integrating sphere accessory. The steady-state photoluminescence (PL) spectra of materials were acquired on Varian Cary Eclipse fluorimeter xenon lamp excitation source and slit width of 5 nm.

Time-resolved photoluminescence (TRPL) curves were recorded using a lab assembled single-photon counter. Samples were photoexcited by 405-nm picosecond diode laser (Alphalas GmbH) operated at a frequency of 13MHz to excite the samples, and a Becker-Hickl HPM-100-50 PMT interfaced to an SPC-130 pulse counter system. This setup has a response time of ~100 ps. Electron paramagnetic resonance (EPR) spectra of material to was ensued on a Bruker model E-580 (EMXnano Bench Top system) spectrometer (Germany) equipped with a 400 W mercury-lamp (Lot Quantum-Design GMBH) as the light source and helium flow cryostat (Oxford CF935 helium flow cryostat), operating at X band microwave frequency (~ 9.64 GHz). The operation setting for EPR measurement was as follows: Power 3.162 mW, center field 33440 G, cavity Q quality factor was kept above 4000. The sample was charged in quartz tube and covered with airtight lids and EPR spectra were accumulated under dark and light at liquid 100 K using liquid nitrogen. Standard samples were used for the calibrations and obtained field values were converted into g value by following expression $g = h f/m_B B$. where, g is Lande factor, h is plank constant

(6.62 10^{-34} J.s), f is frequency (9.64 GHz Hz), m_B is Bohr magneton (9.2740154x10^{-24} J/T) and B is magnetic field is Tesla.

5.2.3 Synthesis of Melem (2,5,8-triamino-s-heptazine)[324, 325]:

For the synthesis of melem (2,5,8 -triamino-*s*-heptazine) a certain amount of melamine was heated at 425 ºC for overnight in an alumina crucible covered with a lid. The obtained powder with yellowish tinge was crushed and suspended in DI water. The obtained suspension was refluxed for several hours to remove un-reacted melamine and other impurities. The resulting white product was collected by centrifugation and dried at room temperature. All the data well-matched with previously reported literature.

5.2.4 Synthesis of 2,5,8-trihydrazino-s-heptazine or melem hydrazine (MH)[326]:

The monomeric unit 2,5,8-trihydrazino-s-heptazine or melem hydrazine was synthesized by hydrothermal reaction between melem and hydrazine hydrate with slight modification in previous literature procedure. In brief, 1.6 g (7.5 mmol) of melem was dispersed in 15 mL (0.25 mol) of 55% aqueous hydrazine hydrate solution and sealed in a 25 mL Teflon lined autoclave. The autoclave was heated at 140 ºC in an oven for 24 hours. After cooling the obtained yellowish solution suspension was transferred to a 100 mL beaker and 10% HCl was added to maintain pH in between 1–2. This solution was filtered to remove un-reacted solid residue containing melem. The filtrate was precipitated by adding 10 % NaOH solution by maintaining pH in between 7.5 – 8.5. The obtained solid was again dissolved in HCl, filtered and re-precipitated in NaOH and this procedure was followed three times. Finally, obtained solid was washed several times with DI water and ethanol and dried under vacuum. All the data were well matched with previously reported literature.

5.2.5 Synthesis of C_3N_5 polymer:

C_3N_5 polymer was synthesized by heating melem hydrazine (2,5,8-trihydrazino-s-heptazine) at a temperature of 450 ºC with a heating rate of 2 ºC and holding at 450 ºC for 2 h. The obtained orange powder was used for subsequent experiments without any further treatment. The BET surface area (S_{BET}) of C_3N_5 was found to be 1.781 $m^2\ g^{-1}$.

5.2.6 Synthesis of g-C_3N_4[327]:

For comparison, graphitic carbon nitride (g-C_3N_4) powder was synthesized by direct heating of melamine at 550 ºC with a heating rate of 8 °C min^{-1} up to 300 ºC and 2 °C min^{-1} up to 550 ºC and finally holding the temperature 550 °C for 4 h. The BET surface area (S_{BET}) of g-C_3N_4 was found to be 11.471 $m^2\ g^{-1}$.

5.2.7 Fabrication of solar cell:

A thin compact layer of TiO_2 was deposited on the cleaned FTO:glass substrate. To prepare the precursor solution for the deposition of compact TiO_2, 369 µL of titanium (IV) isopropoxide and 70 µL of 1.0 M HCl were separately diluted in 2.53 mL of isopropanol. Diluted HCl was added drop by drop into the diluted titanium (IV) isopropoxide solution under stirring. After overnight stirring of the mixed solution, it was filtered using a 0.2 µm filter and deposited over cleaned FTO:glass substrates by spin-casting at 3000 rpm for 30 s, followed by calcination at 450 ºC for 30 min [123-125]. 18NR-T titania paste was dissolved in absolute ethanol in the ratio of 1:3.5 wt% and spin cast on compact TiO_2 layer at 4000 rpm for 40 s followed by annealing at 450 ºC for 30 min. On mesoporous TiO_2 layer 0.1 M of lithium bis(trifluoromethanesulfonyl)-imide dissolved in acetonitrile was spin-coated at 3000 rpm for 30 sec followed by annealing at 450 ºC for 30 min.

On FTO/TiO_2 by spin-casting followed by calcination at 500 ºC for 30 min. Then 636.4 mg of PbI_2 and 90 mg of $PbBr_2$ was dissolved in 1 mL of DMF and 160 µL of DMSO. For g-C_3N_4/C_3N_5 based device 4 wt% of g-C_3N_4/C_3N_5 relative to PbX_2 (where X=I and Br) was added in the PbX_2 solution. All the solutions were stirred at 70 °C for 12 h. A solution of 1100 mg of FAI and 110 mg of MABr was dissolved in 15 mg of 2-propanol. PbX_2 solution was spin-coated over mesoporous TiO_2 layer at 4000 rpm for 30 sec followed by annealing at 70 °C for 10 min. Then the prepared FAI/MABr solution was spin-coated over the PbX_2 layer at 2000 rpm for 30 sec followed by annealing at 140 °C for 30 mins. A hole transporting layer was deposited by spin-casting a solution containing 70 mg of Spiro-OMeTAD mixed with 1 mL of chlorobenzene and additives, namely 8.8 mg of lithium bis(trifluoromethanesulfonyl)-imide, 28 µL of 4-tert-butylpyridine and 35 µL of acetonitrile at 4000 rpm for 30 sec. A 70-nm thick layer of gold was then thermally evaporated to complete the devices. The current-voltage characteristics of the samples were measured using a Keithley 4200 semiconductor parameter analyzer. For solar cell testing, one sun AM1.5 G illumination from a collimated Class A solar simulator (Newport Instruments) was used. Solid state impedance spectroscopy (SSIS) was performed in a two-electrode configuration using a CHI-600E potentiostat.

5.3 Results and discussions:

The surface morphology of the C_3N_5 polymer was investigated using a He-ion microscope equipped with an electron flood gun to facilitate positive charge neutralization accumulated from the He-ion beam (Figure 5.2a). The He-ion images of MHP show a rough, crumpled graphenic scaffold with some erupted morphologies which indicate that the high-temperature treatment of MH monomeric unit facilitated polymerization into an irregular sheet-like structure. The fine structure of C_3N_5 material was determined using high-resolution transmission electron microscopy

(HR-TEM) (Figure 5.2b-d). The carbon nitride-like layered sheet architecture is clearly evident in the TEM image of C_3N_5 at 50 nm scale bar (Figure 5.2b). Under long-duration exposure of the electron beam, C_3N_5 started to degrade and shrink which likely resulted due to high energy electrons breaking the –N=N– linkage. HR-TEM images at 10 nm and 5 nm scale bar show crystallite fringes of nanoporous multilayered sheets with an interplanar *d*-spacing of 0.32 nm, corresponding to the 002 planes of the graphitic structure (Figure 5.2c, d, and inset). The observed *d*-spacing in C_3N_5 was identical to g-C_3N_4 from which we infer that during the thermal polymerization step, the stacking pattern of sheets in C_3N_5 remains similar to that in bulk g-C_3N_4. The broad, less intense ring in the SAED pattern was attributed due to diffraction of electrons by the 002 plane; however, the low intensity of the ring suggests amorphous nature of the material (inset of Figure 5.2d).

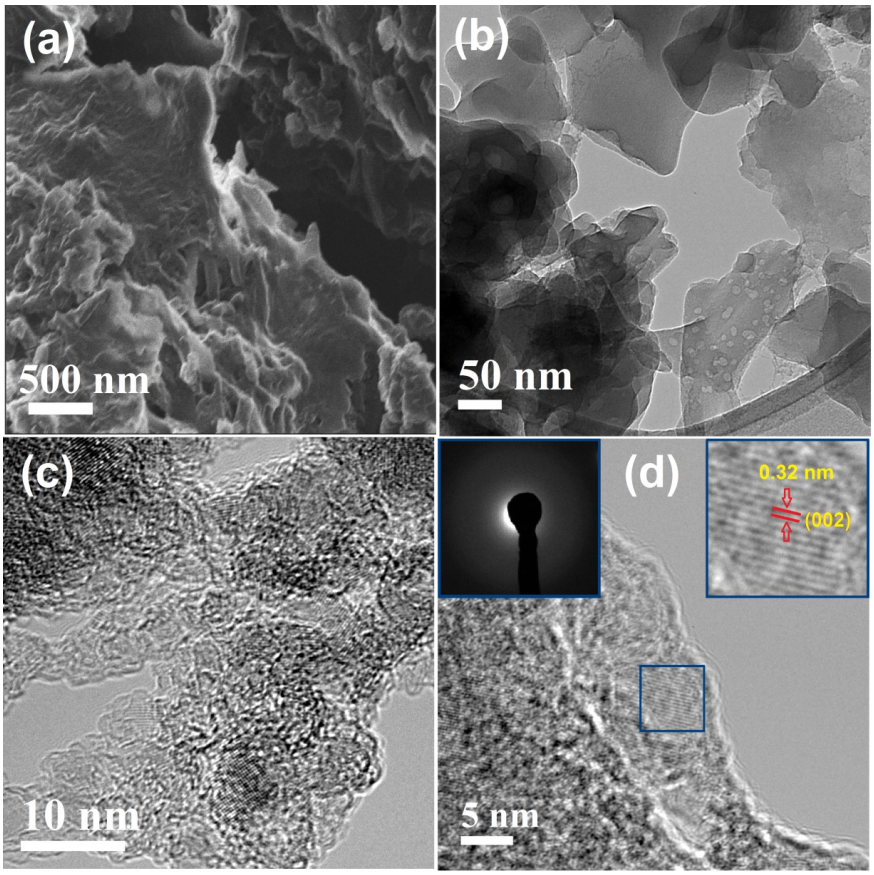

Figure 5.2. (a) He-ion image of C_3N_5, and HR-TEM images of C_3N_5 (b) at 50 nm, (c) at 10 nm and (d) at 5 nm scale bar; left and right insets showing SAED diffraction pattern and interplanar *d* spacing, respectively.

Figure 5.3a displays the diffuse reflectance UV-Vis (DR-UV-Vis) spectra of g-C_3N_4 and C_3N_5. The DR-UV-Vis spectra of g-C_3N_4 shows a characteristic absorption peak between 200–400 nm with a band tail extended up to 450 nm due to charge transfer from the populated valence band of the nitrogen atom (2p orbitals) to the conduction band of the carbon atom (2p orbitals) of carbon nitride. The less intense absorption band at 330 nm is due to π→π* transition in the conjugated network while another intense peak at *ca.* 387 nm appeared due to n→π* transition from nitrogen nonbonding orbital to the aromatic nonbonding orbital[321, 328-330]. The DR-UV-Vis spectrum of C_3N_5 demonstrates a drastic change in the UV-Vis absorption profile in comparison to g-C_3N_4 due to a more extended π conjugated network (Figure 5.3a) [321, 331]. A broad absorption peak around 393 nm in the UV-Vis spectrum of C_3N_5 was attributed to n→π* transition from the nitrogen nonbonding orbital to the π conjugated nonbonding orbital. The absorption spectrum of C_3N_5 was red-shifted showing band tailing up to 670 nm, due to an extended π conjugated network arising from the overlap between N2p orbitals of bridging azo moieties and N2p in heptazine π conjugated system. Further residual $–NH_2$ also contributes to the delocalized aromatic π conjugated system. Due to this, the position of the valence band gets upshifted and π→π* transition occurs at relatively low energy which facilitates the absorption of a large fraction of the visible spectrum and results in the sample displaying an orange color. Further, the optical bandgaps of g-C_3N_4 and C_3N_5 were determined using a Tauc plot by plotting a graph between $(\alpha h\nu)^{1/2}$ vs $h\nu$ and extrapolation of the linear tangent to abscissa; where α is absorption coefficient, h is plank constant and ν is the light frequency (Figure A24a). From the Tauc plot, the value of bandgap for g-C_3N_4 was estimated to be 2.65 eV corresponding to a band-edge at a wavelength of 467 nm, in good

agreement with the bandgap values reported in the literature.[332, 333] The bandgap value of C_3N_5 was calculated to be 1.76 eV corresponding to a band-edge at a wavelength of 707 nm.

Photoluminescence (PL) spectra were collected by exciting samples using 360 nm photons to probe radiative recombination (Figure 5.3b). The PL spectrum of melem consists of an intense emission peak centered at 441 nm which is indicative of radiative recombination of carriers within melem unit [328, 334]. It is important to note here that melem exhibits excitation wavelength-dependent PL emission. On the other hand, g-C_3N_4 showed a sharp emission peak at 468 nm which did not shift upon changing the excitation wavelength. This peak is attributed to fast interlayer carrier recombination in multilayered sheets of bulk g-C_3N_4 [331]. Surprisingly, C_3N_5 does not exhibit any distinguishing PL peaks which might be indicative of efficient charge separation between the bulk and the surface. Such charge transfer excitonic states involving the bulk and the surface, have also been observed in other conjugated organic semiconductors that possess an extended π-conjugated network that prevents radiative recombination by delocalizing the Frenkel exciton. However, due to conductive conjugated surface, non-radiative charge recombination can take place over new localized states in the sheets scaffold [201, 335].

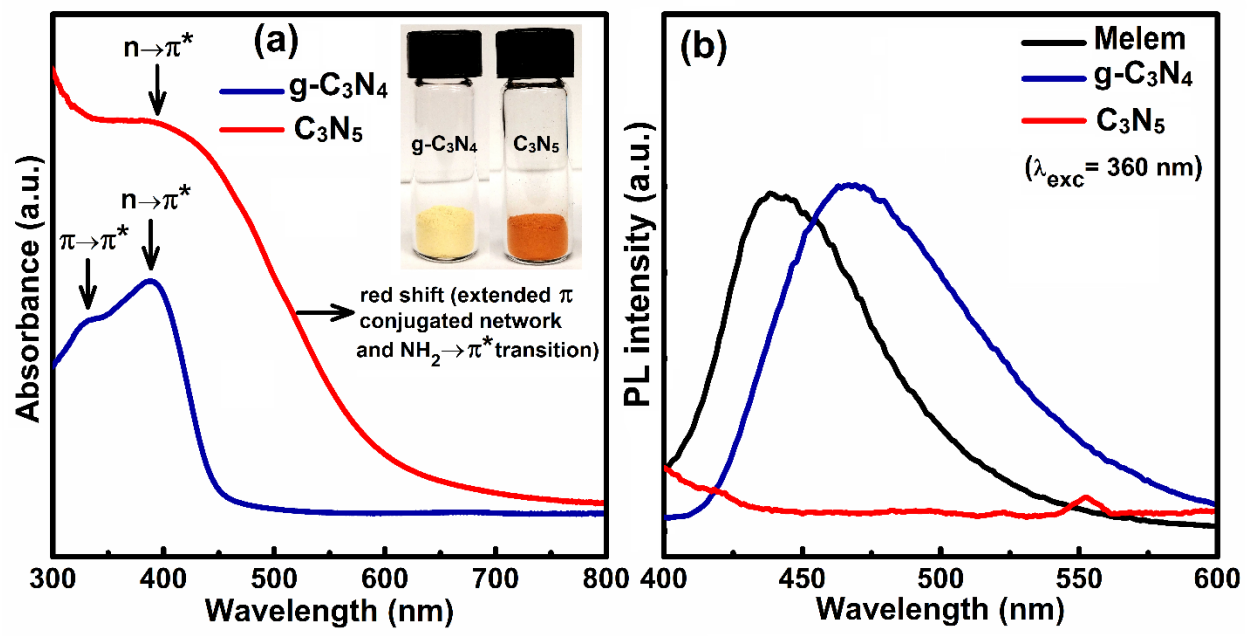

Figure 5.3. (a) DR-UV-Vis spectra of g-C_3N_4 (blue) and C_3N_5 (red), with inset showing photographs of g-C_3N_4 and C_3N_5 samples and (b) Steady-state PL spectra of melem (black), g-C_3N_4 (blue) and C_3N_5 (red) obtained using an excitation wavelength of 360 nm.

In order to investigate the lifetime of excited charged species, and charge separation processes, we collected time-resolved photoluminescence (TRPL) spectra of g-C_3N_4 and C_3N_5 using a single photon picosecond pulsed laser at a wavelength of 405 nm. Figure 5.4 displays the PL lifetime decay curves of g-C_3N_4 and C_3N_5. The PL decay curve was fitted tri-exponentially using the following equation:

$$I(t) = A_1 e^{-t/\tau 1} + A_2 e^{-t/\tau 2} + A_3 e^{-t/\tau 3} \qquad (5.1)$$

where, A_1, A_2, and A_3 represent the normalized amplitudes of each decay component and τ_1, τ_2 and τ_3 are values of the lifetime components respectively. The existence of three radiative lifetimes in the fitted PL lifetime spectra of g-C_3N_4 and C_3N_5 was in good agreement with previously

reported carbon nitride-based materials. [336, 337] The obtained values of lifetimes and their fractional components are given in Table 5.1.

The three components in the PL lifetime decay curve of g-C_3N_4 can be assigned to various energy states in g-C_3N_4 formed by the overlap of C and N sp^2 and sp^3 hybridized orbitals and the presence of lone pairs of electrons which allow for various radiative transitions. g-C_3N_4 is composed of tri-s-triazine (C_6N_7) units inter-connected with tertiary nitrogen atoms where C-N sp^3 hybridized state constitute high energy σ and σ* molecular orbitals while C-N sp^2 hybridization gives rise to a conjugated network resulting in low energy π bonding and π* antibonding orbital which constitutes the valence and conduction bands respectively [338]. The presence of unbonded lone pairs of electrons on pyridinic N atoms creates energy levels just below the π bonding orbital and their overlap with the π conjugated system can further decrease the energy of the π molecular orbital resulting in reduction of the bandgap [339, 340]. The first two shorter lifetime components of 3.31 and 0.75 ns with 34% and 63% contribution in g-C_3N_4 correspond to charge carrier recombination from σ* and π* antibonding to π MO [341]. The third longer lifetime component of 25.02 ns with a relative low contribution originated due to intersystem crossing (ISC) of electron from σ* and π* orbital followed by radiative relaxation to conjugated π orbital and trap assisted radiative recombination [342-347]. The first two lifetimes of C_3N_5 at 8.10 and 2.11 ns with 7 % and 26 % contributions in the PL decay curve were significantly longer lived in comparison to g-C_3N_4, strongly suggesting that the introduction of azo moiety extends π conjugated network which facilitates better charge carrier mobility on C_3N_5 sheets (delocalized the exciton, as mentioned previously) and prevents faster charge carrier recombination [348]. Further, due to extended conjugation, the difference between σ* and π* band gets decreased which is also evident in Mott-Schottky measurement (Figure A24b) [339]. The low energy difference between σ* and π*

accelerates the transfer of electrons from σ* and π* orbital via intersystem crossing followed by radiative relaxation which was evident from higher percentage contribution of the third-lifetime component (73%).

Table 5.1. The PL lifetime of photogenerated charge carrier and their relative contribution in g-C_3N_4 and C_3N_5.

Sample	τ_1(ns) [A_1]	τ_1(ns) [A_1]	τ_1(ns) [A_1]	Average lifetime (τ_{avg}) ns
g-C_3N_4	3.31 [0.34]	0.75 [0.63]	25.02 [0.05]	12.43
C_3N_5	8.10 [0.07]	2.11 [0.26]	0.28 [0.73]	4.40

The average lifetime (τ_{avg}) which is regarded as a coherent measure to evaluate the rate of spontaneous emission was calculated from the three-lifetime components using the following expression.

$$\tau_{avg} = (A_1\tau_1^2 + A_2\tau_2^2 + A_3\tau_3^2)/ (A_1\tau_1 + A_2\tau_2 + A_3\tau_3) \quad (5.2)$$

From equation (5.2), the average lifetimes of g-C_3N_4 and C_3N_5 were calculated to be 12.43 and 4.40 ns respectively. The decreased lifetime of the C_3N_5 in comparison to g-C_3N_4 coupled with the very weak photoluminescence of C_3N_5 (as seen in Figure 5.3b) is indicative of fast quenching of the C_3N_5 luminescence. The fast quenching might originate from improved charge separation in C_3N_5 due to a larger conjugated π network but might also be due to stronger non-radiative transitions. Fast exciton dissociation with concomitant high carrier mobility can result in photogenerated electrons finding trap sites (and moving to them) and recombining by non-radiative processes [201]. The aforementioned processes are highly likely in C_3N_5 since the presence of azo bonds extends the π network because of overlap of N2p orbital on azo nitrogens with the π network of heptazine motif due to which electrons can move within C_3N_5 scaffold freely. The

lower PL lifetime of C_3N_5 in comparison to g-C_3N_4 was consistent with steady-state PL where C_3N_5 shows prodigious quenching in its PL spectrum.

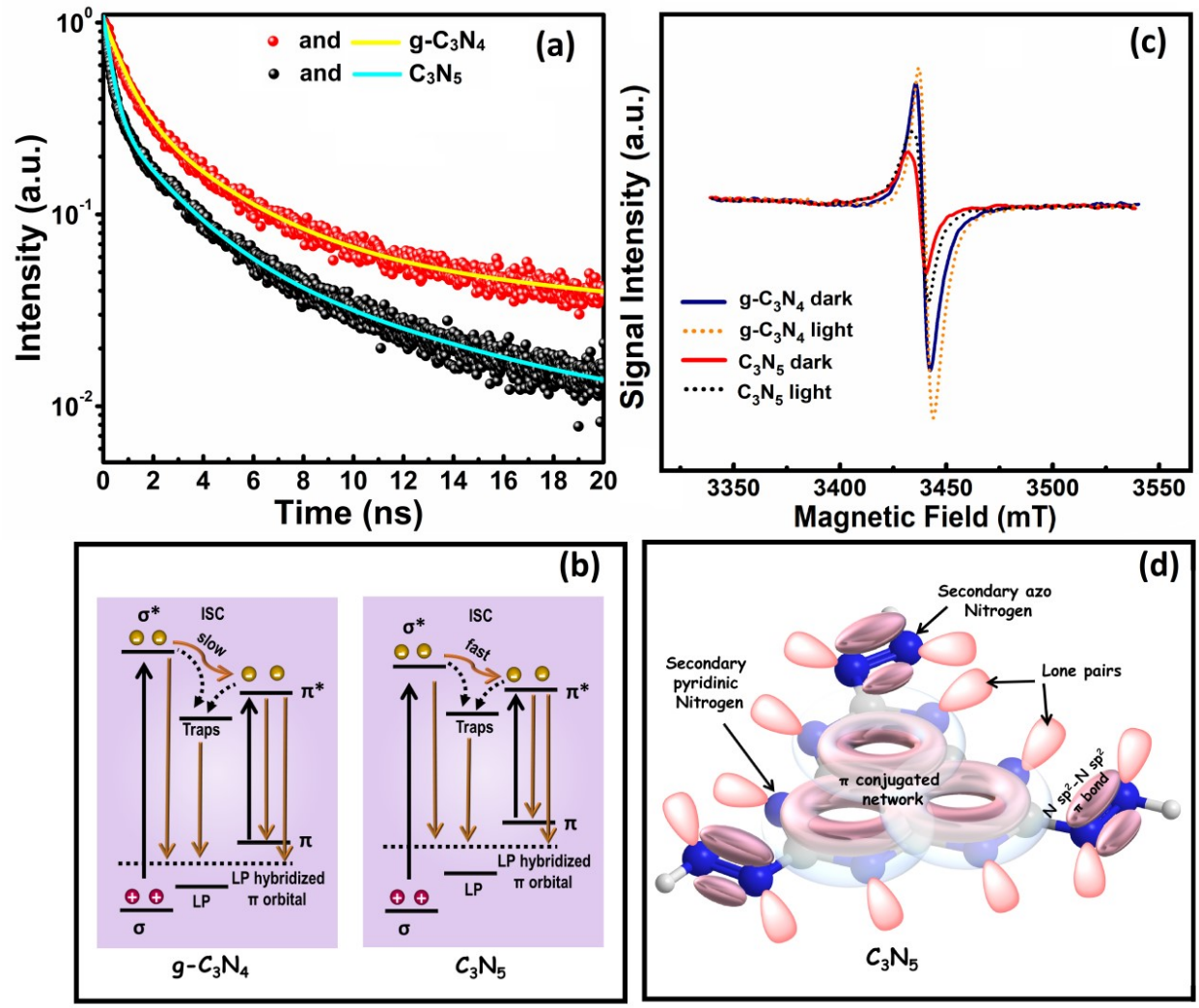

Figure 5.4. (a) PL lifetime decay curves of g-C_3N_4 (red; tri-exponential fit, yellow line) and C_3N_5 (black, tri-exponential fit, cyan), (b) Schematics of various energy levels bands and possible route of charge carriers recombination (c) X-band EPR spectra of g-C_3N_4 in the dark (blue), after light irradiation (orange dots) and C_3N_5 in the dark (red) and after light irradiation (black dots) at room temperature, (d) Plausible molecular orbital overlap representation of C_3N_5.

Electron paramagnetic resonance (EPR) spectra of g-C_3N_4 and C_3N_5 to elucidate electronic nature and band excited paramagnetic species were collected under dark and UV irradiation at room temperature (Figure 5.4b). The EPR spectra of g-C_3N_4 under dark conditions exhibits an intense Lorentzian EPR resonance signal located at a g-factor of 2.003. The observed EPR signal originated due to the presence of unpaired electrons in the sp_2 hybridized aromatic π-system which was in good agreement with previous reports [349-352]. The EPR signal intensity of g-C_3N_4 increased after UV irradiation, attributed to populated unpaired electrons in the conduction band due to π-π* and N non-bonding to π* (n-π*) transition followed by slow relaxation *via* ISC. The observed EPR signal of C_3N_5 was also observed at 2.003 g-value which implies basic graphitic heptazine skeleton remains intact in C_3N_5 framework [353, 354]. Further, after irradiation with UV light, the EPR signal intensity of C_3N_5 was also enhanced due to increased numbers of unpaired electrons in the conduction band. However, the overall EPR signal intensity of C_3N_5 in both the dark and under UV illumination was significantly weaker in comparison to g-C_3N_4 which was attributed to a lesser number of unpaired electrons in C_3N_5, which in turn can be taken as evidence of the presence of extra N atoms outside the heptazine nucleus in comparison to conventional N-rich carbon nitride materials where N atoms substitute C atoms in the heptazine motif. It is well documented in the literature that substitution of sp^2 hybridized +4 state C atom in heptazine motif with sp^2 hybridized +3 state N atom will liberate extra electrons in the aromatic system which will distort electronic symmetry [331, 355-357] and also increase EPR signal intensity. However, in the case of C_3N_5, the additional N atom makes an azo bond with an N atom outside the ring via π overlap and the extra electrons remain in the form of lone pairs (Figure 5.4d).

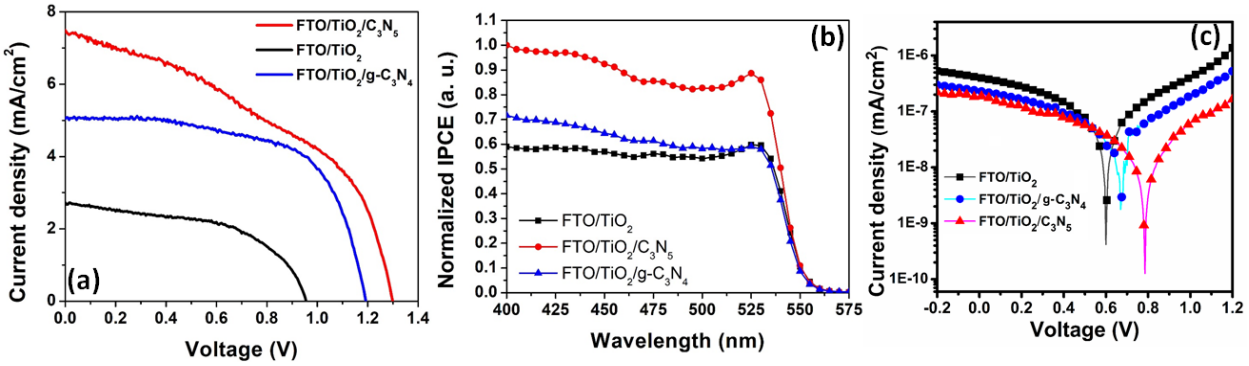

Figure 5.5. **(a)** *J-V* characteristics under AM 1.5 one sun illumination of halide perovskite solar cells comprising an active layer of $MAPbBr_3$ and different electron transport layers (b) Action spectra showing the relative external quantum yields of halide perovskite solar cells comprising an active layer of $MAPbBr_3$ and different electron transport. (c) *J-V* characteristics in the dark of halide perovskite solar cells comprising an active layer of $MAPbBr_3$ and different electron transport layers – TiO_2 (black curve), g-C_3N_4 (blue curve) and C_3N_5 (red curve). In every case, spiro-OMeTAD was used as the hole transport layer.

To demonstrate the optoelectronic application of our newly synthesized graphenic semiconductor, we employed C_3N_5 as the electron transport layer (ETL) in $MAPbBr_3$ based perovskite solar cells and obtained a good result. Carbon-based materials have frequently been used as hole transport layers (HTLs) or hole collection electrodes in $MAPbBr_3$ based solar cells but have almost never been used (effectively) as ETLs to boost the open-circuit photovoltage. Using C_3N_5 as the ETL and with no optimization of any kind, we measured a V_{oc} of 1.3 V, J_{sc} of 7.5 mA cm^{-2} and a fill factor (FF) of 0.4 to obtain a power conversion efficiency (PCE) of 4.2 % (Figure 5.5). Some context is needed to appreciate the significance of the aforementioned result. Methylammonium lead bromide ($MAPbBr_3$) is a halide perovskite with an electronic bandgap of 2.23 eV which has two major advantages for solar cell applications in comparison to the more commonly used methylammonium lead iodide ($MAPbI_3$) – in theory, it enables the construction

of much higher V_{oc} solar cells that can be used to power electrocatalytic and electrochemical reactions and secondly, $MAPbBr_3$ is known to have superior ambient stability (less moisture sensitivity) and operational stability (due to the absence of phase transitions and enhanced thermal stability at a high working temperature) compared to $MAPbI_3$ [358, 359]. However, until recently, most works in this area failed to achieve the expected high V_{oc} value, and the typical V_{oc} values obtained using were in the range 0.90-1.16 V [360]. The use of carbon-based charge transport layers has enabled a dramatic improvement in the performance of $MAPbBr_3$-based photovoltaic devices by generating photovoltages in excess of 1.3 V (as high as 1.6 V) without suffering a corresponding penalty in the short circuit current (J_{sc}). The first such report was by Wu *et al.*[361] wherein indene-C60 bisadduct (ICBA) was used as the acceptor in conjunction with $MAPbBr_3$ to realize a high V_{oc} perovskite solar cell. Shortly thereafter, Li *et al*. used carbon nanotubes as an efficient hole collector for $MAPbBr_3$ solar cells and achieved a V_{oc} of 1.4 V.[362] $MAPbBr_3$ sandwiched between modified PEDOT:PSS (hole transport layer) and $PC_{61}BM$ (electron transport layer) resulted in a solar cell with a V_{oc} of 1.52 V[363] while a graphitic carbon anode (with no hole transport layer) and TiO_2 electron transport layer were used by Liang *et al.* to realize a $MAPbBr_3$ solar cell with a V_{oc} as high as 1.57 V [364]. The origin of the poor V_{oc} values was poorly understood for a long time. Even now, there are two distinct explanations, one based on active layer material quality issues and another based on high interfacial recombination. For instance, vapor-deposited $MAPbBr_3$ films were found to generate high V_{oc} values in comparison with solution-deposited films, which was attributed to the superior morphology and grain size in the vapor-deposited films, and supported the explanation invoking material quality [365]. The second explanation was supported by the observation of high V_{oc} values when hole transport layers with deep HOMO levels were used, indicating that the separation of the electron- and hole- quasi-Fermi levels at the charge extraction

interfaces, was the controlling mechanism determining V_{oc} [366]. Our examination of $MAPbBr_3$ solar cells using C_3N_5 as the ETL provides a way to reconcile the above explanations. On the one hand, the high CB position of C_3N_5 is better aligned with the CB of $MAPbBr_3$ and enables an optimal value for the electron quasi-Fermi level at the perovskite- C_3N_5 interface. On the other hand, the low dark current observed using C_3N_5 ETL in comparison to both TiO_2 and g-C_3N_4 ETLs (Figure 5.5c) indicates suppression of trap-mediated hopping through $MAPbBr_3$ due to the insertion of C_3N_5 as a midgap state-free barrier layer, thus enabling the circumventing of active layer material quality issues. In summary, it is noteworthy that an unoptimized ETL made with a brand-new semiconductor (C_3N_5) that was cast into films from a particulate suspension, generated a V_{oc} value of 1.3 V, higher than that generated by TiO_2 and g-C_3N_4 ETLs.

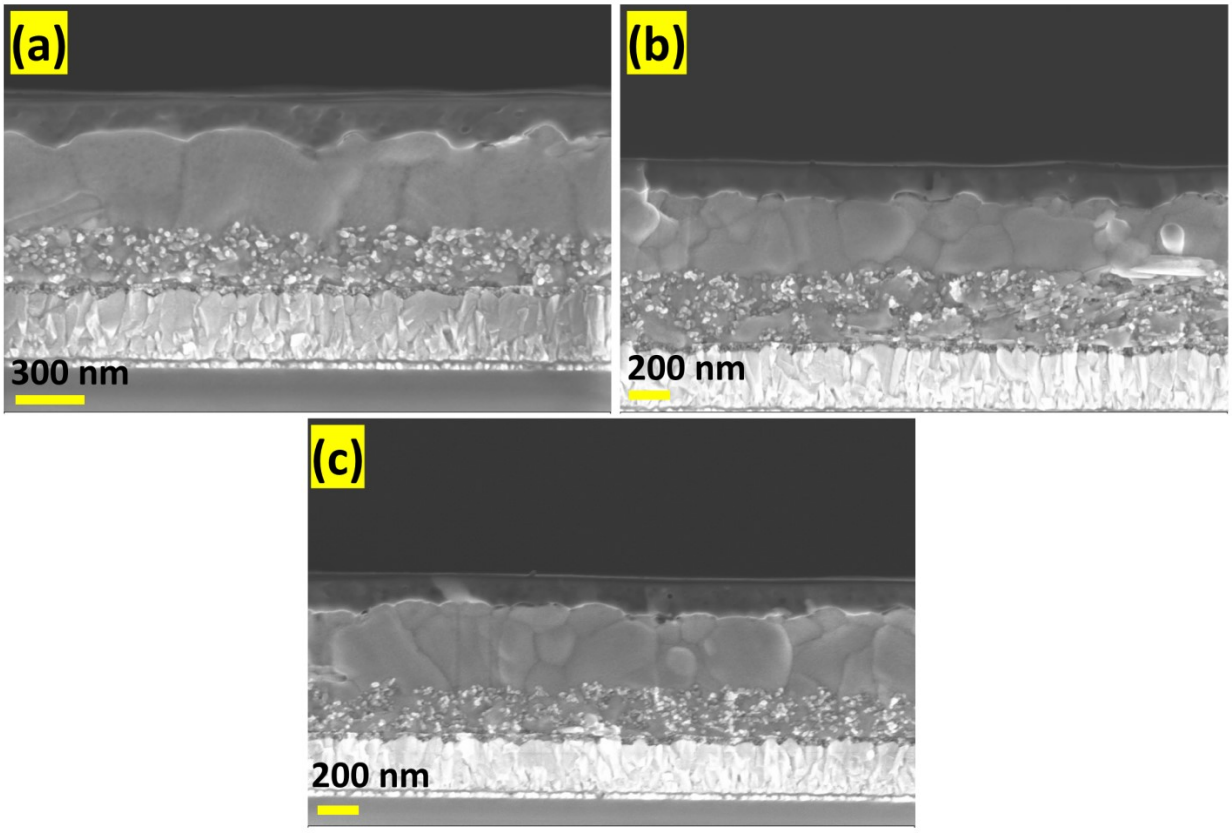

Figure 5.6. Cross-sectional FE-SEM images of perovskite solar cell made composed of (a) perovskite layer with bare PbX_2, (b) with 4 wt% of g-C_3N_4 and (c) with 4 wt% of C_3N_5 in PbX_2 solution.

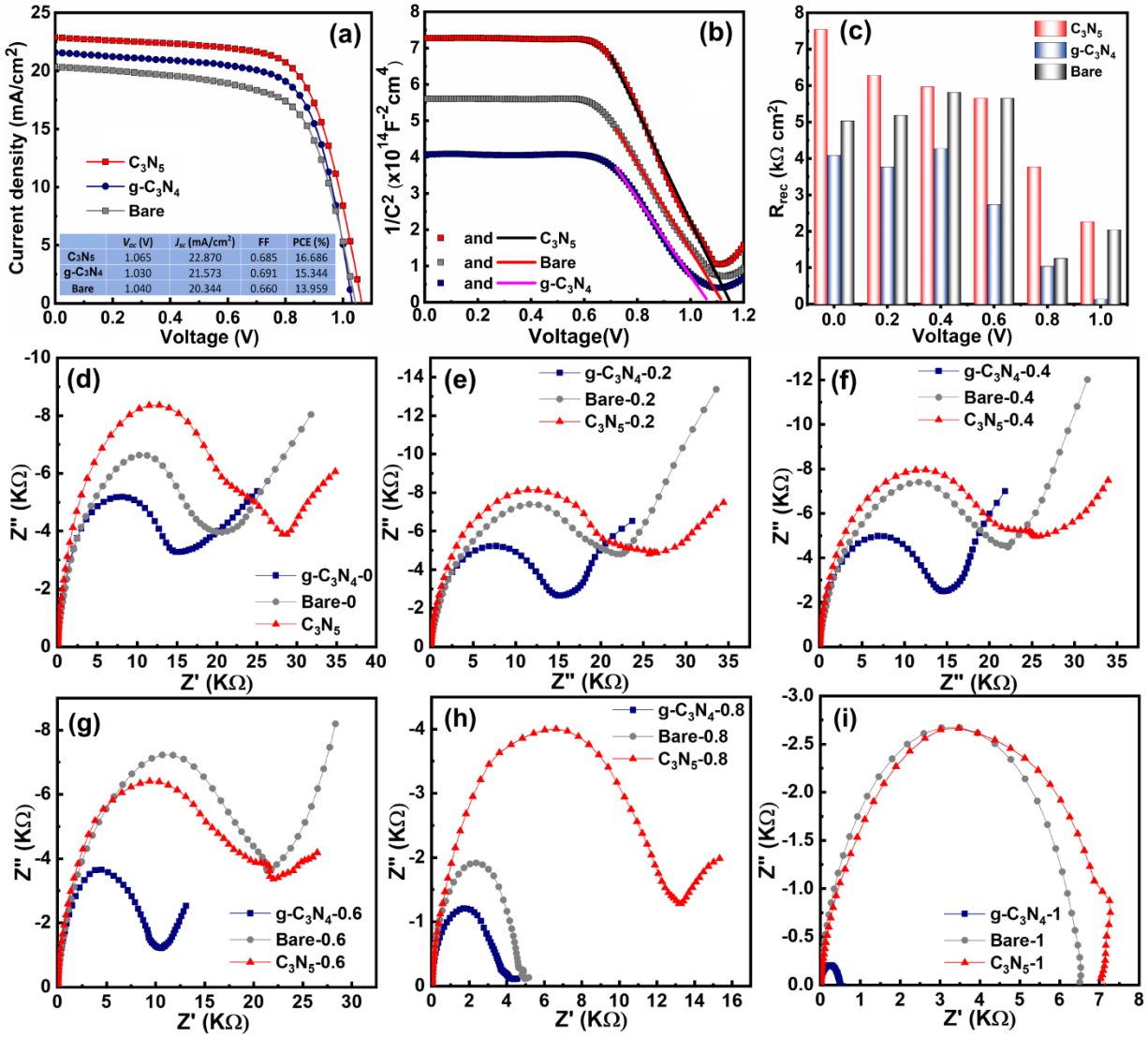

Figure 5.7. (a) Current-voltage characteristics of perovskite solar cells made with bare PbX_2, 4 wt% of g-C_3N_4 and C_3N_5 under AM1.5 G one sun illumination. (b) Mott-Schottky plot of the perovskite solar cells based undoped and g-C_3N_4/C_3N_5-doped perovskite active layers. (c) Recombination resistance of perovskite solar cell based on undoped and doped Perovskite layer with CN and MHP in dark. The corresponding equivalent circuit is shown in insets where Rs is

series resistance, C is high-frequency capacitance, R is recombination resistance, and Q is a constant phase element (CPE) with coefficient N. (d-i) Nyquist plots for perovskite solar cells made with bare PbX_2, g-C_3N_4 and C_3N_5 doping under dark condition at 0.0, 0.2, 0.4, 0.6, 0.8 and 1.0 V.

Table 5.2. Photovoltaic performance of HPSCs made with bare PbX_2, 4 wt% g-C_3N_4 and C_3N_5 in PbX_2 solution under AM1.5 G solar simulated light.

		V_{oc}(V)	J_{sc}(mA/cm^2)	FF	PCE (%)
C_3N_5	Maximum	1.065	22.870	0.685	16.686
	Average	1.026±0.043	22.560±1.039	0.654±0.044	15.142±1.442
g-C_3N_4	Maximum	1.030	21.573	0.691	15.344
	Average	0.984±0.042	21.204±0.565	0.670±0.017	13.981±0.949
Bare	Maximum	1.040	20.344	0.660	13.959
	Average	1.041±0.035	20.394±0.200	0.647±0.020	13.713±0.245

The photovoltaic performance of halide perovskite solar cells is highly dependent on grain size and defect-free lattice states. The presence of small numbers of defects and trap sites have detrimental effects. The trap assisted recombinations can be minimized by passivating perovskite layer with graphenic materials due to their high carrier mobility and surface area materials which can efficiently capture charge improve transportation behavior resulting in better photoconversion efficiency [193, 367-370]. Further, incorporation of graphenic semiconductors with perovskite precursor provides crystallization of the surface which helps in increasing grain size and minimizing defect density at grain boundaries. The increased conjugation in C_3N_5 should lead to electron-rich conductive surfaces with high charge carrier density and better carrier mobility than g-C_3N_4. To verify this assumption, we have blended $MA_xFA_{1-x}Pb(I_{0.85}Br_{0.15})_3$ based perovskite with different wt% of C_3N_5 and g-C_3N_4. Under optimized conditions, 4 wt% doping of g-C_3N_4 and C_3N_5 with

respect to PbX_2 was found to be best performing and C_3N_5 outperformed g-C_3N_4 and bare PbX_2 based solar cell architecture, attributed to better charge separation in more conjugated C_3N_5 scaffold and reduced trap sites.

Figure 5.6 shows the cross-sectional view and Figure 5.7 shows the *J-V* curves of the best performing solar cell devices based on undoped and doped perovskite layers while photovoltaic performances of solar cells are summarized in Table 5.2. Solar cells made with a compact undoped perovskite solar cell yielded a short circuit current density (J_{sc}) of about 20.344 mA/cm^2, an open-circuit voltage (V_{oc}) of 1.04 V and fill factor (FF) of about 66% resulting in the overall power conversion efficiency (PCE) of about 13.959%. Perovskite solar cells made with a g-C_3N_4-doped perovskite layer showed a J_{sc} of 21.573 mA/cm^2, V_{oc} of 1.03V and fill factor of about 69.1% and corresponding PCE of about 15.344%. C_3N_5 doped perovskite solar cells displayed a PCE value of 16.689% resulting from V_{oc} of 1.065V, J_{sc} of 22.87 mA/cm^2 and FF of 68.5%.

Capacitance-voltage measurement on fabricated devices with doped/undoped perovskite layer was measured at 10 kHz frequency in dark to determine bulk properties such as doping density (N_D) and energy equilibrium at the contacts which is related to the flat-band potential (V_{fb}).[167, 263, 291, 292, 294, 295, 299] Mott-Schottky plots for the devices made with doped and undoped perovskite layer are shown in Figure 5.7(b).

$$\frac{1}{C_{sc}^2} = \frac{2}{e\varepsilon_0\varepsilon_r N_D}\left\{(V - V_{FB}) - \frac{kT}{e}\right\} \qquad (5.3)$$

$$N_D = \frac{2}{e\varepsilon_0\varepsilon_r n} \qquad (5.4)$$

V_{fb} and N_D were calculated by using equation (5.3) and equation (5.4) respectively, where C_{sc} is the space-charge capacitance (*i.e.* film capacitance) per unit area; ε_r is the dielectric constant of the material, ε_0 is the vacuum permittivity, *k* is Boltzmann constant, *T* is the temperature in Kelvin, *e* is the electron charge and *V* is the applied potential. The measured V_{fb} of bare undoped, g-C_3N_4_doped and C_3N_5 doped perovskite solar cells was found to be 1.12, 1.08 and 1.15 V respectively, while carrier concentration of the respective devices was found to be 1.74×10^{16}, 1.96×10^{16} and 1.36×10^{16} cm^{-3}. This proves that the doping perovskite layer with C_3N_5 significantly improves the charge transport in the device compared to the undoped and g-C_3N_4-doped devices.

To explore the charge transport characteristics, hole-only devices with the architecture of FTO/PEDOT: PSS/Perovskite/Spiro-oMeTAD/Au were measured by the space charge limited current (SSLC) model described by the following equation,

$$J = \frac{9}{8L^3}\,\epsilon_0\epsilon_r\mu V^2 \qquad (5.5)$$

where ϵ_0, ϵ_r, μ and L are permittivity of the free space, relative permittivity of the perovskite, carrier mobility in perovskite layer and thickness of perovskite layer respectively. The hole mobility in pure perovskite was found to be 2.55×10^{-3} cm^2/VS while that of g-C_3N_4 and C_3N_5 doped perovskite was found to be 3.28×10^{-3} cm^2/VS and 4.33×10^{-3} cm^2/VS respectively (Figure 5.7).

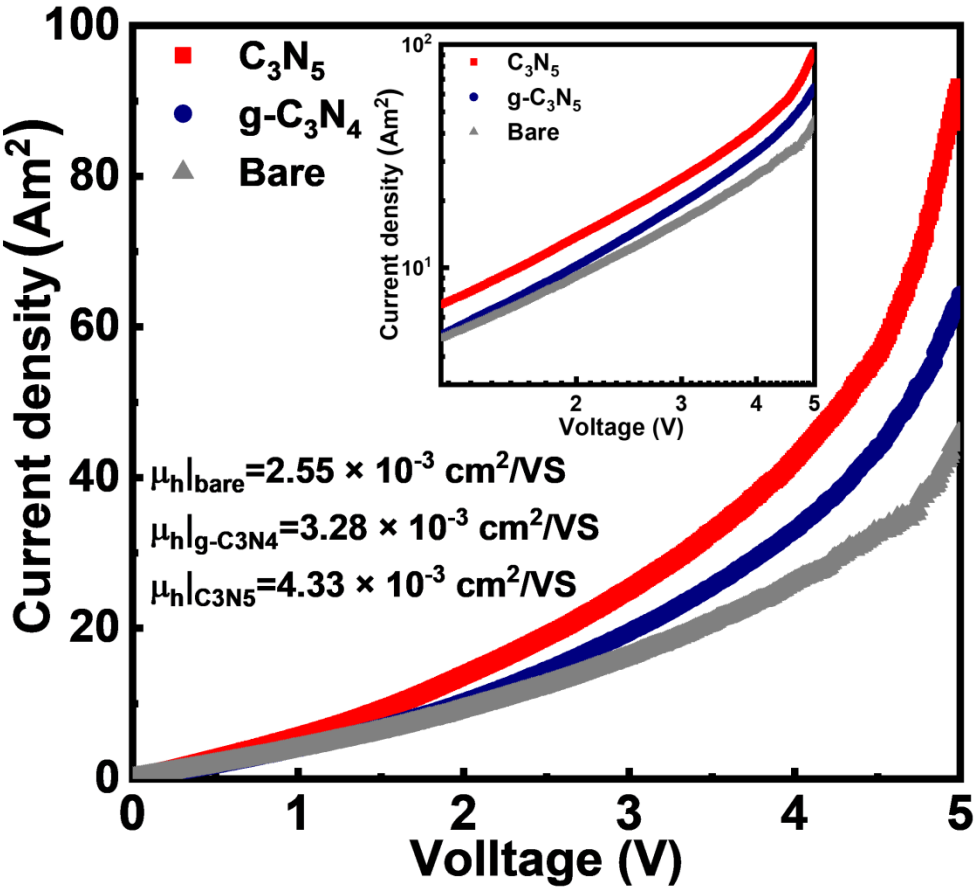

Figure 5.8. *J-V* curves of hole only device in linear scale (inset is in log-log scale) with the structure of FTO/PEDOT:PSS/Perovskite/Spiro-oMeTAD/Au

To get insight into the charge transfer properties of perovskite solar cells based on undoped and doped perovskite layer, solid-state impedance spectroscopy measurements in the frequency range from 0.1 Hz to 1 MHz at different applied bias under dark condition were performed. The resulting Nyquist plots were fitted with the circuit shown in inset of Figure 5.7c, where R_s is series resistance, R_{rec} and C represents the resistance and capacitance at the interface between the active layer and charge transport layer and Q is a constant phase element (CPE) with coefficient N. The resulting recombination resistance of different solar cells obtained after fitting the Nyquist plot observed from the low-frequency region at different voltages is shown in Figure 5.7 (d-i). C_3N_5

doped device showed higher value of R_{rec} compared to the g-C_3N_4 doped and undoped devices. As the electron and hole transporting layers for all kinds of devices are same, the difference in R_{rec} is mostly governed by the change in the interfacial property of perovskite layer induced by doping with C_3N_5 and g-C_3N_4. Interfacial recombination is inversely proportional to the recombination resistance, therefore, it can be concluded that the interfacial charge recombination in perovskite solar cells significantly gets suppressed by doping with MHP while it increases by doping with g-C_3N_4 resulting in an improved V_{oc} in C_3N_5 based device followed by the undoped and doped devices.

5.3 Conclusion:

We reported the synthesis of modified carbon nitride framework C_3N_5 polymer containing exceptionally high N:C atomic ratio (5:3) melem hydrazine as the monomeric unit. Solar cell devices using C_3N_5 ETL and $MAPbBr_3$ displayed improved V_{oc} of 1.3 V and power conversion efficiency (PCE) of 4.2 % higher than carbon nitride ETL which demonstrates the versatility of the newly synthesized low bandgap graphenic semiconductor.

Chapter-6 Conclusion and Future Works

6.1 Conclusions:

A common thread running through this dissertation is the exploitation of nanophotonic effects and the optimization of charge transport layers and perovskite active layer to enhance the performance of HPSCs. In this work, conventionally used mesoporous TiO_2 nanorods were replaced by hydrothermally grown TiO_2 nanorod arrays to improve the light-harvesting and charge collection efficiencies in perovskite solar cells. Backscattering of incident light was found to be reduced, and forward scattering was found to be improved in nanorod based devices compared to the nanoparticle-based devices. Because of higher forward scattering, IPCE of nanorod based devices was found to be improved drastically throughout the absorption range of perovskite resulting in higher short circuit current density. Because of better transfer of photogenerated charge to the nanorods and high mobility of single crystal nanorods, the charge recombination in nanorod based devices were found to be lower which is crucial to achieving a high value of fill factor in the solar cells. Hence, I have shown that by replacing the nanoparticle-based ETL with optimized nanorod based ETL, current density and fill factor of solar cells can be improved which leads to the higher value of power conversion efficiency.

The hole transport layer in perovskite solar cells plays an equally important role as the electron transport layer. Commonly used hole transporting layers such as Spiro-OMeTAD, P3HT and PEDOT: PSS suffers from low mobility and promotes device degradation. Thus, it very important to replace such a hole transporting layer with inorganic p-type material with high hole mobility. To leverage the excellent hole transport properties of NiO, hole transporting properties

of mesh-like NiO nanostructures grown by the hydrothermal technique have been explored. The *p-i-n* type halide perovskite solar cells that use Ni^{3+}-doped NiO nanomesh hole transport layers were found to consistently generate open circuit voltage values > 1.10 V upon AM1.5G one sun illumination. Compared to traditional spin-cast NiO thin films, the hydrothermally grown NiO nanostructures showed 20 times higher surface area, excellent charge transfer, and transport properties as proved by TRPL, IMPS, IMVS, CV and KPFM measurements. Introducing Ni^{3+} defects in NiO result in more *p*-type behavior of the material because of which nanostructured NiO was found to be more electrically conductive than the defect-free compact NiO leading to lower series resistance and improved electron blocking properties of the nanostructured NiO based perovskite solar cells. Consequently, perovskite solar cells based on a nanostructured NiO hole transporting layer demonstrate improved photovoltaic performance.

Traps and grain boundaries in the perovskite layer act as the recombination centers in the solar cells. To make $V_{oc}FF/V_{SQ}FF_{SQ}$=1, it is very important to reduce recombination at the grain boundaries. It can be done in by passivating the traps and grain boundaries with high mobility semiconductors such as graphenic carbon nitrides. To fill the traps generated because of thermal degradation of the perovskite layer, doping of the perovskite layer with graphitic semiconductors was performed. 1.3- and 1.7-times improvement in the hole mobility of the perovskite layer were observed when perovskite was doped with g-C_3N_4 and C_3N_5 respectively because of which the FF and V_{oc} of solar cells were found to be improved resulting in higher power conversion efficiency. As graphenic carbon nitride and modified carbon nitride are wide bandgap (2.65-1.76 eV), *n*-type, high mobility semiconductors their electron-transporting properties in perovskite solar cells have been explored. Conduction band position of g-C_3N_4 and C_3N_5 was found to be at -3.65 eV and -3.78 eV respectively, while the conduction band of TiO_2 which conventional electron transporting

layer in *n-i-p* type perovskite solar cells lies in the range of -4.1 eV to -4.3 eV. The open-circuit voltage of perovskite solar cells depends on the difference in the quasi-Fermi levels of the electron and hole transport layers. The conduction band of $MAPbBr_3$ lies at ~-3.58 eV. By replacing TiO_2 with g-C_3N_4 and C_3N_5, the open-circuit voltage of $MAPbBr_3$ based solar cells improved from 0.95 V to 1.19 V (for g-C_3N_4) and 1.30 V (for C_3N_5) respectively. It was found that a large band offset between the conduction band of TiO_2 and that of $MAPbBr_3$ promotes charge recombination at the interface because of which the V_{oc} of the wide-bandgap perovskite solar cells based on the TiO_2 was low compared to the carbon nitride-based solar cells.

6.2 Future Works:

Current work has been focused on the optimization *n*-type, *p*-type and perovskite layers in the perovskite solar cells by using 1D and 2D semiconducting materials. Future work can be carried out in the following aspects of the perovskite solar cells.

The two most important power loss mechanism in solar cells with a single bandgap absorber layer is the thermalization loss of the photon energy higher than the bandgap and inability of the absorber to absorb the photon with lesser energy than its bandgap. These two parameters account for about 50% loss of solar energy. Thermalization loss can be reduced by engineering the architecture of solar cells using graded bandgap absorbers. The high energy photons should get absorbed in the first layer followed by the absorption of low energy photons in subsequent layers. Keeping that in mind, a low-cost, solid-state, dye sensitized-perovskite tandem solar cells can be designed and fabricated. For example, $MAPbBr_3$ absorbs photons till ~550 nm and SQ2 absorbs from ~550 nm to ~750 nm. Nanostructured NiO can be fabricated on the FTO substrate by using the technique described in chapter 4. A monolayer of SQ2 can be deposited on a

nanostructured NiO layer followed by deposition of the $MAPbBr_3$ perovskite layer and n-type PCBM/ZnO layer can be deposited on the perovskite layer followed by the deposition of Al to complete the device. Similarly, n-i-p device (FTO/TNR/SQ2/$MAPbBr_3$/Spiro/Au) can also be fabricated. The open-circuit voltage of solid-state dye-sensitized solar cells based on SQ2 is typically found to be 0.6 eV, rising in some cases to 0.75 eV and is widely thought to be determined by the difference in the upper energy level of the electron transport layer (TiO_2 conduction band or LUMO of PCBM) and the HOMO level of the hole transport layer (Spiro-OMeTAD or P3HT). The open-circuit voltage in perovskite solar cells is determined by the difference in the quasi-Fermi levels of electrons and holes in the halide perovskite active layer. $MAPbBr_3$ has a bandgap of 2.3 eV and open-circuit voltage of perovskite solar cells made by using $MAPbBr_3$ as an active layer have been reported to have an open-circuit voltage higher than 1.5 V. Therefore, it is interesting to examine what happens to the open-circuit voltage and current of the solar cells when SQ2 is sandwiched between the ETL/HTL and the perovskite.

Currently, most state-of-the-art perovskite solar cells utilize a mesoporous TiO_2 film which provides structural support to the light-absorbing perovskite layer and acts as the electron transport layer at the same time. However high annealing temperature about 500° C is required to sinter the mesoporous TiO_2 layer. Because of elevated temperature annealing requirements, mesoporous TiO_2 cannot be used to fabricate flexible perovskite solar cells as the flexible substrates are generally made up of plastics such as polyethylene terephthalate (PET), polyimide (Kapton), etc. Thus, a low-temperature processable electron transport layer is required to fabricate flexible solar cells. The high electron mobility of ZnO (200–300 cm^2/Vs for the bulk material and about 1000 cm^2/Vs for single crystal) makes it an ideal choice of electron transport layer for perovskite solar cells. ZnO is an *n*-type semiconductor with a bandgap of 3.37 eV and higher electron mobility than

TiO_2 [371, 372]. This results in a lower recombination loss in ZnO compared to TiO_2, which makes ZnO superior in balancing charge transport in perovskite. Additionally, ZnO can be deposited using low-temperature processes such as electrodeposition which do not require additional high-temperature calcination steps. An electrochemical deposition allows the deposition of high-quality crystalline ZnO at low temperatures. By tuning the variables (time, temperature, applied bias, the concentration of Zinc salt) in the electrodeposition process, the morphology of ZnO can be tunned from nanorods to thin-films. By changing the concentration of Zinc salt used in the electrodeposition process, the diameter, length and aspect ratio can be easily tunned. Therefore, high-efficiency flexible perovskite solar cells can be fabricated by using electrodeposited ZnO nanostructures as an electron transporting layer.

6.3 Issues to be addressed before commercialization:

Marginal change in film quality of perovskite with similar composition shows significant variation in the overall conversion efficiency of solar cells. Electro-optical properties of the same perovskite material vary significantly with the method of synthesis [373]. Ionization energy and Fermi level position of perovskite vary significantly depending upon the fabrication method. [67, 374, 375] Even devices prepared by the same researcher or by a different group may have a large variation in photoconversion efficiencies indicating the huge variation in optoelectronic properties of perovskite layer as a function of sample treatment and handling [374]. Bandgap, photoluminescence, radiative recombination, carrier concentrations, diffusion lengths, etc. depend on the localized defects in the crystal and thus vary significantly from sample to sample as a result of imperfect control of their fabrication. The high-efficiency perovskite solar cells are made by using lead which is not environment-friendly. Even though proper encapsulation of the solar cells

and Pb-recycling (currently being done for lead-acid batteries) can minimize the adverse effect of Pb on the environmentenergy Pb-free perovskite solar cells before putting it in the market for the large-scale power generation. Several attempts have been made by fully or partially replacing Pb with Sn or Bi, however, by doing so the power conversion efficiency and stability of such devices have found to worsen. Maximum efficiency so far has been reported for the Pb-free perovskite solar cell is still under 10%.

Another major issue holding back the commercialization of perovskite solar cells is the presence of hysteresis in the current-voltage behavior of the solar cells. The presence of such a hysteretic *J-V* characteristic is a challenge for determining the actual power conversion efficiency of perovskite solar cells. The magnitude of hysteresis has also been found to be dependent on scan direction, scan voltage range, and scan rate. It has been found that the dielectric permittivity of perovskite solar cells at low frequency increases more than 1000 times under one sun illumination compared to dark conditions. This large photo-induced dielectric permittivity causes a large low-frequency capacitance and slow decay process in perovskite solar cells which is responsible for the non-steady-state current in perovskite solar cells resulting in hysteretic *J-V* curves. The physical origin of hysteresis has been linked to various physical parameters such as carrier trapping, ion migration, perovskite grain size, light soaking, bias soaking, and ferroelectric effects. Trap passivation at the grain boundaries and interfaces is used to reduce the hysteresis, however, the trapping process happens in a millisecond time scale which is faster than the JV hysteresis behavior. It indicates that there must be some other factors on which hysteresis depends such as ion migration. However, the time scale of ion migration is still not studied properly. If the time scale of ion migration is on the order of several minutes, it should not be affecting the hysteresis behavior of solar cells. Hence a detailed study must have to be done on the identification of factors

responsible to create hysteresis behavior and resolving them by designing advanced device structures with better characteristics.

The instability of perovskite is one of the biggest hindrances for its commercialization. The stability of perovskite depends on several parameters such as temperature, light illumination and thermal treatments among which moisture is considered to be the biggest challenge. Perovskites degrade in the presence of moisture because of the hygroscopic nature of monovalent amine salt which is lost via hydrolysis reaction in the presence of moisture leaving PbI_2 behind. The degradation of perovskites can be represented by the following reactions;

$$CH_3NH_3PbI_3 \leftrightharpoons PbI_2\ (s) + CH_3NH_3I\ (aq)$$

$$CH_3NH_3I\ (aq) \leftrightharpoons CH_3NH_2\ (aq) + HI\ (aq)$$

$$4HI\ (aq) + O_2\ (g) \leftrightharpoons 2I_2\ (s) + 2H_2O\ (l)$$

$$2HI\ (aq) \leftrightharpoons H_2\ (g) + I_2\ (s)$$

For the decomposition reaction of $CH_3NH_3PbI_3$ to PbI_2 and CH_3NH_3I, the change in Gibbs free energy at 300K is about very small (0.16 eV/formula unit) which means even though the perovskite is chemically stable it is very delicate and the reaction can be easily shifted in the other direction. To overcome this issue several initiatives are being taken for example application of 2D and 0D perovskites as the photoactive layers, however, the efficiency of such solar cells is still incomparable with the 3D perovskites. The electron transporting layer and hole transporting layers also plays a huge role in the device Several reports have claimed that the photoactivity of TiO_2 which is used as an electron transporting layer helps promotes device degradation similarly the acidic nature of PEDOT:PSS which is generally used as an HTL in *p-i-n* type solar cells also

promotes devices degradation. Hence a tremendous effort is yet to be devoted towards the design and fabrication of materials for stable and high-efficiency perovskite solar cells.

Bibliography:

1. Nations, U. World Population Prospects https://population.un.org/wpp/Publications/Files/WPP2017_KeyFindings.pdf.
2. Administration, U. S. E. I. https://www.eia.gov/todayinenergy/detail.php?id=32912.
3. Council, W. E. World Energy Resources 2016. https://www.worldenergy.org/wp-content/uploads/2016/10/World-Energy-Resources-Full-report-2016.10.03.pdf.
4. Petrolium, B. Statistical Review of World Energy. https://www.bp.com/content/dam/bp/en/corporate/pdf/energy-economics/statistical-review/bp-stats-review-2018-full-report.pdf.
5. Tsao, J.; Lewis, N.; Crabtree, G. J., US department of Energy. Solar faqs. 2006.
6. Green, M. A.; Emery, K.; Hishikawa, Y.; Warta, W.; Dunlop, E. D. Solar cell efficiency tables (version 46). *Prog. Photovoltaics* 2015, 23, 805-812.
7. Bhandari, K. P.; Collier, J. M.; Ellingson, R. J.; Apul, D. S. Energy payback time (EPBT) and energy return on energy invested (EROI) of solar photovoltaic systems: A systematic review and meta-analysis. *Renewable and Sustainable Energy Reviews* 2015, 47, 133-141.
8. Yue, D.; You, F.; Darling, S. B. Domestic and overseas manufacturing scenarios of silicon-based photovoltaics: Life cycle energy and environmental comparative analysis. *Solar Energy* 2014, 105, 669-678.
9. Scharber, M. C.; Sariciftci, N. S. Efficiency of bulk-heterojunction organic solar cells. *Progress in Polymer Science* 2013, 38, 1929-1940.
10. Hardin, B. E.; Snaith, H. J.; McGehee, M. D. The renaissance of dye-sensitized solar cells. *Nature Photonics* 2012, 6, 162-169.
11. Gao, P.; Gratzel, M.; Nazeeruddin, M. K. Organohalide lead perovskites for photovoltaic applications. *Energy & Environmental Science* 2014, 7, 2448-2463.
12. Kisslinger, R.; Hua, W.; Shankar, K. Bulk Heterojunction Solar Cells Based on Blends of Conjugated Polymers with II–VI and IV–VI Inorganic Semiconductor Quantum Dots. *Polymers* 2017, 9, 35.
13. Espinosa, N.; Hosel, M.; Angmo, D.; Krebs, F. C. Solar cells with one-day energy payback for the factories of the future. *Energy & Environmental Science* 2012, 5, 5117-5132.
14. Gong, J.; Darling, S. B.; You, F. Perovskite photovoltaics: life-cycle assessment of energy and environmental impacts. *Energy & Environmental Science* 2015, 8, 1953-1968.
15. Yin, W.-J.; Shi, T.; Yan, Y. Unique Properties of Halide Perovskites as Possible Origins of the Superior Solar Cell Performance. *Advanced Materials* 2014, 26, 4653-4658.
16. Kojima, A.; Teshima, K.; Shirai, Y.; Miyasaka, T. Novel Photoelectrochemical Cell with Mesoscopic Electrodes Sensitized by Lead-halide Compounds (5). *Meeting Abstracts* 2007, MA2007-02, 352.
17. Kojima, A.; Teshima, K.; Shirai, Y.; Miyasaka, T. Organometal Halide Perovskites as Visible-Light Sensitizers for Photovoltaic Cells. *Journal of the American Chemical Society* 2009, 131, 6050-6051.
18. Lee, M. M.; Teuscher, J.; Miyasaka, T.; Murakami, T. N.; Snaith, H. J. Efficient Hybrid Solar Cells Based on Meso-Superstructured Organometal Halide Perovskites. *Science* 2012, 338, 643-647.
19. Polman, A.; Knight, M.; Garnett, E. C.; Ehrler, B.; Sinke, W. C. Photovoltaic materials: Present efficiencies and future challenges. *Science* 2016, 352, aad4424.
20. Jeon, N. J.; Na, H.; Jung, E. H.; Yang, T.-Y.; Lee, Y. G.; Kim, G.; Shin, H.-W.; Il Seok, S.; Lee, J.; Seo, J. A fluorene-terminated hole-transporting material for highly efficient and stable perovskite solar cells. *Nature Energy* 2018, 3, 682-689.

21. (NREL), N. R. E. L. Efficiency chart of best research-cell efficiencies https://www.nrel.gov/pv/assets/pdfs/best-research-cell-efficiencies.20200128.pdf.
22. Kim, H.-S.; Lee, C.-R.; Im, J.-H.; Lee, K.-B.; Moehl, T.; Marchioro, A.; Moon, S.-J.; Humphry-Baker, R.; Yum, J.-H.; Moser, J. E.; Grätzel, M.; Park, N.-G. Lead Iodide Perovskite Sensitized All-Solid-State Submicron Thin Film Mesoscopic Solar Cell with Efficiency Exceeding 9%. *Scientific Reports* 2012, 2, 591.
23. Kojima, A.; Teshima, K.; Shirai, Y.; Miyasaka, T. Organometal Halide Perovskites as Visible-Light Sensitizers for Photovoltaic Cells. *J. Am. Chem. Soc.* 2009, 131, 6050-+.
24. Liang, K. N.; Mitzi, D. B.; Prikas, M. T. Synthesis and characterization of organic-inorganic perovskite thin films prepared using a versatile two-step dipping technique. *Chemistry of Materials* 1998, 10, 403-411.
25. Burschka, J.; Pellet, N.; Moon, S.-J.; Humphry-Baker, R.; Gao, P.; Nazeeruddin, M. K.; Gratzel, M. Sequential deposition as a route to high-performance perovskite-sensitized solar cells. *Nature* 2013, 499, 316-319.
26. Liu, M.; Johnston, M. B.; Snaith, H. J. Efficient planar heterojunction perovskite solar cells by vapour deposition. *Nature* 2013, 501, 395-398.
27. Chen, C. W.; Kang, H. W.; Hsiao, S. Y.; Yang, P. F.; Chiang, K. M.; Lin, H. W. Efficient and Uniform Planar-Type Perovskite Solar Cells by Simple Sequential Vacuum Deposition. *Advanced Materials* 2014, 26, 6647-6652.
28. Bhachu, D. S.; Scanlon, D. O.; Saban, E. J.; Bronstein, H.; Parkin, I. P.; Carmalt, C. J.; Palgrave, R. G. Scalable route to CH3NH3PbI3 perovskite thin films by aerosol assisted chemical vapour deposition. *J. Mater. Chem. A* 2015, 3, 9071-9073.
29. Wei, Z. H.; Chen, H. N.; Yan, K. Y.; Yang, S. H. Inkjet Printing and Instant Chemical Transformation of a CH3NH3PbI3/Nanocarbon Electrode and Interface for Planar Perovskite Solar Cells. *Angew. Chem.-Int. Edit.* 2014, 53, 13239-13243.
30. Li, S. G.; Jiang, K. J.; Su, M. J.; Cui, X. P.; Huang, J. H.; Zhang, Q. Q.; Zhou, X. Q.; Yang, L. M.; Song, Y. L. Inkjet printing of CH3NH3PbI3 on a mesoscopic TiO2 film for highly efficient perovskite solar cells. *J. Mater. Chem. A* 2015, 3, 9092-9097.
31. Barrows, A. T.; Pearson, A. J.; Kwak, C. K.; Dunbar, A. D. F.; Buckley, A. R.; Lidzey, D. G. Efficient planar heterojunction mixed-halide perovskite solar cells deposited via spray-deposition. *Energy & Environmental Science* 2014, 7, 2944-2950.
32. Boopathi, K. M.; Ramesh, M.; Perumal, P.; Huang, Y. C.; Tsao, C. S.; Chen, Y. F.; Lee, C. H.; Chu, C. W. Preparation of metal halide perovskite solar cells through a liquid droplet assisted method. *J. Mater. Chem. A* 2015, 3, 9257-9263.
33. Hwang, K.; Jung, Y. S.; Heo, Y. J.; Scholes, F. H.; Watkins, S. E.; Subbiah, J.; Jones, D. J.; Kim, D. Y.; Vak, D. Toward Large Scale Roll-to-Roll Production of Fully Printed Perovskite Solar Cells. *Advanced Materials* 2015, 27, 1241-1247.
34. Malinkiewicz, O.; Yella, A.; Lee, Y. H.; Espallargas, G. M.; Graetzel, M.; Nazeeruddin, M. K.; Bolink, H. J. Perovskite solar cells employing organic charge-transport layers. *Nat Photon* 2014, 8, 128-132.
35. Subbiah, A. S.; Halder, A.; Ghosh, S.; Mahuli, N.; Hodes, G.; Sarkar, S. K. Inorganic Hole Conducting Layers for Perovskite-Based Solar Cells. *The Journal of Physical Chemistry Letters* 2014, 5, 1748-1753.
36. You, J.; Hong, Z.; Yang, Y.; Chen, Q.; Cai, M.; Song, T.-B.; Chen, C.-C.; Lu, S.; Liu, Y.; Zhou, H.; Yang, Y. Low-Temperature Solution-Processed Perovskite Solar Cells with High Efficiency and Flexibility. *ACS Nano* 2014, 8, 1674-1680.
37. Zhu, Z.; Bai, Y.; Zhang, T.; Liu, Z.; Long, X.; Wei, Z.; Wang, Z.; Zhang, L.; Wang, J.; Yan, F.; Yang, S. High-Performance Hole-Extraction Layer of Sol–Gel-Processed NiO Nanocrystals for Inverted Planar Perovskite Solar Cells. *Angewandte Chemie International Edition* 2014, 53, 12571-12575.

38. Hou, Y.; Chen, W.; Baran, D.; Stubhan, T.; Luechinger, N. A.; Hartmeier, B.; Richter, M.; Min, J.; Chen, S.; Quiroz, C. O. R.; Li, N.; Zhang, H.; Heumueller, T.; Matt, G. J.; Osvet, A.; Forberich, K.; Zhang, Z.-G.; Li, Y.; Winter, B.; Schweizer, P.; Spiecker, E.; Brabec, C. J. Overcoming the Interface Losses in Planar Heterojunction Perovskite-Based Solar Cells. *Advanced Materials* 2016, 28, 5112-5120.
39. Zuo, C.; Ding, L. Solution-Processed Cu2O and CuO as Hole Transport Materials for Efficient Perovskite Solar Cells. *Small* 2015, 11, 5528-5532.
40. Bhande, S. S.; Ambade, R. B.; Shinde, D. V.; Ambade, S. B.; Patil, S. A.; Naushad, M.; Mane, R. S.; Alothman, Z. A.; Lee, S.-H.; Han, S.-H. Improved Photoelectrochemical Cell Performance of Tin Oxide with Functionalized Multiwalled Carbon Nanotubes–Cadmium Selenide Sensitizer. *ACS Applied Materials & Interfaces* 2015, 7, 25094-25104.
41. Guarnera, S.; Abate, A.; Zhang, W.; Foster, J. M.; Richardson, G.; Petrozza, A.; Snaith, H. J. Improving the Long-Term Stability of Perovskite Solar Cells with a Porous Al2O3 Buffer Layer. *The Journal of Physical Chemistry Letters* 2015, 6, 432-437.
42. Ke, W.; Fang, G.; Wan, J.; Tao, H.; Liu, Q.; Xiong, L.; Qin, P.; Wang, J.; Lei, H.; Yang, G.; Qin, M.; Zhao, X.; Yan, Y. Efficient hole-blocking layer-free planar halide perovskite thin-film solar cells. *Nature Communications* 2015, 6, 6700.
43. Chen, C.-M.; Lin, Z.-K.; Huang, W.-J.; Yang, S.-H. WO3 Nanoparticles or Nanorods Incorporating Cs2CO3/PCBM Buffer Bilayer as Carriers Transporting Materials for Perovskite Solar Cells. *Nanoscale Research Letters* 2016, 11, 464.
44. Hwang, I.; Yong, K. Novel CdS Hole-Blocking Layer for Photostable Perovskite Solar Cells. *ACS Applied Materials & Interfaces* 2016, 8, 4226-4232.
45. Jiang, Q.; Zhang, L.; Wang, H.; Yang, X.; Meng, J.; Liu, H.; Yin, Z.; Wu, J.; Zhang, X.; You, J. Enhanced electron extraction using SnO2 for high-efficiency planar-structure HC(NH2)2PbI3-based perovskite solar cells. *Nature Energy* 2016, 2, 16177.
46. Yeom, E. J.; Shin, S. S.; Yang, W. S.; Lee, S. J.; Yin, W.; Kim, D.; Noh, J. H.; Ahn, T. K.; Seok, S. I. Controllable synthesis of single crystalline Sn-based oxides and their application in perovskite solar cells. *J. Mater. Chem. A* 2017.
47. Mahmood, K.; Swain, B. S.; Kirmani, A. R.; Amassian, A. Highly efficient perovskite solar cells based on a nanostructured WO3-TiO2 core-shell electron transporting material. *J. Mater. Chem. A* 2015, 3, 9051-9057.
48. Lim, E. L.; Yap, C. C.; Jumali, M. H. H.; Teridi, M. A. M.; Teh, C. H. J. N.-M. L. A Mini Review: Can Graphene Be a Novel Material for Perovskite Solar Cell Applications? 2017, 10, 27.
49. Miyata, A.; Mitioglu, A.; Plochocka, P.; Portugall, O.; Wang, J. T.-W.; Stranks, S. D.; Snaith, H. J.; Nicholas, R. J. Direct measurement of the exciton binding energy and effective masses for charge carriers in organic–inorganic tri-halide perovskites. *Nature Physics* 2015, 11, 582.
50. Galkowski, K.; Mitioglu, A.; Miyata, A.; Plochocka, P.; Portugall, O.; Eperon, G. E.; Wang, J. T.-W.; Stergiopoulos, T.; Stranks, S. D.; Snaith, H. J.; Nicholas, R. J. Determination of the exciton binding energy and effective masses for methylammonium and formamidinium lead tri-halide perovskite semiconductors. *Energy & Environmental Science* 2016, 9, 962-970.
51. Park, N.-G.; Miyasaka, T.; Grätzel, M. *Organic-inorganic halide perovskite photovoltaics*. Springer: 2016.
52. Mora-Seró, I. How Do Perovskite Solar Cells Work? *Joule* 2018, 2, 585-587.
53. Courtier, N. E.; Cave, J. M.; Foster, J. M.; Walker, A. B.; Richardson, G. How transport layer properties affect perovskite solar cell performance: insights from a coupled charge transport/ion migration model. *Energy & Environmental Science* 2019, 12, 396-409.
54. Khadka, D. B.; Shirai, Y.; Yanagida, M.; Miyano, K. Degradation of encapsulated perovskite solar cells driven by deep trap states and interfacial deterioration. *Journal of Materials Chemistry C* 2018, 6, 162-170.

55. Alnuaimi, A.; Almansouri, I.; Nayfeh, A. Performance of planar heterojunction perovskite solar cells under light concentration. 2016, 6, 115012.
56. Walukiewicz, W.; Rey-Stolle, I.; Han, G.; Jaquez, M.; Broberg, D.; Xie, W.; Sherburne, M.; Mathews, N.; Asta, M. Bistable Amphoteric Native Defect Model of Perovskite Photovoltaics. *The Journal of Physical Chemistry Letters* 2018, 9, 3878-3885.
57. Aldosari, M.; Grigoriu, L.; Sohrabpoor, H.; Gorji, N. E. Modeling of depletion width variation over time in thin film photovoltaics. 2016, 30, 1650044.
58. Tang, H.; Prasad, K.; Sanjinès, R.; Schmid, P. E.; Lévy, F. Electrical and optical properties of TiO2 anatase thin films. 1994, 75, 2042-2047.
59. Xiong, Y.; Liu, T.; Jiang, X.; Rong, Y.; Han, H. J. S. C. M. N-type metal-oxide electron transport layer for mesoscopic perovskite solar cells. 2016, 59, 757-768.
60. Dymshits, A.; Henning, A.; Segev, G.; Rosenwaks, Y.; Etgar, L. The electronic structure of metal oxide/organo metal halide perovskite junctions in perovskite based solar cells. *Scientific Reports* 2015, 5, 8704.
61. Singh, A. P.; Kumari, S.; Shrivastav, R.; Dass, S.; Satsangi, V. R. Iron doped nanostructured TiO2 for photoelectrochemical generation of hydrogen. *International Journal of Hydrogen Energy* 2008, 33, 5363-5368.
62. Sellers, M. C. K.; Seebauer, E. G. Measurement method for carrier concentration in TiO2 via the Mott–Schottky approach. *Thin Solid Films* 2011, 519, 2103-2110.
63. Marques, F. C.; Jasieniak, J. J. Ionization potential and electron attenuation length of titanium dioxide deposited by atomic layer deposition determined by photoelectron spectroscopy in air. *Applied Surface Science* 2017, 422, 504-508.
64. Wang, Q.; Shao, Y.; Xie, H.; Lyu, L.; Liu, X.; Gao, Y.; Huang, J. Qualifying composition dependent p and n self-doping in CH3NH3PbI3. 2014, 105, 163508.
65. Wang, R.; Zhuo, M.-P.; Li, J.; Zhai, T.; Yang, J.; Fu, K.; Liao, L.-S.; Liu, L.; Duhm, S. Surface CH3NH3+ to CH3+ Ratio Impacts the Work Function of Solution-Processed and Vacuum-Sublimed CH3NH3PbI3 Thin Films. 2019, 6, 1801827.
66. Peng, J.; Chen, Y.; Zheng, K.; Pullerits, T.; Liang, Z. Insights into charge carrier dynamics in organo-metal halide perovskites: from neat films to solar cells. *Chemical Society Reviews* 2017, 46, 5714-5729.
67. Endres, J.; Egger, D. A.; Kulbak, M.; Kerner, R. A.; Zhao, L.; Silver, S. H.; Hodes, G.; Rand, B. P.; Cahen, D.; Kronik, L.; Kahn, A. Valence and Conduction Band Densities of States of Metal Halide Perovskites: A Combined Experimental–Theoretical Study. *The Journal of Physical Chemistry Letters* 2016, 7, 2722-2729.
68. Oga, H.; Saeki, A.; Ogomi, Y.; Hayase, S.; Seki, S. Improved Understanding of the Electronic and Energetic Landscapes of Perovskite Solar Cells: High Local Charge Carrier Mobility, Reduced Recombination, and Extremely Shallow Traps. *Journal of the American Chemical Society* 2014, 136, 13818-13825.
69. Schulz, P.; Tiepelt, J. O.; Christians, J. A.; Levine, I.; Edri, E.; Sanehira, E. M.; Hodes, G.; Cahen, D.; Kahn, A. High-Work-Function Molybdenum Oxide Hole Extraction Contacts in Hybrid Organic–Inorganic Perovskite Solar Cells. *ACS Applied Materials & Interfaces* 2016, 8, 31491-31499.
70. An, Y.; Shang, A.; Cao, G.; Wu, S.; Ma, D.; Li, X. Perovskite Solar Cells: Optoelectronic Simulation and Optimization. 2018, 2, 1800126.
71. Snaith, H. J.; Grätzel, M. Enhanced charge mobility in a molecular hole transporter via addition of redox inactive ionic dopant: Implication to dye-sensitized solar cells. 2006, 89, 262114.
72. Snaith, H. J.; Grätzel, M. Light-Enhanced Charge Mobility in a Molecular Hole Transporter. *Physical Review Letters* 2007, 98, 177402.

73. Park, N.-G.; Segawa, H. Research Direction toward Theoretical Efficiency in Perovskite Solar Cells. *ACS Photonics* 2018, 5, 2970-2977.
74. Stranks, S. D.; Eperon, G. E.; Grancini, G.; Menelaou, C.; Alcocer, M. J. P.; Leijtens, T.; Herz, L. M.; Petrozza, A.; Snaith, H. J. Electron-Hole Diffusion Lengths Exceeding 1 Micrometer in an Organometal Trihalide Perovskite Absorber. *Science* 2013, 342, 341-344.
75. Herz, L. M. Charge-Carrier Mobilities in Metal Halide Perovskites: Fundamental Mechanisms and Limits. *ACS Energy Letters* 2017, 2, 1539-1548.
76. Al-Dainy, G. A.; Bourdo, S. E.; Saini, V.; Berry, B. C.; Biris, A. S. Hybrid Perovskite Photovoltaic Devices: Properties, Architecture and Fabrication Methods. *Energy Technology* 2016.
77. Nelson, J. Continuous-time random-walk model of electron transport in nanocrystalline ${\mathrm{TiO}}_{2}$ electrodes. *Phys. Rev. B* 1999, 59, 15374-15380.
78. van de Lagemaat, J.; Frank, A. J. Nonthermalized Electron Transport in Dye-Sensitized Nanocrystalline TiO2 Films: Transient Photocurrent and Random-Walk Modeling Studies. *The Journal of Physical Chemistry B* 2001, 105, 11194-11205.
79. Zhu, K.; Neale, N. R.; Miedaner, A.; Frank, A. J. Enhanced charge-collection efficiencies and light scattering in dye-sensitized solar cells using oriented TiO2 nanotubes arrays. *Nano Lett.* 2007, 7, 69-74.
80. Feng, X. J.; Zhu, K.; Frank, A. J.; Grimes, C. A.; Mallouk, T. E. Rapid Charge Transport in Dye-Sensitized Solar Cells Made from Vertically Aligned Single-Crystal Rutile TiO2 Nanowires. *Angew. Chem.-Int. Edit.* 2012, 51, 2727-2730.
81. He, D. Q.; Sheng, X.; Yang, J.; Chen, L. P.; Zhu, K.; Feng, X. J. 10(1)over-bar0 Oriented Multichannel ZnO Nanowire Arrays with Enhanced Optoelectronic Device Performance. *Journal of the American Chemical Society* 2014, 136, 16772-16775.
82. Sheng, X.; He, D. Q.; Yang, J.; Zhu, K.; Feng, X. J. Oriented Assembled TiO2 Hierarchical Nanowire Arrays with Fast Electron Transport Properties. *Nano Lett.* 2014, 14, 1848-1852.
83. Zhu, K.; Cong, S.; Lu, Z.; Lou, Y.; He, L.; Li, J.; Ding, J.; Yuang, N.; Rümmeli, M. H.; Zou, G. Enhanced perovskite solar cell performance via defect passivation with ethylamine alcohol chlorides additive. *Journal of Power Sources* 2019, 428, 82-87.
84. Zhu, Y.; Wang, S.; Ma, R.; Wang, C. The improvement of inverted perovskite solar cells by the introduction of CTAB into PEDOT:PSS. *Solar Energy* 2019, 188, 28-34.
85. Zhou, X.; Hu, M.; Liu, C.; Zhang, L.; Zhong, X.; Li, X.; Tian, Y.; Cheng, C.; Xu, B. Synergistic effects of multiple functional ionic liquid-treated PEDOT:PSS and less-ion-defects S-acetylthiocholine chloride-passivated perovskite surface enabling stable and hysteresis-free inverted perovskite solar cells with conversion efficiency over 20%. *Nano Energy* 2019, 63, 103866.
86. Meng, L.; You, J.; Guo, T.-F.; Yang, Y. Recent Advances in the Inverted Planar Structure of Perovskite Solar Cells. *Accounts of Chemical Research* 2016, 49, 155-165.
87. Sun, H.; Hou, X.; Wei, Q.; Liu, H.; Yang, K.; Wang, W.; An, Q.; Rong, Y. Low-temperature solution-processed p-type vanadium oxide for perovskite solar cells. *Chemical Communications* 2016, 52, 8099-8102.
88. Zhang, H.; Cheng, J.; Lin, F.; He, H.; Mao, J.; Wong, K. S.; Jen, A. K. Y.; Choy, W. C. H. Pinhole-Free and Surface-Nanostructured NiOx Film by Room-Temperature Solution Process for High-Performance Flexible Perovskite Solar Cells with Good Stability and Reproducibility. *ACS Nano* 2016, 10, 1503-1511.
89. Rao, H.; Ye, S.; Sun, W.; Yan, W.; Li, Y.; Peng, H.; Liu, Z.; Bian, Z.; Li, Y.; Huang, C. A 19.0% efficiency achieved in CuOx-based inverted CH3NH3PbI3−xClx solar cells by an effective Cl doping method. *Nano Energy* 2016, 27, 51-57.
90. Yu, W.; Li, F.; Wang, H.; Alarousu, E.; Chen, Y.; Lin, B.; Wang, L.; Hedhili, M. N.; Li, Y.; Wu, K.; Wang, X.; Mohammed, O. F.; Wu, T. Ultrathin Cu2O as an efficient inorganic hole transporting material for perovskite solar cells. *Nanoscale* 2016, 8, 6173-6179.

91. Xie, F.; Chen, C.-C.; Wu, Y.; Li, X.; Cai, M.; Liu, X.; Yang, X.; Han, L. Vertical recrystallization for highly efficient and stable formamidinium-based inverted-structure perovskite solar cells. *Energy & Environmental Science* 2017, 10, 1942-1949.
92. Qin, P.-L.; Lei, H.-W.; Zheng, X.-L.; Liu, Q.; Tao, H.; Yang, G.; Ke, W.-J.; Xiong, L.-B.; Qin, M.-C.; Zhao, X.-Z.; Fang, G.-J. Copper-Doped Chromium Oxide Hole-Transporting Layer for Perovskite Solar Cells: Interface Engineering and Performance Improvement. 2016, 3, 1500799.
93. Shalan, A. E.; Oshikiri, T.; Narra, S.; Elshanawany, M. M.; Ueno, K.; Wu, H.-P.; Nakamura, K.; Shi, X.; Diau, E. W.-G.; Misawa, H. Cobalt Oxide (CoOx) as an Efficient Hole-Extracting Layer for High-Performance Inverted Planar Perovskite Solar Cells. *ACS Applied Materials & Interfaces* 2016, 8, 33592-33600.
94. Green, M. A.; Emery, K.; Hishikawa, Y.; Warta, W.; Dunlop, E. D.; Levi, D. H.; Ho-Baillie, A. W. Y. Solar cell efficiency tables (version 49). *Progress in Photovoltaics: Research and Applications* 2017, 25, 3-13.
95. Edri, E.; Kirmayer, S.; Henning, A.; Mukhopadhyay, S.; Gartsman, K.; Rosenwaks, Y.; Hodes, G.; Cahen, D. Why Lead Methylammonium Tri-Iodide Perovskite-Based Solar Cells Require a Mesoporous Electron Transporting Scaffold (but Not Necessarily a Hole Conductor). *Nano Lett.* 2014, 14, 1000-1004.
96. Eperon, G. E.; Stranks, S. D.; Menelaou, C.; Johnston, M. B.; Herz, L. M.; Snaith, H. J. Formamidinium lead trihalide: a broadly tunable perovskite for efficient planar heterojunction solar cells. *Energy & Environmental Science* 2014, 7, 982-988.
97. Xing, G.; Mathews, N.; Sun, S.; Lim, S. S.; Lam, Y. M.; Graetzel, M.; Mhaisalkar, S.; Sum, T. C. Long-Range Balanced Electron- and Hole-Transport Lengths in Organic-Inorganic CH3NH3PbI3. *Science* 2013, 342, 344-347.
98. Polman, A.; Atwater, H. A. Photonic design principles for ultrahigh-efficiency photovoltaics. *Nature Materials* 2012, 11, 174-177.
99. Cui, Y.; van Dam, D.; Mann, S. A.; van Hoof, N. J. J.; van Veldhoven, P. J.; Garnett, E. C.; Bakkers, E. P. A. M.; Haverkort, J. E. M. Boosting Solar Cell Photovoltage via Nanophotonic Engineering. *Nano Lett.* 2016, 16, 6467-6471.
100. Lin, J.; Liu, K.; Chen, X. F. Synthesis of Periodically Structured Titania Nanotube Films and Their Potential for Photonic Applications. *Small* 2011, 7, 1784-1789.
101. Yip, C. T.; Huang, H. T.; Zhou, L. M.; Xie, K. Y.; Wang, Y.; Feng, T. H.; Li, J. S.; Tam, W. Y. Direct and Seamless Coupling of TiO2 Nanotube Photonic Crystal to Dye-Sensitized Solar Cell: A Single-Step Approach. *Advanced Materials* 2011, 23, 5624-+.
102. Guo, M.; Xie, K. Y.; Lin, J.; Yong, Z. H.; Yip, C. T.; Zhou, L. M.; Wang, Y.; Huang, H. T. Design and coupling of multifunctional TiO2 nanotube photonic crystal to nanocrystalline titania layer as semi-transparent photoanode for dye-sensitized solar cell. *Energy & Environmental Science* 2012, 5, 9881-9888.
103. Zhang, X.; Han, F.; Shi, B.; Farsinezhad, S.; Dechaine, G. P.; Shankar, K. Photocatalytic Conversion of Diluted CO2 into Light Hydrocarbons Using Periodically Modulated Multiwalled Nanotube Arrays. *Angewandte Chemie International Edition* 2012, n/a-n/a.
104. Muskens, O. L.; Diedenhofen, S. L.; Kaas, B. C.; Algra, R. E.; Bakkers, E. P. A. M.; Gómez Rivas, J.; Lagendijk, A. Large Photonic Strength of Highly Tunable Resonant Nanowire Materials. *Nano Lett.* 2009, 9, 930-934.
105. Boppella, R.; Mohammadpour, A.; Illa, S.; Farsinezhad, S.; Basak, P.; Shankar, K.; Manorama, S. V. Hierarchical rutile TiO 2 aggregates: A high photonic strength material for optical and optoelectronic devices. *Acta Materialia* 2016, 119, 92-103.
106. Grandidier, J.; Callahan, D. M.; Munday, J. N.; Atwater, H. A. Light Absorption Enhancement in Thin-Film Solar Cells Using Whispering Gallery Modes in Dielectric Nanospheres. *Advanced Materials* 2011, 23, 1272-1276.

107. Mohammadpour, A.; Waghmare, P. R.; Mitra, S. K.; Shankar, K. Anodic Growth of Large-Diameter Multipodal TiO2 Nanotubes. *Acs Nano* 2010, 4, 7421-7430.
108. Liu, D.; Kelly, T. L. Perovskite solar cells with a planar heterojunction structure prepared using room-temperature solution processing techniques. *Nat. Photonics* 2014, 8, 133-138.
109. Yeom, E. J.; Shin, S. S.; Yang, W. S.; Lee, S. J.; Yin, W.; Kim, D.; Noh, J. H.; Ahn, T. K.; Seok, S. I. Controllable synthesis of single crystalline Sn-based oxides and their application in perovskite solar cells. *J. Mater. Chem. A* 2017, 5, 79-86.
110. Ke, W.; Fang, G.; Liu, Q.; Xiong, L.; Qin, P.; Tao, H.; Wang, J.; Lei, H.; Li, B.; Wan, J.; Yang, G.; Yan, Y. Low-Temperature Solution-Processed Tin Oxide as an Alternative Electron Transporting Layer for Efficient Perovskite Solar Cells. *Journal of the American Chemical Society* 2015, 137, 6730-6733.
111. Feng, X.; Zhu, K.; Frank, A. J.; Grimes, C. A.; Mallouk, T. E. Rapid Charge Transport in Dye-Sensitized Solar Cells Made from Vertically Aligned Single-Crystal Rutile TiO2 Nanowires. *Angewandte Chemie International Edition* 2012, 51, 2727-2730.
112. Law, M.; Greene, L. E.; Johnson, J. C.; Saykally, R.; Yang, P. Nanowire dye-sensitized solar cells. *Nat Mater* 2005, 4, 455-459.
113. Kim, H.-S.; Lee, J.-W.; Yantara, N.; Boix, P. P.; Kulkarni, S. A.; Mhaisalkar, S.; Grätzel, M.; Park, N.-G. High Efficiency Solid-State Sensitized Solar Cell-Based on Submicrometer Rutile TiO2 Nanorod and CH3NH3PbI3 Perovskite Sensitizer. *Nano Lett.* 2013, 13, 2412-2417.
114. Gu, Z.; Chen, F.; Zhang, X.; Liu, Y.; Fan, C.; Wu, G.; Li, H.; Chen, H. Novel planar heterostructure perovskite solar cells with CdS nanorods array as electron transport layer. *Solar Energy Materials and Solar Cells* 2015, 140, 396-404.
115. Liu, H.; Huang, Z.; Wei, S.; Zheng, L.; Xiao, L.; Gong, Q. Nano-structured electron transporting materials for perovskite solar cells. *Nanoscale* 2016, 8, 6209-6221.
116. Mahmood, K.; Swain, B. S.; Amassian, A. 16.1% Efficient Hysteresis-Free Mesostructured Perovskite Solar Cells Based on Synergistically Improved ZnO Nanorod Arrays. *Advanced Energy Materials* 2015, 5, 1500568-n/a.
117. Qiu, J.; Qiu, Y.; Yan, K.; Zhong, M.; Mu, C.; Yan, H.; Yang, S. All-solid-state hybrid solar cells based on a new organometal halide perovskite sensitizer and one-dimensional TiO2 nanowire arrays. *Nanoscale* 2013, 5, 3245-3248.
118. Jiang, Q.; Sheng, X.; Li, Y.; Feng, X.; Xu, T. Rutile TiO2 nanowire-based perovskite solar cells. *Chemical Communications* 2014, 50, 14720-14723.
119. O'Regan, B. C.; Durrant, J. R.; Sommeling, P. M.; Bakker, N. J. Influence of the TiCl4 Treatment on Nanocrystalline TiO2 Films in Dye-Sensitized Solar Cells. 2. Charge Density, Band Edge Shifts, and Quantification of Recombination Losses at Short Circuit. *The Journal of Physical Chemistry C* 2007, 111, 14001-14010.
120. Bandara, J.; Shankar, K.; Basham, J.; Wietasch, H.; Paulose, M.; Varghese, O. K.; Grimes, C. A.; Thelakkat, M. Integration of TiO2 nanotube arrays into solid-state dye-sensitized solar cells. *Eur. Phys. J. Appl. Phys.* 2011, 53, 20601.
121. Meen, T.-H.; Jhuo, Y.-T.; Chao, S.-M.; Lin, N.-Y.; Ji, L.-W.; Tsai, J.-K.; Wu, T.-C.; Chen, W.-R.; Water, W.; Huang, C.-J. Effect of TiO2 nanotubes with TiCl4 treatment on the photoelectrode of dye-sensitized solar cells. *Nanoscale Research Letters* 2012, 7, 579.
122. Shockley, W.; Queisser, H. J. Detailed Balance Limit of Efficiency of p-n Junction Solar Cells. *Journal of Applied Physics* 1961, 32, 510-519.
123. Yang, B.; Dyck, O.; Poplawsky, J.; Keum, J.; Puretzky, A.; Das, S.; Ivanov, I.; Rouleau, C.; Duscher, G.; Geohegan, D.; Xiao, K. Perovskite Solar Cells with Near 100% Internal Quantum Efficiency Based on Large Single Crystalline Grains and Vertical Bulk Heterojunctions. *Journal of the American Chemical Society* 2015, 137, 9210-9213.

124. Ball, J. M.; Lee, M. M.; Hey, A.; Snaith, H. J. Low-temperature processed meso-superstructured to thin-film perovskite solar cells. *Energy & Environmental Science* 2013, 6, 1739-1743.
125. Chaudhary, D. K.; Kumar, P.; Kumar, L. Evolution in surface coverage of CH 3 NH 3 PbI 3− X Cl X via heat assisted solvent vapour treatment and their effects on photovoltaic performance of devices. *RSC Advances* 2016, 6, 94731-94738.
126. Tétreault, N.; Grätzel, M. Novel nanostructures for next generation dye-sensitized solar cells. *Energy & Environmental Science* 2012, 5, 8506-8516.
127. Fakharuddin, A.; Di Giacomo, F.; Ahmed, I.; Wali, Q.; Brown, T. M.; Jose, R. Role of morphology and crystallinity of nanorod and planar electron transport layers on the performance and long term durability of perovskite solar cells. *Journal of Power Sources* 2015, 283, 61-67.
128. Cui, Y.; He, X.; Zhu, M.; Li, X. Preparation of anatase TiO2 microspheres with high exposure (001) facets as the light-scattering layer for improving performance of dye-sensitized solar cells. *Journal of Alloys and Compounds* 2017, 694, 568-573.
129. Yu, H.; Pan, J.; Bai, Y.; Zong, X.; Li, X.; Wang, L. Hydrothermal Synthesis of a Crystalline Rutile TiO2 Nanorod Based Network for Efficient Dye-Sensitized Solar Cells. *Chemistry-A European Journal* 2013, 19, 13569-13574.
130. Hore, S.; Vetter, C.; Kern, R.; Smit, H.; Hinsch, A. Influence of scattering layers on efficiency of dye-sensitized solar cells. *Solar Energy Materials and Solar Cells* 2006, 90, 1176-1188.
131. Zhang, H.; Yu, H.; Han, Y.; Liu, P.; Zhang, S.; Wang, P.; Cheng, Y.; Zhao, H. Rutile TiO2 microspheres with exposed nano-acicular single crystals for dye-sensitized solar cells. *Nano Res.* 2011, 4, 938-947.
132. Peng, J.-D.; Lee, C.-P.; Velayutham, D.; Suryanarayanan, V.; Ho, K.-C. Dye-sensitized solar cells containing mesoporous TiO2 spheres as photoanodes and methyl sulfate anion based biionic liquid electrolytes. *J. Mater. Chem. A* 2015, 3, 6383-6391.
133. Huo, J.; Hu, Y.; Jiang, H.; Huang, W.; Li, C. SnO2 nanorod@TiO2 hybrid material for dye-sensitized solar cells. *J. Mater. Chem. A* 2014, 2, 8266-8272.
134. Varghese, O. K.; Paulose, M.; Grimes, C. A. Long vertically aligned titania nanotubes on transparent conducting oxide for highly efficient solar cells. *Nat Nano* 2009, 4, 592-597.
135. Löper, P.; Stuckelberger, M.; Niesen, B.; Werner, J.; Filipič, M.; Moon, S.-J.; Yum, J.-H.; Topič, M.; De Wolf, S.; Ballif, C. Complex Refractive Index Spectra of CH3NH3PbI3 Perovskite Thin Films Determined by Spectroscopic Ellipsometry and Spectrophotometry. *The Journal of Physical Chemistry Letters* 2015, 6, 66-71.
136. Wang, X.; Li, Z.; Xu, W.; Kulkarni, S. A.; Batabyal, S. K.; Zhang, S.; Cao, A.; Wong, L. H. TiO2 nanotube arrays based flexible perovskite solar cells with transparent carbon nanotube electrode. *Nano Energy* 2015, 11, 728-735.
137. Mohammadpour, A.; Farsinezhad, S.; Wiltshire, B. D.; Shankar, K. Majority carrier transport in single crystal rutile nanowire arrays. *physica status solidi (RRL) – Rapid Research Letters* 2014, n/a-n/a.
138. Mohammadpour, A.; Wiltshire, B. D.; Zhang, Y.; Farsinezhad, S.; Askar, A. M.; Kisslinger, R.; Ren, Y.; Kar, P.; Shankar, K. 100-fold improvement in carrier drift mobilities in alkanephosphonate-passivated monocrystalline TiO_2 nanowire arrays. *Nanotechnology* 2017, 28, 144001.
139. Yan, W.; Li, Y.; Ye, S.; Li, Y.; Rao, H.; Liu, Z.; Wang, S.; Bian, Z.; Huang, C. Increasing open circuit voltage by adjusting work function of hole-transporting materials in perovskite solar cells. *Nano Res.* 2016, 9, 1600-1608.
140. Suarez, B.; Gonzalez-Pedro, V.; Ripolles, T. S.; Sanchez, R. S.; Otero, L.; Mora-Sero, I. Recombination study of combined halides (Cl, Br, I) perovskite solar cells. *The journal of physical chemistry letters* 2014, 5, 1628-1635.

141. Mora-Seró, I.; Giménez, S.; Fabregat-Santiago, F.; Azaceta, E.; Tena-Zaera, R.; Bisquert, J. Modeling and characterization of extremely thin absorber (eta) solar cells based on ZnO nanowires. *Phys. Chem. Chem. Phys.* 2011, 13, 7162-7169.
142. Mali, S. S.; Shim, C. S.; Park, H. K.; Heo, J.; Patil, P. S.; Hong, C. K. Ultrathin Atomic Layer Deposited TiO2 for Surface Passivation of Hydrothermally Grown 1D TiO2 Nanorod Arrays for Efficient Solid-State Perovskite Solar Cells. *Chemistry of Materials* 2015, 27, 1541-1551.
143. Lv, M.; Dong, X.; Fang, X.; Lin, B.; Zhang, S.; Xu, X.; Ding, J.; Yuan, N. Improved photovoltaic performance in perovskite solar cells based on CH3NH3PbI3 films fabricated under controlled relative humidity. *RSC Advances* 2015, 5, 93957-93963.
144. Mora-Sero, I.; Gimenez, S.; Fabregat-Santiago, F.; Azaceta, E.; Tena-Zaera, R.; Bisquert, J. Modeling and characterization of extremely thin absorber (eta) solar cells based on ZnO nanowires. *Physical Chemistry Chemical Physics* 2011, 13, 7162-7169.
145. Kim, H.-S.; Mora-Sero, I.; Gonzalez-Pedro, V.; Fabregat-Santiago, F.; Juarez-Perez, E. J.; Park, N.-G.; Bisquert, J. Mechanism of carrier accumulation in perovskite thin-absorber solar cells. *Nature communications* 2013, 4.
146. Etgar, L.; Gao, P.; Qin, P.; Graetzel, M.; Nazeeruddin, M. K. A hybrid lead iodide perovskite and lead sulfide QD heterojunction solar cell to obtain a panchromatic response. *J. Mater. Chem. A* 2014, 2, 11586-11590.
147. Wang, C.; Li, Y.; Zhang, C.; Shi, L.; Tong, S.; Guo, B.; Zhang, J.; He, J.; Gao, Y.; Su, C.; Yang, J. Enhancing the performance of planar heterojunction perovskite solar cells using stable semiquinone and amine radical modified hole transport layer. *Journal of Power Sources* 2018, 390, 134-141.
148. Wang, J. T.-W.; Ball, J. M.; Barea, E. M.; Abate, A.; Alexander-Webber, J. A.; Huang, J.; Saliba, M.; Mora-Sero, I.; Bisquert, J.; Snaith, H. J.; Nicholas, R. J. Low-Temperature Processed Electron Collection Layers of Graphene/TiO_2 Nanocomposites in Thin Film Perovskite Solar Cells. *Nano Lett.* 2014, 14, 724-730.
149. Dong, J.; Zhao, Y.; Shi, J.; Wei, H.; Xiao, J.; Xu, X.; Luo, J.; Xu, J.; Li, D.; Luo, Y.; Meng, Q. Impressive enhancement in the cell performance of ZnO nanorod-based perovskite solar cells with Al-doped ZnO interfacial modification. *Chemical Communications* 2014, 50, 13381-13384.
150. Mahmood, K.; Swain, B. S.; Jung, H. S. Controlling the surface nanostructure of ZnO and Al-doped ZnO thin films using electrostatic spraying for their application in 12% efficient perovskite solar cells. *Nanoscale* 2014, 6, 9127-9138.
151. Kim, J. H.; Liang, P.-W.; Williams, S. T.; Cho, N.; Chueh, C.-C.; Glaz, M. S.; Ginger, D. S.; Jen, A. K.-Y. High-Performance and Environmentally Stable Planar Heterojunction Perovskite Solar Cells Based on a Solution-Processed Copper-Doped Nickel Oxide Hole-Transporting Layer. *Advanced Materials* 2015, 27, 695-701.
152. Jung, J. W.; Chueh, C.-C.; Jen, A. K.-Y. A Low-Temperature, Solution-Processable, Cu-Doped Nickel Oxide Hole-Transporting Layer via the Combustion Method for High-Performance Thin-Film Perovskite Solar Cells. *Advanced Materials* 2015, 27, 7874-7880.
153. Shin, S. S.; Yeom, E. J.; Yang, W. S.; Hur, S.; Kim, M. G.; Im, J.; Seo, J.; Noh, J. H.; Seok, S. I. Colloidally prepared La-doped $BaSnO_3$ electrodes for efficient, photostable perovskite solar cells. *Science* 2017, 356, 167-171.
154. Alaee, R.; Filter, R.; Lehr, D.; Lederer, F.; Rockstuhl, C. A generalized Kerker condition for highly directive nanoantennas. *Opt. Lett.* 2015, 40, 2645-2648.
155. Luk'yanchuk, B. S.; Voshchinnikov, N. V.; Paniagua-Domínguez, R.; Kuznetsov, A. I. Optimum Forward Light Scattering by Spherical and Spheroidal Dielectric Nanoparticles with High Refractive Index. *ACS Photonics* 2015, 2, 993-999.
156. Kuznetsov, A. I.; Miroshnichenko, A. E.; Brongersma, M. L.; Kivshar, Y. S.; Luk'yanchuk, B. Optically resonant dielectric nanostructures. *Science* 2016, 354, aag2472.

157. Person, S.; Jain, M.; Lapin, Z.; Sáenz, J. J.; Wicks, G.; Novotny, L. Demonstration of Zero Optical Backscattering from Single Nanoparticles. *Nano Lett.* 2013, 13, 1806-1809.
158. Wang, Z.; An, N.; Shen, F.; Zhou, H.; Sun, Y.; Jiang, Z.; Han, Y.; Li, Y.; Guo, Z. Enhanced Forward Scattering of Ellipsoidal Dielectric Nanoparticles. *Nanoscale Research Letters* 2017, 12, 58.
159. Shibanuma, T.; Albella, P.; Maier, S. A. Unidirectional light scattering with high efficiency at optical frequencies based on low-loss dielectric nanoantennas. *Nanoscale* 2016, 8, 14184-14192.
160. Kerker, M.; Wang, D. S.; Giles, C. L. Electromagnetic scattering by magnetic spheres. *J. Opt. Soc. Am.* 1983, 73, 765-767.
161. Paramasivam, I.; Jha, H.; Liu, N.; Schmuki, P. A Review of Photocatalysis using Self-organized TiO2 Nanotubes and Other Ordered Oxide Nanostructures. *Small* 2012, 8, 3073-3103.
162. Mohammadpour, A.; Kar, P.; Wiltshire, B. D.; Askar, A. M.; Shankar, K. Electron Transport, Trapping and Recombination in Anodic TiO_2 Nanotube Arrays. *Current Nanoscience* 2015, 11, 593-614.
163. Liang, X.; Cheng, Y.; Xu, X.; Dong, R.; Li, D.; Zhou, Z.; Wei, R.; Dong, G.; Tsang, S.-W.; Ho, J. C. Enhanced performance of perovskite solar cells based on vertical TiO_2 nanotube arrays with full filling of $CH_3NH_3PbI_3$. *Applied Surface Science* 2018, 451, 250-257.
164. Zhu, Y.; Song, Z.; Zhou, H.; Wu, D.; Lu, R.; Wang, R.; Wang, H. Self-powered, broadband perovskite photodetector based on ZnO microspheres as scaffold layer. *Applied Surface Science* 2018, 448, 23-29.
165. Thakur, U. K.; Kisslinger, R.; Shankar, K. One-dimensional electron transport layers for perovskite solar cells. *Nanomaterials* 2017, 7, 95.
166. Thakur, U. K.; Askar, A. M.; Kisslinger, R.; Wiltshire, B. D.; Kar, P.; Shankar, K. Halide perovskite solar cells using monocrystalline TiO_2 nanorod arrays as electron transport layers: Impact of nanorod morphology. *Nanotechnology* 2017, 28, 274001.
167. Liu, Z.; Zhu, A.; Cai, F.; Tao, L.; Zhou, Y.; Zhao, Z.; Chen, Q.; Cheng, Y.-B.; Zhou, H. Nickel oxide nanoparticles for efficient hole transport in p-i-n and n-i-p perovskite solar cells. *J. Mater. Chem. A* 2017, 5, 6597-6605.
168. Wu, S.; Cheng, C.; Jin, J.; Wang, J.; Peng, T. Low-Temperature Processed Nanostructured Rutile TiO_2 Array Films for Perovskite Solar Cells With High Efficiency and Stability. *Solar RRL* 2018, 2, 1700164.
169. Kumar, A.; Madaria, A. R.; Zhou, C. Growth of aligned single-crystalline rutile TiO_2 nanowires on arbitrary substrates and their application in dye-sensitized solar cells. *The Journal of Physical Chemistry C* 2010, 114, 7787-7792.
170. Wu, W.-Q.; Lei, B.-X.; Rao, H.-S.; Xu, Y.-F.; Wang, Y.-F.; Su, C.-Y.; Kuang, D.-B. Hydrothermal Fabrication of Hierarchically Anatase TiO_2 Nanowire arrays on FTO Glass for Dye-sensitized Solar Cells. *Scientific Reports* 2013, 3, 1352.
171. Howard, C. J.; Sabine, T. M.; Dickson, F. Structural and thermal parameters for rutile and anatase. *Crystallographica Section B* 1991, 47, 462-468.
172. Sedach, P. A.; Gordon, T. J.; Sayed, S. Y.; Fürstenhaupt, T.; Sui, R.; Baumgartner, T.; Berlinguette, C. P. Solution growth of anatase TiO_2 nanowires from transparent conducting glass substrates. *Journal of Materials Chemistry* 2010, 20, 5063-5069.
173. Liu, B.; Aydil, E. S. Growth of Oriented Single-Crystalline Rutile TiO_2 Nanorods on Transparent Conducting Substrates for Dye-Sensitized Solar Cells. *Journal of the American Chemical Society* 2009, 131, 3985-3990.
174. Wang, X.; Liu, Y.; Zhou, X.; Li, B.; Wang, H.; Zhao, W.; Huang, H.; Liang, C.; Yu, X.; Liu, Z.; Shen, H. Synthesis of long TiO_2 nanowire arrays with high surface areas via synergistic assembly route for highly efficient dye-sensitized solar cells. *Journal of Materials Chemistry* 2012, 22, 17531-17538.
175. Abd-Lefdil, M.; Diaz, R.; Bihri, H.; Ait Aouaj, M.; Rueda, F. J. E. P. J. A. P. Preparation and characterization of sprayed FTO thin films. *The European Physical Journal-Applied Physics* 2007, 38, 217-219.

176. Zhu, L.; Hong, M.; Ho, G. W. Fabrication of wheat grain textured TiO_2/CuO composite nanofibers for enhanced solar H_2 generation and degradation performance. *Nano Energy* 2015, 11, 28-37.
177. Yan, J.; Wu, H.; Chen, H.; Zhang, Y.; Zhang, F.; Liu, S. F. Fabrication of TiO_2/C_3N_4 heterostructure for enhanced photocatalytic Z-scheme overall water splitting. *Applied Catalysis B: Environmental* 2016, 191, 130-137.
178. Park, J.; Back, T.; Mitchel, W. C.; Kim, S. S.; Elhamri, S.; Boeckl, J.; Fairchild, S. B.; Naik, R.; Voevodin, A. A. Approach to multifunctional device platform with epitaxial graphene on transition metal oxide. *Scientific Reports* 2015, 5, 14374.
179. Tahir, M.; Amin, N. S. Indium-doped TiO_2 nanoparticles for photocatalytic CO_2 reduction with H_2O vapors to CH_4. *Applied Catalysis B: Environmental* 2015, 162, 98-109.
180. Yan, J.; Wu, G.; Guan, N.; Li, L.; Li, Z.; Cao, X. Understanding the effect of surface/bulk defects on the photocatalytic activity of TiO_2: anatase versus rutile. *Physical Chemistry Chemical Physics* 2013, 15, 10978-10988.
181. Das, C.; Richter, M.; Tallarida, M.; Schmeisser, D. Electronic properties of atomic layer deposition films, anatase and rutile TiO_2 studied by resonant photoemission spectroscopy. *Journal of Physics D: Applied Physics* 2016, 49, 275304.
182. Izumi, Y. Recent advances in the photocatalytic conversion of carbon dioxide to fuels with water and/or hydrogen using solar energy and beyond. *Coordination Chemistry Reviews* 2013, 257, 171-186.
183. Habisreutinger, S. N.; Schmidt-Mende, L.; Stolarczyk, J. K. Photocatalytic Reduction of CO_2 on TiO_2 and Other Semiconductors. *Angewandte Chemie International Edition* 2013, 52, 7372-7408.
184. Jing, L.; Li, S.; Song, S.; Xue, L.; Fu, H. Investigation on the electron transfer between anatase and rutile in nano-sized TiO_2 by means of surface photovoltage technique and its effects on the photocatalytic activity. *Solar Energy Materials and Solar Cells* 2008, 92, 1030-1036.
185. Scanlon, D. O.; Dunnill, C. W.; Buckeridge, J.; Shevlin, S. A.; Logsdail, A. J.; Woodley, S. M.; Catlow, C. R. A.; Powell, M. J.; Palgrave, R. G.; Parkin, I. P.; Watson, G. W.; Keal, T. W.; Sherwood, P.; Walsh, A.; Sokol, A. A. Band alignment of rutile and anatase TiO_2. *Nature Materials* 2013, 12, 798.
186. Hurum, D. C.; Agrios, A. G.; Gray, K. A.; Rajh, T.; Thurnauer, M. C. Explaining the Enhanced Photocatalytic Activity of Degussa P25 Mixed-Phase TiO_2 Using EPR. *The Journal of Physical Chemistry B* 2003, 107, 4545-4549.
187. Hurum, D. C.; Gray, K. A.; Rajh, T.; Thurnauer, M. C. Recombination Pathways in the Degussa P25 Formulation of TiO_2: Surface versus Lattice Mechanisms. *The Journal of Physical Chemistry B* 2005, 109, 977-980.
188. Liu, J.; Huo, J.; Zhang, M.; Dong, X. Branched TiO_2 nanorod arrays owning the surface anatase/rutile junctions for dye sensitized solar cells. *Thin Solid Films* 2017, 623, 25-30.
189. Deák, P.; Aradi, B.; Frauenheim, T. Band Lineup and Charge Carrier Separation in Mixed Rutile-Anatase Systems. *The Journal of Physical Chemistry C* 2011, 115, 3443-3446.
190. Wang, W.-K.; Chen, J.-J.; Zhang, X.; Huang, Y.-X.; Li, W.-W.; Yu, H.-Q. Self-induced synthesis of phase-junction TiO_2 with a tailored rutile to anatase ratio below phase transition temperature. *Scientific Reports* 2016, 6, 20491.
191. Li, G.; Richter, C. P.; Milot, R. L.; Cai, L.; Schmuttenmaer, C. A.; Crabtree, R. H.; Brudvig, G. W.; Batista, V. S. Synergistic effect between anatase and rutile TiO_2 nanoparticles in dye-sensitized solar cells. *Dalton Transactions* 2009, 10078-10085.
192. Ding, J.; Li, Y.; Hu, H.; Bai, L.; Zhang, S.; Yuan, N. J. N. R. L. The influence of anatase-rutile mixed phase and ZnO blocking layer on dye-sensitized solar cells based on TiO_2nanofiberphotoanodes. *Nanoscale research letters* 2013, 8, 9.
193. Zhu, Z.; Ma, J.; Wang, Z.; Mu, C.; Fan, Z.; Du, L.; Bai, Y.; Fan, L.; Yan, H.; Phillips, D. L.; Yang, S. Efficiency Enhancement of Perovskite Solar Cells through Fast Electron Extraction: The Role of Graphene Quantum Dots. *Journal of the American Chemical Society* 2014, 136, 3760-3763.

194. Bi, D.; Yi, C.; Luo, J.; Décoppet, J.-D.; Zhang, F.; Zakeeruddin, Shaik M.; Li, X.; Hagfeldt, A.; Grätzel, M. Polymer-templated nucleation and crystal growth of perovskite films for solar cells with efficiency greater than 21%. *Nature Energy* 2016, 1, 16142.
195. Wang, L.; McCleese, C.; Kovalsky, A.; Zhao, Y.; Burda, C. Femtosecond Time-Resolved Transient Absorption Spectroscopy of $CH_3NH_3PbI_3$ Perovskite Films: Evidence for Passivation Effect of PbI_2. *Journal of the American Chemical Society* 2014, 136, 12205-12208.
196. Xing, G.; Mathews, N.; Sun, S.; Lim, S. S.; Lam, Y. M.; Grätzel, M.; Mhaisalkar, S.; Sum, T. C. Long-Range Balanced Electron- and Hole-Transport Lengths in Organic-Inorganic $CH_3NH_3PbI_3$. *Science* 2013, 342, 344-347.
197. Gunawan, O.; Todorov, T. K.; Mitzi, D. B. Loss mechanisms in hydrazine-processed $Cu_2ZnSn(Se,S)_4$ solar cells. *Applied Physics Letters* 2010, 97, 233506.
198. Yin, J.; Cao, J.; He, X.; Yuan, S.; Sun, S.; Li, J.; Zheng, N.; Lin, L. Improved stability of perovskite solar cells in ambient air by controlling the mesoporous layer. *J. Mater. Chem. A* 2015, 3, 16860-16866.
199. Po-Wei, L.; Chien-Yi, L.; Chu-Chen, C.; Fan, Z.; T., W. S.; Xu-Kai, X.; Jiangjen, L.; K.-Y., J. A. Additive Enhanced Crystallization of Solution-Processed Perovskite for Highly Efficient Planar-Heterojunction Solar Cells. *Advanced Materials* 2014, 26, 3748-3754.
200. Chen, Q.; Zhou, H.; Song, T.-B.; Luo, S.; Hong, Z.; Duan, H.-S.; Dou, L.; Liu, Y.; Yang, Y. Controllable self-induced passivation of hybrid lead iodide perovskites toward high performance solar cells. *Nano Lett.* 2014, 14, 4158-4163.
201. Shalom, M.; Inal, S.; Fettkenhauer, C.; Neher, D.; Antonietti, M. Improving Carbon Nitride Photocatalysis by Supramolecular Preorganization of Monomers. *Journal of the American Chemical Society* 2013, 135, 7118-7121.
202. Kang, Y.; Yang, Y.; Yin, L.-C.; Kang, X.; Wang, L.; Liu, G.; Cheng, H.-M. Selective Breaking of Hydrogen Bonds of Layered Carbon Nitride for Visible Light Photocatalysis. *Advanced Materials* 2016, 28, 6471-6477.
203. Stewart, R. J.; Grieco, C.; Larsen, A. V.; Maier, J. J.; Asbury, J. B. Approaching bulk carrier dynamics in organo-halide perovskite nanocrystalline films by surface passivation. *The journal of physical chemistry letters* 2016, 7, 1148-1153.
204. Nie, W.; Tsai, H.; Asadpour, R.; Blancon, J.-C.; Neukirch, A. J.; Gupta, G.; Crochet, J. J.; Chhowalla, M.; Tretiak, S.; Alam, M. A. High-efficiency solution-processed perovskite solar cells with millimeter-scale grains. *Science* 2015, 347, 522-525.
205. Yang, W. S.; Park, B.-W.; Jung, E. H.; Jeon, N. J.; Kim, Y. C.; Lee, D. U.; Shin, S. S.; Seo, J.; Kim, E. K.; Noh, J. H. Iodide management in formamidinium-lead-halide–based perovskite layers for efficient solar cells. *Science* 2017, 356, 1376-1379.
206. Huang, F.; Pascoe, A. R.; Wu, W. Q.; Ku, Z.; Peng, Y.; Zhong, J.; Caruso, R. A.; Cheng, Y. B. Effect of the Microstructure of the Functional Layers on the Efficiency of Perovskite Solar Cells. *Advanced Materials* 2017, 29.
207. Ranjan, R.; Prakash, A.; Singh, A.; Singh, A.; Garg, A.; Gupta, R. K. Effect of tantalum doping in a TiO_2 compact layer on the performance of planar spiro-OMeTAD free perovskite solar cells. *J. Mater. Chem. A* 2018, 6, 1037-1047.
208. S., Y. J.; Jan, S.; Jincheol, K.; Mahboubi, S. A.; Shujuan, H.; Jonathan, L.; Joong, J. N.; Il, S. S.; A., G. M.; Anita, H.-B. Critical Role of Grain Boundaries for Ion Migration in Formamidinium and Methylammonium Lead Halide Perovskite Solar Cells. *Advanced Energy Materials* 2016, 6, 1600330.
209. Yun, J. S.; Ho-Baillie, A.; Huang, S.; Woo, S. H.; Heo, Y.; Seidel, J.; Huang, F.; Cheng, Y.-B.; Green, M. A. Benefit of Grain Boundaries in Organic–Inorganic Halide Planar Perovskite Solar Cells. *The Journal of Physical Chemistry Letters* 2015, 6, 875-880.

210. Chan, K. Y.; Joong, J. N.; Hong, N. J.; Seok, Y. W.; Jangwon, S.; S., Y. J.; Anita, H.-B.; Shujuan, H.; A., G. M.; Jan, S.; Kyu, A. T.; Il, S. S. Beneficial Effects of PbI2 Incorporated in Organo-Lead Halide Perovskite Solar Cells. *Advanced Energy Materials* 2016, 6, 1502104.
211. Faraji, N.; Qin, C.; Matsushima, T.; Adachi, C.; Seidel, J. Grain Boundary Engineering of Halide Perovskite $CH_3NH_3PbI_3$ Solar Cells with Photochemically Active Additives. *The Journal of Physical Chemistry C* 2018, 122, 4817-4821.
212. Salado, M.; Kokal, R. K.; Calio, L.; Kazim, S.; Deepa, M.; Ahmad, S. Identifying the charge generation dynamics in Cs+-based triple cation mixed perovskite solar cells. *Physical Chemistry Chemical Physics* 2017, 19, 22905-22914.
213. Yu, Z.; Sun, L. Recent Progress on Hole-Transporting Materials for Emerging Organometal Halide Perovskite Solar Cells. 2015, 5, 1500213.
214. Adhikari, N.; Dubey, A.; Khatiwada, D.; Mitul, A. F.; Wang, Q.; Venkatesan, S.; Iefanova, A.; Zai, J.; Qian, X.; Kumar, M.; Qiao, Q. Interfacial Study To Suppress Charge Carrier Recombination for High Efficiency Perovskite Solar Cells. *ACS Applied Materials & Interfaces* 2015, 7, 26445-26454.
215. Ono, L. K.; Qi, Y. Surface and Interface Aspects of Organometal Halide Perovskite Materials and Solar Cells. *The Journal of Physical Chemistry Letters* 2016, 7, 4764-4794.
216. Mohammadpour, A.; Farsinezhad, S.; Wiltshire, B. D.; Shankar, K. Majority carrier transport in single crystal rutile nanowire arrays. *physica status solidi (RRL) - Rapid Research Letters* 2014, 8, 512-516.
217. Pockett, A.; Eperon, G. E.; Sakai, N.; Snaith, H. J.; Peter, L. M.; Cameron, P. J. Microseconds, milliseconds and seconds: deconvoluting the dynamic behaviour of planar perovskite solar cells. *Physical Chemistry Chemical Physics* 2017, 19, 5959-5970.
218. Heo, J. H.; Han, H. J.; Kim, D.; Ahn, T. K.; Im, S. H. Hysteresis-less inverted $CH_3NH_3PbI_3$ planar perovskite hybrid solar cells with 18.1% power conversion efficiency. *Energy & Environmental Science* 2015, 8, 1602-1608.
219. Guillén, E.; Ramos, F. J.; Anta, J. A.; Ahmad, S. Elucidating transport-recombination mechanisms in perovskite solar cells by small-perturbation techniques. *The Journal of Physical Chemistry C* 2014, 118, 22913-22922.
220. Yang, Y.; Ri, K.; Mei, A.; Liu, L.; Hu, M.; Liu, T.; Li, X.; Han, H. The size effect of TiO_2 nanoparticles on a printable mesoscopic perovskite solar cell. *J. Mater. Chem. A* 2015, 3, 9103-9107.
221. Zong, X.; Sun, Z.; Wang, H.; Wang, J.; Liang, M.; Xue, S. A tubular perovskite solar cell: improvement of charge separation at the perovskite/HTM interface. *Chemical Communications* 2015, 51, 14076-14079.
222. Giordano, F.; Abate, A.; Baena, J. P. C.; Saliba, M.; Matsui, T.; Im, S. H.; Zakeeruddin, S. M.; Nazeeruddin, M. K.; Hagfeldt, A.; Graetzel, M. Enhanced electronic properties in mesoporous TiO_2 via lithium doping for high-efficiency perovskite solar cells. *Nature communications* 2016, 7, 10379.
223. Zhao, Y.; Nardes, A. M.; Zhu, K. Mesoporous perovskite solar cells: material composition, charge-carrier dynamics, and device characteristics. *Faraday discussions* 2015, 176, 301-312.
224. Zhao, Y.; Nardes, A. M.; Zhu, K. Solid-state mesostructured perovskite CH3NH3PbI3 solar cells: charge transport, recombination, and diffusion length. *The journal of physical chemistry letters* 2014, 5, 490-494.
225. Zhao, Y.; Zhu, K. Charge transport and recombination in perovskite $(CH_3NH_3)PbI_3$ sensitized TiO_2 solar cells. *The Journal of Physical Chemistry Letters* 2013, 4, 2880-2884.
226. Bi, D.; Yang, L.; Boschloo, G.; Hagfeldt, A.; Johansson, E. M. Effect of different hole transport materials on recombination in $CH_3NH_3PbI_3$ perovskite-sensitized mesoscopic solar cells. *The journal of physical chemistry letters* 2013, 4, 1532-1536.
227. Pockett, A.; Eperon, G. E.; Peltola, T.; Snaith, H. J.; Walker, A.; Peter, L. M.; Cameron, P. J. Characterization of planar lead halide perovskite solar cells by impedance spectroscopy, open-circuit

photovoltage decay, and intensity-modulated photovoltage/photocurrent spectroscopy. *The Journal of Physical Chemistry C* 2015, 119, 3456-3465.
228. Cui, Q.; Zhao, X.; Lin, H.; Yang, L.; Chen, H.; Zhang, Y.; Li, X. Improved efficient perovskite solar cells based on Ta-doped TiO_2 nanorod arrays. *Nanoscale* 2017, 9, 18897-18907.
229. Sheng, X.; Chen, L. P.; Xu, T.; Zhu, K.; Feng, X. J. Understanding and removing surface states limiting charge transport in TiO_2 nanowire arrays for enhanced optoelectronic device performance. *Chemical Science* 2016, 7, 1910-1913.
230. Gao, X.; Li, J.; Gollon, S.; Qiu, M.; Guan, D.; Guo, X.; Chen, J.; Yuan, C. A TiO 2 nanotube network electron transport layer for high efficiency perovskite solar cells. *Physical Chemistry Chemical Physics* 2017, 19, 4956-4961.
231. Correa-Baena, J.-P.; Abate, A.; Saliba, M.; Tress, W.; Jesper Jacobsson, T.; Gratzel, M.; Hagfeldt, A. The rapid evolution of highly efficient perovskite solar cells. *Energy & Environmental Science* 2017, 10, 710-727.
232. Calió, L.; Kazim, S.; Grätzel, M.; Ahmad, S. Hole-Transport Materials for Perovskite Solar Cells. *Angewandte Chemie International Edition* 2016, 55, 14522-14545.
233. Ameen, S.; Rub, M. A.; Kosa, S. A.; Alamry, K. A.; Akhtar, M. S.; Shin, H. S.; Seo, H. K.; Asiri, A. M.; Nazeeruddin, M. K. Perovskite Solar Cells: Influence of Hole Transporting Materials on Power Conversion Efficiency. *ChemSusChem* 2016, 9, 10-27.
234. Dhingra, P.; Singh, P.; Rana, P. J. S.; Garg, A.; Kar, P. Hole-Transporting Materials for Perovskite-Sensitized Solar Cells. *Energy Technology* 2016, 4, 891-938.
235. Swetha, T.; Singh, S. P. Perovskite solar cells based on small molecule hole transporting materials. *J. Mater. Chem. A* 2015, 3, 18329-18344.
236. Teh, C. H.; Daik, R.; Lim, E. L.; Yap, C. C.; Ibrahim, M. A.; Ludin, N. A.; Sopian, K.; Mat Teridi, M. A. A review of organic small molecule-based hole-transporting materials for meso-structured organic-inorganic perovskite solar cells. *J. Mater. Chem. A* 2016, 4, 15788-15822.
237. Liu, D.; Yongsheng, L. Recent progress of dopant-free organic hole-transporting materials in perovskite solar cells. *Journal of Semiconductors* 2017, 38, 011005.
238. Vivo, P.; Salunke, J. K.; Priimagi, A. Hole-Transporting Materials for Printable Perovskite Solar Cells. *Materials* 2017, 10, 1087.
239. Schloemer, T. H.; Christians, J. A.; Luther, J. M.; Sellinger, A. Doping strategies for small molecule organic hole-transport materials: impacts on perovskite solar cell performance and stability. *Chemical Science* 2019, 10, 1904-1935.
240. Lai, X.; Meng, F.; Zhang, Q.-Q.; Wang, K.; Li, G.; Wen, Y.; Ma, H.; Li, W.; Li, X.; Kyaw, A. K. K.; Wang, K.; Sun, X. W.; Du, M.; Guo, X.; Wang, J.; Huang, W. A Bifunctional Saddle-Shaped Small Molecule as a Dopant-Free Hole Transporting Material and Interfacial Layer for Efficient and Stable Perovskite Solar Cells. 2019, 3, 1900011.
241. Teh, C. H.; Daik, R.; Lim, E. L.; Yap, C. C.; Ibrahim, M. A.; Ludin, N. A.; Sopian, K.; Mat Teridi, M. A. A review of organic small molecule-based hole-transporting materials for meso-structured organic–inorganic perovskite solar cells. *J. Mater. Chem. A* 2016, 4, 15788-15822.
242. Li, Y.; Cole, M. D.; Gao, Y.; Emrick, T.; Xu, Z.; Liu, Y.; Russell, T. P. High-Performance Perovskite Solar Cells with a Non-doped Small Molecule Hole Transporting Layer. *ACS Applied Energy Materials* 2019, 2, 1634-1641.
243. Urieta-Mora, J.; García-Benito, I.; Molina-Ontoria, A.; Martín, N. Hole transporting materials for perovskite solar cells: a chemical approach. *Chemical Society Reviews* 2018, 47, 8541-8571.
244. Li, W.; Liu, C.; Li, Y.; Kong, W.; Wang, X.; Chen, H.; Xu, B.; Cheng, C. Polymer Assisted Small Molecule Hole Transport Layers Toward Highly Efficient Inverted Perovskite Solar Cells. 2018, 2, 1800173.

245. Hwang, H.; Park, S.; Heo, J. H.; Kim, W.; Ahn, H.; Kim, T.-S.; Im, S. H.; Son, H. J. Enhancing performance and stability of perovskite solar cells using hole transport layer of small molecule and conjugated polymer blend. *Journal of Power Sources* 2019, 418, 167-175.
246. Ulfa, M.; Zhu, T.; Goubard, F.; Pauporté, T. Molecular versus polymeric hole transporting materials for perovskite solar cell application. *J. Mater. Chem. A* 2018, 6, 13350-13358.
247. Tsai, C.-H.; Li, N.; Lee, C.-C.; Wu, H.-C.; Zhu, Z.; Wang, L.; Chen, W.-C.; Yan, H.; Chueh, C.-C. Efficient and UV-stable perovskite solar cells enabled by side chain-engineered polymeric hole-transporting layers. *J. Mater. Chem. A* 2018, 6, 12999-13004.
248. Lim, J.; Kong, S. Y.; Yun, Y. J. Hole Transport Behaviour of Various Polymers and Their Application to Perovskite-Sensitized Solid-State Solar Cells 2018, 2018, 6.
249. Marques, A. S.; Szostak, R.; Marchezi, P. E.; Nogueira, A. F. Perovskite solar cells based on polyaniline derivatives as hole transport materials. *Journal of Physics: Energy* 2018, 1, 015004.
250. Völker, S. F.; Collavini, S.; Delgado, J. L. Organic Charge Carriers for Perovskite Solar Cells. 2015, 8, 3012-3028.
251. Heo, J. H.; Im, S. H.; Noh, J. H.; Mandal, T. N.; Lim, C.-S.; Chang, J. A.; Lee, Y. H.; Kim, H.-j.; Sarkar, A.; Nazeeruddin, M. K.; Grätzel, M.; Seok, S. I. Efficient inorganic–organic hybrid heterojunction solar cells containing perovskite compound and polymeric hole conductors. *Nature Photonics* 2013, 7, 486.
252. Noh, J. H.; Im, S. H.; Heo, J. H.; Mandal, T. N.; Seok, S. I. Chemical Management for Colorful, Efficient, and Stable Inorganic–Organic Hybrid Nanostructured Solar Cells. *Nano Lett.* 2013, 13, 1764-1769.
253. Manders, J. R.; Tsang, S.-W.; Hartel, M. J.; Lai, T.-H.; Chen, S.; Amb, C. M.; Reynolds, J. R.; So, F. Solution-Processed Nickel Oxide Hole Transport Layers in High Efficiency Polymer Photovoltaic Cells. 2013, 23, 2993-3001.
254. Ruscello, M.; Sarkar, T.; Levitsky, A.; Matrone, G. M.; Droseros, N.; Schlisske, S.; Sachs, E.; Reiser, P.; Mankel, E.; Kowalsky, W.; Banerji, N.; Stingelin, N.; Frey, G. L.; Hernandez-Sosa, G. Nanocomposite of nickel oxide nanoparticles and polyethylene oxide as printable hole transport layer for organic solar cells. *Sustainable Energy & Fuels* 2019, 3, 1418-1426.
255. Irwin, M. D.; Servaites, J. D.; Buchholz, D. B.; Leever, B. J.; Liu, J.; Emery, J. D.; Zhang, M.; Song, J.-H.; Durstock, M. F.; Freeman, A. J.; Bedzyk, M. J.; Hersam, M. C.; Chang, R. P. H.; Ratner, M. A.; Marks, T. J. Structural and Electrical Functionality of NiO Interfacial Films in Bulk Heterojunction Organic Solar Cells. *Chemistry of Materials* 2011, 23, 2218-2226.
256. Berry, J. J.; Widjonarko, N. E.; Bailey, B. A.; Sigdel, A. K.; Ginley, D. S.; Olson, D. C. Surface Treatment of NiO Hole Transport Layers for Organic Solar Cells. *IEEE Journal of Selected Topics in Quantum Electronics* 2010, 16, 1649-1655.
257. Huang, S.; Wang, Y.; Shen, S.; Tang, Y.; Yu, A.; Kang, B.; Silva, S. R. P.; Lu, G. Enhancing the performance of polymer solar cells using solution-processed copper doped nickel oxide nanoparticles as hole transport layer. *Journal of Colloid and Interface Science* 2019, 535, 308-317.
258. Singh, A.; Gupta, S. K.; Garg, A. Inkjet printing of NiO films and integration as hole transporting layers in polymer solar cells. *Scientific Reports* 2017, 7, 1775.
259. Singh, R.; Kumar, S.; Bedi, R. K.; Saxena, V.; Aswal, D. K.; Mahajan, A. Optimization of Ni2+/Ni3+ ratio in reduced graphene oxide/nickel oxide nanohybrids for platinum free dye sensitized solar cells. *Journal of Physics and Chemistry of Solids* 2018, 123, 191-197.
260. Brisse, R.; Faddoul, R.; Bourgeteau, T.; Tondelier, D.; Leroy, J.; Campidelli, S.; Berthelot, T.; Geffroy, B.; Jousselme, B. Inkjet Printing NiO-Based p-Type Dye-Sensitized Solar Cells. *ACS Applied Materials & Interfaces* 2017, 9, 2369-2377.
261. Lee, H.; Huang, Y.-T.; Horn, M. W.; Feng, S.-P. Engineered optical and electrical performance of rf–sputtered undoped nickel oxide thin films for inverted perovskite solar cells. *Scientific Reports* 2018, 8, 5590.

262. Mali, S. S.; Kim, H.; Kim, H. H.; Shim, S. E.; Hong, C. K. Nanoporous p-type NiOx electrode for p-i-n inverted perovskite solar cell toward air stability. *Materials Today* 2018.
263. Liu, Z.; Chang, J.; Lin, Z.; Zhou, L.; Yang, Z.; Chen, D.; Zhang, C.; Liu, S.; Hao, Y. High-Performance Planar Perovskite Solar Cells Using Low Temperature, Solution–Combustion-Based Nickel Oxide Hole Transporting Layer with Efficiency Exceeding 20%. *Advanced Energy Materials* 2018, 8, 1703432.
264. Qin, P.; He, Q.; Ouyang, D.; Fang, G.; Choy, W. C. H.; Li, G. J. S. C. C. Transition metal oxides as hole-transporting materials in organic semiconductor and hybrid perovskite based solar cells. 2017, 60, 472-489.
265. Pitchaiya, S.; Natarajan, M.; Santhanam, A.; Asokan, V.; Yuvapragasam, A.; Madurai Ramakrishnan, V.; Palanisamy, S. E.; Sundaram, S.; Velauthapillai, D. A review on the classification of organic/inorganic/carbonaceous hole transporting materials for perovskite solar cell application. *Arabian Journal of Chemistry* 2018.
266. Kung, P.-K.; Li, M.-H.; Lin, P.-Y.; Chiang, Y.-H.; Chan, C.-R.; Guo, T.-F.; Chen, P. A Review of Inorganic Hole Transport Materials for Perovskite Solar Cells. 2018, 5, 1800882.
267. Ozaki, T. Variationally optimized atomic orbitals for large-scale electronic structures. *Physical Review B* 2003, 67, 155108.
268. Even, J.; Pedesseau, L.; Jancu, J.-M.; Katan, C. Importance of Spin–Orbit Coupling in Hybrid Organic/Inorganic Perovskites for Photovoltaic Applications. *The Journal of Physical Chemistry Letters* 2013, 4, 2999-3005.
269. Ködderitzsch, D.; Hergert, W.; Temmerman, W. M.; Szotek, Z.; Ernst, A.; Winter, H. Exchange interactions in NiO and at the NiO(100) surface. *Physical Review B* 2002, 66, 064434.
270. Arai, K.; Okuda, T.; Tanaka, A.; Kotsugi, M.; Fukumoto, K.; Ohkochi, T.; Nakamura, T.; Matsushita, T.; Muro, T.; Oura, M.; Senba, Y.; Ohashi, H.; Kakizaki, A.; Mitsumata, C.; Kinoshita, T. Three-dimensional spin orientation in antiferromagnetic domain walls of NiO studied by x-ray magnetic linear dichroism photoemission electron microscopy. *Physical Review B* 2012, 85, 104418.
271. Combescot, M.; Betbeder-Matibet, O. Coherent effects in the physics of composite excitons. *Physical Review B* 2006, 74, 045110.
272. Wang, Q.-K.; Wang, R.-B.; Shen, P.-F.; Li, C.; Li, Y.-Q.; Liu, L.-J.; Duhm, S.; Tang, J.-X. Energy Level Offsets at Lead Halide Perovskite/Organic Hybrid Interfaces and Their Impacts on Charge Separation. 2015, 2, 1400528.
273. Polman, A.; Knight, M.; Garnett, E. C.; Ehrler, B.; Sinke, W. C. Photovoltaic materials: Present efficiencies and future challenges. *Science* 2016, 352.
274. Guo, Y.; Yin, X.; Liu, J.; Chen, W.; Wen, S.; Que, M.; Tian, Y.; Yang, Y.; Que, W. Effect of the post-annealing temperature on the thermal-decomposed NiOx hole contact layer for perovskite solar cells. *Journal of Advanced Dielectrics* 2018, 08, 1850006.
275. Sha, W. E. I.; Ren, X.; Chen, L.; Choy, W. C. H. The efficiency limit of CH3NH3PbI3 perovskite solar cells. 2015, 106, 221104.
276. Pazos-Outón, L. M.; Xiao, T. P.; Yablonovitch, E. Fundamental Efficiency Limit of Lead Iodide Perovskite Solar Cells. *The Journal of Physical Chemistry Letters* 2018, 9, 1703-1711.
277. Mironova-Ulmane, N.; Kuzmin, A.; Steins, I.; Grabis, J.; Sildos, I.; Pärs, M. Raman scattering in nanosized nickel oxide NiO. *Journal of Physics: Conference Series* 2007, 93, 012039.
278. Kaur, N.; Comini, E.; Zappa, D.; Poli, N.; Sberveglieri, G. Nickel oxide nanowires: vapor liquid solid synthesis and integration into a gas sensing device. *Nanotechnology* 2016, 27, 205701.
279. Dryza, V.; Bieske, E. J. Electron Injection and Energy-Transfer Properties of Spiropyran–Cyclodextrin Complexes Coated onto Metal Oxide Nanoparticles: Toward Photochromic Light Harvesting. *The Journal of Physical Chemistry C* 2015, 119, 14076-14084.

280. Godin, R.; Sherman, B. D.; Bergkamp, J. J.; Chesta, C. A.; Moore, A. L.; Moore, T. A.; Palacios, R. E.; Cosa, G. Charge-Transfer Dynamics of Fluorescent Dye-Sensitized Electrodes under Applied Biases. *The Journal of Physical Chemistry Letters* 2015, 6, 2688-2693.
281. Ksenia, F.; M., F. J.; Johannes, S.; Markus, D.; Sebastian, B.; Jürgen, Z.; Laurence, P.; Jiri, R.; Ernst-Wilhelm, S.; Thomas, B.; Dina, F.-R. Ultrasmall Dispersible Crystalline Nickel Oxide Nanoparticles as High-Performance Catalysts for Electrochemical Water Splitting. *Advanced Functional Materials* 2014, 24, 3123-3129.
282. Patil, P. S.; Kadam, L. D. Preparation and characterization of spray pyrolyzed nickel oxide (NiO) thin films. *Applied Surface Science* 2002, 199, 211-221.
283. Li, X.; Zhang, X.; Li, Z.; Qian, Y. Synthesis and characteristics of NiO nanoparticles by thermal decomposition of nickel dimethylglyoximate rods. *Solid State Communications* 2006, 137, 581-584.
284. Boschloo, G.; Hagfeldt, A. Spectroelectrochemistry of Nanostructured NiO. *The Journal of Physical Chemistry B* 2001, 105, 3039-3044.
285. El-Kemary, M.; Nagy, N.; El-Mehasseb, I. Nickel oxide nanoparticles: Synthesis and spectral studies of interactions with glucose. *Materials Science in Semiconductor Processing* 2013, 16, 1747-1752.
286. Yin, J.; Li, Y.; Lv, F.; Fan, Q.; Zhao, Y.-Q.; Zhang, Q.; Wang, W.; Cheng, F.; Xi, P.; Guo, S. NiO/CoN Porous Nanowires as Efficient Bifunctional Catalysts for Zn–Air Batteries. *ACS Nano* 2017, 11, 2275-2283.
287. Guan, C.; Wang, Y.; Hu, Y.; Liu, J.; Ho, K. H.; Zhao, W.; Fan, Z.; Shen, Z.; Zhang, H.; Wang, J. Conformally deposited NiO on a hierarchical carbon support for high-power and durable asymmetric supercapacitors. *J. Mater. Chem. A* 2015, 3, 23283-23288.
288. Guo, W.; Sun, W.; Wang, Y. Multilayer CuO@ NiO hollow spheres: microwave-assisted metal–organic-framework derivation and highly reversible structure-matched stepwise lithium storage. *ACS Nano* 2015, 9, 11462-11471.
289. Yin, X.; Chen, P.; Que, M.; Xing, Y.; Que, W.; Niu, C.; Shao, J. Highly efficient flexible perovskite solar cells using solution-derived NiO x hole contacts. *ACS Nano* 2016, 10, 3630-3636.
290. Nardi, K. L.; Yang, N.; Dickens, C. F.; Strickler, A. L.; Bent, S. F. Creating highly active atomic layer deposited NiO electrocatalysts for the oxygen evolution reaction. *Advanced Energy Materials* 2015, 5, 1500412.
291. Guo, X.; Tan, Q.; Liu, S.; Qin, D.; Mo, Y.; Hou, L.; Liu, A.; Wu, H.; Ma, Y. High-efficiency solution-processed CdTe nanocrystal solar cells incorporating a novel crosslinkable conjugated polymer as the hole transport layer. *Nano Energy* 2018, 46, 150-157.
292. Jahandar, M.; Heo, J. H.; Song, C. E.; Kong, K.-J.; Shin, W. S.; Lee, J.-C.; Im, S. H.; Moon, S.-J. Highly efficient metal halide substituted CH3NH3I(PbI2)1−X(CuBr2)X planar perovskite solar cells. *Nano Energy* 2016, 27, 330-339.
293. Chen, W.; Wu, Y.; Fan, J.; Djurišić, A. B.; Liu, F.; Tam, H. W.; Ng, A.; Surya, C.; Chan, W. K.; Wang, D.; He, Z.-B. Understanding the Doping Effect on NiO: Toward High-Performance Inverted Perovskite Solar Cells. 2018, 8, 1703519.
294. He, Q.; Yao, K.; Wang, X.; Xia, X.; Leng, S.; Li, F. Room-Temperature and Solution-Processable Cu-Doped Nickel Oxide Nanoparticles for Efficient Hole-Transport Layers of Flexible Large-Area Perovskite Solar Cells. *ACS Applied Materials & Interfaces* 2017, 9, 41887-41897.
295. Kirchartz, T.; Gong, W.; Hawks, S. A.; Agostinelli, T.; MacKenzie, R. C. I.; Yang, Y.; Nelson, J. Sensitivity of the Mott–Schottky Analysis in Organic Solar Cells. *The Journal of Physical Chemistry C* 2012, 116, 7672-7680.
296. Cho, A.; Ahn, S.; Yun, J. H.; Gwak, J.; Song, H.; Yoon, K. A hybrid ink of binary copper sulfide nanoparticles and indium precursor solution for a dense CuInSe2 absorber thin film and its photovoltaic performance. *Journal of Materials Chemistry* 2012, 22, 17893-17899.
297. Almora, O.; Aranda, C.; Mas-Marzá, E.; Garcia-Belmonte, G. On Mott-Schottky analysis interpretation of capacitance measurements in organometal perovskite solar cells. 2016, 109, 173903.

298. Zhou, Z.; Zhang, Y.; Shen, Y.; Liu, S.; Zhang, Y. Molecular engineering of polymeric carbon nitride: advancing applications from photocatalysis to biosensing and more. *Chemical Society Reviews* 2018, 47, 2298-2321.
299. Niu, G.; Wang, S.; Li, J.; Li, W.; Wang, L. Oxygen doping in nickel oxide for highly efficient planar perovskite solar cells. *J. Mater. Chem. A* 2018, 6, 4721-4728.
300. Cho, A.-N.; Park, N.-G. Impact of Interfacial Layers in Perovskite Solar Cells. 2017, 10, 3687-3704.
301. Semeniuk, O.; Juska, G.; Oelerich, J. O.; Wiemer, M.; Baranovskii, S. D.; Reznik, A. Charge transport mechanism in lead oxide revealed by CELIV technique. *Sci. Rep.-UK* 2016, 6, 33359.
302. Scott, J. C.; Malliaras, G. G. Charge injection and recombination at the metal–organic interface. *Chem. Phys. Lett.* 1999, 299, 115-119.
303. Adler, D.; Feinleib, J. Electrical and Optical Properties of Narrow-Band Materials. *Physical Review B* 1970, 2, 3112-3134.
304. Islam, M. B.; Yanagida, M.; Shirai, Y.; Nabetani, Y.; Miyano, K. NiOx Hole Transport Layer for Perovskite Solar Cells with Improved Stability and Reproducibility. *ACS Omega* 2017, 2, 2291-2299.
305. Pae, S. R.; Byun, S.; Kim, J.; Kim, M.; Gereige, I.; Shin, B. Improving Uniformity and Reproducibility of Hybrid Perovskite Solar Cells via a Low-Temperature Vacuum Deposition Process for NiOx Hole Transport Layers. *ACS Applied Materials & Interfaces* 2018, 10, 534-540.
306. Kim, J. K. PEG-assisted Sol-gel Synthesis of Compact Nickel Oxide Hole-Selective Layer with Modified Interfacial Properties for Organic Solar Cells. 2019, 11, 120.
307. Wen, J.; Xie, J.; Chen, X.; Li, X. A review on g-C3N4-based photocatalysts. *Applied Surface Science* 2017, 391, 72-123.
308. Ong, W.-J.; Tan, L.-L.; Ng, Y. H.; Yong, S.-T.; Chai, S.-P. Graphitic carbon nitride (g-C3N4)-based photocatalysts for artificial photosynthesis and environmental remediation: are we a step closer to achieving sustainability? *Chemical Reviews* 2016, 116, 7159-7329.
309. Zheng, Y.; Lin, L.; Wang, B.; Wang, X. Graphitic carbon nitride polymers toward sustainable photoredox catalysis. *Angewandte Chemie International Edition* 2015, 54, 12868-12884.
310. Kumar, P.; Boukherroub, R.; Shankar, K. Sunlight-driven water-splitting using two dimensional carbon based semiconductors. *J. Mater. Chem. A* 2018.
311. Cao, S.; Low, J.; Yu, J.; Jaroniec, M. Polymeric photocatalysts based on graphitic carbon nitride. *Advanced Materials* 2015, 27, 2150-2176.
312. Wang, Y.; Wang, X.; Antonietti, M. Polymeric graphitic carbon nitride as a heterogeneous organocatalyst: from photochemistry to multipurpose catalysis to sustainable chemistry. *Angewandte Chemie International Edition* 2012, 51, 68-89.
313. Wang, Y.; Zhang, J.; Wang, X.; Antonietti, M.; Li, H. Boron-and Fluorine-Containing Mesoporous Carbon Nitride Polymers: Metal-Free Catalysts for Cyclohexane Oxidation. *Angewandte Chemie International Edition* 2010, 49, 3356-3359.
314. Zhang, Y.; Mori, T.; Ye, J.; Antonietti, M. Phosphorus-doped carbon nitride solid: enhanced electrical conductivity and photocurrent generation. *Journal of the American Chemical Society* 2010, 132, 6294-6295.
315. Hong, J.; Xia, X.; Wang, Y.; Xu, R. Mesoporous carbon nitride with in situ sulfur doping for enhanced photocatalytic hydrogen evolution from water under visible light. *Journal of Materials Chemistry* 2012, 22, 15006-15012.
316. Wang, Y.; Di, Y.; Antonietti, M.; Li, H.; Chen, X.; Wang, X. Excellent visible-light photocatalysis of fluorinated polymeric carbon nitride solids. *Chemistry of Materials* 2010, 22, 5119-5121.
317. Ran, J.; Ma, T. Y.; Gao, G.; Du, X.-W.; Qiao, S. Z. Porous P-doped graphitic carbon nitride nanosheets for synergistically enhanced visible-light photocatalytic H 2 production. *Energy & Environmental Science* 2015, 8, 3708-3717.

318. Lin, J.; Pan, Z.; Wang, X. Photochemical reduction of CO2 by graphitic carbon nitride polymers. *ACS Sustainable Chemistry & Engineering* 2013, 2, 353-358.
319. Wang, Y.; Li, H.; Yao, J.; Wang, X.; Antonietti, M. Synthesis of boron doped polymeric carbon nitride solids and their use as metal-free catalysts for aliphatic C–H bond oxidation. *Chemical Science* 2011, 2, 446-450.
320. Yang, S.; Gong, Y.; Zhang, J.; Zhan, L.; Ma, L.; Fang, Z.; Vajtai, R.; Wang, X.; Ajayan, P. M. Exfoliated graphitic carbon nitride nanosheets as efficient catalysts for hydrogen evolution under visible light. *Advanced Materials* 2013, 25, 2452-2456.
321. Kumar, A.; Kumar, P.; Joshi, C.; Ponnada, S.; Pathak, A. K.; Ali, A.; Sreedhar, B.; Jain, S. L. A [Fe (bpy) 3] 2+ grafted graphitic carbon nitride hybrid for visible light assisted oxidative coupling of benzylamines under mild reaction conditions. *Green Chemistry* 2016, 18, 2514-2521.
322. Kumar, A.; Kumar, P.; Pathak, A. K.; Chokkapu, A. N.; Jain, S. L. Carbon Nitride Grafted Cobalt Complex (Co@ npg-C3N4) for Visible Light− Assisted Esterification of Aldehydes. *ChemistrySelect* 2017, 2, 3437-3443.
323. Mane, G. P.; Talapaneni, S. N.; Lakhi, K. S.; Ilbeygi, H.; Ravon, U.; Al-Bahily, K.; Mori, T.; Park, D. H.; Vinu, A. Highly Ordered Nitrogen-Rich Mesoporous Carbon Nitrides and Their Superior Performance for Sensing and Photocatalytic Hydrogen Generation. *Angewandte Chemie International Edition* 2017, 56, 8481-8485.
324. Sattler, A.; Schönberger, S.; Schnick, W. Melemium Methylsulfonates HC6N7 (NH2) 3H2C6N7 (NH2) 3 (SO3Me) 3· H2O and H2C6N7 (NH2) 3 (SO3Me) 2· H2O. *Zeitschrift für anorganische und allgemeine Chemie* 2010, 636, 476-482.
325. Makowski, S. J.; Köstler, P.; Schnick, W. Formation of a Hydrogen-Bonded Heptazine Framework by Self-Assembly of Melem into a Hexagonal Channel Structure. *Chemistry-A European Journal* 2012, 18, 3248-3257.
326. Saplinova, T.; Bakumov, V.; Gmeiner, T.; Wagler, J.; Schwarz, M.; Kroke, E. 2, 5, 8-Trihydrazino-s-heptazine: A Precursor for Heptazine-based Iminophosphoranes. *Zeitschrift für anorganische und allgemeine Chemie* 2009, 635, 2480-2487.
327. Yan, S.; Li, Z.; Zou, Z. Photodegradation performance of g-C3N4 fabricated by directly heating melamine. *Langmuir* 2009, 25, 10397-10401.
328. Cui, Y.; Zhang, J.; Zhang, G.; Huang, J.; Liu, P.; Antonietti, M.; Wang, X. Synthesis of bulk and nanoporous carbon nitride polymers from ammonium thiocyanate for photocatalytic hydrogen evolution. *Journal of Materials Chemistry* 2011, 21, 13032-13039.
329. Tonda, S.; Kumar, S.; Kandula, S.; Shanker, V. Fe-doped and-mediated graphitic carbon nitride nanosheets for enhanced photocatalytic performance under natural sunlight. *Journal of Materials Chemistry A* 2014, 2, 6772-6780.
330. Jiang, J.; Ou-yang, L.; Zhu, L.; Zheng, A.; Zou, J.; Yi, X.; Tang, H. Dependence of electronic structure of gC 3 N 4 on the layer number of its nanosheets: a study by Raman spectroscopy coupled with first-principles calculations. *Carbon* 2014, 80, 213-221.
331. Zhang, J.; Zhang, M.; Lin, S.; Fu, X.; Wang, X. Molecular doping of carbon nitride photocatalysts with tunable bandgap and enhanced activity. *Journal of Catalysis* 2014, 310, 24-30.
332. Sharma, P.; Sasson, Y. A photoactive catalyst Ru-g-C3N4 for hydrogen transfer reaction of aldehydes and ketones. *Green Chemistry* 2017, 19, 844-852.
333. Yuan, B.; Chu, Z.; Li, G.; Jiang, Z.; Hu, T.; Wang, Q.; Wang, C. Water-soluble ribbon-like graphitic carbon nitride (g-C3N4): green synthesis, self-assembly and unique optical properties. *Journal of Materials Chemistry C* 2014, 2, 8212-8215.
334. Zheng, H.; Chen, W.; Gao, H.; Wang, Y.; Guo, H.; Guo, S.; Tang, Z.; Zhang, J. Melem: an efficient metal-free luminescent material. *Journal of Materials Chemistry C* 2017, 5, 10746-10753.

335. Shalom, M.; Guttentag, M.; Fettkenhauer, C.; Inal, S.; Neher, D.; Llobet, A.; Antonietti, M. In situ formation of heterojunctions in modified graphitic carbon nitride: Synthesis and noble metal free photocatalysis. *Chemistry of materials* 2014, 26, 5812-5818.
336. Kang, Y.; Yang, Y.; Yin, L. C.; Kang, X.; Wang, L.; Liu, G.; Cheng, H. M. Selective breaking of hydrogen bonds of layered carbon nitride for visible light photocatalysis. *Advanced Materials* 2016, 28, 6471-6477.
337. Yang, P.; Ou, H.; Fang, Y.; Wang, X. A facile steam reforming strategy to delaminate layered carbon nitride semiconductors for photoredox catalysis. *Angewandte Chemie International Edition* 2017, 56, 3992-3996.
338. Alibart, F.; Lejeune, M.; Durand Drouhin, O.; Zellama, K.; Benlahsen, M. Influence of disorder on localization and density of states in amorphous carbon nitride thin films systems rich in π-bonded carbon atoms. *Journal of Applied Physics* 2010, 108, 053504.
339. Zhang, Y.; Pan, Q.; Chai, G.; Liang, M.; Dong, G.; Zhang, Q.; Qiu, J. Synthesis and luminescence mechanism of multicolor-emitting gC 3 N 4 nanopowders by low temperature thermal condensation of melamine. *Scientific reports* 2013, 3, 1943.
340. Sun, C.; Tay, B.; Lau, S.; Sun, X.; Zeng, X.; Li, S.; Bai, H.; Liu, H.; Liu, Z.; Jiang, E. Bond contraction and lone pair interaction at nitride surfaces. *Journal of Applied Physics* 2001, 90, 2615-2617.
341. Niu, P.; Liu, G.; Cheng, H.-M. Nitrogen vacancy-promoted photocatalytic activity of graphitic carbon nitride. *The Journal of Physical Chemistry C* 2012, 116, 11013-11018.
342. Chen, L. C.; Teng, C. Y.; Lin, C. Y.; Chang, H. Y.; Chen, S. J.; Teng, H. Architecting nitrogen functionalities on graphene oxide photocatalysts for boosting hydrogen production in water decomposition process. *Advanced Energy Materials* 2016, 6, 1600719.
343. Yeh, T. F.; Teng, C. Y.; Chen, S. J.; Teng, H. Nitrogen-Doped Graphene Oxide Quantum Dots as Photocatalysts for Overall Water-Splitting under Visible Light Illumination. *Advanced Materials* 2014, 26, 3297-3303.
344. Yeh, T.-F.; Chen, S.-J.; Yeh, C.-S.; Teng, H. Tuning the electronic structure of graphite oxide through ammonia treatment for photocatalytic generation of H2 and O2 from water splitting. *The Journal of Physical Chemistry C* 2013, 117, 6516-6524.
345. Shi, R.; Li, Z.; Yu, H.; Shang, L.; Zhou, C.; Waterhouse, G. I.; Wu, L. Z.; Zhang, T. Effect of nitrogen doping level on the performance of N-doped carbon quantum dot/TiO2 composites for photocatalytic hydrogen evolution. *ChemSusChem* 2017, 10, 4650-4656.
346. Chen, L. C.; Teng, C. Y.; Lin, C. Y.; Chang, H. Y.; Chen, S. J.; Teng, H. Architecting nitrogen functionalities on graphene oxide photocatalysts for boosting hydrogen production in water decomposition process. *Advanced Energy Materials* 2016, 6.
347. Run, S.; Zi, L.; Huijun, Y.; Lu, S.; Chao, Z.; N., W. G. I.; Li-Zhu, W.; Tierui, Z. Effect of Nitrogen Doping Level on the Performance of N-Doped Carbon Quantum Dot/TiO2 Composites for Photocatalytic Hydrogen Evolution. *ChemSusChem* 2017, 10, 4650-4656.
348. Liang, Q.; Li, Z.; Huang, Z. H.; Kang, F.; Yang, Q. H. Holey graphitic carbon nitride nanosheets with carbon vacancies for highly improved photocatalytic hydrogen production. *Advanced Functional Materials* 2015, 25, 6885-6892.
349. Guo, Q.; Zhang, Y.; Qiu, J.; Dong, G. Engineering the electronic structure and optical properties of gC 3 N 4 by non-metal ion doping. *Journal of Materials Chemistry C* 2016, 4, 6839-6847.
350. Sun, J.; Zhang, J.; Zhang, M.; Antonietti, M.; Fu, X.; Wang, X. Bioinspired hollow semiconductor nanospheres as photosynthetic nanoparticles. *Nature Communications* 2012, 3, 1139.
351. Liu, Q.; Chen, T.; Guo, Y.; Zhang, Z.; Fang, X. Ultrathin g-C3N4 nanosheets coupled with carbon nanodots as 2D/0D composites for efficient photocatalytic H2 evolution. *Applied Catalysis B: Environmental* 2016, 193, 248-258.

352. Ye, X.; Cui, Y.; Wang, X. Ferrocene-Modified Carbon Nitride for Direct Oxidation of Benzene to Phenol with Visible Light. *ChemSusChem* 2014, 7, 738-742.
353. Chen, Z.; Sun, P.; Fan, B.; Liu, Q.; Zhang, Z.; Fang, X. Textural and electronic structure engineering of carbon nitride via doping with π-deficient aromatic pyridine ring for improving photocatalytic activity. *Applied Catalysis B: Environmental* 2015, 170, 10-16.
354. Zhang, M.; Duan, Y.; Jia, H.; Wang, F.; Wang, L.; Su, Z.; Wang, C. Defective graphitic carbon nitride synthesized by controllable co-polymerization with enhanced visible light photocatalytic hydrogen evolution. *Catalysis Science & Technology* 2017, 7, 452-458.
355. Fang, J.; Fan, H.; Li, M.; Long, C. Nitrogen self-doped graphitic carbon nitride as efficient visible light photocatalyst for hydrogen evolution. *J. Mater. Chem. A* 2015, 3, 13819-13826.
356. Qin, J.; Wang, S.; Ren, H.; Hou, Y.; Wang, X. Photocatalytic reduction of CO2 by graphitic carbon nitride polymers derived from urea and barbituric acid. *Applied Catalysis B: Environmental* 2015, 179, 1-8.
357. Luo, L.; Zhang, M.; Wang, P.; Wang, Y.; Wang, F. Nitrogen rich carbon nitride synthesized by copolymerization with enhanced visible light photocatalytic hydrogen evolution. *New Journal of Chemistry* 2018, 42, 1087-1091.
358. Zheng, X. J.; Chen, B.; Yang, M. J.; Wu, C. C.; Orler, B.; Moore, R. B.; Zhu, K.; Priya, S. The Controlling Mechanism for Potential Loss in CH3NH3PbBr3 Hybrid Solar Cells. *Acs Energy Letters* 2016, 1, 424-430.
359. Askar, A. M.; Bernard, G. M.; Wiltshire, B.; Shankar, K.; Michaelis, V. K. Multinuclear magnetic resonance tracking of hydro, thermal, and hydrothermal decomposition of CH3NH3PbI3. *The Journal of Physical Chemistry C* 2017, 121, 1013-1024.
360. Zhao, Y.; Nardes, A. M.; Zhu, K. Mesoporous perovskite solar cells: material composition, charge-carrier dynamics, and device characteristics. *Faraday Discussions* 2014, 176, 301-312.
361. Wu, C. G.; Chiang, C. H.; Chang, S. H. A perovskite cell with a record-high-V-oc of 1.61 V based on solvent annealed CH3NH3PbBr3/ICBA active layer. *Nanoscale* 2016, 8, 4077-4085.
362. Li, Z.; Boix, P. P.; Xing, G. C.; Fu, K. W.; Kulkarni, S. A.; Batabyal, S. K.; Xu, W. J.; Cao, A. Y.; Sum, T. C.; Mathews, N.; Wong, L. H. Carbon nanotubes as an efficient hole collector for high voltage methylammonium lead bromide perovskite solar cells. *Nanoscale* 2016, 8, 6352-6360.
363. Zuo, C. T.; Ding, L. M. Modified PEDOT Layer Makes a 1.52 V V-oc for Perovskite/PCBM Solar Cells. *Advanced Energy Materials* 2017, 7.
364. Liang, Y. Q.; Wang, Y. J.; Mu, C.; Wang, S.; Wang, X. N.; Xu, D. S.; Sun, L. C. Achieving High Open-Circuit Voltages up to 1.57 V in Hole-Transport-Material-Free MAPbBr(3) Solar Cells with Carbon Electrodes. *Advanced Energy Materials* 2018, 8.
365. Sheng, R.; Ho-Baillie, A.; Huang, S. J.; Chen, S.; Wen, X. M.; Hao, X. J.; Green, M. A. Methylammonium Lead Bromide Perovskite-Based Solar Cells by Vapor-Assisted Deposition. *J. Phys. Chem. C* 2015, 119, 3545-3549.
366. Ryu, S.; Noh, J. H.; Jeon, N. J.; Kim, Y. C.; Yang, S.; Seo, J. W.; Seok, S. I. Voltage output of efficient perovskite solar cells with high open-circuit voltage and fill factor. *Energy & Environmental Science* 2014, 7, 2614-2618.
367. Chen, X.; Liu, Q.; Wu, Q.; Du, P.; Zhu, J.; Dai, S.; Yang, S. Incorporating Graphitic Carbon Nitride (g-C3N4) Quantum Dots into Bulk-Heterojunction Polymer Solar Cells Leads to Efficiency Enhancement. *Advanced Functional Materials* 2016, 26, 1719-1728.
368. He, M.; Chen, Y.; Liu, H.; Wang, J.; Fang, X.; Liang, Z. Chemical decoration of CH 3 NH 3 PbI 3 perovskites with graphene oxides for photodetector applications. *Chemical Communications* 2015, 51, 9659-9661.
369. Hadadian, M.; Correa-Baena, J. P.; Goharshadi, E. K.; Ummadisingu, A.; Seo, J. Y.; Luo, J.; Gholipour, S.; Zakeeruddin, S. M.; Saliba, M.; Abate, A. Enhancing Efficiency of Perovskite Solar Cells via

N-doped Graphene: Crystal Modification and Surface Passivation. *Advanced Materials* 2016, 28, 8681-8686.
370. Jiang, L. L.; Wang, Z. K.; Li, M.; Zhang, C. C.; Ye, Q. Q.; Hu, K. H.; Lu, D. Z.; Fang, P. F.; Liao, L. S. Passivated Perovskite Crystallization via g-C3N4 for High-Performance Solar Cells. *Advanced Functional Materials* 2018, 28, 1705875.
371. Tiwana, P.; Docampo, P.; Johnston, M. B.; Snaith, H. J.; Herz, L. M. Electron Mobility and Injection Dynamics in Mesoporous ZnO, SnO2, and TiO2 Films Used in Dye-Sensitized Solar Cells. *ACS Nano* 2011, 5, 5158-5166.
372. Chandiran, A. K.; Abdi-Jalebi, M.; Nazeeruddin, M. K.; Grätzel, M. Analysis of Electron Transfer Properties of ZnO and TiO2 Photoanodes for Dye-Sensitized Solar Cells. *ACS Nano* 2014, 8, 2261-2268.
373. Stoumpos, C. C.; Malliakas, C. D.; Kanatzidis, M. G. Semiconducting Tin and Lead Iodide Perovskites with Organic Cations: Phase Transitions, High Mobilities, and Near-Infrared Photoluminescent Properties. *Inorganic Chemistry* 2013, 52, 9019-9038.
374. Emara, J.; Schnier, T.; Pourdavoud, N.; Riedl, T.; Meerholz, K.; Olthof, S. Impact of Film Stoichiometry on the Ionization Energy and Electronic Structure of $CH_3NH_3PbI_3$ Perovskites. 2016, 28, 553-559.
375. Schulz, P.; Whittaker-Brooks, L. L.; MacLeod, B. A.; Olson, D. C.; Loo, Y.-L.; Kahn, A. Electronic Level Alignment in Inverted Organometal Perovskite Solar Cells. 2015, 2, 1400532.

Appendix-A Supporting Data

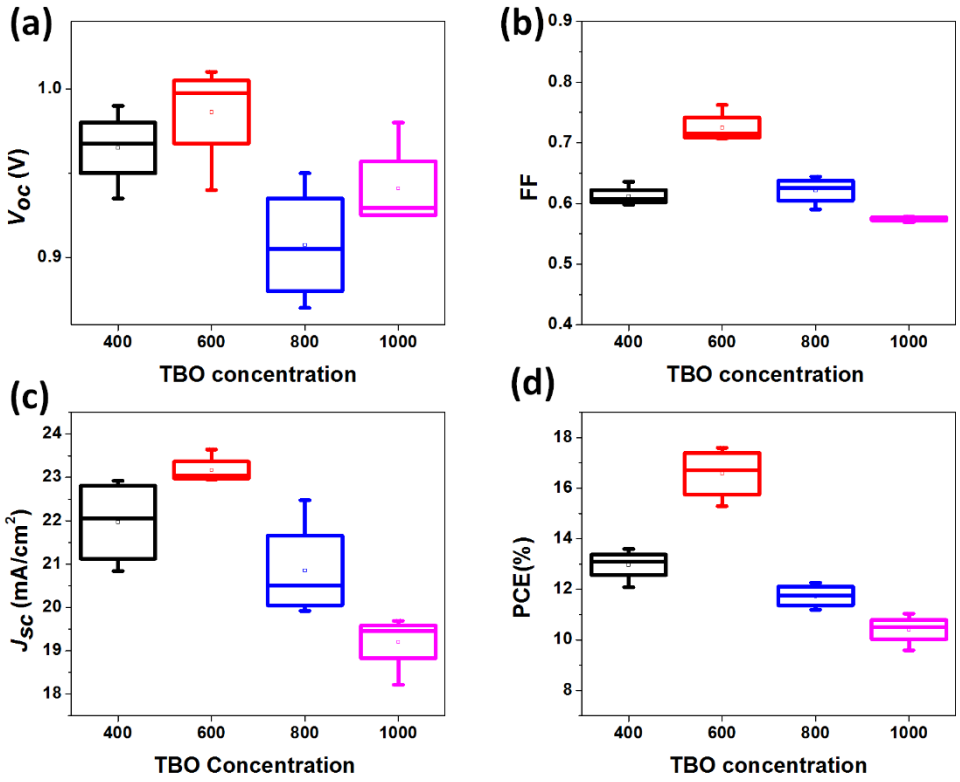

Figure A1: Effect of the dimension of TNRs on photovoltaic performance of perovskite solar cells, measured under AM 1.5 G simulated solar irradiance. Black, red, blue and magenta line represents TNRs synthesized with 400 µl, 600 µl, 800 µl and 1000 µl of TBO in precursor.

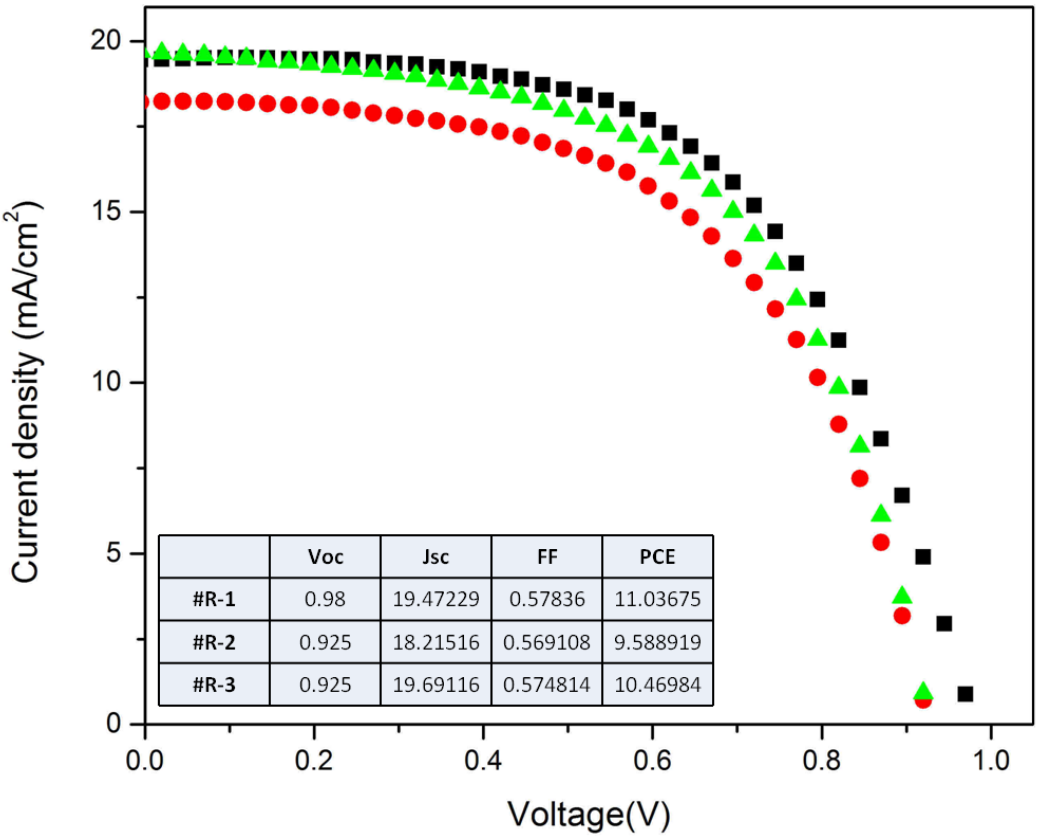

	Voc	Jsc	FF	PCE
#R-1	0.98	19.47229	0.57836	11.03675
#R-2	0.925	18.21516	0.569108	9.588919
#R-3	0.925	19.69116	0.574814	10.46984

Figure A2. J-V curves of halide perovskite solar cells constructed using nanorods ~ 150 nm in width and ~ 1 µm in length, formed using 1000 µl of TBO in the hydrothermal precursor solution. The data were measured at AM 1.5G with an intensity of 100 mW cm^{-2}.

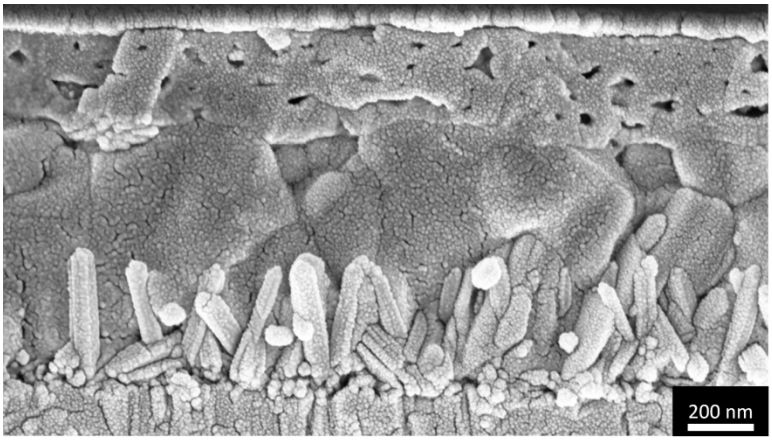

Figure A3: Cross-sectional SEM image of PSC fabricated over TNR synthesized by 600µl of TBO in precursor solution.

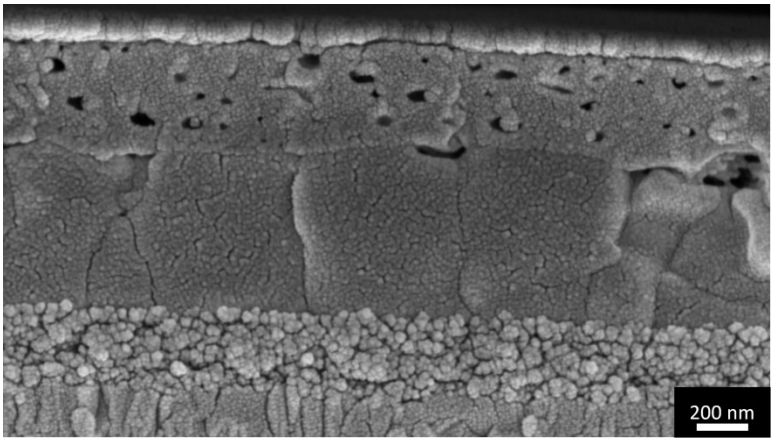

Figure A4: Cross-sectional SEM image of PSC fabricated over 200 nm of mesoporous TiO_2.

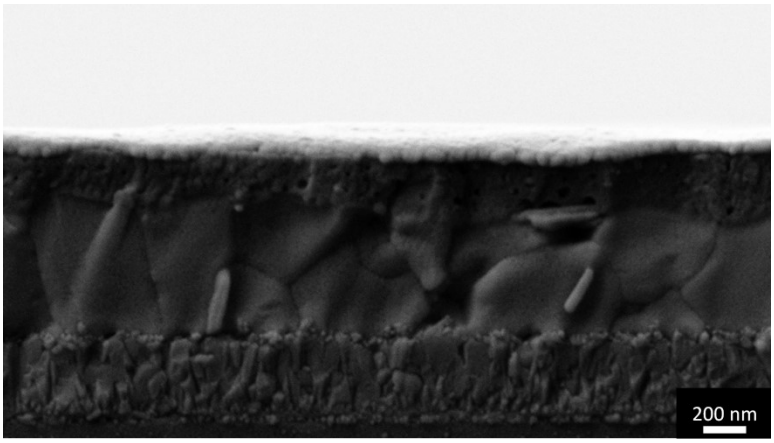

Figure A5: Cross-sectional SEM image of PSC fabricated over compact TiO_2.

Table A1: The fitted decay times for carrier dynamics probed for the different electron transporting layer. Where, $I(t) = A_1\exp(-t/\tau_1) + A_2\exp(-t/\tau_2)$.

	A_1	τ_1 (ns)	A_2	τ_2 (ns)	R-sqr	Chi-sqr
Planer	48%	2.4	52%	0.42	0.9272	2.50E-05
TNPs	65%	0.13	35%	1.36	0.9726	7.18E-04
TNRs	58%	0.087	42%	0.27	0.9985	2.20E-05

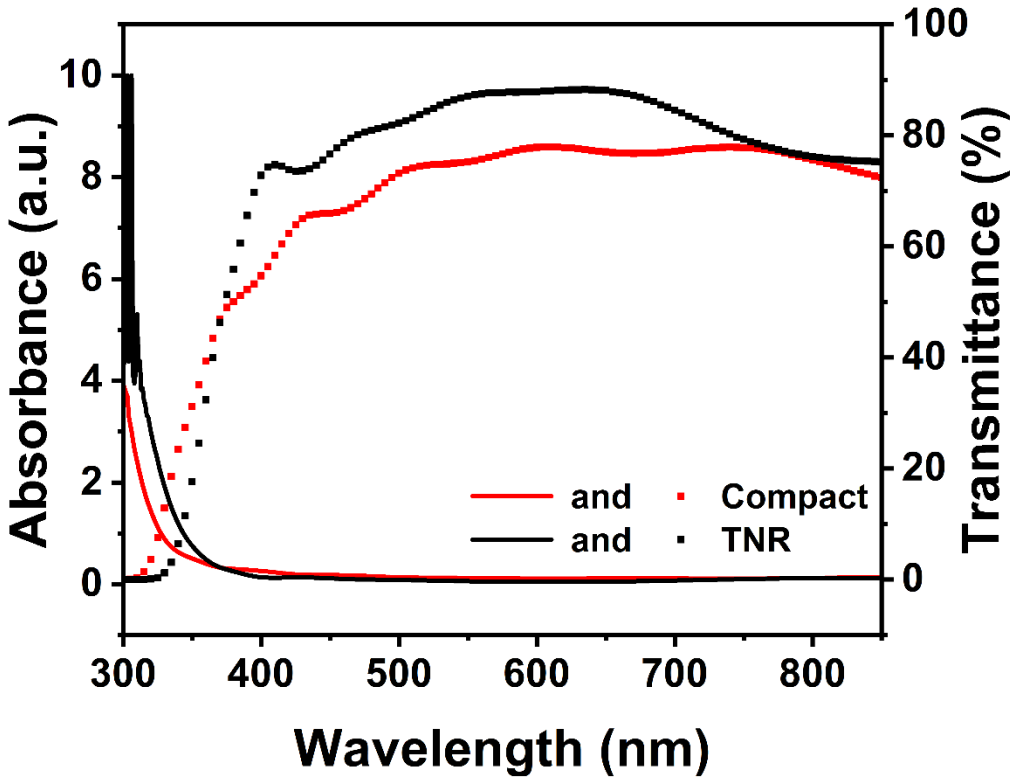

Figure A6 Absorptance and transmittance spectra of compact TiO_2 and HATNR array deposited over the FTO substrate.

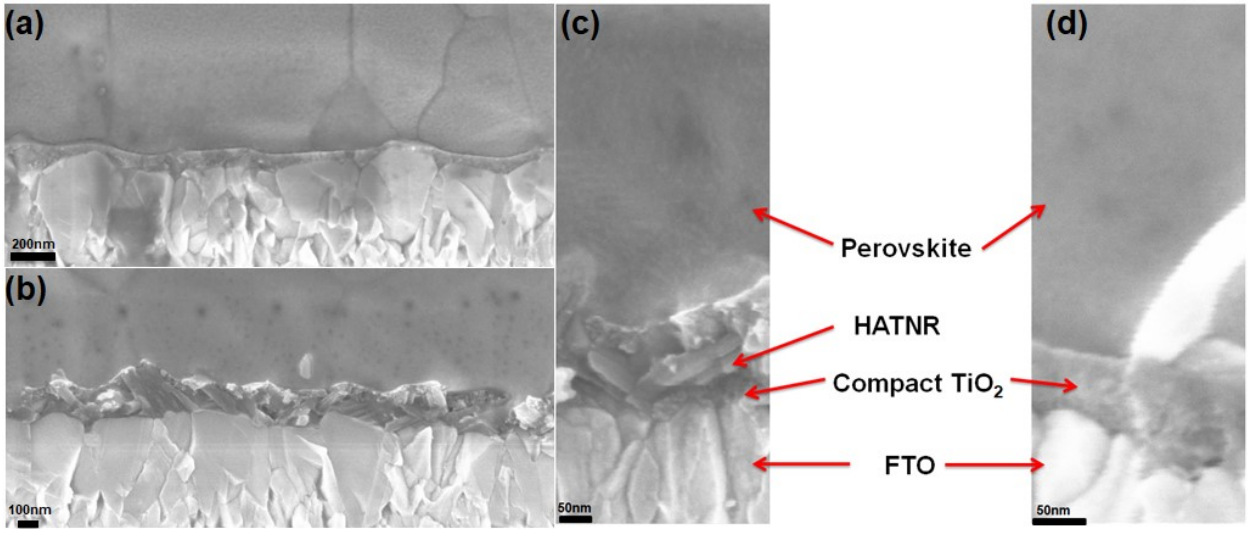

Figure A7 High-resolution FESEM images showing a cross-sectional view of a perovskite solar cell (with different magnification) made with compact TiO_2 layer (a) and (d) HATNRs (b) and (c).

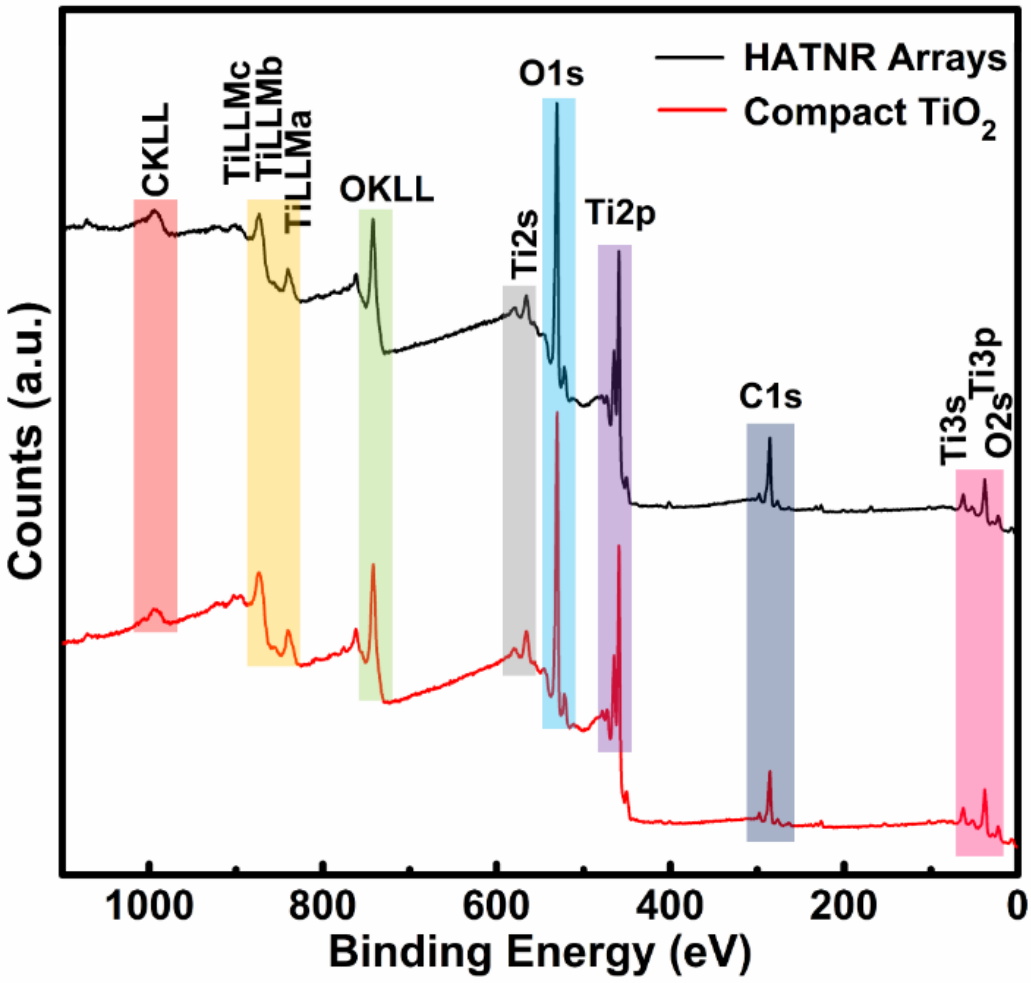

Figure A8. XPS elemental survey scan of compact TiO_2 (red) and HATNR arrays (black).

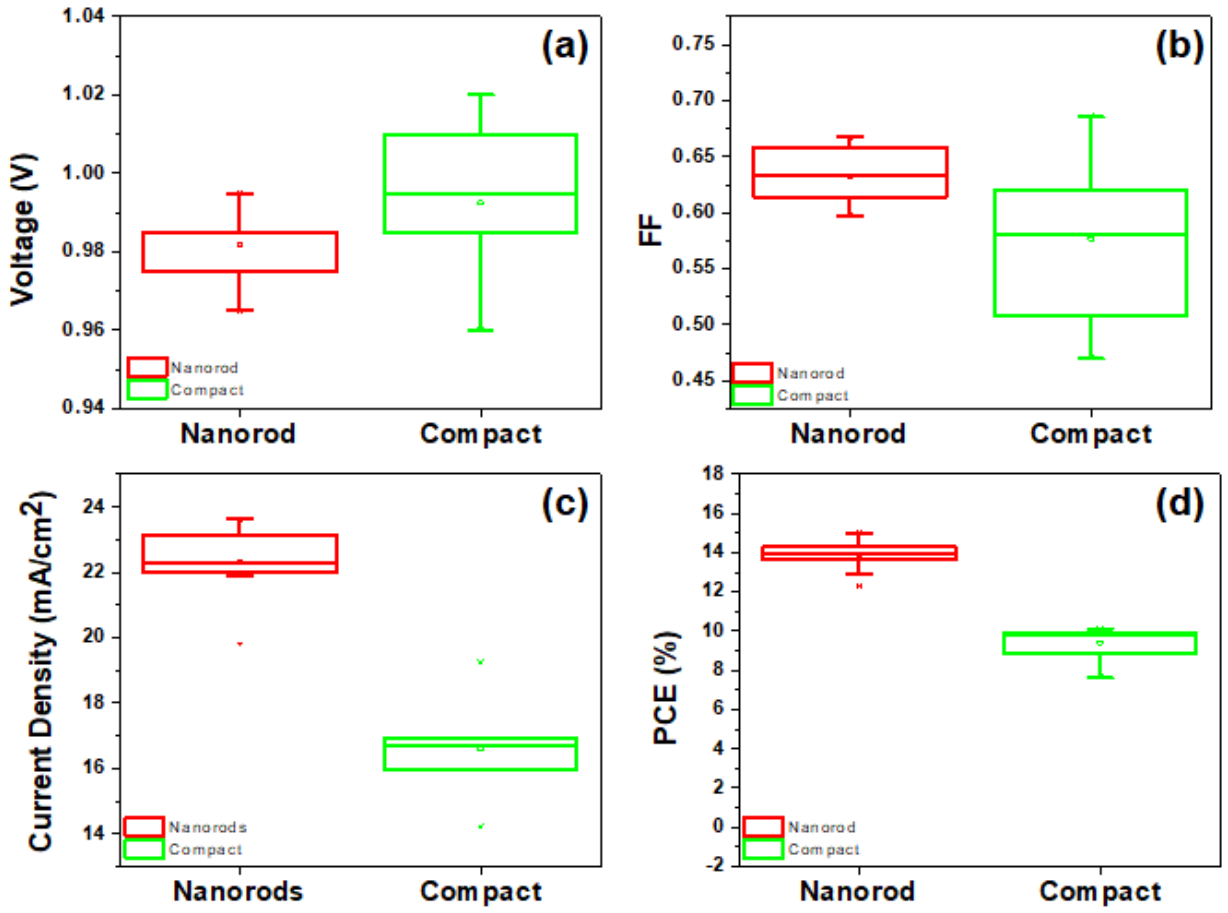

Figure A9. Summary of the performance of halide perovskite solar cells for compact TiO_2 and HATNR morphologies: (a) V_{oc}, (b) FF, (c) J_{sc}, and (d) PCE. All the performance data were measured at AM 1.5G.

Table A2. Photovoltaic performance of perovskite solar cells made with compact TiO_2 and HATNR under AM 1.5G simulated light.

		V_{oc} (V)	J_{sc} (mA/cm^2)	FF	PCE (%)
HATNRs	Average	0.98±0.01	22.32±1.07	0.63±0.02	13.87±0.8
	Champion	0.99	22.85	0.67	15.03
Compact TiO_2	Average	0.99±0.02	16.59±1.55	0.58±0.07	9.42±0.79
	Champion	0.99	16.58	0.62	10.12

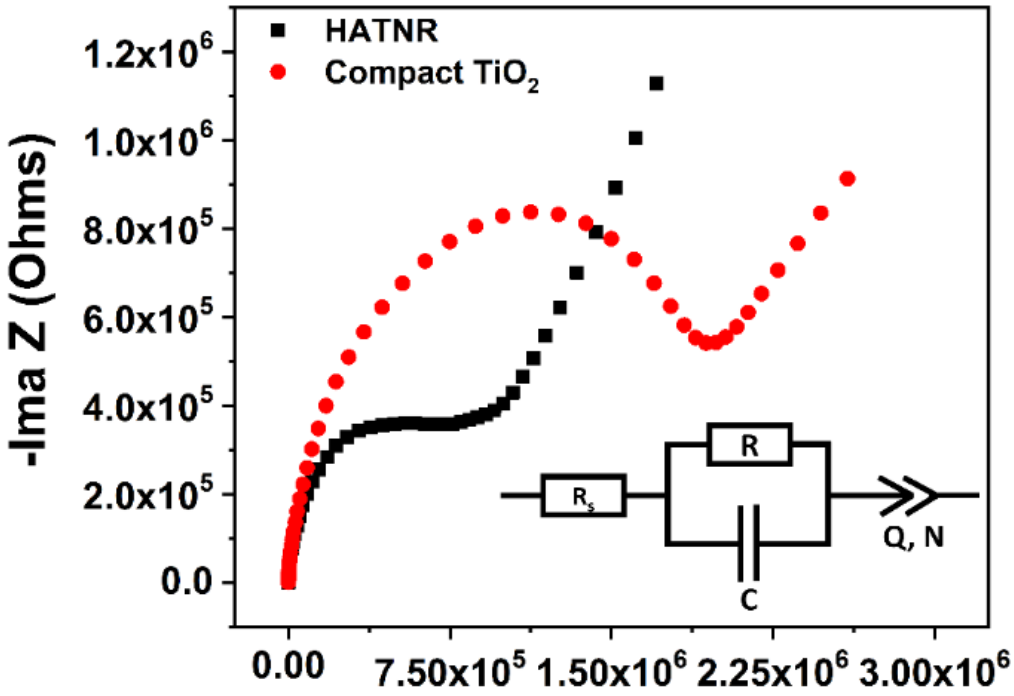

Figure A10. Nyquist plots for HATNR and compact TiO_2 obtained in dark condition at open circuit. Equivalent circuit for the plots is shown in the inset, wherein Rs is series resistance, C is high-frequency capacitance, R is recombination resistance, and Q is a constant phase element (CPE) with coefficient N. Upon fitting the equivalent circuit (shown in the inset) R is $5x10^5$ and $15.2x10^5$ Ohms for HATNRs and compact TiO_2, respectively. C is $2.5x10^{-10}$ and $1.5x10^{-9}$ F for HATNR and compact TiO_2, respectively.

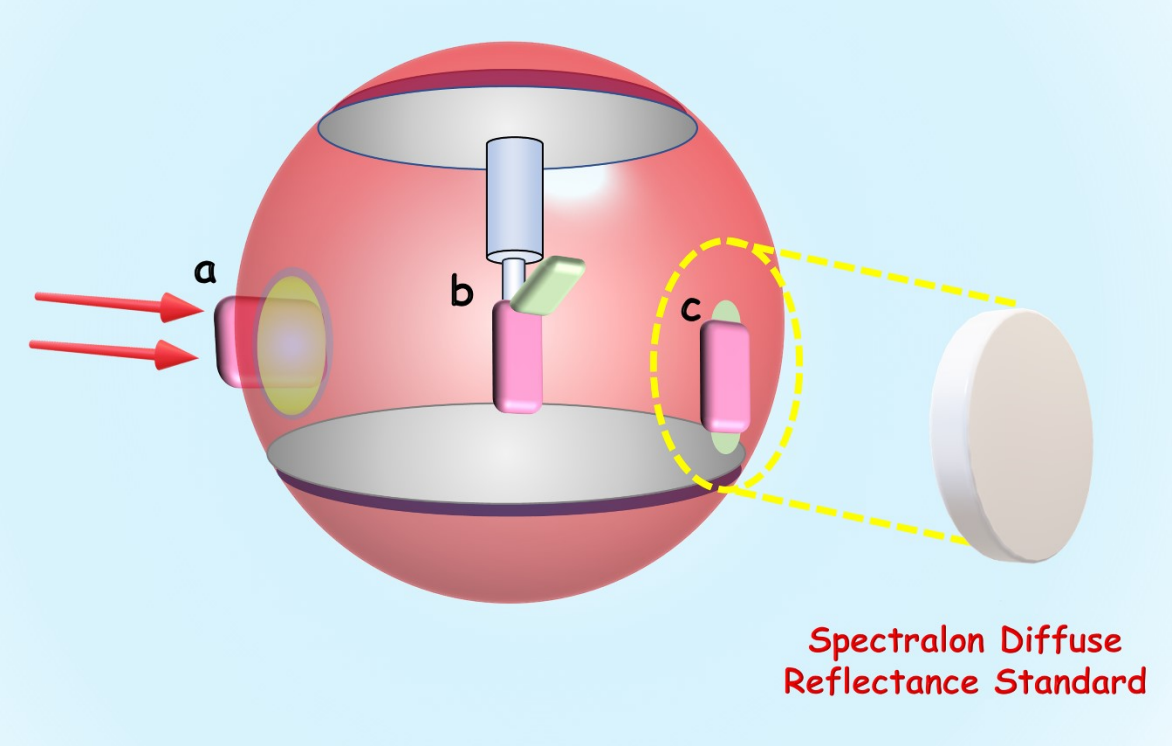

Figure A11. Schematic illustration of the integrating sphere accessory used for UV-Vis-NIR spectroscopic measurements, and the placement of samples corresponding to different configurations. ‘a’, ‘b’ and ‘c’ refer to different possible sample positions.

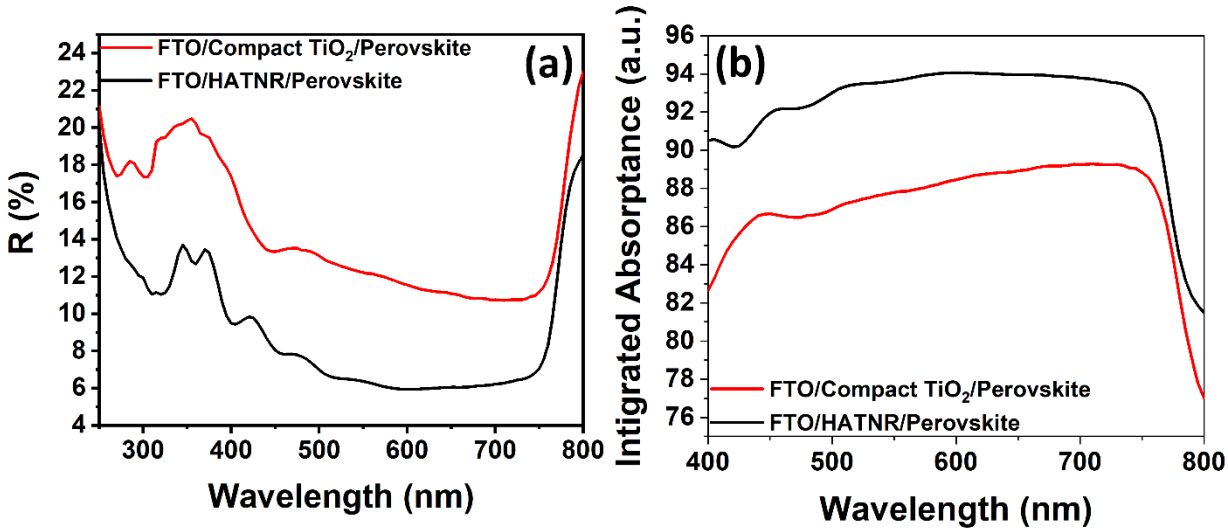

Figure A12. UV-Vis spectra showing diffuse reflectance (a) and integrated absorptance (b) measured from samples consisting of perovskite layers deposited over compact TiO_2 ETL (red) and HATNR ETL (black) on FTO substrate.

Table A3: Calculated HOMO and LUMO energies for perovskites particles and their energies of adsorption on the NiO surface for two different geometries G2 and G3.

	HOMO, eV	**LUMO, eV**	**E_{ads}, G2, eV**	**E_{ads}, G3, eV**
$CH_3NH_3PbBr_3$	-5.60	-3.99	6.12	9.75
$CH_3NH_3PbI_3$	-5.59	-4.08	4.13	8.01

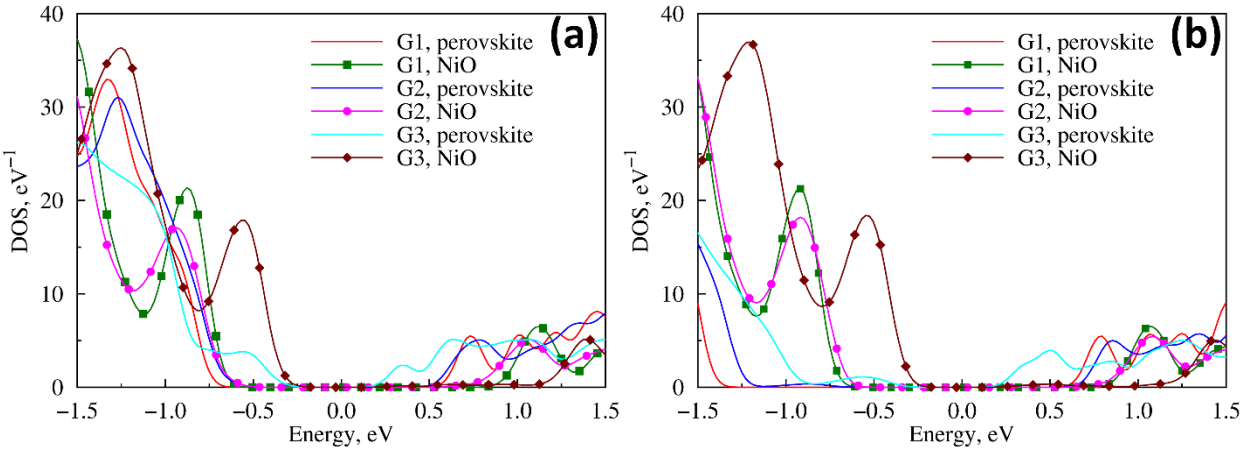

Figure A13: Density of state distribution for NiO surface and (a) $MAPbI_3$ cluster and (b) $MAPbBr_3$ cluster.

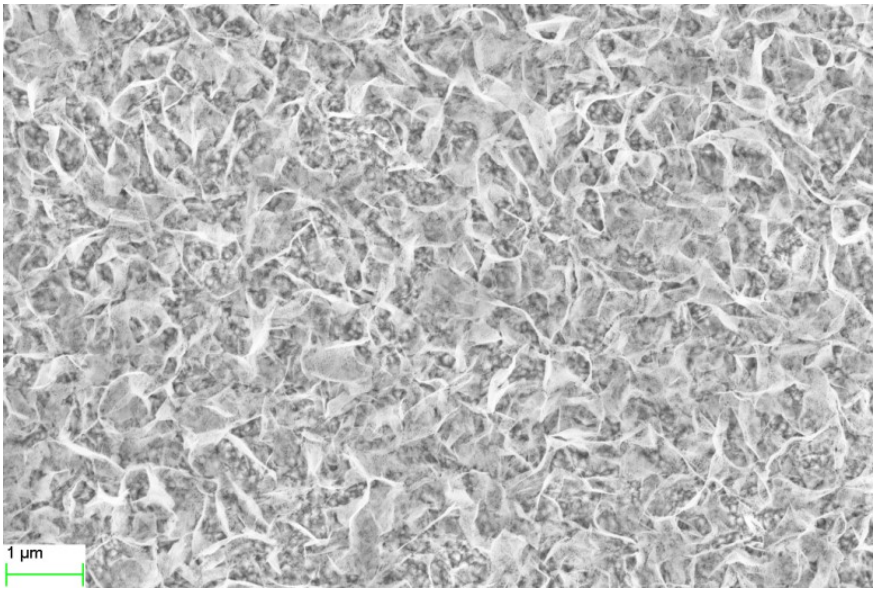

Figure A14: Top SEM image of NiO nanostructure made with 0.5 mM concentration of $NiCl_2.6H_2O$ in growth solution showing exposed FTO substrate.

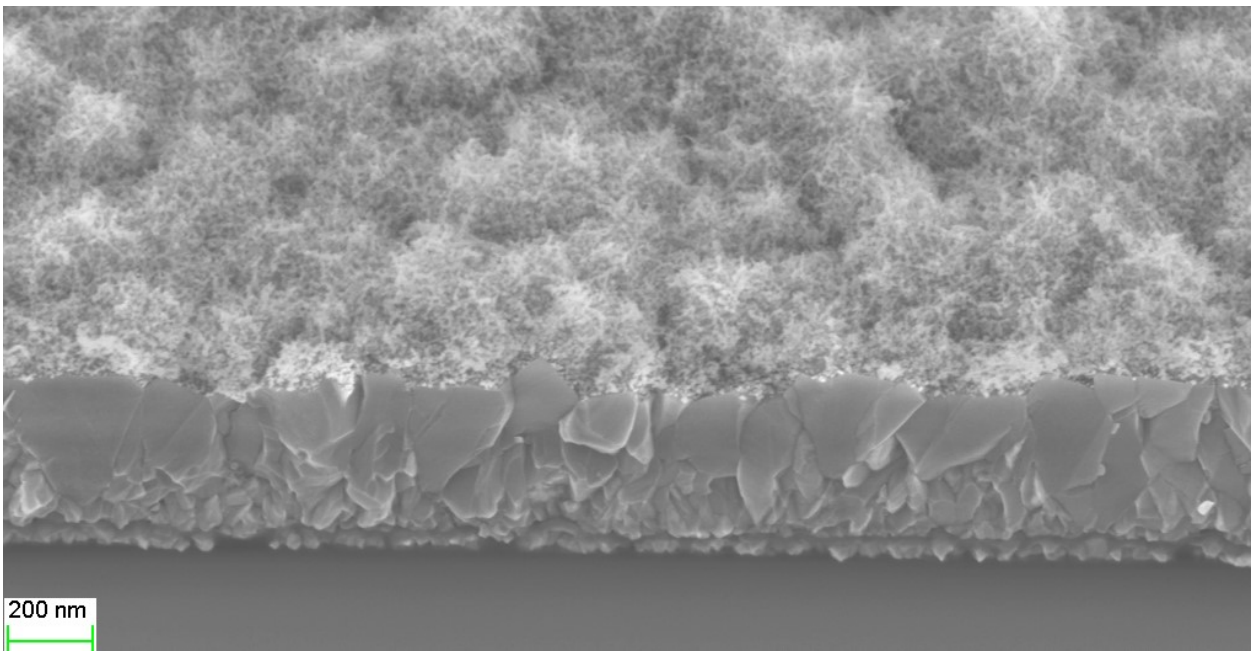

Figure A15: Tilted cross-sectional SEM image of NiO nanostructure made with a 1mM concentration of $NiCl_2.6H_2O$ in growth solution shows conformal deposition of NiO on FTO substrate.

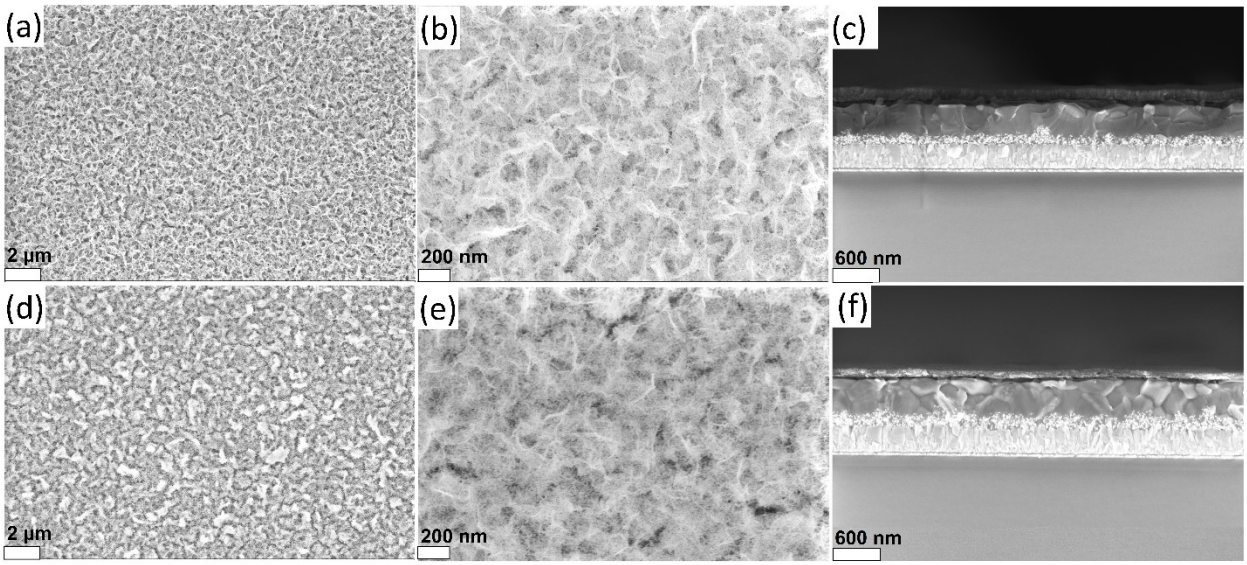

Figure A16: Top-view FESEM images of NiO nanostructure (a, b) made with 3 mM and (d,e) 5 mM of $NiCl_2.6H_2O$. Cross-sectional image of perovskite solar cell made with (c) 3mM and (f) 5mM of $NiCl_2.6H_2O$.

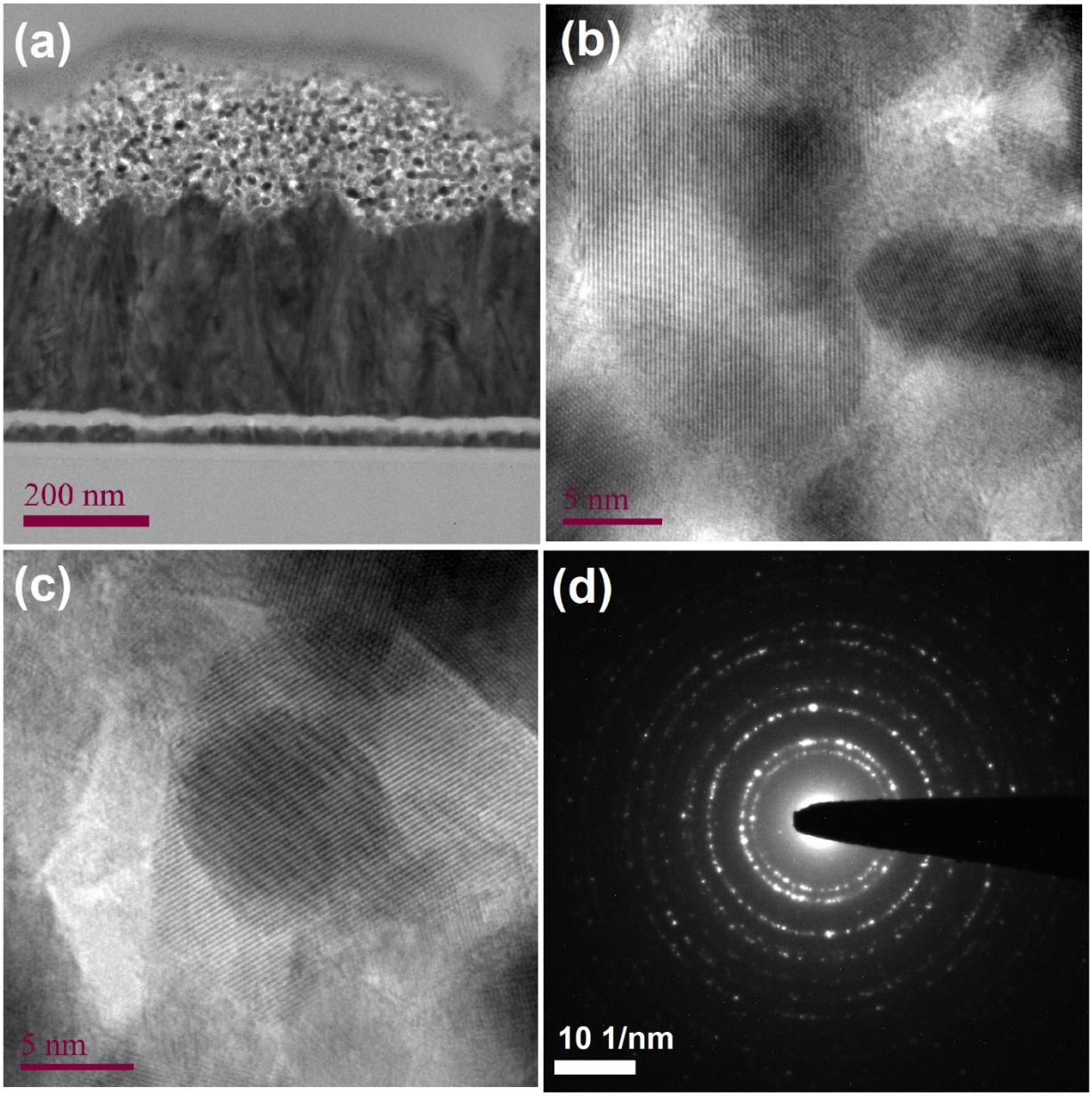

Figure A17: HR-TEM image of nanostructure NiO thin film (1 mM $NiCl_2.6H_2O$) (a) side view of FIB snipped sample, (b) and (c) high magnification TEM images at 5 nm scale bar showing lattice fringes, and (d) SAED pattern showing diffraction rings.

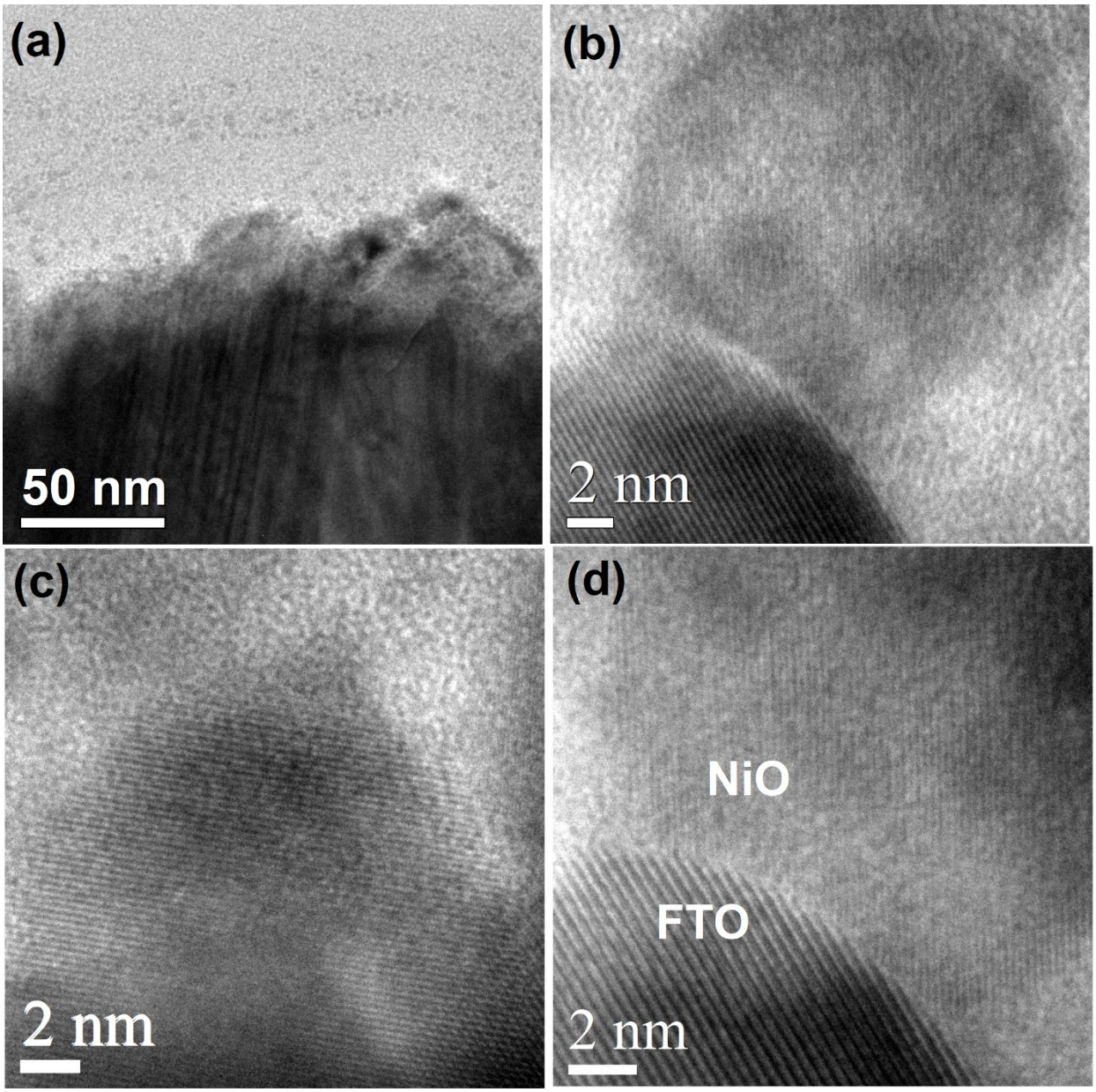

Figure A18: HR-TEM image of compact NiO thin film (a) side view of FIB snipped sample, (b) and (c) high magnification TEM images at 5 nm scale bar and (d) TEM image showing FTO and NiO interfacial contact.

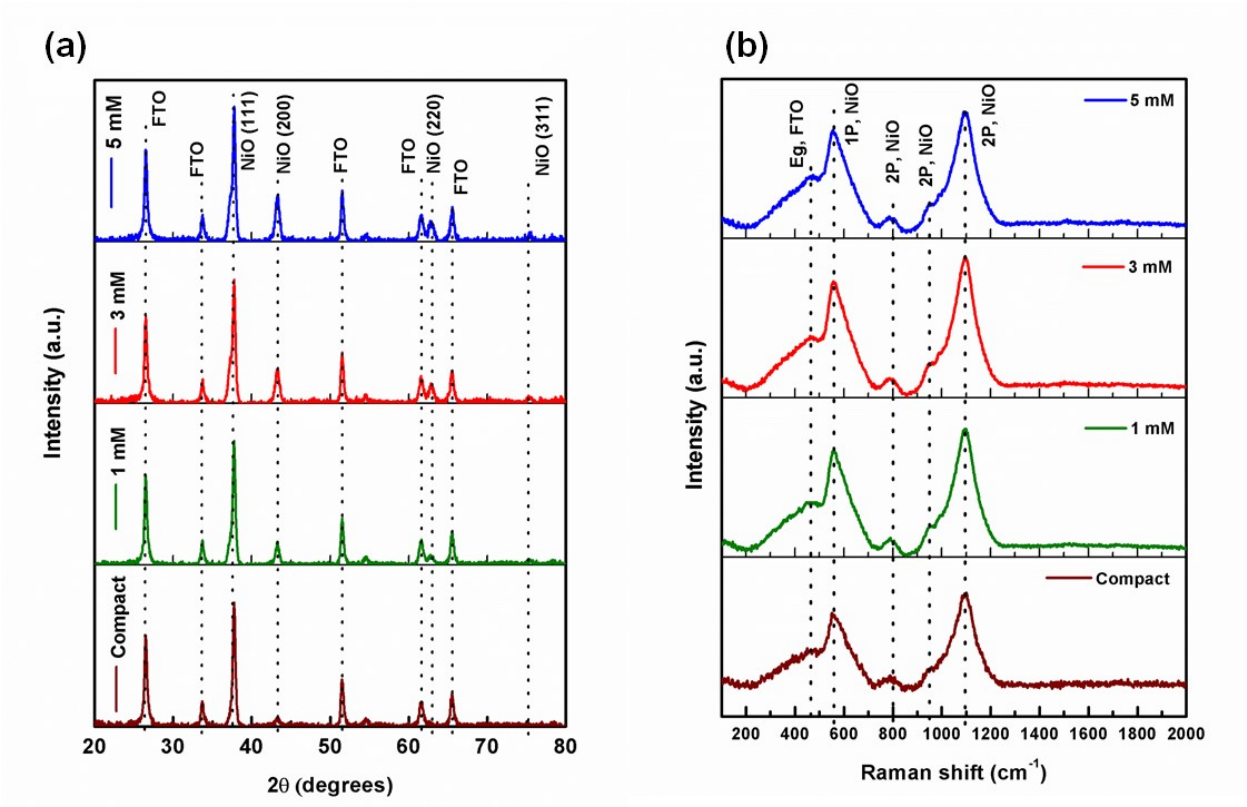

Figure A19: (a) XRD spectra and (b) Raman spectra of compact NiO and NiO nanostructures prepared with different concertation of $NiCl_2.6H_2O$ in the hydrothermal growth solution.

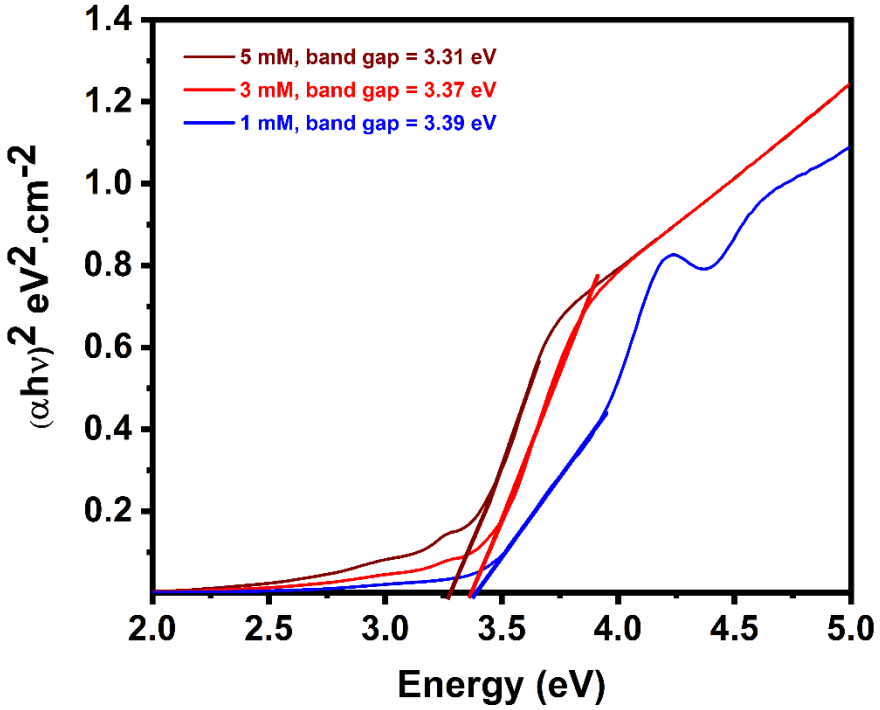

Figure A20: Tauc plots of NiO nanostructures made with different concentrations of $NiCl_2.6H_2O$ in growth solution.

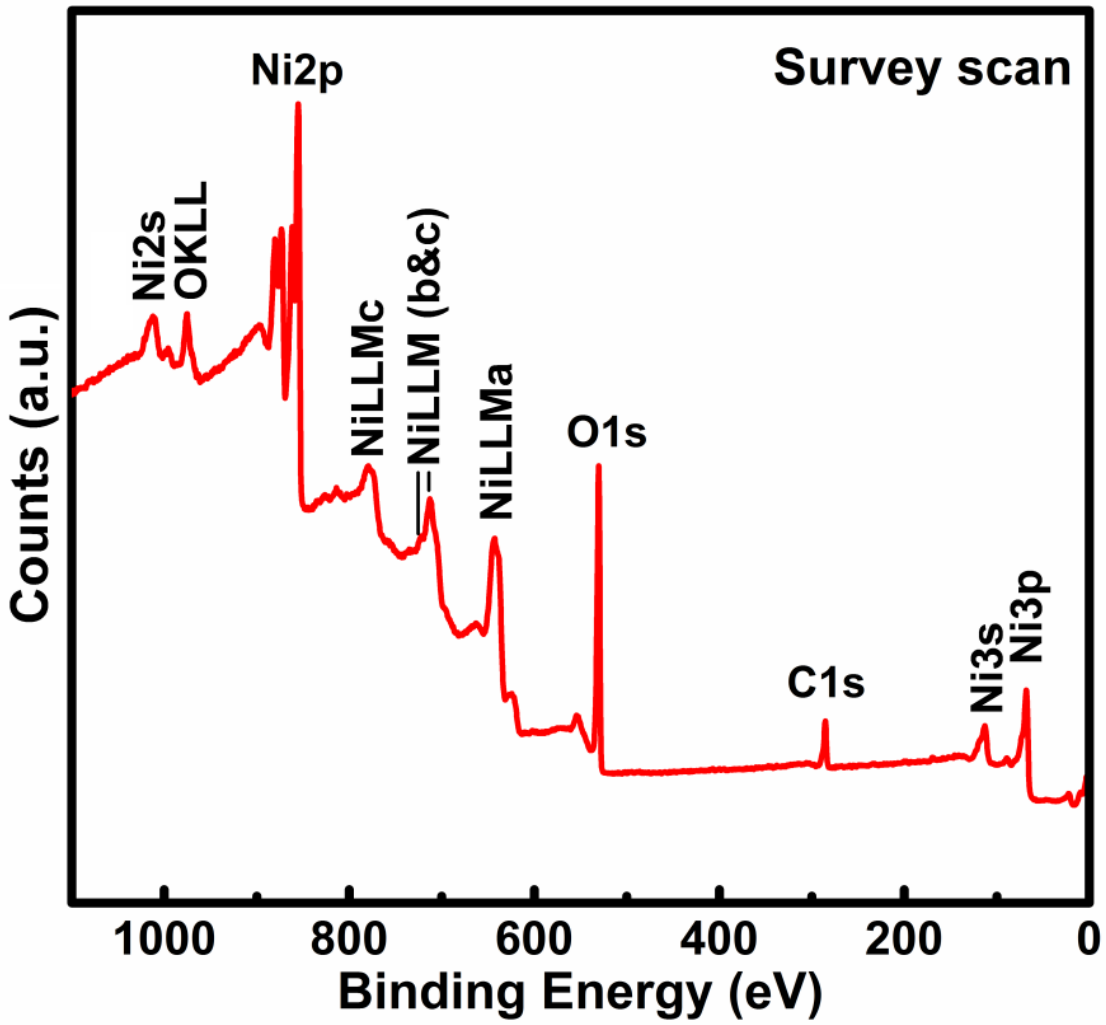

Figure A21: XPS elemental survey scan of NiO network thin film.

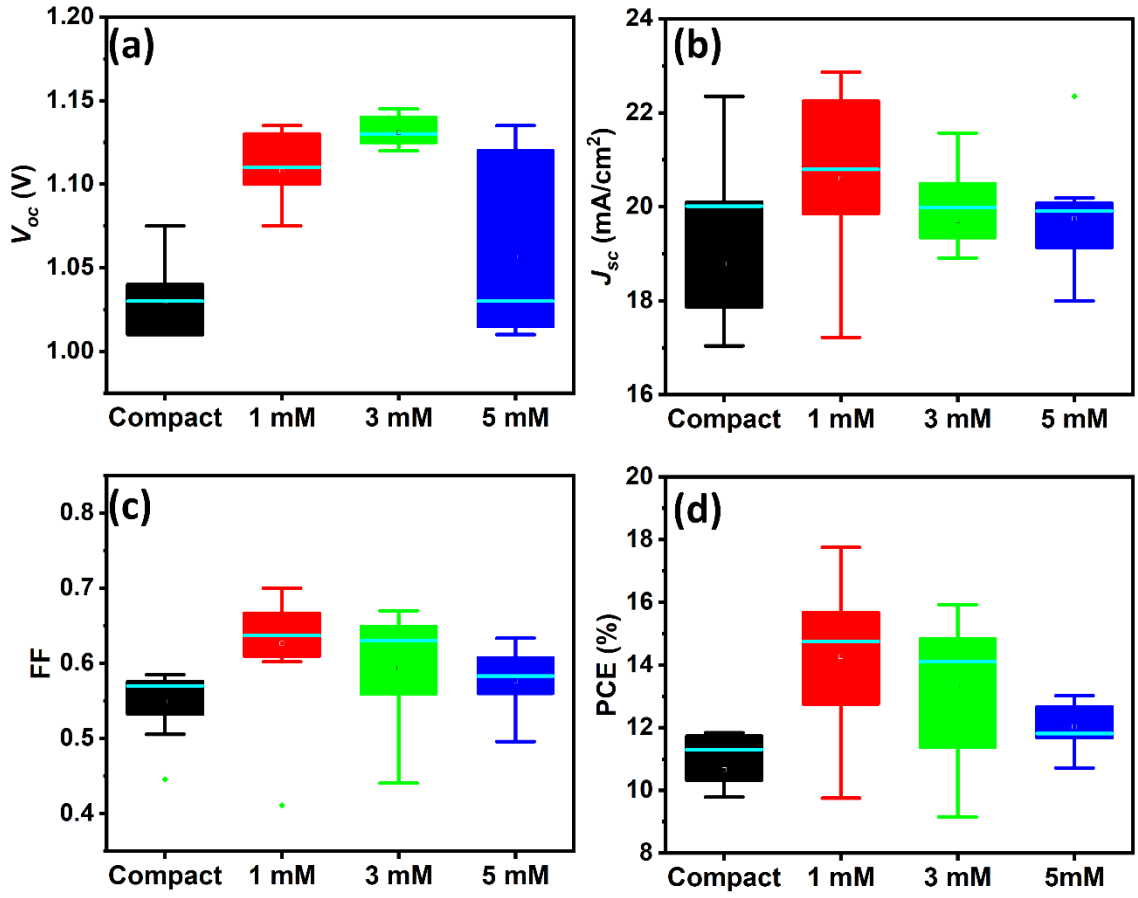

Figure A22: Box charts of (a) V_{oc}, (b) J_{sc}, (c) FF and (d) PCE for perovskite solar cells based on compact NiO and NiO nanostructure made with different concentration of $NiCl_2.6H_2O$.

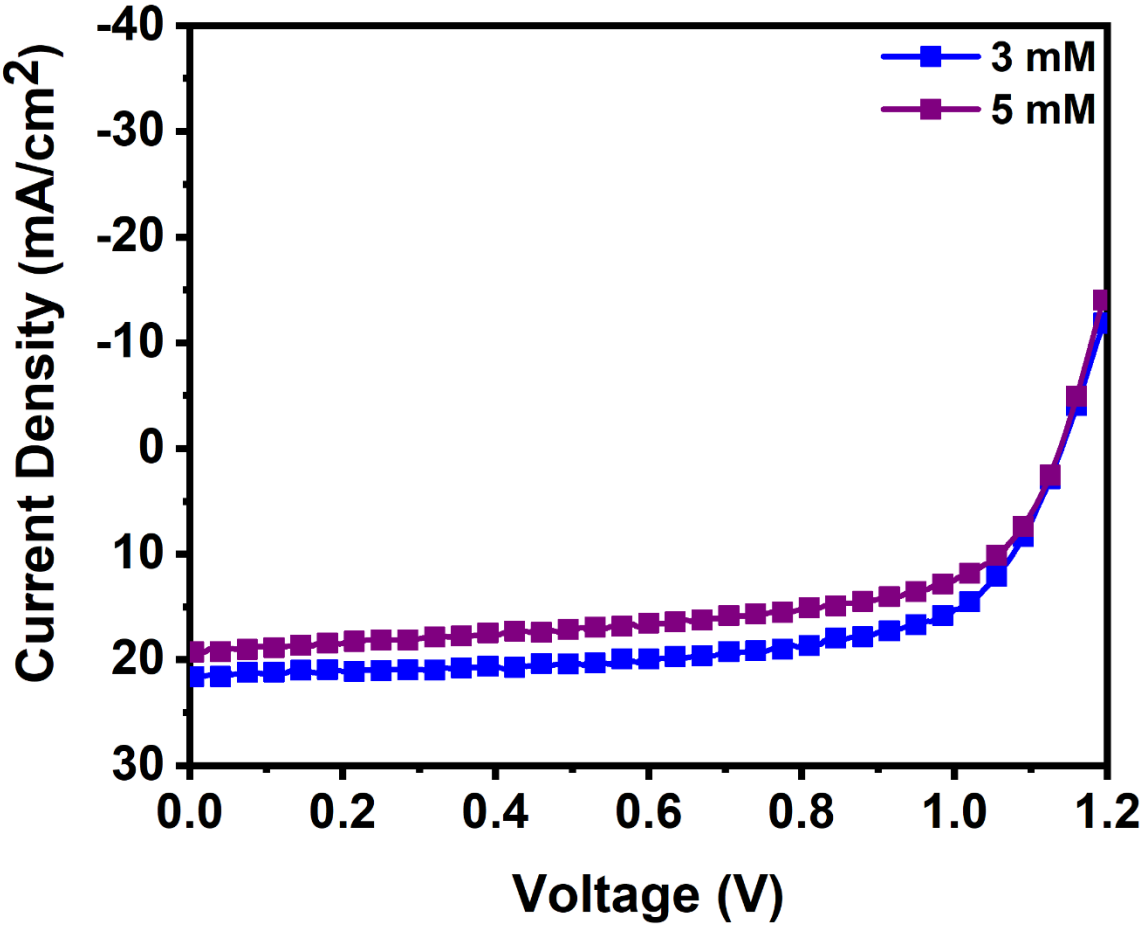

Figure A23: Current-voltage curves of perovskite solar cell made with nanostructure NiO hole transporting layer made with 3 mM and 5 mM of $NiCl_2.6H_2O$. The measurement was carried out under AM1.5 G illumination at 100 mW/cm^2 with an active area of 6 mm^2.

Table A4: Fitting parameters of time-resolved photoluminescence spectra for HTL free perovskite layer and perovskite layer deposited over compact and nanostructured NiO coated FTO substrate. The values of the goodness-of-fit parameter (r^2) are all close to 1.0

	A_1	τ_1 (ns)	A_2	τ_2(ns)	A_3	τ_3(ns)	τ_{avg} (ns)
Bare FTO	0.43	11.92	0.39	151.37	-	-	54.73
FTO/Compact NiO	0.89	1.71	0.13	13.19	0.041	569.89	20.17
FTO/NiO nanostructure	0.85	1.55	0.19	8.37	0.013	122.25	1.51

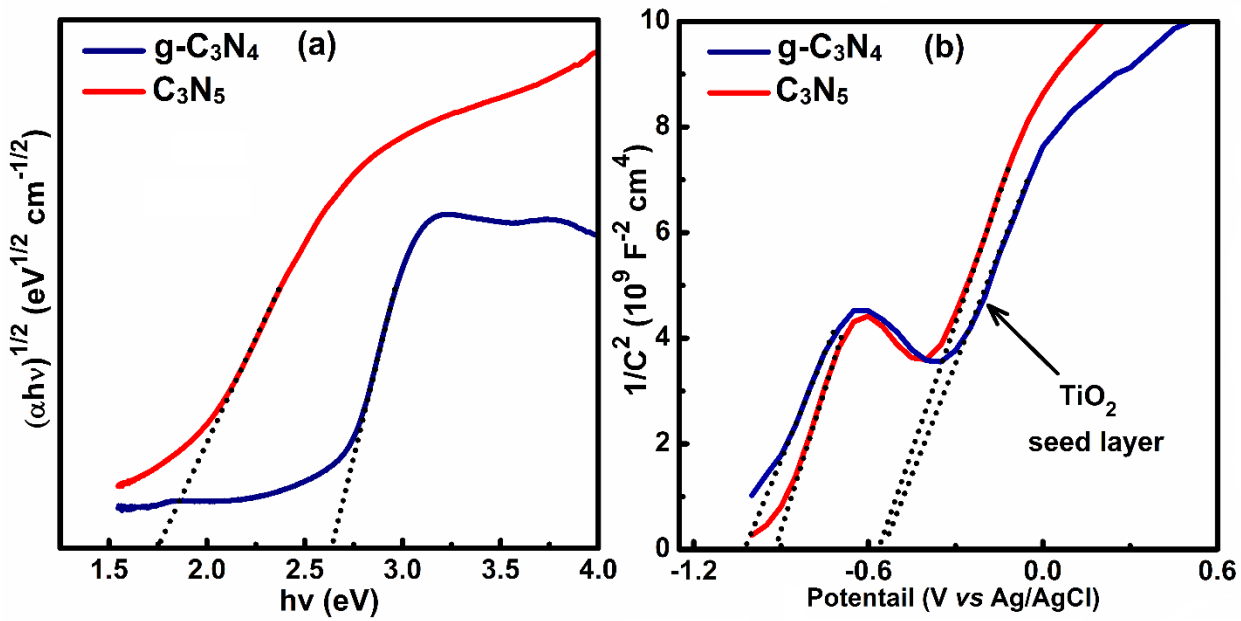

Figure A24. (a) Tauc plot of g-C_3N_4 (blue) and C_3N_5 (red) for bandgap determination and (b) Mott Schottky plot of g-C_3N_4 (blue) and C_3N_5 (red) in 0.5 M Na_2SO_4 at 1K frequency.